



Water mixing processes in the critical zone: evidence from trace elements and Sr-Nd-Pb-U isotopes

Cristina Moragues Quiroga

► To cite this version:

Cristina Moragues Quiroga. Water mixing processes in the critical zone: evidence from trace elements and Sr-Nd-Pb-U isotopes. Geochemistry. Université de Strasbourg, 2018. English. NNT: 2018STRAH002 . tel-02534980

HAL Id: tel-02534980

<https://theses.hal.science/tel-02534980>

Submitted on 7 Apr 2020

HAL is a multi-disciplinary open access archive for the deposit and dissemination of scientific research documents, whether they are published or not. The documents may come from teaching and research institutions in France or abroad, or from public or private research centers.

L'archive ouverte pluridisciplinaire **HAL**, est destinée au dépôt et à la diffusion de documents scientifiques de niveau recherche, publiés ou non, émanant des établissements d'enseignement et de recherche français ou étrangers, des laboratoires publics ou privés.

**ÉCOLE DOCTORALE DES SCIENCES DE LA TERRE
ET DE L'ENVIRONNEMENT, ED413**

Laboratoire d'Hydrologie et de Géochimie de Strasbourg, UMR 7517

THÈSE présentée par :

Cristina Moragues-Quiroga

soutenue le : **29 mars 2018**

pour obtenir le grade de : **Docteur de l'université de Strasbourg**

Discipline/ Spécialité : **Géochimie de l'environnement**

**Water mixing processes in the Critical Zone:
evidence from trace elements
and Sr-Nd-Pb-U isotopes**

THÈSE dirigée par :
M. STILLE Peter

Directeur de recherches, UniStra

RAPPORTEURS :
Mme. DIA Aline
M. PINAY Gilles

Directeur de recherches, CNRS
Directeur de recherches, IRSTEA

AUTRES MEMBRES DU JURY :

Mme. SCHMITT Anne-Désirée
M. LEGOUT Arnaud
M. HISSLER Christophe

MCF – MCUPH, UniStra (examineur)
Chargé de recherches, INRA (examineur)
Senior R&T associate, LIST (co-directeur)

Acknowledgements

During the last four years, many people were involved in this research providing academic, technical or moral help to make the present thesis and a great life experience happen.

First and foremost, I would like to express my deepest gratitude to both Dr. Christophe Hissler and Dr. Peter Stille for giving me the opportunity to perform this work under their guidance.

I would also like to thank Dr. Christophe Hissler for his constant scientific support as well as for his readiness to discuss and encourage me to discover new things. His motivation and great efforts to conceal geochemistry and hydrology were essential for the success of this thesis and manifold research perspectives that opened up.

Dr. Peter Stille, on the other hand, cannot be thanked enough. His supervision, advice and availability for in-depth discussions brought this work forward even after his retirement. Whether “in the region” or “in the North”, his immense knowledge would reach and shed light into my research, his supervision becoming a cornerstone for this work, and he himself a mentor for me.

I would like to sincerely thank Dr. Arnaud Legout for following the progress of this work, giving constructive input and rising important questions to it, as well as welcoming me at INRA Nancy.

I am grateful to Dr. François Chabaux for academically adopting me when needed and for the scientific and tutoring support at LHyGeS.

Special thanks go to Dr. Anne-Desirée Schmitt and to Dr. Aline Dia and Dr. Gilles Pinay as president and reporters of my thesis jury respectively. I highly appreciate their effort to come to Luxembourg and read the manuscript, and their challenging and fruitful questions during the defence.

I was very fortunate to count on an extended scientific, technical and administrative team to carry out this project, both in Luxembourg and Strasbourg: I am very grateful

- *to Dr. Laurent Pfister, on the one hand for his great management work as head of the CAT research group, but also for his scientific, strategic and moral support all along my PhD studies. I feel lucky and happy of having been part of the CAT team under his lead.*
- *To Dr. Phillippe Ackerer, Dr. Damien Lemarchand and Dr. Gwenaël Imfeld, for their assistance and support regarding my situation between LHyGeS and LIST.*
- *to Dr. Eric Pelt, it was not always easy with my lab work at LHyGeS regarding Sr, Nd, Pb, U... and Th(!) isotopes, but I am extremely thankful for his dedicated time and efforts to teach and help me to get it all done in the most accurate and precise way possible. I equally appreciate the many discussions in the fields of geochemistry, sociology and psychology, - I really had some intensive learning about both science and life!*
- *to François Barnich, for all his formation hours and analytical work to measure the many physico-chemical parameters of my many water samples, and for being the haven of peace (inside and outside the lab) any research group could wish.*
- *to Jérôme Juilleret, for his help in the field and labs, and for the very instructive and fruitful discussions and contributions about the geological aspects of this work.*
- *to Jeff Iffly, for introducing me so nicely the Weierbach, its devices, and data, for the great help dealing with them, and for the 24 hours back up during the sampling campaigns.*
- *to Laurent Gourdol, for his contributions and support on all the statistical analyses of this work, and also in the field.*
- *to Thierry Perrone, for his easy-going and constant support in the LHyGeS labs.*
- *to Johanna Ziebel, Delphine Collard, René Boutin, Giles Morvan and Amélie Aubert, for so much and so good analytical work done in the spectrometry and mineralogy labs for this project.*
- *to Elisabeth Cloth, Sabrina Gaillet and Leyla Ermis, for all their administrative assistance, predisposition to help and good mood.*
- *to the National Research Fund of Luxembourg, for the financial support.*

A great thank you goes to all the friends and colleagues I met in Luxembourg and Strasbourg that made work and life in these places so appealing and fun, in particular

- *to my CAT girls, Marta, Barbara and Níria, for the super fun talks and the constant moral and scientific support, which reached unknown limits at the time of writing my manuscript and preparing my defence.*

- to Michael, “Nikito”, Enrico, Julian, Gwen, Jeremy and Stan, for making possible, together with the rest of the CAT group, such a professional and joyful work environment.
- to Annelie, Marco and Fintan, for the moral (and physical) support, the music and sports!
- to the other ERIN colleagues, Mahmood, Anne, Jasper, the 2 diatomist Carlos, Kanishka, Philippe, Oli, and some of the greatest characters of MRT/Uni.lu, Vene, Olivier, Miguel, David, Inma, Alex.... thank you so much for the good times around food, coffee or a beer that made the time at LIST so enriching and enjoyable.
- to the LHyGeS people, Jean-Michel, Eric L., Mylène, Marionne, Ivan, Coralie, Julian, Justine, Anne, Marianna, Arnaud, Pablo, Fatima... and especially to Clio, for welcoming me in their group even if I was there only for short periods and often too busy, for their patience when I “blocked” the labs, for teaching me most of the French I know (baaaah... mais oui!) and for the good times around “un verre” at the Milano.
- to Richard, for being always so caring and for the very helpful life and science talks.
- to the first colleagues I met during the CRP Lippman times, Anna, Jay, Laura, Giovanni, Andrew... for their help in my first steps as a very young researcher in Luxembourg, as well as to Chiara, who deserves a line apart for additionally making me feel home.
- to Anne Z. and Loes, for warmly welcoming me in research (and even in their houses) as an intern and for encouraging me to pursue this PhD.
- to Xavier and Aina, for taking so much care of me from beginning till end, in spite of having a construction site at home.
- to my Howald family, Canan, Ben, Mourad and Gaia, for the great times around the kitchen table after work, as to Amaia and Javi, for giving me that Spanish spark back every time we met.

Last but not least, I would like to thank to my unconditional and most beloved supporters. Many thanks to my mother, Sol, for her constant motivation and exemplary courage in life and for transmitting me, together with my father, the love for nature that brought me here. I am grateful to my sister and best friend, Solete, for holding my hand ever since we met and for bringing a good bit of reality and lots of happiness to the end of my thesis by making me aunt of the loveliest boy, Juan. For that, thanks to him too. Thanks to the other men of my family, Kiko, Toni, and Felipe, for their constant good-humoured cheering. And finally, I am most thankful to Mads. I thank him from the bottom of my heart for standing by my side no matter the distance, the issue or the mood; for being a source of comfort, joy, common sense and also scientific spirit all along this PhD journey and particularly at the very challenging end.

Contents

INTRODUCTION	1
CHAPTER 1. STUDY SITE.....	7
1.1 GEOLOGICAL AND GEOMORPHOLOGICAL SETTINGS.....	7
1.1.1 <i>Regolith stratigraphy and classification</i>	9
1.2 CLIMATE AND HYDROLOGICAL SETTINGS	12
CHAPTER 2. MATERIALS AND METHODS	15
2.1 SAMPLING STRATEGY AND METHODS.....	15
2.1.1 <i>Dusts</i>	15
2.1.2 <i>Organic horizons: litter and humus</i>	16
2.1.3 <i>Regolith materials</i>	16
2.1.4 <i>Waters</i>	17
2.2 LEACHING EXPERIMENTS.....	19
2.3 MINERALIZATION OF SAMPLES	19
2.3.1 <i>Dusts, litter, whole regolith and leaching residues</i>	19
2.3.2 <i>Waters</i>	20
2.3.3 <i>Leachates</i>	20
2.4 ANALYTICAL METHODS	20
2.4.1 <i>Mineralogical analysis of the regolith materials: XRD and SEM</i>	21
2.4.2 <i>Major and trace element concentrations analysis</i>	22
2.4.3 <i>O and H stable isotope analysis</i>	23
2.4.4 <i>Sr, Pb, Nd and U isotope analysis</i>	24
CHAPTER 3. STRATIGRAPHIC AND GEOCHEMICAL CHARACTERIZATION OF THE WEIERBACH REGOLITH	26
3.1 RESULTS	28
3.1.1 <i>Mineralogical composition of the regolith components</i>	28
3.1.2 <i>Chemical composition of the regolith components</i>	29

3.1.3	<i>Pb, Sr, Nd and U isotopic compositions of the regolith components.....</i>	33
3.2	DISCUSSION.....	34
3.2.1	<i>Major and trace element behaviour within the studied regolith system.....</i>	34
3.2.2	<i>Impact of atmosphere-derived anthropogenic depositions on the PPSD.....</i>	37
3.2.3	<i>Impact of volcanic events on the PPSD.....</i>	39
3.2.4	<i>Impact of the saprolite (SP) on PPSD.....</i>	41
3.3	CONCLUSION.....	43
CHAPTER 4. HYDROLOGICAL AND GEOCHEMICAL CHARACTERIZATION OF THE WATERS IN THE WEIERBACH CATCHMENT		45
4.1	RESULTS.....	46
4.1.1	<i>Long term (2009-2016) characterization of the waters in the Weierbach catchment</i>	48
4.1.2	<i>Event-scale evolution of the catchment waters.....</i>	66
4.2	INTERPRETATION AND DISCUSSION.....	70
4.2.1	<i>Hydrochemical classification according to major element concentrations.....</i>	70
4.2.2	<i>Hydrochemical processes at the Weierbach catchment.....</i>	73
4.3	CONCLUSION.....	77
CHAPTER 5. WATER-ROCK-ATMOSPHERE INTERACTIONS AND WATER CIRCULATION PATTERNS AT CATCHMENT SCALE		79
5.1	RESULTS.....	80
5.1.1	<i>Chemical characterization of the labile and residual pools of the system</i>	80
5.1.2	<i>Sr and Nd isotopic characterization of leachates and comparison with the waters..</i>	83
5.1.3	<i>Pb and U isotopic characteristics of leachates whole rocks and waters.....</i>	87
5.2	DISCUSSION.....	90
5.2.1	<i>The chemical partitioning of Sr and Nd isotopes.....</i>	90
5.2.2	<i>The impact of atmosphere-derived Sr, Nd and Pb on the waters chemical and isotopic compositions.....</i>	94
5.2.3	<i>The origin and the chemical partitioning of U and the ²³⁴U enrichments in the waters</i>	97
5.2.4	<i>The hydrological functioning of the system: evidence of O-Sr-Pb-U isotopes</i>	100
5.3	CONCLUSION.....	103
CONCLUSIONS AND PERSPECTIVES		106
BIBLIOGRAPHY		113
APPENDICES.....		135
SUMMARY IN FRENCH		171

List of Tables

Table 1.1. Regolith structure and stratigraphic characterisation, including location of the samples (dashed lines: Lithic discontinuities; UL: Upper Layer; BL: Basal Layer).	10
Table 2.1. Blanks contamination in Sr, Nd, Pb and U according to Isotopic Dilution (ID) and measured $^{234}\text{U}/^{238}\text{U}$ ratios ($\pm 2\text{SE}$: Standard Error); (WR: Whole Rock PPSD and SP samples).....	25
Table 3.1. Major (% oxide) and trace element (ppm) composition of the regolith (D.L.: Detection Limit; NA: not analysed).	30
Table 3.2. Sr, Nd, Pb and U radiogenic isotope ratios of all analysed regolith samples(NA: not analysed).	34
Table 4.1. Loadings and explained variance for the first 7 Principal Components (PC).....	54

List of Figures

Figure 1.1. (a) Location of the Weierbach catchment in the Luxembourg Ardennes region, in the Rhenish Massif; (b) map of regolith and water sampling points in the Weierbach catchment.....	8
Figure 2.1. Picture of the passive SIGMA-2 dust collector.....	16
Figure 2.2. Scheme of all analytical methods used for the study of regolith (PPSD and SP), atmospheric dusts (AD), litter (OL), humus (OH), and water samples of the Weierbach catchment.....	21
Figure 2.3. Major and trace element concentrations of blank tests for materials used for (a) waters sampling and processing and (b) leaching experiments (dashed lines: minimal leachate concentrations).....	23
Figure 3.1. Depth-dependent patterns of mineralogical composition from XRD analyses expressed in relative abundances (PPSDce: PPSD coarse elements; dashed lines: lithic discontinuities; shaded area: redox sensitive zone).	28
Figure 3.2. Hierarchical cluster analysis performed on major and trace elements: (a) dendrogram defined using Pearson correlation distance as distance measure and Ward's method for the linkage rule; (b) coloured z-transformed concentrations matrix (row names correspond to regolith layers, parameter columns are ordered as the dendrogram); and (c) z-transformed concentrations as a function of depth for the 3 parameter groups defined (the thick black lines correspond to the median of each group, the thin coloured lines correspond to individual parameters of each subgroup as defined by the colour of the parameter labels in the dendrogram (a)).	31

Figure 3.3. Major and trace element concentrations of (a) OH and PPSD samples and (b) SP samples, normalized to the SP5 sample concentrations, representing the fresh slate bedrock.....	32
Figure 3.4. Depth dependent patterns of PAAS-normalized LaN/YbN and EuN/YbN ratios and Ce anomaly (CeN/CeN*) (dashed lines: lithic discontinuities; shaded area: redox sensitive horizons).....	33
Figure 3.5. Depth-dependent variation of (a) $^{206}\text{Pb}/^{207}\text{Pb}$, (b) $^{87}\text{Sr}/^{86}\text{Sr}$, (c) $^{143}\text{Nd}/^{144}\text{Nd}$ and (d) $^{234}\text{U}/^{238}\text{U}$ of all analysed samples (shaded area: redox sensitive horizons).	34
Figure 3.6. Relationships between (a) $^{87}\text{Sr}/^{86}\text{Sr}$ vs. Rb/Sr ratio and (b) $^{206}\text{Pb}/^{207}\text{Pb}$ vs. U/Pb ratio of all analysed samples and a lichen sample from Hissler et al. (2008) representing the anthropogenic end member.	38
Figure 3.7. $^{87}\text{Sr}/^{86}\text{Sr}$ vs. $^{143}\text{Nd}/^{144}\text{Nd}$ diagram describing mixing hyperbolas between the unweathered slate sample of this study (SP5) as the continental crust end member (Sr: 98.2 ppm, $^{87}\text{Sr}/^{86}\text{Sr}$: 0.7416; Nd: 37.9 ppm, $^{143}\text{Nd}/^{144}\text{Nd}$: 0.51193) and a mantle representing end member according to the study of Wörner et al. (1985) (Sr: 500 ppm; $^{87}\text{Sr}/^{86}\text{Sr}$: 0.70477; Nd: 49 ppm; $^{143}\text{Nd}/^{144}\text{Nd}$: 0.51262); and between SP5 and the lichen representing the atmospheric derived anthropogenic end member (Sr: 1.17 ppm, $^{87}\text{Sr}/^{86}\text{Sr}$: 0.7152; Nd: 0.17 ppm, $^{143}\text{Nd}/^{144}\text{Nd}$: 0.51205, from Hissler et al., 2008). Included are the loess signatures from UK, France and Belgium from Gallet et al. (1998) and Kaiserstuhl (Germany) from Taylor et al. (1983)(grey circles: Nb enriched PPSD samples).....	39
Figure 3.8. $\epsilon\text{Nd(T)}$ values vs. stratigraphic ages of the PPSD and SP samples of this study and of rock materials which originated from similar palaeographic environments reported by Michard et al. (1985) and Ohr et al. (1994). Modified after Michard et al. (1985).....	43
Figure 4.1. Bar plot showing the percentage of observations from the long term water dataset available for each chemical element and over the detection limit. The red bar indicates the boundary set for the parameters selection.....	46
Figure 4.2. Distribution of the selected dataset through the bi-weekly samplings. The selection of 39 parameters accounted each more than 70 values and yielded 1173 complete observations including rain (R), throughfall (TH1-2-3), SS at 10, 20, 40 and 60 cm depth (SS10-20-40-60), groundwater collected from wells GW1, GW2, GW3, GW5, GW6 and GW7, riparian waters (RP), spring waters (SP), and stream water (SW) collected at the outlet (SW1) and tributaries SW2 and SW3 together.	47
Figure 4.3. Boxplots of ionic balance percentage for the Weierbach waters. The red dashed lines indicate the $\pm 10\%$ limits. The black line in each box corresponds to the median of the data, the upper and lower limits of the boxes are the interquartile range (IQR), the whiskers are	

the first and third quantiles plus or minus 1.5 times the IQR, and points are outliers beyond the range of the whiskers.47

Figure 4.4. Boxplots of water pH (a), water electrical conductivity (b) and alkalinity (mg/L HCO_3^-) for the Weierbach waters. The black line in each box corresponds to the median of the data, the upper and lower limits of the boxes are the interquartile range (IQR), the whiskers are the first and third quantiles plus or minus 1.5 times the IQR, and points are outliers beyond the range of the whiskers. Letters above groups indicate statistically significant differences according to Kruskal-Wallis tests ($p\text{-value} < 2.2\text{e-}16$).....49

Figure 4.5. Hierarchical cluster analysis performed on water chemical variables (a, top dendrogram, colours correspond to geochemical groups) and catchment waters (b, left dendrogram, colours correspond to samples). The dendrograms (a,b) are defined using Euclidian distance as distance measure and Ward's method for the linkage rule; (c) is the coloured log z-transformed concentrations matrix (blue to red colours indicate weak to strong values).....50

Figure 4.6. Correlation matrix for the parameters studied in the catchment waters.....52

Figure 4.7. Histogram of eigenvalues representing the explained variance of each generated principal component.52

Figure 4.8. Projection on the components 1 and 2 space of (a) hydrochemical parameters (*loadings*) and (b) observations (*scores*), including envelopes corresponding to clusters identified in HCA. The colour code in (a) corresponds to the geochemical groups (TD) identified in the HCA (Fig.4.5) and in (b) to the water type. TF and R group all TF and R sampling points. SS20 groups soil solutions collected at 10 and to 20 cm depth and SS60 those collected at 40 and 60 cm depth. SW includes SW collected at the outlet (SW1) and the tributaries (SW2 and SW3).....55

Figure 4.9. Time series of the waters *scores* of components 1 (a) and 2 (b).56

Figure 4.10. Scatterplot of the waters *scores* of components 1 (a) and 2 (b) against discharge (Q:mm/d).57

Figure 4.11. PAAS-normalized REE distribution patterns of the Weierbach waters.....58

Figure 4.12. Time-series of the Ce anomalies ($\text{Ce/Ce}^*\text{N}$) for (a) soil solutions, (b) groundwaters from GW1 well, (c) groundwaters from GW2 well, (d) groundwaters from GW3 well, (e) riparian waters, and (f) streamwaters. Shaded areas represent wetness periods. Horizontal gray lines at $(\text{Ce/Ce}^*)\text{N} = 1$ indicate lack of anomaly.....59

Figure 4.13. Total REE concentration against pH for (a) soil solutions, (b) groundwaters and (c) streamwaters.60

Figure 4.14. Total REE concentration against alkalinity for (a) soil solutions, (b) groundwaters and (c) streamwaters.....	61
Figure 4.15. Total REE concentration against DOC for (a) soil solutions, (b) groundwaters and (c) streamwaters.	61
Figure 4.16. PAAS-normalized La/Yb ratios plotted against pH for (a) soil solutions, (b) groundwaters and (c) streamwaters.....	61
Figure 4.17. PAAS-normalized La/Yb ratios plotted against alkalinity for (a) soil solutions, (b) groundwaters and (c) streamwaters.....	62
Figure 4.18. PAAS-normalized La/Yb ratios plotted against DOC for (a) soil solutions, (b) groundwaters and (c) streamwaters.....	62
Figure 4.19. Ce anomaly ((Ce/Ce*)N) plotted against alkalinity for (a) soil solutions and (b) groundwaters. A zoom of GW1 in (b) is shown.....	62
Figure 4.20. Ce anomaly ((Ce/Ce*)N) plotted against alkalinity for (a) soil solutions and (b) groundwaters. A zoom of GW1 in (b) is shown.....	63
Figure 4.21. Ce anomaly ((Ce/Ce*)N) plotted against DOC for (a) soil solutions and (b) groundwaters. A zoom of GW1 in (b) is shown.....	63
Figure 4.22 Stable isotope compositions of (a) the ensemble of the Weierbach waters and (b-e) of each water type relative to the LMWL (dashed line: $\delta^2\text{H} = 5.3 * \delta^{18}\text{O} + 7.3$) and the GMWL (solid line: $\delta^2\text{H} = 8 * \delta^{18}\text{O} + 10$).....	64
Figure 4.23. $\delta^{18}\text{O}$ time series for (a) rain and throughfall (R, TF), (b) soil solutions (SS), (c) groundwaters from GW1, GW2, GW3, GW5, GW6 and GW7 wells, (d) riparian and spring waters (RP, SP), and (e) streamwaters (SW1, SW2, SW3). Shaded areas represent wetness periods.	65
Figure 4.24. Temporal dynamics of pH, electrical conductivity ($\mu\text{S}/\text{cm}$) and alkalinity (HCO_3^- mg/L) for the studied storm event for (a-c) soil solutions at 20 and 60 cm depth (SS20, SS60), (d-f) groundwaters collected at the wells GW1, GW2, GW3, GW5, GW6 and GW7, and (g-i) streamwater collected at the outlet (SW1), riparian (RP) and spring water (SP). Grey histograms on top of the plots represent precipitation during the event. Dashed lines in the background of the plots represent soil volumetric water content at 20 and 60 cm depth (a-c), GW1 and GW3 depths (d-f), and SW1 discharge (g-i).....	67
Figure 4.25. Temporal dynamics of major and trace element concentrations during the studied storm event. (a) Representation of the 2 main temporal concentration patterns before (day 1: 29/01/16) and during the event (2: 30/01/16 - 1 st discharge peak; 3: 31/01/16; 4: 01/02/16 - 2 nd discharge peak). (b) Representation of the temporal patterns of some	

elements (according to a) in soil solutions (SS20, SS60), groundwaters collected in GW3, GW5, GW7, and streamwater collected at the catchment outlet (SW1) ([c] indicates high concentrations in the long term). Elements shown are those enriched in SW1 at the first discharge peak. 68

Figure 4.26. Stable isotope compositions of the ensemble of the Weierbach waters relative to the LMWL (dashed line: $\delta^2\text{H} = 5.3 \cdot \delta^{18}\text{O} + 7.3$) and the GMWL (solid line: $\delta^2\text{H} = 8 \cdot \delta^{18}\text{O} + 10$). 69

Figure 4.27. $\delta^{18}\text{O}$ time series for the Weierbach waters during the storm event. Top grey histogram represents the precipitation during the event and the blue dotted line in the background the discharge. 70

Figure 4.28. Piper diagram of the Weierbach waters. Envelopes correspond to clusters identified in HCA. 71

Figure 5.1. Major and trace element extraction yields (% of the total mass) for (a) L1 leachates (0.05N HAc), (b) L2 leachates (1N HCl) and (c) L3 leachates (2N HNO_3). (d) Total extraction yield. 81

Figure 5.2. PAAS-normalized REE distribution patterns of (a) bulk regolith samples, (b) L1 leachates (0.05N HAc), (c) L2 leachates (1N HCl), (c) L3 leachates (2N HNO_3), (d) residues, and (e) soil solutions (SS20,SS60 and comparison with PPSD1-3 leachates). 82

Figure 5.3. Depth dependent patterns of PAAS-normalized (a) LaN/YbN , (b) EuN/YbN ratios and (c) Ce anomaly (CeN/CeN^*) for bulk regolith samples (PPSD and SP), L1 (0.05N HAc), L2 (1N HCl) and L3 (2N HNO_3) leachates, and residue (R) samples (dashed lines: lithic discontinuities referred in Chapter 1; shaded area: redox sensitive horizons). 83

Figure 5.4. Sr isotopic composition of the organic horizons, bulk, leachate and residue regolith samples and a selection of waters. Numbers inside leachate symbols correspond to regolith sample number as reported in Chapter 3. 84

Figure 5.5. $^{87}\text{Sr}/^{86}\text{Sr}$ ratios as a function of Ca/P ratios for the SP leachates (a). (b) Zoom of L2 and L3 SP samples including apatite reference Ca/P ratios. Numbers inside leachate sample symbols correspond to regolith sample number as reported in Chapter 3. 85

Figure 5.6. $^{87}\text{Sr}/^{86}\text{Sr}$ ratios of the SP leachates as a function of the corresponding concentrations in (a) Fe, (b) Al, and (c) Mg. Numbers inside leachate sample symbols correspond to regolith sample number as reported in Chapter 3. 85

Figure 5.7. Nd isotopic composition of the organic horizons, bulk, leachate and residue regolith samples, a selection of waters, and a lichen sample from Hissler et al. (2008). Crosses inside water symbols indicate sampling in dry conditions. 86

- Figure 5.8. $^{143}\text{Nd}/^{144}\text{Nd}$ ratios as a function of Ca/P ratios for (a) the L2 and L3 SP leachates including apatite reference Ca/P ratios, and (b) PPSD leachates. Numbers inside leachate sample symbols correspond to regolith sample number as reported in Chapter 3. 87
- Figure 5.9. $^{208}\text{Pb}/^{204}\text{Pb}$ vs. $^{206}\text{Pb}/^{204}\text{Pb}$ for atmospheric dusts, organic horizons, bulk, leachate and residue regolith samples, a selection of waters, a lichen from Hissler et al. (2008) and gasoline soot reference from Lahd Geagea et al. (2008). Crosses inside water symbols indicate sampling in dry conditions. 88
- Figure 5.10. $^{206}\text{Pb}/^{207}\text{Pb}$ vs. $^{87}\text{Sr}/^{86}\text{Sr}$ for atmospheric dusts, organic horizons, bulk, leachate and residue regolith samples and a selection of waters. Industrial reference), gasoline soot and traffic isotopic signatures from Lahd Geagea et al. (2008), a lichen sample from Hissler et al. (2008) and incinerator dusts samples from Hissler et al (2016) are given for comparison. Crosses inside water symbols indicate sampling in dry conditions. 88
- Figure 5.11. (a) $^{206}\text{Pb}/^{207}\text{Pb}$ vs. $^{234}\text{U}/^{238}\text{U}$ and (b) $^{87}\text{Sr}/^{86}\text{Sr}$ vs. $^{234}\text{U}/^{238}\text{U}$ for atmospheric dusts, organic horizons, bulk, leachate and residue regolith samples and a selection of waters. Numbers inside leachate sample symbols correspond to regolith sample number as reported in Chapter 3. Crosses inside water symbols indicate sampling in dry conditions. 89
- Figure 5.12. Schematic isochron diagrams for (a) Rb-Sr system and (b) Sm-Nd system for cogenetic apatite, feldspar and mica. 90
- Figure 5.13. Relationship between Sr and Nd isotopic compositions of atmospheric dusts, organic horizons, bulk, leachate and residue regolith samples and a selection of waters. The diagram describes the mixing curve of alteration products between a Ca-bearing phosphate phase and a plagioclase end member. Arrows indicate elemental enrichments towards mica compositions. A lichen sample (+) from Hissler et al. (2008) is given as atmospheric reference. Numbers inside leachate sample symbols correspond to regolith sample number as reported in Chapter 3. Crosses inside water symbols indicate sampling in dry conditions. 93
- Figure 5.14. Relationship between leaching yields of Pb (%) and (a) P (%), and (b) Fe (%). The number 5 inside leachate sample symbols indicates SP5 regolith sample (as reported in Chapter 3). 95
- Figure 5.15. (a) $^{87}\text{Sr}/^{86}\text{Sr}$ vs. $^{234}\text{U}/^{238}\text{U}$ for a selection of waters. (b) Zoom excluding TF. Numbers inside water sample symbols correspond to sampling day (1: 29/01/16; 2: 30/01/16 - 1st discharge peak; 3: 31/01/16; 4: 01/02/16 - 2nd discharge peak). Crosses inside water symbols indicate sampling in dry conditions. 98
- Figure 5.16. Mixing diagrams of (a) Sr, (b) U, and (c) Pb for the analysed waters. Numbers inside water sample symbols correspond to sampling day (1: 29/01/16; 2: 30/01/16 - 1st

discharge peak; 3: 31/01/16; 4: 01/02/16 - 2nd discharge peak). Crosses inside water symbols indicate sampling in dry conditions..... 99

Figure 5.17. (a) $^{87}\text{Sr}/^{86}\text{Sr}$ vs. $\delta^{18}\text{O}$ for the analysed waters. (b) Zoom excluding TF and SS20. Numbers inside water sample symbols correspond to sampling day (1: 29/01/16; 2: 30/01/16 - 1st discharge peak; 3: 31/01/16; 4: 01/02/16 - 2nd discharge peak). Crosses inside water symbols indicate sampling in dry conditions. 100

Figure 5.18. (a) $^{234}\text{U}/^{238}\text{U}$ vs. $\delta^{18}\text{O}$ for the analysed waters. (b) Zoom excluding TF and SS20. Numbers inside water sample symbols correspond to sampling day (1: 29/01/16; 2: 30/01/16 - 1st discharge peak; 3: 31/01/16; 4: 01/02/16 - 2nd discharge peak). Crosses inside water symbols indicate sampling in dry conditions. 101

Figure 5.19. Conceptual model of water circulation dynamics at the Weierbach catchment under different hydrological conditions according to the $\delta^{18}\text{O}$, $^{87}\text{Sr}/^{86}\text{Sr}$, $^{234}\text{U}/^{238}\text{U}$ and $^{204}\text{Pb}/^{206}\text{Pb}$ signatures of the studied waters. 102

List of Main Abbreviations and Acronyms

BL: Basal PPSD Layer	OH: Organic-Humus sample
CZ: Critical Zone	OL: Organic-Litter sample
D.L.: Detection Limit	PCA: Principal Components Analysis
DOC: Dissolved Organic Carbon	PPSD: Pleistocene Periglacial Slope Deposits/samples 1-4
EC: (Water) Electrical Conductivity	PPSDce: PPSD - coarse element sample
GMWL: Global Meteoric Water Line	R: Rain
GW: Groundwater (1-7)	REE: Rare Earth Elements
HCA: Hierarchical Cluster Analysis	RP: Riparian zone/water
HREE: Heavy Rare Earth Elements	SD: Standard Deviation
IL: Intermediate PPSD Layer	SE: Standard Error
IQR: Inter-Quartile Range	SOC: Soil Organic Carbon
L1: Leachate 1 (0.05N Hac)	SP: Slate profile / samples 1-5
L2: Leachate 2 (1N HCl)	SP: Spring (water)
L3: Leachate 3 (2N HNO ₃)	SS: Soil Solution (20-60)
LMWL: Local Meteoric Water Line	SW: Streamwater
LREE: Light Rare Earth Elements	TD: Top dendrogram geochemical group (1-8)
MREE: Middle Rare Earth Elements	TF: Throughfall
MVSA: Multivariate Statistic Analyses	UL: Upper PPSD Layer
NA: Not Available	VWC: Volumetric soil water content
O: Organic	WR: Whole Rock / Bulk samples

Introduction

The Critical Zone (CZ) is the section of the external terrestrial surface that ranges from the top of the vegetation canopy to the deepest saturated regolith zones (National Research Council, 2001). Water fluxes connect the different CZ compartments and participate of physical and biogeochemical processes responsible of their formation and alteration such as weathering and vegetation nutrient cycling. The CZ is additionally controlled by climate, tectonic and human factors such that, for example, transported sediments or atmospheric deposits of natural or anthropogenic origin can importantly alter its structure and fluxes (Brantley et al., 2006). The heterogeneity of the different CZ compartments and fluxes, and more specifically regolith production and transformation, results in the production of “hot spots” that greatly determine the hydrochemical response in the streamwater (Chorover et al., 2011; McClain et al., 2003; West et al., 2013). Therefore, the spatial and temporal geochemical characterization of regolith compartments and the waters they host is of especial interest in catchment hydrology in order to assess hydrological connectivity and understand stream hydrochemical fluctuations (Brantley et al., 2007; Brooks et al., 2015; Chorover et al., 2011).

Since the 1960s, major geochemical elements (Na^+ , K^+ , Ca^{2+} , Mg^{2+} , H_4SiO_4 , SO_4^{2-} , Cl^- , NO_3^- , alkalinity and DOC), stable isotopes of O and H, temperature and electric conductivity in water are commonly used for runoff generation studies at hillslope and catchment scales (Barthold et al., 2010; Burns et al., 2001; Christophersen and Hooper, 1992; Hooper et al., 1990; Inamdar, 2011; Wenninger et al., 2004). While these parameters have become increasingly popular in hydrological processes studies, fundamental assumptions related to their application as tracers were found to be rarely met (Klaus and McDonnell, 2013). For instance, hydrological mixing models assume that tracers must give significantly different compositions to each of the studied end members and must have a conservative behavior, i.e. concentrations must not change due to biogeochemical processes over a considered time(/space) scale (Hooper et al., 1990; Inamdar et al., 2013). In nature, however, major elements are ubiquitous and participate of various

processes such as chemical weathering and precipitation processes and vegetation nutrient cycling. Similarly, stable isotopes of water are sensitive to fractionation due to temperature or pressure changes. Consequently, although considerable progress has been made on determining water transit time at catchment scale (Brooks et al., 2010; McGuire and McDonnell, 2006; Stumpp et al., 2007), their use as tracers of hydrological processes or sources at catchment scale is rather limited and can lead to false conclusions about catchments functioning (Barthold et al., 2011). Moreover, we still lack understanding of what eventually triggers the complex temporal dynamics in the physico-chemistry of subsurface waters.

Until now, research studies in the CZ compartments and hydrological processes have largely remained uncoupled – stymieing the capability for identifying water pools and flow paths in hydrological research. Recent work has shown that there is an urgent need for interdisciplinary research on this topic (Brooks et al., 2015). Indeed, if we are to bring new understanding to the fundamental functions of water collection, mixing, storage and release, we eventually need to focus on the interrelationship between (*at least*) regolith properties and water hydro-chemical dynamics. Such approach requires the application of a larger hydrological tracer toolbox that allows the characterization and comparison of both solid/organo-mineral and liquid/aqueous phases. In the last decades, trace elements and some of their radiogenic isotope ratios have been shown as promising tracers of pedogenetic and eco-hydrological processes.

Trace elements have been often dismissed from fresh water's total dissolved solids studies due to their low natural combined mass (concentrations below 1mg/L) compared to that of major ions, and the fact that only recent technological advances allowed their accurate measurement (Gaillardet et al., 2003). However weathering/precipitation and solute transport mechanisms can be better understood with the additional use of trace elements because they become more fractionated than major elements during these processes. This is not only because they are highly mineral specific, but also because some of them are sensitive to DOC, pH and redox fluctuations. Therefore different lithologies and even regolith horizons/layers can deliver different trace element compositions into solutions. Moreover, given their extended use for industrial purposes, trace metals are also very useful for tracing the impact of anthropogenic activities in the ecosystems. Work by Ladouche et al. (2001) and El Azzi et al. (2016) shows how trace elements can be good complementary tools to differentiate areas contributing to the streamflow generation and pollutants transfer under different flow conditions.

Among the trace elements, Rare Earth Elements (REE) behave as a rather homogeneous group due to their trivalent electronic configuration. A gradual decrease in the REE ionic radii with increasing atomic number results in a slightly distinct response (fractionation) of light REE (LREE, La–Sm) and heavy REE (HREE, Dy–Lu) to leaching, precipitation, adsorption or complexation processes (Brookins, 1989). Exceptional behaviours are found for Ce, which is tetravalent in oxidizing conditions, and Eu, which is bivalent in reducing conditions such those

found in the mantle and lower crust. REE concentrations and distribution patterns are therefore especially sensitive to the changes in redox conditions, pH and abundance of (organic/inorganic) complex-ligands involved in water-rock interactions and transport processes (Aubert et al., 2002b; Braun et al., 1998; Condie, 1991; Dupré et al., 1999; Elderfield et al., 1990; Goldstein et al., 1984; Hissler et al., 2015; Pourret et al., 2007; Sholkovitz, 1995; Smedley, 1991; Stille et al., 2009; Taylor and McLennan, 1981; Tricca et al., 1999; Viers et al., 1997). Indeed, previous REE mappings and physico-chemical monitoring of soil- and groundwaters and their host rocks at (sub-)catchment scale and along different time scales have been proven useful in order to distinguish water sources and flowpaths (Davranche et al., 2011; Dia et al., 2000; Gruau et al., 2004; Vázquez-Ortega et al., 2016).

The knowledge and prediction of the specific origin dynamics of trace elements (and associated major elements) in the CZ is improved with the study of isotopic ratios like $^{87}\text{Sr}/^{86}\text{Sr}$, $^{143}\text{Nd}/^{144}\text{Nd}$, $^{206}\text{Pb}/^{207}\text{Pb}$ and $^{234}\text{U}/^{238}\text{U}$. The Sr, Nd, Pb and U isotopic systems are tools long used by geochronologists and petrologists before they were applied in weathering and hydrological studies. Their interest resides on their stability – conversely to $\delta^{18}\text{O}$ and $\delta^2\text{H}$, they do not fractionate during bio-geo-physico-chemical processes in the environment - and on their large variations between sources. These characteristics allow the assignment of a fingerprint for specific water-rock interactions. Knowing the isotopic source characteristics in the system, they can be used to characterize weathering processes, assess water sources and flowpaths, and quantify natural and anthropogenic contributions (Aubert et al., 2002a; Hissler et al., 2016, 2015; Pierret et al., 2014; Schaffhauser et al., 2014; Stille et al., 2011, 2009).

In order to better understand the application of the Sr, Pb, Nd and U isotope systems, it is important to recall on the basics of their functioning. The radiogenic isotope composition of an element is represented as the relative abundance of the radiogenic to the non-radiogenic isotope of that element. Widely used radiogenic isotope ratios are $^{87}\text{Sr}/^{86}\text{Sr}$ for Sr; $^{207}\text{Pb}/^{204}\text{Pb}$, $^{206}\text{Pb}/^{204}\text{Pb}$, and $^{208}\text{Pb}/^{204}\text{Pb}$ for Pb; and $^{143}\text{Nd}/^{144}\text{Nd}$ for Nd (e.g. Faure, 1977). Their variability in the different rocks and minerals is the result of the decay of ^{87}Rb to ^{87}Sr , ^{235}U to ^{207}Pb , ^{238}U to ^{206}Pb , ^{232}Th to ^{208}Pb and ^{147}Sm to ^{143}Nd . Each of these so-called “parent-daughter” decays takes a specific time to happen which depends on the decay constant of the radioactive parent nuclide under consideration (λ). The time it takes for half of the parent nuclide to decay, known as half-life, is 48.8, 0.704, 4.47, 14.0 and 106 byr for ^{87}Rb , ^{235}U , ^{238}U and ^{147}Sm respectively (Faure, 1977). Therefore, their isotopic ratios are rather constant in their specific mineral phases.

Strontium isotopes are greatly abundant in nature and show little fractionation as well as a large variability of the $^{87}\text{Sr}/^{86}\text{Sr}$ ratios. Thanks to its ionic similarities with Ca and its facility to substitute it, Sr is often found in Ca-rich minerals like plagioclase, apatite and Ca-carbonates. Although much less abundant, Nd is particularly interesting because it can isotopically represent REE patterns and its chemical behaviour in the hydrosphere is strongly determined by chemical

and mineral affinities. Given the long half-life of ^{147}Sm , Sm/Nd ratios are able to record the original mineral composition. Both $^{87}\text{Sr}/^{86}\text{Sr}$ and $^{143}\text{Nd}/^{144}\text{Nd}$ isotope ratios have been greatly used (often concurrently) in crustal rocks dating, weathering studies and for differentiating atmospheric and natural inputs (Chabaux et al., 2005; Hissler et al., 2016; P Stille et al., 2006; Stille et al., 2009) and/or sources of water contributions to a stream (Aubert et al., 2001; Négrel and Petelet-Giraud, 2005; Petelet-Giraud et al., 2016; Tricca et al., 1999).

When studying the dynamics of heavy metals in the environment, Pb isotopes such as ^{204}Pb , ^{206}Pb , ^{207}Pb and ^{208}Pb are good tracers due to the stability of their relative proportions in the hydrosphere and its large abundance linked to anthropogenic activities. The different isotopic ratios of Pb found in the environment (natural or anthropogenic) depend only on the original mineral the studied Pb proceeds from. Industrial Pb is characterized by low Pb isotopic signatures (e.g., $^{206}\text{Pb}/^{207}\text{Pb}$ ratios between 1.039 and 1.16) derived from ancient ore bodies (e.g., Australian, Canadian) that are totally different from those of average crustal rocks ($^{206}\text{Pb}/^{207}\text{Pb} > 1.18$) (e.g. Stille and Shields, 1997). For this reason, Pb is extremely useful to differentiate between anthropogenic and natural sources (Carignan and Gariépy, 1995; Semlali et al., 2004; Stückrad et al., 2008). Furthermore, given that the isotopic variability of the Pb ore bodies is transferred to the materials and residues produced through industrial activities, different anthropogenic contributions can also be identified (Carignan et al., 2005, 2002; Flegal et al., 1989; Monna et al., 1997; Stille et al., 2011). With this purpose, Carignan and colleagues (2002, 2005) analysed lichens and fly ashes from waste combustors along NE-USA and France respectively and were able to depict mappings of atmospheric Pb sources and distribution. Similarly, for the Luxemburgish case, Hissler et al. (2008) were able to differentiate Pb pollution from old and actual steel production activities in the air and streams of the southern industrial zone of the country.

Uranium isotopes (^{235}U , ^{238}U and ^{234}U) have a different functioning than Sr, Nd and Pb isotope systems. Uranium isotopes are part of (α and β) decay series, in which the U nuclides are radioactive themselves and end up forming stable Pb nuclides (e.g. Faure, 1977). The $^{234}\text{U}/^{238}\text{U}$ isotope ratios represent the relative activity (decay rate) of one isotope to another, reason why they are known as “activity ratios”. It is considered that, if nothing disturbs a U-bearing mineral during ~ 1 myr, then the $^{234}\text{U}/^{238}\text{U}$ approaches secular equilibrium ($^{234}\text{U}/^{238}\text{U} \sim 1$). ^{234}U has a half-life of 0.25 myr and is known to be preferentially released during rock weathering. This is because the α decay of ^{238}U emits recoil energy that damages the crystal lattice, thereby allowing ^{234}U to migrate to unstable positions where it can oxidize into water-soluble uranyl ions (Faure, 1977). Hence, water and secondary U-bearing minerals tend to have $^{234}\text{U}/^{238}\text{U} > 1$ and leave behind “residual” mineral phases with $^{234}\text{U}/^{238}\text{U} < 1$. Therefore, these activity ratios are broadly used for tracing weathering reactions and water sources and pathways because they are affected by water-rock interactions which yield different values for different rocks and

solutions (Chabaux et al., 2013; Faure, 1977; Huckle et al., 2016; Pelt et al., 2008; Riotte and Chabaux, 1999).

Mixing calculations involving these tracers also rely on assumptions like the inclusion of all potential sources and their good isotopic differentiation. In order to tackle this issue, the combination of various isotopic systems and chemical elements is highly recommended. This approach delivers contrasting information that increases the precision on the understanding of mechanisms controlling the tracers behaviour and on end member's determination (Blum and Erel, 2003; Graustein, 1989). Several pedological and hydrological studies effectively coupled the use of trace elements concentrations and two isotopic systems in the same samples; often the above mentioned Sr and Nd, but also Sr and U (Paces and Wurster, 2014; Pierret et al., 2014; Prunier et al., 2015; Schaffhauser et al., 2014). A few of them used Sr, Nd and Pb isotopic systems concurrently for tracing the crustal evolution through river sediments and suspended loads (Allègre et al., 1996; Garçon et al., 2014), atmospheric dusts (Biscaye et al., 1997; Grousset and Biscaye, 2005; Guéguen et al., 2012) and weathering profiles (Hissler et al., 2015). Studies using these three tools also demonstrated their great added value for characterizing the natural baseline composition of dusts, soils and waters and differentiating it from different anthropogenic interferences (Hissler et al., 2016, 2008; M. Lahd Geagea et al., 2008; Majdi Lahd Geagea et al., 2008; Steinmann and Stille, 1997). To our knowledge Sr, Nd, Pb and U isotopic systems have never been applied together in the same suit of samples for studying water-rock-atmosphere interactions.

Hypothesis, objectives and thesis outline

Previous research carried out in a nested catchment set-up in the Attert River basin (Luxembourg) has shown, through the combination of physiographic and hydrological studies, strong geological control on catchment functions of water collection, mixing and release within the hillslope-riparian-stream continuum (Pfister et al., 2017; Wrede et al., 2015). Currently, we lack understanding of what processes trigger different runoff responses (single or double peaks) to precipitation events in the Devonian part of the Attert River basin. We hypothesize that the highly contrasted hydrological behaviour between summer and winter seasons is largely triggered by ground- and soil- water fluctuations within the slate regolith.

The general objective of this PhD project is thus to study the mixing of water in the subsurface through a unique portfolio of complementary groups of tracers (major elements and stable isotopes and trace elements and Sr-Nd-Pb-U radiogenic isotopes) which enables investigating regolith weathering (/precipitation) processes and solutes transport within the CZ.

Within this framework, the specific objectives were:

- 1 - Characterize the regolith's potential "hot spots" of interaction with water.
- 2 - Characterize the hydrological and geochemical behaviour of the Weierbach waters.
- 3 - Characterize the water circulation dynamics and reservoirs connectivity at catchment scale.

The body of this manuscript is composed of five chapters.

Chapter 1 depicts the geological, climatological and hydrological settings of the Weierbach catchment.

Chapter 2 presents the different samples studied in this project as well as their sampling and analytical strategy. The analytical methods used are described along with blank quality data.

Chapter 3 is dedicated to the characterization of the regolith profile of the Weierbach catchment as interactive medium for waters. More specifically, we make use of mineralogical analyses, major and trace elements concentrations (combined in hierarchical cluster analysis) and the Sr-Nd-Pb-U isotope ratios to identify geochemically different regolith zones. Their origin and evolution is tracked according to geological and hydrological events as well as natural and anthropogenic atmospheric-derived depositions. This study was published in CATENA in 2017 (Moragues-Quiroga et al., 2017).

Chapter 4 reports on the geochemical characterization of the Weierbach waters in the long term- and, to a lesser extent, storm event- time scales. This chapter is a first metaanalysis of water chemistry data acquired at the catchment scale. Precipitation, soil solution, groundwater, riparian and streamwater samples are studied according to their major and trace element concentrations, stable isotopes composition and physico-chemical characteristic. The combined use of these tools through multi-variate statistical analysis allows the discrimination of the different water pools and the assessment of their main hydrochemical dynamics.

Chapter 5 focuses on the geochemical interactions between water, regolith and atmosphere in the Weierbach catchment. Major and trace element concentrations and Sr-Nd-Pb-U isotope analyses are here applied additionally on a suit of catchment waters and on laboratory leachates of the regolith samples. The objectives of this study are twofold: (i) on the one hand we assess the mineral and atmospheric components which impact the water chemistry; (ii) on the other hand, we further enlarge our understanding on water origin and dynamics and eventually shed light on the conceptualization of the system functioning. This work is in preparation for submission to peer-reviewed journals as two separate papers, each of them dealing with each of the above described objectives of this chapter.

Following that, the general conclusions and perspective of the present work are provided in the frame of the previous hydrological understanding of the Weierbach catchment.

Chapter 1. Study site

All the work of this dissertation is based on the Weierbach experimental catchment, located in the NW of the Grand Duchy of Luxembourg. The Weierbach catchment has been densely monitored since 2009 by the Luxembourg Institute of Science and Technology, formerly known as the Centre Recherche Public Gabriel Lippmann. The study site is a 45 ha headwater catchment of the Attert River Basin (288 ha; latitude: 49° 50' 05.5"N; longitude: 05° 47' 47.6"E) with altitudes ranging from 422 to 512 m a.s.l. (Fig.1.1). As such, it is formed by a steep valley that breaks through a plateau, being the hillslopes remarkably steep in the east side (mean slope = 5.25°). The Weierbach catchment is mainly forested with beech (*Fagus sylvatica* L.) and oak (*Quercus petraea* (Matt.) Liebl.) covers (70%), and to a lesser extent with spruces (*Picea abies*, 15%) and douglas-fir (15%). These trees are subject to selective cutting, for which several soil tracks around the catchment are set in place. A plateau area used for agricultural fields and meadows surrounds the forested catchment. Previous surveys carried out in the area point to a total disconnection between the agricultural lands and the stream network (Martínez-Carreras et al., 2010). In subsections 1.1 and 1.2 a detailed description of the geological, climate and hydrological setting is given.

1.1 Geological and geomorphological settings

Geologically speaking, the Weierbach catchment is located in the Luxembourg Ardennes Massif (Oesling), close to the Belgian border (Fig.1.1). The studied plateau is assumed to be representative of the regolith landform unit called “haute surface de l’Oesling” in Luxembourg, which developed at 500 m a.s.l. (Désiré-Marchand, 1985). A regolith landform unit represents an area characterized by similar landform and regolith attributes (Eggleton, 2001). Indeed, landforms are used as surrogates for mapping regoliths since both are usually spatially and genetically related (Craig et al., 1999). This “haute surface de l’Oesling” is the Luxembourg part of an extensive Dano-Montian surface of the eastern part of central Ardennes and Eifel at altitudes above 500 m (Demoulin, 2003) and correlates in Germany with the mapped “S2” surface, developed by pedimentation under semi-arid climate during the Upper Eocene/Lower Oligocene (Hugué, 1998).

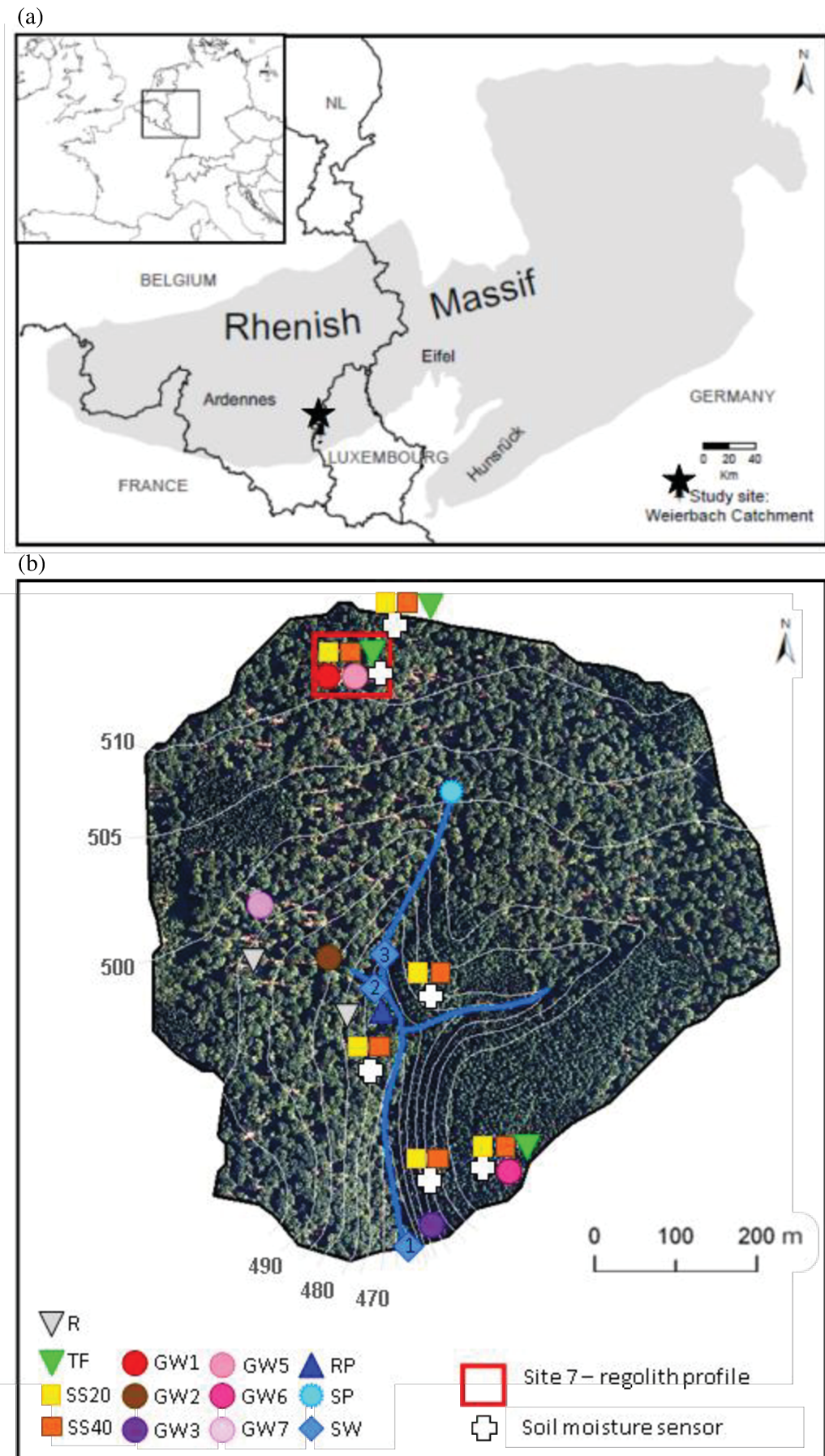


Figure 1.1. (a) Location of the Weierbach catchment in the Luxembourg Ardennes region, in the Rhenish Massif; (b) map of regolith and water sampling points in the Weierbach catchment.

Désiré-Marchand (1985) explained that this “haute surface” was generated by gradual redevelopment of the original flat surface (S1 surface) and, consequently, the above *in situ* regolith recorded many weathering stages during the geological times and can be considered polygenetic. The geological substratum of the Weierbach catchment is composed of Devonian metamorphic schists, phyllites and slates (Juilleret et al., 2011) covered by Pleistocene Periglacial Slope Deposits (PPSD), which have been recognized to be the parent material of the soil in the Rhenish Massif (Deckers, 1966; Kwaad and Mùcher, 1977; Müller, 1954; Sauer, 2002; Sauer and Felix-Henningsen, 2006). PPSD generally consist of up to 3 different layers, with great variability in the occurrence and thickness of the layers depending on the geographical and topographical location (Ad-hoc-Arbeitsgruppe Boden, 2005; Dietze and Kleber, 2010; Semmel and Terhorst, 2010), and can be described as follows:




- an upper layer (UL) found in every topographic position. This layer always contains admixed loess and presents a homogenous thickness of 30 to 70 cm. This layer is characterized by higher silt content in comparison to the underlying soil layers.
- an intermediate layer (IL) which contains rock fragments originating from the bedrock below and also loess, as its presence is strongly controlled by topography and bound to sites especially prone to loess deposition.
- a basal layer (BL) composed almost exclusively of bedrock fragments present in the surrounding slopes. During the formation of the basal layer, bedrock and periglacial debris formed the surface before the onset of loess accumulation. The BL is therefore almost free of allochthonous material like loess and varies greatly in thickness. Rock fragments are usually oriented parallel to the slope and may appear in multiple layers.

According to Dietze and Kleber (2010), the above described layers form a continuous drape in Central European subdued mountains like the Rhenish Massif and may occur as a complete series of 3 layers (UL-IL-BL) or may be reduced to only upper and basal layers (UL-BL). The latter sequence (UL-BL) is the most widespread and corresponds to the one covering the Weierbach catchment (Sauer and Felix-Henningsen, 2006) (Table 1.1).

1.1.1 Regolith stratigraphy and classification

Prior to the sampling, the studied regolith profile was observed and described (i) from a soil pit for the upper part (0 to 140 cm depth); and (ii) by core drilling for the deeper part (140 to 735 cm depth). The following description was made according to the Guidelines for Soil Description (FAO, 2006) and completed with the description of the subsolum material according to Juilleret et al (2016). As regolith encompasses in its upper parts the solum (where pedogenic processes and biota are dominant) and in its lower parts the subsolum (where the original rock structure or fabric of the Bedrock is preserved), we described and subdivided the profile according to solum and subsolum part following the methodology of Juilleret et al (2016) (Table 1.1).

Table 1.1. Regolith structure and stratigraphic characterisation, including location of the samples (dashed lines: Lithic discontinuities; UL: Upper Layer; BL: Basal Layer).

Stratigraphy	Regolith profile	Horizons layers	Diagnostic material	Sample depth (cm)	Sample name
PPSD (UL)		O		-1 – 0	OH
		Ah		0 – 4	PPSD1
		B	Cambic	4 – 45	PPSD2
PPSD (BL)		2Cg1	Regolithic	45 – 80	PPSD3
		2Cg2	Regolithic	110	PPSD4
Slate substrate		3CR	Saprolithic	190	SP1
		3CR	Saprolithic	270	SP2
		3CR	Saprolithic	320	SP3
		3CR	Saprolithic	380	SP4
		3R	Paralithic	735	SP5

The solum (from -1 to 45 cm) showed 3 horizons described as follows (Table 1.1): a very thin layer of fresh to highly decomposed organic material (O horizon) on top of a thin very dark greyish brown (10YR 3/2) silty clay Ah horizon and a brownish yellow (10 YR 6/6) silty clay loam B Cambic horizon. Both organo-mineral horizon were not sticky, non-plastic and showed a soft dry consistency. We estimated fine and very fine root density on vertical plane at 8 to 16 roots cm⁻² for Ah and B horizons. No earthworm channels were observed. Rock fragments of slate nature and of fine-to-medium gravel size (2 to 20 mm) were common in the Ah and B horizons with respective volume contributions of 13% and 27%.

The upper Subsolum (45-140 cm) observed from the soil pit (Table 1.1) is represented by: an olive yellow (2.5 Y 6/8) loam 2Cg1 horizon, and an olive yellow (2.5 Y 6/6) sandy loam 2Cg2 horizon. The estimated root density on the vertical plane was below 8 roots cm⁻² in both C layers. The stone content increases significantly in these two horizons and ranges from 40% to 50% of the volume for the respective 2Cg1 and 2Cg2 horizons. Common faint mottling of medium size and a few soft iron-manganese-oxide traces in the earth material around rock fragments were observed. This upper subsolum is defined as Regolithic layer (Juilleret et al.,

2016). The colours of the deeper subsolum material (140-735 cm) ranged from light grey (2.5 Y 7/2) to brownish yellow (10YR 6/6). Gleyic properties were observed between 340 and 380 cm depth (WRB, IUSS Working Group 2015). As the material was mechanically weakened by water, we classified it as saprolithic (Juilleret et al., 2016). From 450 to 735 cm depth, the material consisted of longer intact slate rock cores of several centimetres length (5 to 7 cm) mainly of grey colour (GLEY 1 5/N). Some of the longer cores showed cracks covered by sesquioxides interpreted as a mechanical weakened part inherited from the cleavage planes where waters flow. This deeper material is classified as paralithic according to Juilleret et al. (2016). The abrupt increase and the change in size of rock fragments between B and 2Cg1 horizons allowed us to diagnose a lithic discontinuity. The irregular orientation of the longer axes of slate rock fragments inherited from the underlying geological substratum in the 2Cg1 and 2Cg2 layers were interpreted as indications of cryoturbation. Below the 2Cg2 layer, the observation of the cores from the deeper subsolum showed that rock fragments have a different orientation, mainly vertical. The orientation of the slate rock fragments is inherited from the almost vertical cleavage planes of the geological substratum (Juilleret et al., 2011). This observation allows us to diagnose a lithic discontinuity between the 2Cg2 horizon and the geological substratum 3CR layer below.

According to the PPSD classification, we concluded that Ah and B horizons developed in the UL. Indeed, Ah and B horizons present higher silt content with a cumulate thickness of 45 cm, while the underlying 2Cg1 and 2Cg2 are characterized by a dominant amount of rock fragments originated from cryoturbation. Consequently, the studied profile presents a transported regolith part made of PPSD on top of the in situ slate weathered substratum and is organized as follows (Table 1.1):

- 1) An organic topsoil, which encompasses the O horizon and constitutes the upper part of the solum.
- 2) An organo-mineral compartment developed in the PPSD which can be subdivided in solum and upper subsolum. The solum part is composed of Ah and B horizons. The upper subsolum can be divided into 2Cg1 and 2Cg2 horizons and contains regolith material according to Juilleret et al. (2016).
- 3) A lower mineral subsolum, which contains saprolithic and paralithic materials according to Juilleret et al. (2016). This third compartment represents the in situ regolith profile made of weathered slate substratum and referred to as 3CR and 3R layers. These layers are separated from the above PPSD compartment by a lithic discontinuity.

The studied regolith profile can be classified as Haplic HEMIMODER (Jabiol et al., 2013) developing on a Dystric Cambisol (Ruptic, Endoskeletal, Siltic, Protosodic) (IUSS Working Group, 2015) overlying a Regolith Saprrolite (Gleyic, Ruptic, Rootic, Siltic, Skeletic) [Slatic] (Juilleret et al., 2016). In order to simplify the presentation of the results and the discussions, the

name of the samples of the regolith layers (Table 1.1 – OH, PPSD, SP) will be used in the following document as reference of the regolith compartments.

We fulfilled the same pedo-stratigraphic report for four other profiles in the same plateau area. We searched for a profile that minimized the effect of erosion of the plateau unit (“haute surface de l’Oesling”) and permitted thicker layers to be investigated. Given the homogeneity we observed in situ and in later chemical analyses, this extensive sampling allowed us to choose the studied profile as a representative example of the geological system, on which we therefore focus this work. The profile description is considered as a general framework that, although very informative, does not allow by itself the distinction of the origin of the various contributions to the regolith composition, for which geochemical analyses are needed. Indeed, the pedo-stratigraphic study informs about the physical properties of the material and its position within the regolith profile. But, this does not yield any precise information about in how far the in situ soil has been modified by external contributions such as aeolian depositions (loess or volcanic dust). In addition, only geochemical and isotopic investigations allow us to understand the chemical evolution of the different parts of the regolith.

1.2 Climate and hydrological settings

The Weierbach catchment is dominated by a semi-oceanic climate with an evenly distributed mean annual total precipitation of 953 mm and a mean annual potential evapotranspiration of 593 mm (2006-2014, Pfister et al., 2017). Air temperature monthly means calculated for 1971-2000 give a maxima of ca. 18°C in July and a minima of 0°C in January, with about 80 days per year of values below 0°C at 2 m above ground (Martínez-Carreras et al., 2010, Pfister et al., 2005). While the mean annual discharge values of the Weierbach are around 478 mm (2006-2014, Pfister et al., 2017), the stream suffers a strong seasonality, to the point of drying out completely for some days or weeks during the extremely dry summers. During the field campaigns comprised in the present work (Summer 2014-February 2016), this happened in August 2015, whereas during the whole summer 2014 the discharge volume was similar to what is usually observed during wetter periods (Schwab, 2017). Previous studies by Wrede and colleagues (2015) have shown the sensitivity of the rainfall-runoff response in the Weierbach to varying wetness conditions, such that either one- or two- peak hydrographs occur if the antecedent system condition was dry or wet respectively. Generally, the double discharge peak consists of a first flashy response to a rainfall event and a second one which is general 1-2 days delayed and extended in time (Glaser et al., 2016; Klaus et al., 2015; Martínez-Carreras et al., 2015; Martinez-Carreras et al. 2016; Pfister et al., 2017; Schwab et al., 2016).

Figure 1.2 presents the time series from March 2009 to February 2016 for precipitation, soil moisture as the percentage of Volumetric Water Content (VWC) at 10, 20, 40 and 60 cm depth, groundwater depths from the soil surface and discharge at the outlet of the catchment. Soil

moisture is around 10-20% VWC during dry conditions, making it impossible to sample soil solutions at low tension. The soil VWC increases during wet up periods and reacts almost instantly during precipitation events both in dry and wet periods. Similarly, depths to groundwater level are low (groundwater level close to the surface) during wetness conditions and increase (go deeper) during dry conditions. The groundwaters reaction to the wetness conditions happens almost instantaneously to that of soil solutions.

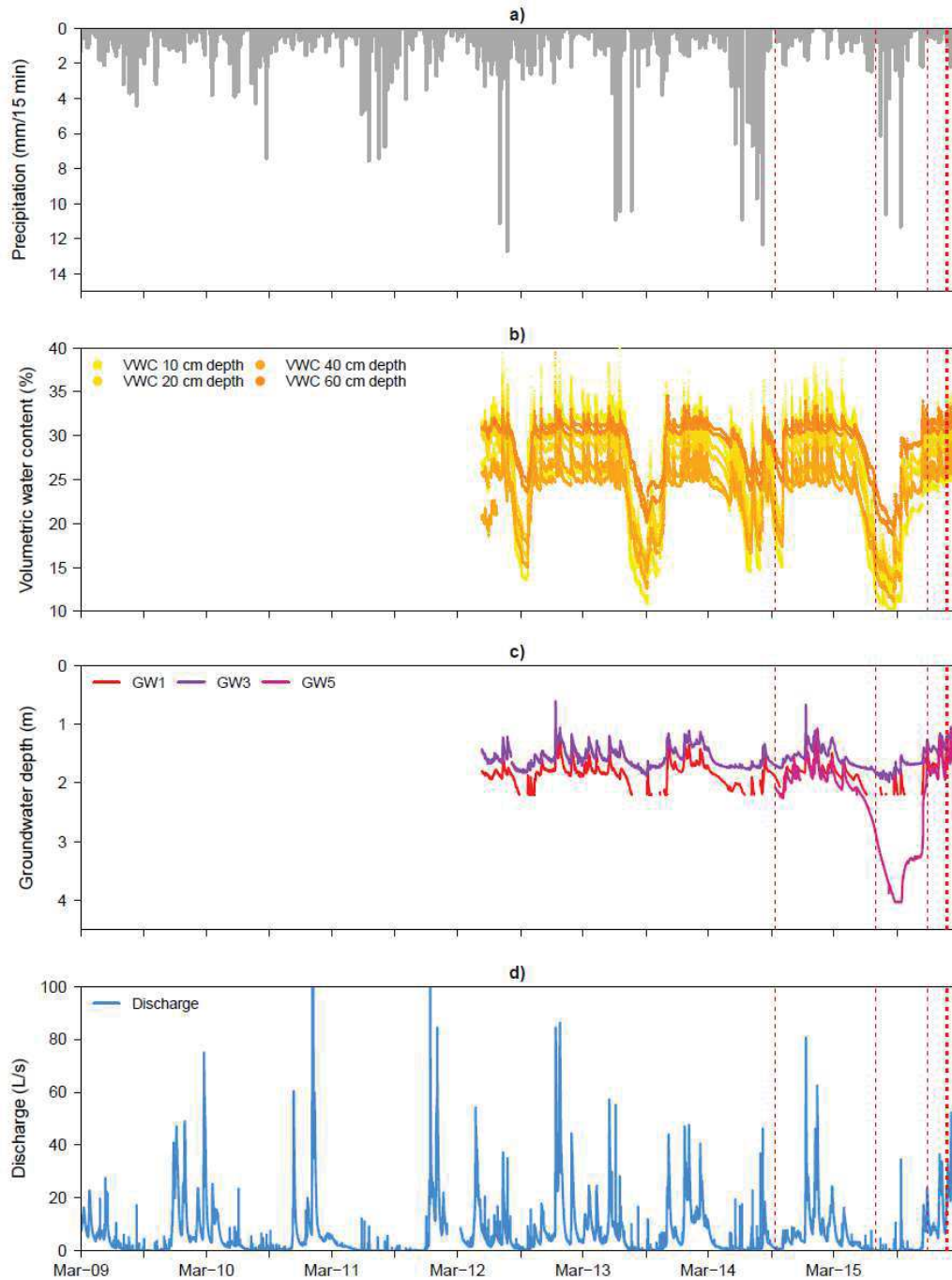


Figure 1.2. Hydrometric time-series of the Weierbach for the long-term bi-weekly samplings (March 2009-February 2016). (a) Precipitation, (b) soil volumetric water content at 10, 20, 40 and 60 cm depth for site 7 (profile scale study site), (c) groundwater depths for wells GW1, GW3 and GW5 (note GW1 empties in dry periods) and (d) discharge at the catchment outlet (SW1).

Discharge increases along wet up periods and, once the system reaches appropriate wetness conditions, precipitation events generate double peak hydrographs (Martínez-Carreras et al., 2016). Figure 1.3 shows a zoom of the same hydrometric time series for the winter event sampled during this thesis. Although the rain event was not very strong (ca 20 mm accumulated in 2 days), it was enough to trigger a double peak hydrograph, as it was expected given the antecedent wetness conditions. While soil moisture response to the precipitation is almost instantaneous to the first discharge peak, groundwaters have a bit more delayed response, coinciding rather with the second discharge peak.

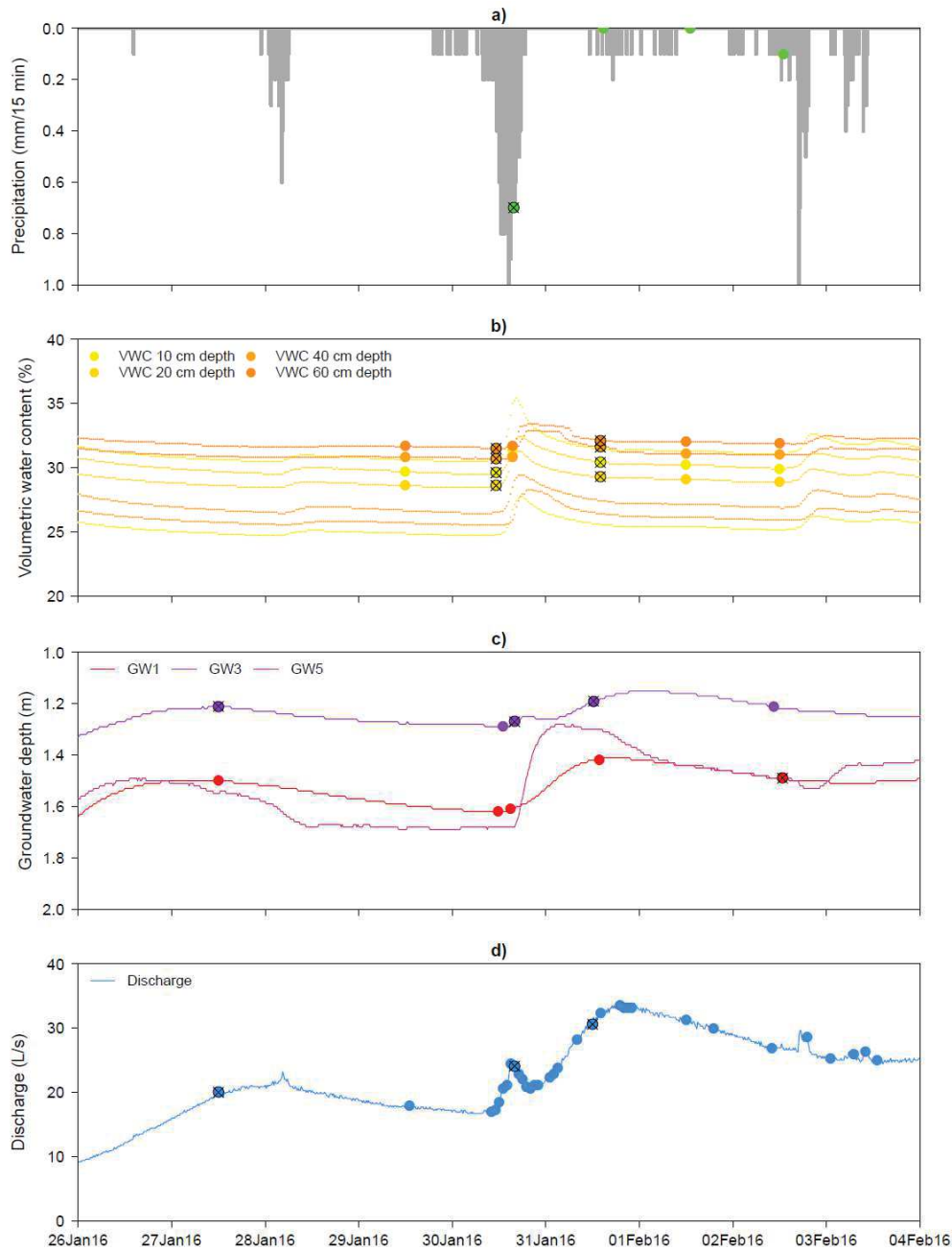


Figure 1.3. Hydrometric time-series of the Weierbach for the winter event sampling (27/01/2016 – 07/02/2016). (a) Precipitation, (b) soil volumetric water content at 10, 20, 40 and 60 cm depth for site 7, (c) groundwater depths for wells GW1, GW3 and GW5, and (d) discharge at the catchment outlet (SW1). Points indicate samples collected along the flood event. Crossed points indicate samples that have been measured for radiogenic isotopes.

Chapter 2. Materials and methods

2.1 Sampling strategy and methods

Different samples of atmospheric dusts, litter, regolith layers and waters have been collected in the Weierbach catchment to qualify the water-system interactions and chemistry dynamics in this setting. In the following sections, a detailed description of the sampling and processing methods is given for each type of sample.

2.1.1 Dusts

Dust samples were collected during one hydrological year under the forest in the Weierbach catchment and in the meadow at an agricultural field in Roodt, nearby the Weierbach catchment. We used a *polypropylene* version of the passive collectors SIGMA-2 produced by the German Meteorological Service in Freiburg, Germany (VDI 2119). The SIGMA-2 passive sampler is primarily used for routine analysis of air quality in German health resorts (VDI 3787, 2010). The special construction of the collector (VDI 2119, 2011) allows the sampling of coarse ($>2.5\mu\text{m}$) particles (Grobéty et al., 2010 and citations therein). For the trace and isotope analysis of these particles the sampling device has successfully been modified (Guéguen et al., 2012a). It is composed of a collection cylinder which contains the sampling dish at the bottom, and a top cover over the cylinder. Both the top of the cylinder and the top cover have interspersed holes/apertures which allow the entry and sedimentation of dust and block the wind, light and precipitation (Fig.2.1). The collectors were placed at a height of ca. 1.70 m from the soil surface.



Figure 2.1. Picture of the passive SIGMA-2 dust collector

Prior to the mineralization, the dust samples were dissolved in 6 ml of distilled HNO_3 in the collection dishes and then transferred with a pipette to savillex® beakers which had been previously tared. The acid was then evaporated and the dusts weighted to finally start the digestion.

2.1.2 Organic horizons: litter and humus

We manually sampled litter and highly decomposed organic material of the OH topsoil horizon under beech/oak and douglas-fir cover on a 4 m² area in order to obtain a sufficient volume for further analyses. We distinguished 3 decomposition litter horizons: full leaves/needles, fragmented leaves/needles and partly decomposed litter (OL, OLv and OF respectively) (Zanella et al., 2011).

The litter samples were first ground to 2 mm with a Titanium blade mill GRINDOMIX GM 200 and then sieved and re-ground with a centrifugal ball mill Pulverisette 6 to <63 μm . We sieved the organic topsoil sample to 1 mm in order to remove the coarse vegetal debris that could remain after the sampling of the OH horizon. Then we fully ground it to 63 μm in a Fritsch centrifugal ball mill Pulverisette 6 in order to homogenise potential semi-decomposed organic particles (Moragues-Quiroga et al., 2017). The organic topsoil sample is therefore not a pure OH sample.

2.1.3 Regolith materials

The sampling strategy was based on the description of the entire regolith presented in section 1.1 and as reported in Moragues-Quiroga et al. (2017). We collected samples from the regolith profile including organic, organo-mineral and mineral material in three different steps from the

surface to the deeper layers. After sampling the organic layers, we performed a soil sampling from the soil pit according to the ISO 10381 guidelines for soil sampling. Special attention was given to collect a representative amount of material for each horizon. According to the stone content, we collected 5 to 10 kg of material for each layer and homogenized it prior to taking representative aliquots for the laboratory analyses. Then, we sampled 5 layers from the core drilling from 140 cm depth (weathered slate) to 735 cm depth (fresh slate bedrock). We encountered some difficulties in obtaining continuous cores as the technique used requires water flow to remove cuttings (Gabrielli and McDonnell, 2012). The material extracted from 140 to 450 cm was made of pieces of rock fragments with muddy matrix. All the samples were stored in plastic bags and air-dried in the laboratory before being prepared for analyses.

We sieved the *solum* and upper *subsolum* first at 2 mm in order to separate the coarse elements (>2 mm fraction), composed of slate rock fragments, and the fine earth (<2 mm fraction), called PPSD matrix in the manuscript. A representative aliquot of coarse elements (PPSDce) was separated and ground to 63 μm . Then, the fine earth was sieved at 63 μm for the mineralogical and chemical characterization of the PPSD matrix. The material collected from the core drillings (lower *subsolum* samples - SP samples) was ground to 63 μm in a Fritsch centrifugal ball mill Pulverisette 6.

2.1.4 Waters

Thanks to the intense monitoring developed in the Weierbach catchment in previous years, we count on geochemical data (concentrations of major and trace elements, nutrients and isotopes as well as physico-chemical parameters) from biweekly samplings from 2009 to 2015. In the frame of this project, we carried out additional samplings at the catchment scale between 2015 and 2016: two punctual samplings in summer 2015 and winter 2015, and one event-scale sampling in winter 2016.

Long term, bi-weekly water sampling

The different sampling points of the catchment operated in a bi-weekly basis are shown in Fig.1.1. Throughfall and rainfall are sampled under deciduous (site 7), spruce and douglas covers in the plateau area with three bulk pluviometers each. Soil solutions were collected with suction cups under vacuum in 6 different points covering from plateau to hillslope areas and depths from 10 to 60 cm depth. Generally, we will here report on soil solution from 10 to 20 cm depth as SS20, and soil solutions from 40 to 60 cm depth as SS60. Groundwater samples are collected from 6 different wells distributed between the plateau and the hillslope areas. The wells GW1 and GW5 are located on the western plateau study site and respectively reach the saprolite at 252 cm depth and the fresher bedrock at 735 cm depth, with a respective screening of 152 and 382 cm at the bottom. On the eastern plateau, characterized by shallower bedrock (ca

65 cm depth), is the GW6 well with 510 cm depth and screened the last 350 cm. The well GW7 is located in the western hillslope, at 600 cm depth in the weathering front, with 400 cm screening at the bottom. GW2 and GW3 are located at the bottom of the hillslope, close to the SW2 spring at 236 cm depth (bottom 136 cm screened) and the catchment outlet (SW1) at 260 cm depth (bottom 160 cm screened) respectively. GW5, GW6 and GW7 wells were drilled in 2014. Water from the riparian soils, hereafter riparian water, is collected with a suction cup. Stream water levels are measured at the outlet of the Weierbach with a pressure transducer (ISCO 4120 Submerge Probe) every 5 minutes. A rating curve is used to transform the levels into discharge (Martínez-Carreras et al., 2015). Streamwater is collected at the outlet (SW1) and also at two tributaries (SW2 and SW3).

Winter event water sampling

Generally the sampling points and protocols described above apply for the winter event sampling carried out during this project. Nevertheless, a choice of sampling points was done in order to adjust the spatial end members' distribution and analytical capacities. Therefore, we decided not to sample rain but only throughfall due to its greater representability of the precipitation in the Weierbach catchment; we also reduced the soil solution sampling points to only 1, in site 7 (deciduous cover) at 20 and 60 cm depth, according to the study regolith profile location. Finally, in order to better compare the groundwater and tributaries/stream physico-chemical characteristics, we added the sampling of the spring of the tributary SW3 (Spring-SP).

We introduced certain measures to avoid contamination of the samples for future isotopic analysis. Waters were generally collected in 3 L volumes with 2 *Volvic* -drinking water- bottles after rinsing them abundantly with the sample. Once in the lab, we measured conductivity and took aliquots for stable isotope analysis using 25 mm syringe filters with 0.45 μm cellulose acetate membrane. Then, we filtered the rest in a Teflon system also with 0.45 μm acetate membrane filters in order to take aliquots for Dissolved Organic Carbon (DOC, ~10 ml), cations and anions (2 x 2 ml), alkalinity and pH (20 ml), trace and major element (2 x 15 ml) and radiogenic isotope (~2L with punctual exceptions) analyses. Thus, the resulting data include water and particulate matter <0.45 μm . The aliquot reserved for radiogenic isotope analyses was stored in polypropylene bottles, which had been previously cleaned with HCl and MilliQ water. The aliquots for trace and major element and for radiogenic isotope analyses were 1‰ acidified with ~13N HNO_3 directly after filtration to stop bacterial activity, oxidation reactions and prevent cations adsorption/precipitation. All aliquots were stored at 4°C in a cold room until their analysis. Prior to the mineralization, the (acidified) water samples were evaporated in 1L savillex® beakers at a maximum temperature of 110°C to avoid projection of sample content out of the beakers.

2.2 Leaching experiments

The leaching experiments consist on the recovery of the mobile -or leachable- pool of the regolith, which is considered to contain elements that are adsorbed on clay minerals or fixed in acid-soluble mineral phases such as Fe-Mn oxyhydroxides, carbonates and phosphate minerals (Hissler et al., 2015; Pierret et al., 2014; Steinmann and Stille, 1997; Stille et al., 2011, 2009). The leaching experiments might be here understood as a simulation of the natural weathering of minerals by the waters, which induces the transport of the mobile or leachable fraction, leaving behind a residual and immobile pool (Sholkovitz et al., 1994). The residual pool is mainly composed of silicate and organic phases and is in balance with the leachable pool. The continuum between the two pools allows their operational definition (Steinmann and Stille, 1997; Stille and Clauer, 1994).

We performed leaching experiments on Site 7 soil (PPSD) samples, a selection of saprolite (SP) layers and the bedrock (namely SP1, SP3, SP4, SP5). Control leaching experiments were carried out on soil horizons and bedrock for results validation. We sequentially leached all the samples in 3 steps with 0.05N acetic acid (HAc), 1N HCl and 2N HNO₃ (Fig.2.2). We conducted the extractions using centrifuge tubes (polypropylene 50 ml) and Teflon filtration systems. Bulk samples weight was ca. 1 g at the beginning of the experiment and the acid volume at the individual extraction steps was 16 ml. The sample-acid mixture was shaken in the centrifuge tubes during 1h in a digital shaker and afterwards filtered in Teflon filtration systems with 0.45μm Durapore HVLP hydrophobe filters. Total extraction time was in average about 1 hour and 15 minutes at room temperature. All Acids were of suprapur quality. We evaporated the recovered solutions in Savilex© beakers, digested them with HNO₃ and separated them into two aliquots for concentration and isotope analyses respectively. After each step, we rinsed the residues with MilliQ water, saved them together with the filters and dried them in the oven at 40°C to then prepare them for the next extraction. At the end of the extraction sequence, we weighted the dry mass of the final residues.

2.3 Mineralization of samples

2.3.1 Dusts, litter, whole regolith and leaching residues

For the total concentration analysis of dusts and litter and for the isotope analysis of all solid samples, the attacks were performed on respectively <55mg and 100 mg aliquots using HNO₃:HF:HClO₄ concentrated acid mixture in Savillex® Teflon vessels at 100°C. The HClO₄ is very efficient in the digestion of the organic matter thanks to its great oxidative power. The addition of a HCl:H₃BO₃ step allows re-dissolving fluoride precipitates which might remove a

significant amount of some trace and rare earth elements from the solution (Aubert et al., 2001; Yokoyama et al., 1999).

For the determination of major and trace element concentrations on the whole regolith and corresponding leaching residue samples, 200 mg aliquots were digested by LiBO_2 alkaline fusion (SARM/CNRS, Nancy, France). After removing the water vapour from the samples by drying them at 110°C , they are calcined at 1000°C to eliminate the mineral water, the organic matter and the carbonates are eliminated. A subsample of 200 mg is then mixed with 750 mg of LiBO_2 and melted at 1000°C under Argon atmosphere. The residue obtained is then digested in HNO_3 (Aubert et al., 2001).

2.3.2 Waters

For the radiogenic isotope analysis, the water samples were evaporated and the remaining solid phase then digested using $\text{HNO}_3\text{:HCl:HF}$ concentrated acid mixture in Savillex® Teflon vessels at 70°C . The HF was here used to help digesting the Si, however it could eventually form fluoride crystals with the cations of the sample (mainly CaF_2 if calcareous waters). The attack was therefore re-started using $\text{HNO}_3\text{:HCl:H}_3\text{BO}_3$ at 100°C which helped dissolving the crystals. We encountered some difficulties to reach the complete dissolution of the samples, due most probably to the high content of cations (silica) after concentrating 3 L of water by evaporation. Consequently, we were obliged to repeat the aforementioned steps and often add a dilution step (in HCl or HNO_3) to ensure the complete dissolution was reached at least once, when we were spiking.

2.3.3 Leachates

After evaporation, leachates were dissolved in 2 ml of 2N HNO_3 twice, first directly after the experiment and second directly before the chemistry. Similar to waters, if the dissolution was not complete due to over-saturation or persistence of organic matter particles, the samples were dissolved in larger volumes by adding MilliQ water or attacked with 3ml of king water (concentrated $\text{HNO}_3\text{/HCl}$) at 100°C overnight respectively. This, once again, was a priority step for the spike application.

2.4 Analytical methods

Fig.2.2 is a scheme of all analytical methods used for the study of the different samples. In the following sections, a detailed description of each method is given.

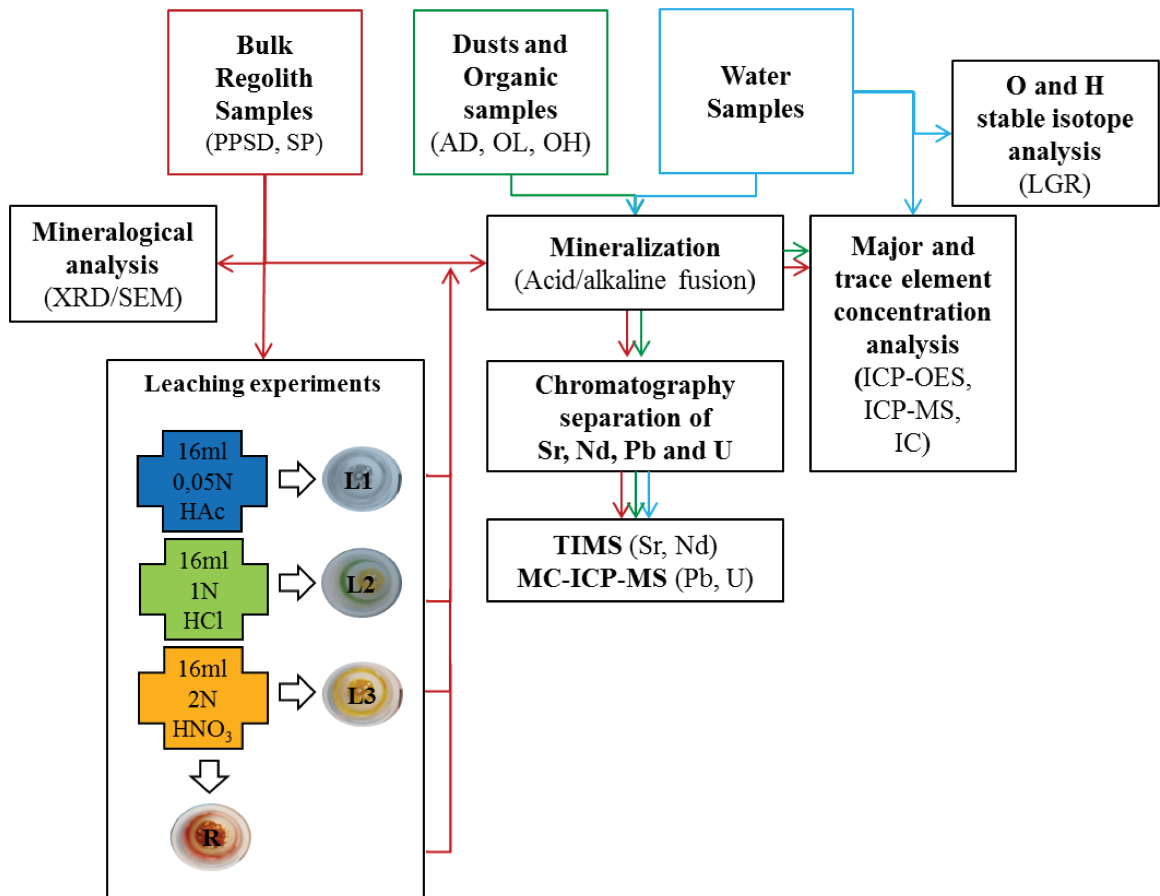


Figure 2.2. Scheme of all analytical methods used for the study of regolith (PPSD and SP), atmospheric dusts (AD), litter (OL), humus (OH), and water samples of the Weierbach catchment.

2.4.1 Mineralogical analysis of the regolith materials: XRD and SEM

We analysed aliquots of all regolith powdered samples for mineralogical contents by X-Ray Diffractometry (XRD, diffractometer RX Bruker, D5000) and all PPSD samples by Scanning Electron Microscopy (SEM, TESCAN Vega II fitted with EDAX X-ray energy dispersive spectrometer) (Moragues-Quiroga et al., 2017).

For the XRD, when considering only the diffractogram of an oriented preparation that has been air dried, some clay minerals are not dissociable (for example : the reflexion (001) of the kaolinite at $\sim 7,15 \text{ \AA}$ is the same as the one of the chlorite (002)). That is why 4 diffraction patterns are registered:

- The normal test (N): measurement of the oriented preparation that has been air dried,
- After treatment with ethylene-glycol (G): the blades are placed during one night in the dessiccator under an ethylene-glycol atmosphere. The objective of this treatment is to inflate the smectite layers by introduction of big ethylene-glycol molecules inside the interlayer spaces. This treatment is generally carried out on the N test, after the N measurement.

- After treatment with hydrazine (H): the blades are placed for a night inside a desiccator under hydrazine – monohydrate atmosphere: the objective of the saturation is to distinguish the kaolinite in presence of chlorite by inflating the minerals from the kaolin family.
- After heating during 4h at 490°C (CH): the kaolinite is destroyed, and the vermiculites and smectites are irreversibly dehydrated.

After the identification of the minerals present in the sample, an estimation of the relative abundance can be done from a semi-quantitative analysis. For this, the most intense diffraction peak of each mineral is divided by a correction factor « I/I_{cor} ». The proportions of each mineral are deduced of the sum of corrected intensities.

2.4.2 Major and trace element concentrations analysis

Dusts, litter, whole regolith and leaching residues

Total concentrations of dusts (¼ mineralized sample ~ 8-52 mg) and litter (¼ mineralized sample ~ 200 mg) were analysed at LIST facilities (Luxembourg) and those of PPSD and SP whole samples and of their corresponding leaching residues (200 mg) were analysed in the Service d'Analyse des Roches et des Minéraux (SARM/CNRS, Nancy, France). Major elements were analysed by Inductively Coupled-Atomic Emission Spectroscopy (ICP-AES). Other trace elements were analysed by Inductively Coupled-Mass Spectroscopy (ICP-MS). Organic matter (OM) was analysed on ~100 mg aliquots of regolith (PPSD and SP) samples by dry combustion (950 °C) measurements of soil organic carbon (SOC) and total nitrogen (TN) contents with a LECO® Truspec CHNS analyser. The quality controls were carried out with international standards and the analytical errors were < 5% for all instruments and laboratories.

Waters and Leachates

Total concentrations of waters and leachates were analysed at LIST (Luxembourg) and LHyGeS (Strasbourg, France) facilities respectively. For the waters, 2 replicates of 15 ml of each filtered and acidified sample were measured by ICP-MS for trace elements. Concentrations of dissolved major cations and anions were measured with an ion chromatograph (Thermo Scientific Dionex ICS-5000+ Reagent-Free HPIC) and alkalinity (HCO₃⁻) by titration with 0.01N HCl up to pH 4.5. Dissolved Organic Carbon (DOC) was analysed on ca. 10 ml aliquots of water samples with a combustion analyzer (Apollo 9000 - Teledyne Tekmar). Aliquots of ½ and ¼ of the PPSD and SP mineralized leachate samples respectively were analysed by ICP-MS/OES for major and trace element concentrations. The different proportions of sample reserved for these measurements are due to improvements in the protocol addressed to the prioritization of potential repetitions of radiogenic isotope analysis. Quality controls were carried out with international standards and the analytical errors were < 5% for both instruments and

laboratories. Additionally, blank tests carried out for the different collection, storage and filtration systems were measured for trace and major element concentrations together with the actual samples (Fig.2.3). The tests carried out on water processing materials generally yield values lower than the detection limit (D.L.), except for Fe, Mn, Co, Ni, Cu, Sr and Dy, which reached up to the double of the D.L (Fig. 2.3-a). However, the minimum average concentrations of these elements in waters were at least 50% higher than the D.L. The tests carried out during the leaching experiments generally gave concentrations over the D.L. (Fig. 2.3-b). In this case, the most weakly concentrated samples had concentrations at least 6% higher than the D.L. (worse cases like Mo or Sb) for the L1 SP leachates and more than 125% over the D.L. for L1-2-3 PPSD and L2-3 SP leachates (all elements).

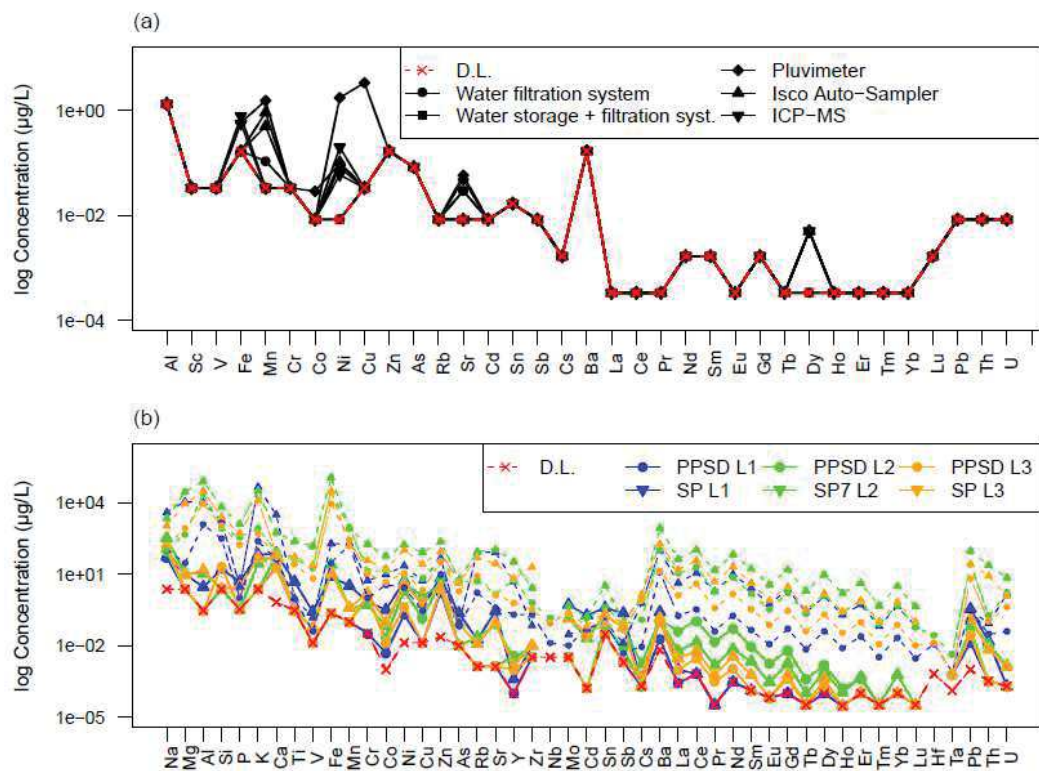


Figure 2.3. Major and trace element concentrations of blank tests for materials used for (a) waters sampling and processing and (b) leaching experiments (dashed lines: minimal leachate concentrations).

2.4.3 O and H stable isotope analysis

$^{18}\text{O}/^{16}\text{O}$ and $^2\text{H}/\text{H}$ isotopic ratios were analysed with a LGR Triple Water Isotope Analyser (T-WIA) at LIST facilities (model 912-0032). An LC PAL liquid auto-injector connected to the analyser allowed automatic and simultaneous measurement of $^{18}\text{O}/^{16}\text{O}$ and $^2\text{H}/\text{H}$ ratios in the water samples. The measurement's precision with this equipment is $< 0.1\%$ for $^{18}\text{O}/^{16}\text{O}$ and $< 0.4\%$ for $^2\text{H}/\text{H}$ (Los Gatos Research Inc., 2008). Vienna Standard Mean Ocean Water (VSMOW) standards ($\delta^2\text{H}$ and $\delta^{18}\text{O}$ in ‰) were used as reference for the data notation transformation.

2.4.4 Sr, Pb, Nd and U isotope analysis

Separation of Sr, Pb, Nd and U

Sr, Pb, Nd and U of a selection of regolith, leachate, residue and water samples were separated from other elements for radiogenic isotope analyses. First, U was separated by chromatography on Biorad AG1x8 anionic resin following procedures developed at the LHyGeS (Strasbourg, France) (Chabaux et al., 1997; Dequincey et al., 2002; Granet et al., 2010; Pelt et al., 2008). Then, the separation of Sr, Pb and Nd was done by extraction chromatography on Eichrom Sr Spec, TRU Spec and Ln Spec resins, respectively, following the procedures of Geagea et al. (2007) and Guéguen et al. (2012) adapted from Pin and Zalduegui (1997) and Deniel and Pin (2001).

MC-ICP-MS: Pb and U isotopes analysis

Pb and U of bulk, leachate and residue regolith samples as well as waters were measured on a Neptune Thermo-Scientific multicollector (MC-ICP-MS).

Mass fractionation of Pb isotopic ratios was corrected online using a SRM 997 Tl isotopic standard following the procedure of the laboratory (Stille et al., 2011). The Pb SRM 981 standard measurement during the sessions gave $^{208}\text{Pb}/^{206}\text{Pb}$ ratios between 2.16604 ± 0.00002 (2SD) and 2.16613 ± 0.00002 (2SD), $^{207}\text{Pb}/^{206}\text{Pb}$ ratios between 0.914651 ± 0.000007 (2SD) and 0.914545 ± 0.000008 (2SD), and $^{206}\text{Pb}/^{204}\text{Pb}$ ratios between 16.9267 ± 0.0004 (2SD) and 16.9295 ± 0.0005 (2SD), which are within the 2014-2017 0.2‰ dispersion observed in the lab and consistent within less than 1‰ with the reference values of Doucelance and Manhès (2001). Mass fractionation and the Faraday/SEM drift during U isotopic measurements by MC-ICPMS were corrected by bracketing against the IRMM-184 natural U standard. The HU1 uraninite was measured 4 to 5 times during each uranium MC-ICPMS session and yielded ($^{234}\text{U}/^{238}\text{U}$) activity ratios between 0.9983 ± 0.0004 (2SD) and 1.0004 ± 0.0014 (2SD), consistent with secular equilibrium within 2‰.

TIMS: Sr and Nd isotopes analysis

We measured Sr and Nd isotopic ratios of dusts, bulk, leachate and residue regolith samples and waters on a Thermo-Scientific Triton (TIMS). The 2014-2017 mean for the Sr SRM 987 standard yields a $^{87}\text{Sr}/^{86}\text{Sr}$ ratio of 0.71026 ± 0.00004 (2SD, n=56) and for the La Jolla standard a $^{143}\text{Nd}/^{144}\text{Nd}$ ratio of 0.51185 ± 0.00002 (2SD, N=46).

Blank assessment for the isotope data

The results of concentration and U isotopic ratios of the ID-blanks run with the bulk, leachate and residue regolith samples as well as with waters are reported in Table 2.1. They suggest, for the bulk regolith samples, a contamination of less than 30 pg for Sr and Nd, ~400 pg for Pb and

23 pg for U which is negligible compared to the amount processed (>200 ng of Sr and Nd and >200 ng of Pb and U for all samples except for the humus sample with 20-30 ng U). For the leachates, the ID-blanks suggest a contamination of up to 0.63 ng for Sr, 2.10 ng for Nd, 5.50 ng for Pb and 0.58 ng for U, which is considered generally high due to the fact that these blanks generally cover complete sample processing protocols (preparation, filtration, attack and chemistry). We assessed the importance of the contamination for the samples measured according to the equation (i):

$$(i) \quad \alpha = \left[\frac{X_{Blank}}{X_{sample}} \right] * 100, \alpha. \text{ is the blank contamination (\%)} \text{ and } [X] \text{ the element measured.}$$

Considering the amounts of sample processed, the contamination was important (> 5%) for the L1 PPSD3 sample for Sr (Sr mass \approx 20 ng) and Nd (Nd mass \approx 5 ng); L1 PPSD3, SP1, SP3 and SP4 samples for Pb (Pb mass between 1 and 20 ng); and the L1 PPSD1 sample for U (U mass \approx 2 ng). Similarly, the analysis of the ID-blanks run with the waters, indicate up to 31 ng of Sr contamination, which is negligible (< 5%) for the mass processed (Sr mass \geq 700) and 0.986 ng of U, which was important (>5%) for most waters (U masses between 3 and 35 ng). For the U isotope data, since we had the $^{234}\text{U}/^{238}\text{U}$ ratios of the blanks, we re-calculated the errors for all samples showing contamination higher than 1% as in equation (ii):

$$(ii) \quad E = SE_m + SD(IR_m + IR_c),$$

where E is the final Error, SE_m is the Standard Error measured, IR_m is the the measured $^{234}\text{U}/^{238}\text{U}$ ratio and IR_c the $^{234}\text{U}/^{238}\text{U}$ ratio corrected according to the blank contamination (α) with equation (iii):

$$(iii) \quad IR_c = \alpha(IR_{Blank}) + (1 - \alpha)(IR_{Sample}).$$

Table 2.1. Blanks contamination in Sr, Nd, Pb and U according to Isotopic Dilution (ID) and measured $^{234}\text{U}/^{238}\text{U}$ ratios ($\pm 2\text{SE}$: Standard Error); (WR: Whole Rock PPSD and SP samples).

Blank sample	Sr	Nd	Pb	U	$^{234}\text{U}/^{238}\text{U}$	2SE
	(ng)					
Clean room (attacks + chemistry WR)	0.03	0.03	0.4	0.023	-	-
Clean room (attacks + chemistry leachates)	0.18	0.01	3.85	0.28	1.103	0.001
Clean room (attacks + chemistry waters)	0.26	-	-	0.986	1.076	0.007
Water filtration system	31	-	-	0.857	1.084	0.007
SP Leaching experiments	0.63	0.14	2.87	0.584	1.094	0.007
SP Leaching experiments*	1.17	0.16	5.50	0.167	-	0.015
PPSD Leaching experiments*	1.04	2.10	5.20	0.306	-	0.010

* Manipulation error during chromatography separation

Chapter 3. Stratigraphic and geochemical characterization of the Weierbach regolith

The work in this chapter has been published in CATENA (doi:10.1016/j.catena.2016.09.015; Moragues-Quiroga et al., 2017). Major parts of the following chapter are identical in content and word with this publication.

Introduction

Regolith represents the unconsolidated mantle of weathered rock and soil material on the Earth's surface (SSGT, 2008). In a broader sense, it encompasses all material from fresh rock to the atmosphere (Eggleton, 2001; Field et al., 2015; National Research Council, 2001; P, 2011; Scott, K.M., Pain, 2008). Regolith is a major compartment of the critical zone where fluxes of water, energy, solutes and matter occur. The production of regolith from the original bedrock influences the chemistry of surface waters and buffers the atmospheric CO₂ concentration (Banwart et al., 2011; Berner and Maasch, 1996; West et al., 2013). The regolith is the terrestrial environmental compartment where most of the water exchanges occur. Its biophysico-chemical properties drastically impact the water that percolates and/or stores in its different parts (organic and mineral soil horizons, weathered bedrock, etc).

On a large scale from a space and time perspective, most of the in situ regolith systems are polygenetic. As an example, Felix-Henningsen (1994) showed that in the Rhenish Massif a weathering mantle representing the in situ regolith with a thickness up to 150 m was formed under warm and humid climates over a long period of time, from the Upper Mesozoic to the Tertiary. Additionally, loose materials produced in the in situ regolith move during erosion processes and contribute to form a transported regolith after redeposition. This means that actual in situ regoliths recorded successive weathering and erosion stages (Barbier, 2012). Therefore in situ regoliths can also be considered as polygenetic (Taylor and Eggleton, 2001), because they

are the result of the accumulation of material from different origins. In the Rhenish Massif, the soil representing the upper part of the regolith is essentially developed from Pleistocene Periglacial Slope Deposits (PPSD - Kleber, 1997; Semmel and Terhorst, 2010) - also called periglacial coverbeds - that cover the weathered in situ regolith to constitute a polygenetic regolith system. These PPSD originate from the combination of atmospheric deposition, solifluction and/or cryoturbation of the former active rock layer during the last glacial period (Kleber, 1997; Semmel and Terhorst, 2010). The distances over which these materials were transported range from a local to regional scale. Hence, the alternation of such contrasting materials creates regolith components which may have a proximal, but not direct, genetic link to the underlying bedrock. Their differentiation in the regolith induced many lithic discontinuities that directly impact the evolution of the regolith and control pedogenesis, water infiltration, interflow and root penetration (Lorz and Phillips, 2006; Völkel et al., 2011).

Atmospheric depositions can significantly contribute to the polygenetic evolution of regoliths and mask the autochthonous contribution coming from the bedrock. On the one hand, atmosphere-derived anthropogenic depositions of trace metals originating from agricultural tillage and fertilization, mining and other industrial activities tend to accumulate in the upper soil layers due to their adsorption by organic matter (Aubert et al., 2002b; Hissler and Probst, 2006; Steinmann and Stille, 1997). Stückrad et al. (2010) and Stille et al. (2011) suggested, based on a combined trace element and Pb isotope study, a contribution of regional ore-vein derived elements to a regolith from the south eastern edge of the Rhenish Massif and from the Vosges Mountains in France, respectively. On the other hand, loess that was deposited during the Pleistocene is widespread throughout Europe. These deposits form a more or less continuous belt along a 2000 km east-west transect from Great Britain and Brittany in northern France to the Dnieper Valley in Ukraine (Catt, 1986; Paepe and Sommé, 1931; Rousseau et al., 2014, 2013). The origin of the European loess is still a matter of discussion. Nevertheless, Sr and Pb isotopic data clearly demonstrate that the sources of the loess deposits are proximal and different for each region (Rousseau et al., 2014). Some of these aeolian deposits present a typical volcanic mineralogical contribution (Kleber and Terhorst, 2013; Pissart, 1995; Semmel and Terhorst, 2010). Impacts of different Pleistocene volcanic eruptions were identified in the upper layers of the western European regoliths and can serve as efficient chronostratigraphic markers of these systems (Pouclet et al., 2008; Pouclet and Juvigne, 2009; Wörner and Schmincke, 1984). The studies of Chauvel et al. (2014) and Gallet et al. (1998) confirm an earlier conclusion reached by (Taylor et al., 1983), that most of these aeolian deposits reflect the chemical composition of the upper continental crust.

The matter and energy exchanges in the critical zone are partly controlled by the structure and evolution of the regoliths; therefore it is especially important to look at the entirety of the regolith when more than one formation occurs in the same profile. Relevant tools are required to

improve the understanding of complex critical zone processes and to investigate this hidden part of the ecosystems. Over the last decades, radiogenic isotope, trace element and mineralogical analyses have become state-of-the-art tools for the characterisation of deposit and regolith formations (Debajyoti, P., White, W. M., Turcotte, 1967; Faure, 1977; Michard et al., 1985; Taylor and McLennan, 1981). Sr, Nd, Pb and U isotopes together with trace and rare earth element (REE) distribution patterns have been shown to be very suitable tools to answer open questions about regoliths formation (Aubert et al., 2001; Dequincey et al., 2002; Hissler et al., 2015; Stille et al., 2011, 2009). However, these techniques are rarely applied concurrently.

In the present study, we combine mineralogical, major and trace element and Sr-Nd-Pb-U radiogenic isotope analyses in order to reach a more comprehensive characterisation of a regolith profile. Our objective is to distinguish the different regolith strata by assessing their origin and evolution, and by evaluating the chemical and isotopical impact between the different strata. Hereby, we also address the question, how far dust from the late-Pleistocene volcanic eruption reached the south-western edge of the Rhenish Massif and mixed with the local loess deposits. To our knowledge, this is one of the few existing studies on a whole regolith system using such a multi-tracing approach.

3.1 Results

3.1.1 Mineralogical composition of the regolith components

The XRD analyses (**Fig.3.1**) indicate that PPSD3 and PPSD4 are enriched in phyllosilicates and clay minerals, mainly chamosite, a Fe-rich polytype of chlorite, and kaolinite. At these depths, chamosite and kaolinite show relative abundances ranging from 17 to 20%. Other chlorite polytypes are much less abundant (rel. abund. < 3%).

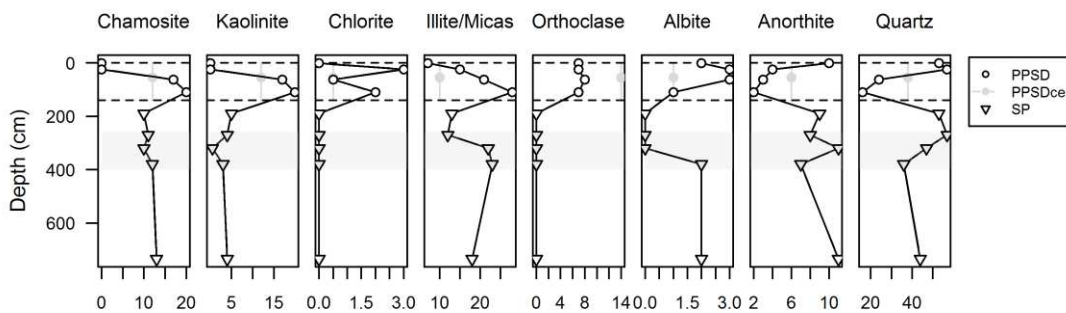


Figure 3.1. Depth-dependent patterns of mineralogical composition from XRD analyses expressed in relative abundances (PPSDco: PPSD coarse elements; dashed lines: lithic discontinuities; shaded area: redox sensitive zone).

The illite/mica group shows increasing abundances with depth in the matrix of the PPSD compartment between 7 and 28%. Similarly, one observes enrichments in orthoclase (rel. abund. 8%) in PPSD3 and PPSD4 and in albite (3%) at the PPSD2 and PPSD3 layers.

Conversely, anorthite is depleted between PPSD2 and PPSD4 (rel. abund. < 3%), and quartz is depleted at the PPSD3 and PPSD4 layers (rel. abund. 16 to 24% respectively), both compared to the above solum horizons (PPSD1 and PPSD2) and the subsolum saprolithic material below (SP), where the relative abundances scatter between 8 and 11% for anorthite and 36 and 57% for quartz. Rock fragments from the PPSD (PPSDce) generally present a mineralogical composition rather similar to the SP compartment, being slightly more enriched in kaolinite (12%) and notably in orthoclase (14%). SEM analyses on all PPSD samples indicate that in this compartment there are REE-bearing minerals such as monazite, xenotime, zircon and florencites. Other Ti-bearing and iron oxide trace minerals observed at these depths are rutile, ilmenite and Ti-magnetite.

3.1.2 Chemical composition of the regolith components

The chemical composition of the entire regolith is shown in Table 3.1. Na₂O and TiO₂ are enriched in the PPSD matrix between PPSD2 and PPSD4 compared to SP. K₂O, Fe₂O₃, MgO and Al₂O₃ tend to increase with depth within the matrix of the PPSD compartment and reach values similar to those of the underlying saprolite (SP samples). CaO concentrations are high at the OH horizon and decrease with depth in PPSD, showing an important depletion on top of the SP regolith compartment, where it slightly increases again towards the fresh bedrock. On the contrary, P₂O₅ is highly enriched at the top (PPSD1) and bottom (PPSD4) of the PPSD and in SP3 similarly to MnO and Fe₂O₃. PPSDce is, compared to the matrix between PPSD₂ and PPSD₄, depleted in TiO₂, K₂O and Al₂O₃. PPSDce is enriched in Fe₂O₃ with respect to the rest of the profile, with the exception of SP3. SiO₂, CaO, MgO and MnO show in PPSDce similar concentrations as in the SP1 compartment, whereas Na₂O and P₂O₅ PPSDce concentrations are rather close to the ones of the soil matrix at the PPSD bottom horizons.

In order to determine groups of major and trace elements that follow similar variation patterns in the regolith with depth, we performed a hierarchical cluster analysis (e.g. Hartigan, 1975; Kaufman, L., Rousseeuw, 1990). Such statistical technique has been widely used for drawing meaningful information from geochemical data (e.g., Bini et al., 2011; Levitan et al., 2015; Schot and van der Wal, 1992). For the linkage rule, we chose the Ward's method (Ward, 1963), which has been successfully used in many previous studies (Gourdol et al., 2013; Lin et al., 2014). For the linkage distance, the Pearson correlation distance (1 – Pearson correlation coefficient) was retained, which is suitable for clustering variables (Reimann et al., 2008). Prior to the analysis, the most universal z-transformation was applied to each parameter (mean subtraction and division by standard deviation) to ensure that each major and trace element is weighted equally (Templ et al., 2008). The resulting dendrogram, illustrating the similarity of the parameters, was cut using two phenon lines to define groups and subgroups of parameters.

Table 3.1. Major (% oxide) and trace element (ppm) composition of the regolith (D.L.: Detection Limit; NA: not analysed).

	D.L.	OH	PPSD1	PPSD2	PPSD3	PPSD4	PPSDce	SP1	SP2	SP3	SP4	SP5
Major elements (% oxide)												
Na ₂ O	0.01	0.05	0.24	0.38	0.38	0.40	0.44	0.30	0.21	0.24	0.27	0.26
MgO	0.015	0.10	0.30	1.02	1.69	1.92	1.57	1.90	1.85	1.73	2.18	1.83
Al ₂ O ₃	0.02	1.31	7.70	16.49	19.12	22.86	13.11	19.13	16.69	18.76	20.01	18.29
SiO ₂	0.02	<0.02	37.82	62.82	60.27	52.92	66.35	62.51	64.16	58.53	59.41	64.35
P ₂ O ₅	0.04	<0.04	0.27	0.16	0.12	0.22	0.21	0.07	0.17	0.29	0.15	0.15
K ₂ O	0.01	0.28	1.31	2.63	3.41	3.92	1.96	3.62	3.07	3.72	4.19	3.77
CaO	0.03	<0.03	0.10	0.08	0.05	0.00	<0.03	0.00	0.00	0.04	0.06	0.15
TiO ₂	0.02	<0.02	0.55	1.01	1.05	1.12	0.64	0.96	0.86	0.93	0.95	0.87
Fe ₂ O ₃	0.02	0.66	3.48	5.77	6.66	7.99	10.90	5.26	7.15	9.15	6.31	5.56
MnO	<0.001	0.05	0.03	0.06	0.05	0.09	0.05	0.02	0.03	0.94	0.05	0.05
Trace elements (ppm)												
Cr	4	15.4	72.6	127.3	151.6	173.8	120.8	166.9	144.0	144.4	149.8	133.6
Co	0.4	1.7	5.0	15.3	17.5	20.9	20.5	16.0	13.8	200.8	61.9	15.3
Ni	5	8	20	60	71	78	83	74	74	131	79	68
Cu	5	12	20	20	23	39	30	17	41	68	36	44
Zn	11	46	84	145	107	147	110	96	115	175	116	101
As	1.5	2.5	14.9	8.2	9.5	13.8	10.1	8.3	14.9	18.2	12.5	7.6
Rb	0.4	12.2	74.1	159.3	175.6	193.3	91.0	166.6	146.1	167.0	187.7	170.4
Sr	2	14	48	94	110	126	61	96	81	102	113	98
Y	0.2	<0.2	15.8	31.5	38.7	36.6	22.2	34.8	31.8	32.6	33.7	28.0
Zr	1	<1	154	283	305	293	168	260	190	177	174	149
Nb	0.09	<0.09	10.28	19.87	19.44	19.66	10.77	15.96	14.61	14.94	15.28	13.93
Cd	0.12	0.25	0.32	0.25	0.27	0.25	0.2	0.25	0.24	0.28	0.19	0.16
Sn	0.45	0.12	9.63	3.76	4.13	4.63	2.44	4.13	3.72	4.30	4.45	4.04
Sb	0.2	0.4	2.9	0.6	0.5	0.5	0.4	0.3	0.7	0.9	0.7	0.4
La	0.09	2.23	22.03	45.30	51.45	61.33	30.62	48.00	41.00	48.29	57.40	44.04
Ce	0.14	4.26	43.15	91.90	102.90	128.00	61.53	96.75	82.07	109.30	124.10	89.11
Pr	0.015	0.502	4.876	10.340	11.640	14.550	7.052	11.580	9.511	11.880	15.150	10.180
Nd	0.06	1.87	17.93	37.48	42.35	54.10	25.80	43.11	35.83	45.39	59.72	37.89
Sm	0.015	0.313	3.250	6.923	7.778	9.712	4.968	8.233	7.068	9.039	11.680	7.216
Eu	0.005	0.058	0.659	1.408	1.562	1.875	1.030	1.602	1.458	1.871	2.348	1.471
Gd	0.013	0.176	2.682	5.668	6.465	7.161	4.099	6.494	6.111	7.474	8.833	5.970
Tb	0.003	0.029	0.446	0.916	1.074	1.104	0.670	1.001	0.973	1.097	1.187	0.892
Dy	0.01	0.17	2.81	5.80	6.89	6.81	4.11	6.21	5.99	6.50	6.76	5.41
Ho	0.002	0.036	0.601	1.201	1.451	1.395	0.847	1.286	1.250	1.326	1.340	1.112
Er	0.01	0.10	1.63	3.26	3.93	3.79	2.28	3.50	3.32	3.53	3.46	2.94
Tm	0.001	0.016	0.241	0.470	0.571	0.563	0.336	0.512	0.484	0.519	0.506	0.429
Yb	0.007	0.110	1.647	3.274	3.904	3.829	2.296	3.447	3.315	3.531	3.409	2.996
Lu	0.003	0.016	0.252	0.508	0.592	0.586	0.357	0.520	0.500	0.543	0.516	0.451
Hf	0.03	<0.03	3.98	7.53	8.02	7.93	4.55	6.99	5.49	5.16	5.18	4.40
Hg	<0.001	<0.001	0.342	0.091	0.050	0.038	<0.001	<0.001	0.040	0.049	0.043	0.031
Pb	0.7	41.6	128.9	19.4	14.6	14.6	8.9	30.3	24.3	33.7	24.5	17.8
Th	0.06	0.66	7.07	13.21	15.07	17.26	10.12	14.53	13.22	14.43	15.21	13.71
U	0.03	0.33	1.93	3.14	3.14	3.51	2.45	3.09	3.82	5.22	5.84	3.83

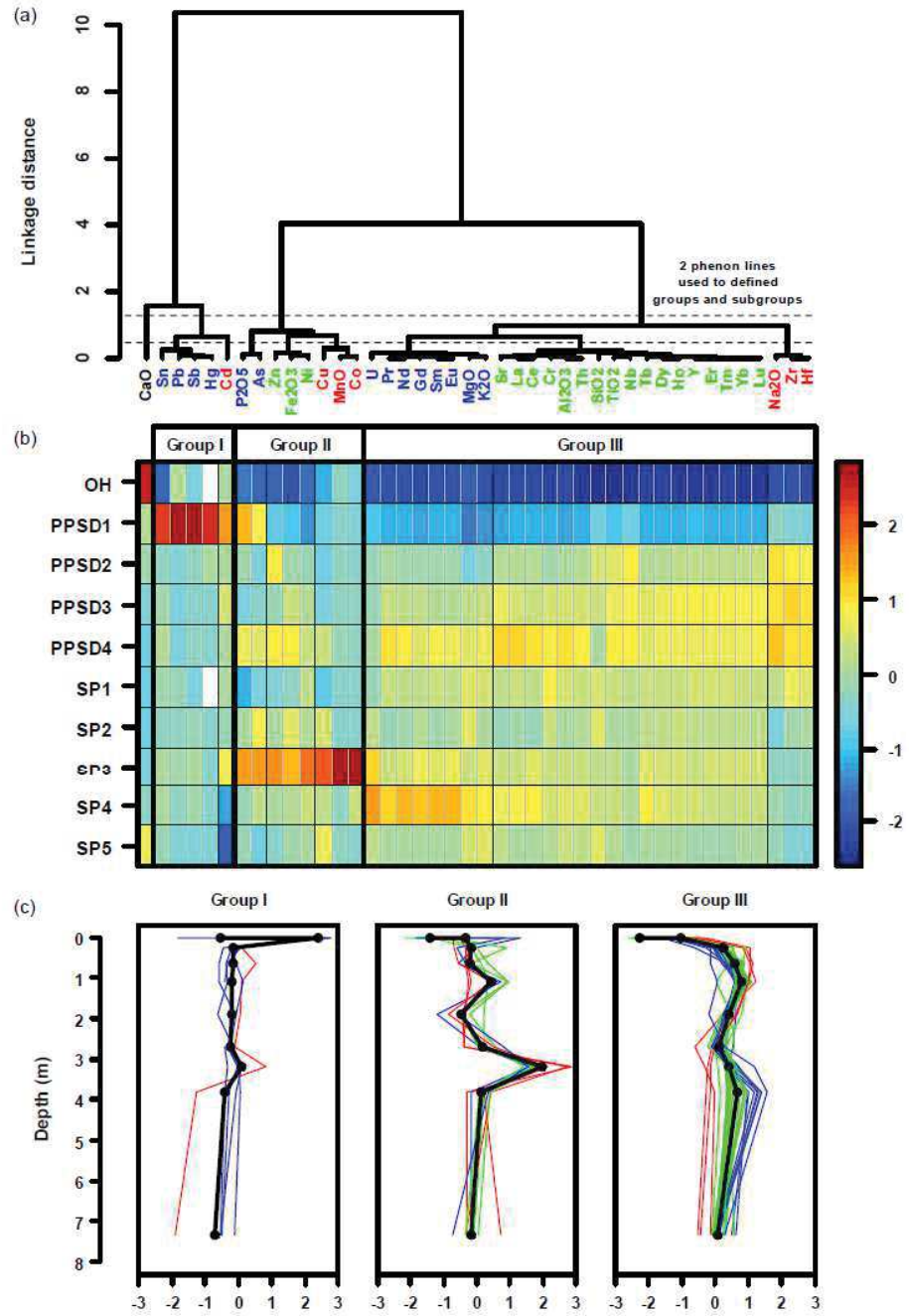


Figure 3.2. Hierarchical cluster analysis performed on major and trace elements: (a) dendrogram defined using Pearson correlation distance as distance measure and Ward's method for the linkage rule; (b) coloured z-transformed concentrations matrix (row names correspond to regolith layers, parameter columns are ordered as the dendrogram); and (c) z-transformed concentrations as a function of depth for the 3 parameter groups defined (the thick black lines correspond to the median of each group, the thin coloured lines correspond to individual parameters of each subgroup as defined by the colour of the parameter labels in the dendrogram (a)).

Defining the number of groups by selecting the position of the phenon line up or down the dendrogram is a subjective evaluation step (Güler et al., 2002). The heights of these two phenon lines were retained by visual inspection of the dendrogram and the associated ordered z-

transformed concentrations matrix and gave us the most satisfactory geochemical parameters groups and subgroups in terms of variations with depth.

The trace elements can be classified in three groups according to the vertical evolution of their concentrations within the regolith profile (Fig.3.2). Group I contains Cd, Sn, Sb, Hg and Pb. Their concentrations are higher in the top layer of the PPSD compartment and are low and almost constant throughout the rest of the regolith profile (SP). Group II is composed of Co, Ni, Cu, Zn and As, which present high concentrations in PPSD4 and are enriched in SP3. Group III includes trace elements having increasing concentrations with depth in the PPSD and a notable decrease in the concentrations between PPSD and SP. These elements can be divided in three subgroups according to their behaviour in the SP compartment: Group IIIa encloses those presenting a concentration increase at 380 cm depth, similar to Mg and K (U, Pr, Nd, Gd, Sm, Eu); Group IIIb those that, similar to Al, Si and Ti, remain stable below 200 cm depth (Cr, Rb, Sr, Y, Nb, Th, La, Ce, Tb, Dy, Ho, Er, Tm, Yb, Lu) and Group IIIc those that continue decreasing after 200 cm depth, like Na (Zr, Hf).

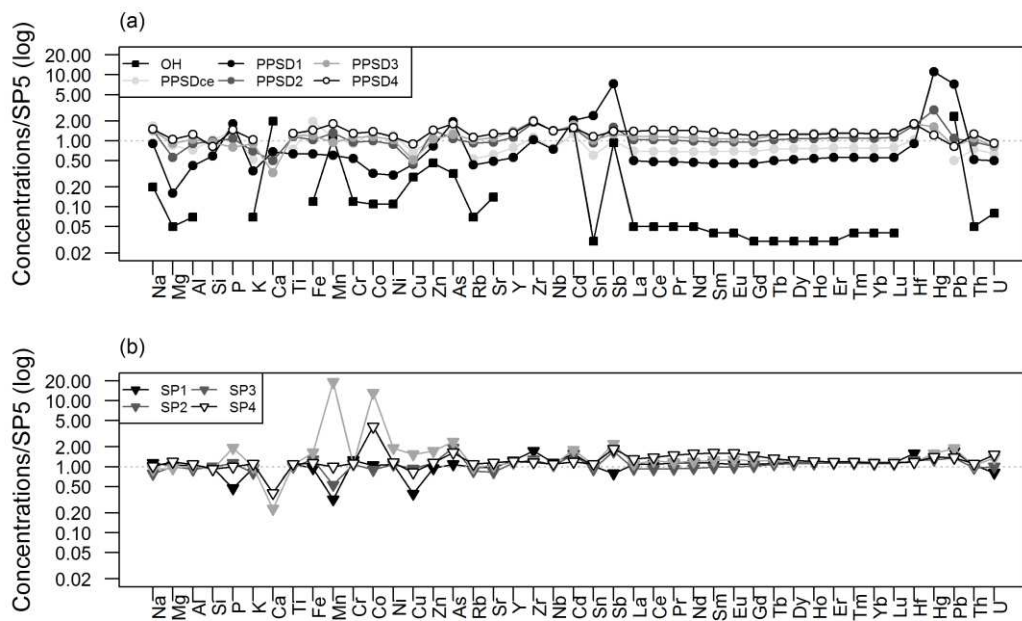


Figure 3.3. Major and trace element concentrations of (a) OH and PPSD samples and (b) SP samples, normalized to the SP5 sample concentrations, representing the fresh slate bedrock.

Major and trace element concentrations of PPSD and SP samples are normalized to the deeper SP lithic material (SP5), which can be considered, at this study site, as the fresh slate (Fig.3.3). Compared to this local reference, OH and PPSD1 are depleted in most of the elements, except the trace elements of group I. The other PPSD and SP samples are slightly enriched and show almost identical distribution patterns with ratios close to 1 for most of the analysed elements. However, the enrichments of the elements of Group II in SP3 and SP4, especially Mn, Co, As and U are different. Compared to the slate reference, Nb is generally slightly enriched in the

PPSD compartment (ratio = 1.4), whereas the underlying SP samples present a ratio of 1.0. This is also not the case for the rock fragments of PSD (PPSDce), whose Nb ratio is 0.77.

Post Archean Australian Shale (PAAS) normalized Rare Earth Element (REE) concentrations of PSD and SP samples show similar distribution patterns (not shown). They display middle REE (MREE) enrichments, which are more notable in coarse materials (PPSDce), in the matrix of PSD4 and in SP, especially at SP4, as indicated by the (Eu/Yb)N ratios (Fig.3.4). Similarly, though to a lesser extent, (La/Yb)N ratios point to a strong enrichment of light-REE (LREE) in PSD4 and SP4, whereas a positive Ce anomaly ($CeN/CeN^*=1.05$) is only observable in SP3. Ce is an especially interesting element as it is one of the most reactive REE. Conversely to most of the other REE, it can pass from state 3+ to 4+ and precipitate as cerianite (CeO_2) in oxidizing conditions (Braun et al., 1990). Here, Ce anomalies are calculated as the enrichment of Ce with respect to other LREE (namely La and Pr) normalised to Post Archean Australian Shales (PAAS) with the equation [$CeN/CeN^*=CeN/(0.5LaN+0.5PrN)$].

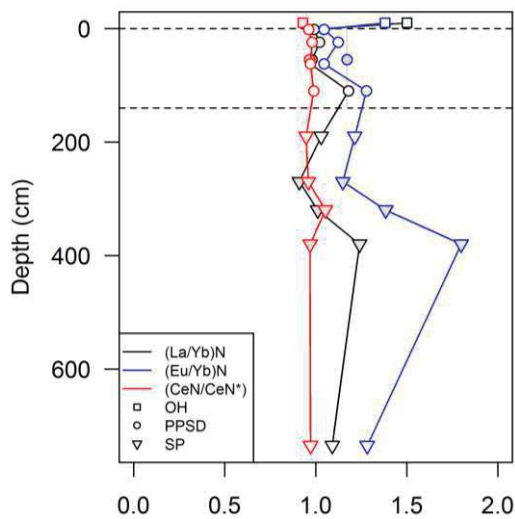


Figure 3.4. Depth dependent patterns of PAAS-normalized LaN/YbN and EuN/YbN ratios and Ce anomaly (CeN/CeN^*) (dashed lines: lithic discontinuities; shaded area: redox sensitive horizons).

3.1.3 Pb, Sr, Nd and U isotopic compositions of the regolith components

All isotope data are given in Table 3.2. $^{87}Sr/^{86}Sr$ and $^{206}Pb/^{207}Pb$ ratios are low in OH and PSD1 (0.7218 and 1.153 respectively) and increase with depth through PSD2 and PSD3 up to 0.7387 and 1.220, respectively (Fig. 3.5-a and -b). $^{87}Sr/^{86}Sr$ ratio decreases in PSD4 (0.7366), increases again in the saprolithic material of the SP and has the highest isotopic ratio in the lithic material at SP5 (0.7416). $^{206}Pb/^{207}Pb$ ratio still increases beyond PSD4 and, after a remarkable decrease at the lithic discontinuity between PSD and SP, increases again until the deeper part of the regolith (1.214), similar to $^{87}Sr/^{86}Sr$. The coarser materials of the PSD (PPSDce) display $^{87}Sr/^{86}Sr$ ratios close to the values of the lower PSD (0.73736) and high $^{206}Pb/^{207}Pb$ ratios compared to both PSD and SP compartments. The $^{143}Nd/^{144}Nd$ ratios show rather small variations between 0.51192 and 0.51198 throughout the profile (Fig.3.5-c). The

ratio is slightly higher for the OH horizon (0.51195) compared to the other soil horizons (0.51192).

Table 3.2. Sr, Nd, Pb and U radiogenic isotope ratios of all analysed regolith samples(NA: not analysed).

Sample	$^{87}\text{Sr}/^{86}\text{Sr}$	$^{143}\text{Nd}/^{144}\text{Nd}$	$^{206}\text{Pb}/^{207}\text{Pb}$	$^{234}\text{U}/^{238}\text{U}$
OH	0.72181	0.511951	1.153	0.933
PPSD1	0.73023	0.511919	1.162	NA
PPSD2	0.73399	0.511922	1.204	NA
PPSD3	0.73866	0.511923	1.215	0.961
PPSD4	0.73657	0.511931	1.220	NA
PPSDce	0.73736	NA	1.226	NA
SP1	0.74141	0.511961	1.200	0.949
SP2	0.74205	0.511927	1.202	1.053
SP3	0.73912	0.511959	1.199	1.038
SP4	0.73915	0.511983	1.206	0.953
SP5	0.74160	0.511933	1.214	0.947

The ($^{234}\text{U}/^{238}\text{U}$) activity ratios scatter between 0.947 and 0.960 along the profile with the exception of the 270 and 320 cm depth horizons. At these depths, SP2 and SP3 show ($^{234}\text{U}/^{238}\text{U}$) activity ratios higher than 1 (1.05 and 1.04 respectively – Fig.3.5-d).

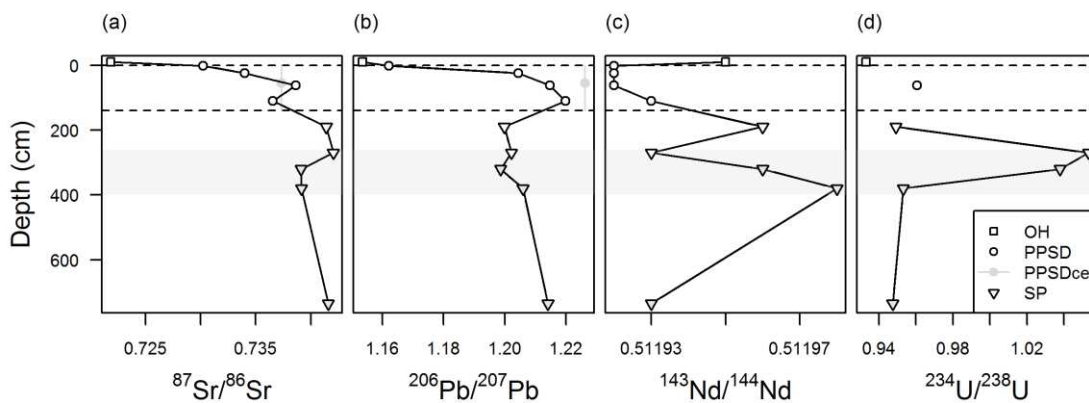


Figure 3.5. Depth-dependent variation of (a) $^{206}\text{Pb}/^{207}\text{Pb}$, (b) $^{87}\text{Sr}/^{86}\text{Sr}$, (c) $^{143}\text{Nd}/^{144}\text{Nd}$ and (d) $^{234}\text{U}/^{238}\text{U}$ of all analysed samples (shaded area: redox sensitive horizons).

3.2 Discussion

3.2.1 Major and trace element behaviour within the studied regolith system

The cluster analysis on the PSD matrix and SP samples indicates that there are three groups of elements that have different origins and contrasted behaviours during weathering and pedogenetic processes (Fig.3.2). Even though the coarse elements of the PSD are not included in this statistical assessment, and thus uncertainty increases, the results allow discerning the

chemical zonations according to the soil fraction that is responsible for most of the processes described below.

Group I includes elements such as Cd, Sn, Sb, Hg and Pb, which are only enriched in the surface Ah horizon (PPSD1) and are probably atmosphere-derived and of anthropogenic origin. The Ah horizon is located directly under the organic horizon (OH) and is as a consequence rich in organic matter, which is known to trap heavy metals and subsequently release them by leaching into the soil (Hissler and Probst, 2006; Steinmann and Stille, 1997; Stille et al., 2011, 2009). This is especially observable in the Pb isotope data (Fig.3.5-b). According to the work of Redon et al. (2013), depth patterns of Sn, Sb, Hg and Pb present a disconnection between upper soil horizons and the rest of the regolith as well as the PPSD coarse materials (PPSDce; Table 3.1), supporting the hypothesis that they do not derive from the underlying saprolite but from the atmosphere. In contrast is the slight Cd enrichment at 320 cm depth (SP3) compared to the horizons underneath, which resembles that of the elements of Group II and thus cannot be attributed to anthropogenic deposition at the top of the regolith.

Group II comprises Co, Ni, Cu, Zn and As, which show similar distribution patterns to P₂O₅, MnO and Fe₂O₃ with a strong enrichment at 320 cm depth (SP3) in the saprolithic material. At the same time, Group IIIa comprises U and Pr, Nd, Gd, Sm, Eu, whose depth patterns resemble those of MgO and K₂O with a strong enrichment at SP4. All of them also show also high concentrations in the lowermost horizon of the PPSD. These trace elements are sensitive to being mobilised during changing redox conditions in the regolith profile, e.g. groundwater table fluctuations. The fractionation and mobilisation/accumulation can be either direct by valence alteration into soluble/stable forms or due to the dissolution-precipitation of Fe and Mn-(oxy)hydroxides in which these trace elements get preferentially sorbed. Of particular interest here is the slight but meaningful positive Ce anomaly that can be observed in SP3 ($CeN/CeN^*=1.05$ compared to ratios between 0.92 and 0.98 for the other samples). During water saturation periods (winter), the anoxic conditions in the saprolite result in a reducing environment which favours the leaching of REE. In the formed solution, Ce, as the majority of the lanthanides, presents a trivalent state (3+). When the water table flows downwards (summer), water is mainly retained only at the smallest pores of the soil aggregates and in the clay fraction of the saprolithic material. Oxygen can get into the interfaces, favouring Ce³⁺ to Ce⁴⁺ oxidation. In these oxic conditions, Ce can precipitate as cerianite e.g. on the hydrated surface of manganese oxides (Braun et al., 1990; Steinmann and Stille, 1997). This means, in this case Ce might be mobilised from the upper horizons and immobilised at 320 cm depth. In agreement is the evolution of the U geochemistry within the studied profile (Figures 3.2 and 3.5, and Table 3.1). U concentrations tend to increase from 3.09 ppm at the top of the SP compartment to 5.84 ppm at SP4. Under oxidising conditions, Uranium can oxidise to the uranyl ion ($U(VI)O_2^{+2}$) and form compounds that are soluble in water. As with Ce, the uranyl

ion can get released into the solution at SP1, migrate downwards and re-deposit as it co-precipitates with Fe oxy-hydroxides at the “summer” redox interface (SP3-SP4) (Bruno et al., 1995; Duff et al., 2002). In figure 3.5, the ($^{234}\text{U}/^{238}\text{U}$) activity ratios lower than 1 above SP2 (270 cm) and below SP3 (320 cm) (<0.96) but higher than 1 in between (>1.04) indicate, respectively, a ^{234}U depletion and enrichment of the regolith. During water-rock interaction, ^{234}U and ^{238}U have different mobilities, with a preferential leaching of ^{234}U compared to ^{238}U due to the so-called alpha recoil process (more details in e.g., Chabaux et al. (2003, 2008); DePaolo et al. (2006,2012)). For a material old enough to be at secular equilibrium (i.e., $^{234}\text{U}/^{238}\text{U} = 1$), such a process leads to a preferential enrichment of ^{234}U in waters compared to its parent ^{238}U , and hence to ($^{234}\text{U}/^{238}\text{U}$) activity ratios higher than 1 in the waters and lower than 1 in the residual materials (see also Pierret et al., 2014; Prunier et al., 2015; Schaffhauser et al., 2014; and references therein). Thus, during long periods of water saturation and intense weathering of the rock, ^{234}U is leached from the minerals, giving ($^{234}\text{U}/^{238}\text{U}$) activity ratios below 1 in the saprolithic materials. This seems to be the case in the studied saprolithic material above SP2 and below SP3. In the studied regolith, the water table fluctuates between 320 cm depth during low hydrological conditions and 108 cm depth during winter saturation periods (according to field monitoring hydrological data, not shown). Thus, we hypothesise that ^{234}U is mobilised above 270 cm depth and potentially accumulated around the permanent water table level (SP3-SP4), where the redox potential allows the above-mentioned co-precipitation. Conversely, the permanently saturated layer between SP3 and SP5 (735 cm) favours the downward flow of ^{234}U , whereas below SP5 depth we are on the impermeable and slightly weathered slate bedrock. This hypothesis is supported by occurrences of gleyic properties with rusty patches observed from drill cores of the saprolithic material between 340 and 380 cm depth, which correspond to strong reduction processes and iron segregation (WRB, IUSS Working Group 2015).

In summary, the depth patterns of the Ce anomaly and ($^{234}\text{U}/^{238}\text{U}$) activity ratios together with the other redox sensitive elements, definitely point to the effect of the seasonal water table fluctuation between 108 and 380 cm depth. The regolith above SP1 is preserved from the weathering process and conserves element concentrations untouched. Whereas between SP1 and SP4, the historical exposure of the material to alternating oxic and anoxic conditions (redox conditions) favoured the dissolution-precipitation processes that control the dynamics of the redox sensitive and allied elements. Below SP4, most labile elements may be flushed away from the saprolite into deeper groundwater.

On the other hand, the behaviour of all elements from Group III in the matrix of the PPSD compartment is also related to the stability of some specific residual trace mineral phases. Zr and Hf reside in zircons, Th in monazite, Y in xenotime and Nb in Ti-bearing minerals. Similarly, PPSD4, representing the lowermost part of PPSD matrix, is enriched in LREE compared to the upper horizons (Figures 3.2 and 3.4) pointing to an important presence of

phosphate and LREE bearing trace minerals such as monazite and florencite. At last, the Eu positive anomaly of PPSD's coarse materials (PPSDce), surely relates to their greater feldspars abundance (Vázquez-Ortega et al., 2015) (Figures 3.1 and 3.4).

Finally, vegetation life cycles (nutrition, evapotranspiration) might also have an important impact in the overall chemical composition. In this regolith, beech and oak have the greatest root density between 20 to 40 cm depth (up to 16 roots cm⁻²). The roots uptake of macronutrients and other oligoelements is probably a major cause of element fractionation between the upper and lower PPSD layers. In this sense, Ca must be accumulated in the OH horizon due to biological cycling and litter decomposition (Stille et al., 2009). Phosphate concentration is high in the Ah horizon for the same reason. Then it decreases at the level of the maximum root uptake at 20 to 40 cm depth (PPSD2-3). At these depths, also Mg, K, Fe, Al and most of the REE are depleted compared to the lower PPSD4 horizon. Further studies on the vegetation are needed to better understand its geochemical impact on the regolith studied here.

3.2.2 Impact of atmosphere-derived anthropogenic depositions on the PPSD

The ⁸⁷Sr/⁸⁶Sr and ²⁰⁶Pb/²⁰⁷Pb isotope ratios decrease with decreasing depth within the organic (OH) and organo-mineral (PPSD) compartments (Figures 3.5-a and b and Table 3.2), whereas the corresponding ¹⁴³Nd/¹⁴⁴Nd ratios are only very weakly scattered, ranging between 0.51192 and 0.51195 (Fig.3.5-c and Table 3.2). The comparatively lower Pb and Sr isotopic compositions of the organic compartment (OH sample) can be related to anthropogenic impacts (Stille et al., 2011). Indeed, the current local atmospheric baseline isotopic compositions determined on lichens show significantly lower ²⁰⁶Pb/²⁰⁷Pb (1.162) and ⁸⁷Sr/⁸⁶Sr (0.7152) but higher ¹⁴³Nd/¹⁴⁴Nd (0.51205) ratios (Hissler et al., 2008). In a ⁸⁷Sr/⁸⁶Sr vs Rb/Sr diagram the PPSD data show a mixing trend with the OH horizon and the Ah organo-mineral soil horizon (PPSD1) with the lowest isotopic composition values and Rb/Sr ratios similar to the lichen (0.87 and 1.54 respectively) (Fig.3.6a). Similar relationships are observable in the ²⁰⁶Pb/²⁰⁷Pb vs U/Pb diagram (Fig.3.6b). Again, OH and PPSD1 samples have Pb isotopic composition and U/Pb ratios similar to lichen (U/Pb = 0.01 for both samples). Therefore, the Rb-Sr and U-Pb isotope systems of the uppermost regolith samples are strongly influenced by recent atmosphere-derived inputs.

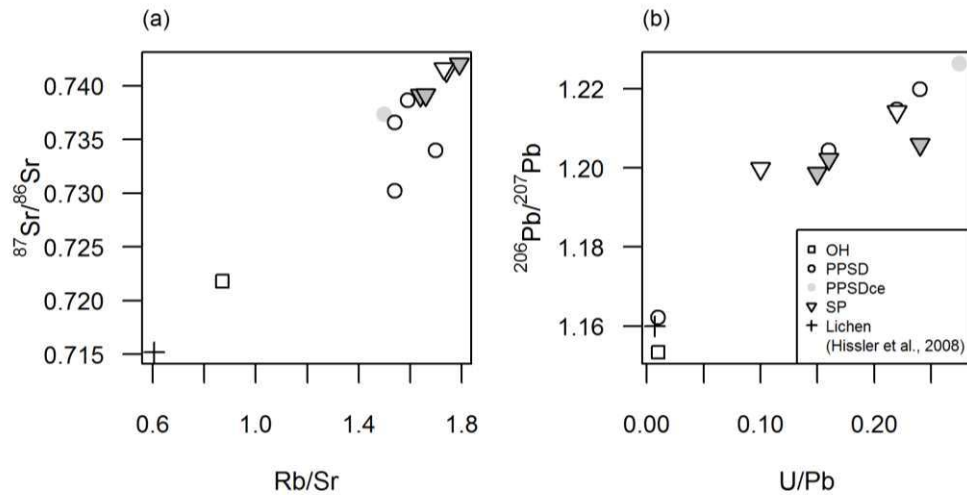


Figure 3.6. Relationships between (a) $^{87}\text{Sr}/^{86}\text{Sr}$ vs. Rb/Sr ratio and (b) $^{206}\text{Pb}/^{207}\text{Pb}$ vs. U/Pb ratio of all analysed samples and a lichen sample from Hissler et al. (2008) representing the anthropogenic end member.

This is not the case for the Sm-Nd isotope system, which is not to be affected by atmospheric deposition (not shown). If mixing occurred between anthropogenic, atmosphere-derived and soil particles then the regolith isotope data should describe a mixing hyperbola in the $^{87}\text{Sr}/^{86}\text{Sr}$ vs. $^{143}\text{Nd}/^{144}\text{Nd}$ diagram (Faure, 1977). This is indeed the case (Fig.3.7). The shape of the curve is controlled by the end-members Sr/Nd ratios. The atmospheric end member is the lichen (Sr : 1.17ppm, $^{87}\text{Sr}/^{86}\text{Sr}$: 0.7152 ; Nd : 0.17ppm, $^{143}\text{Nd}/^{144}\text{Nd}$: 0.51205) (Hissler et al., 2008) and the geogenic end member corresponding to the lithic material representing fresh slate bedrock (SP5) (Sr : 98.2ppm, $^{87}\text{Sr}/^{86}\text{Sr}$: 0.7416 ; Nd : 37.9ppm, $^{143}\text{Nd}/^{144}\text{Nd}$: 0.51193). The resulting Sr/Nd ratios are 6.9 for the lichen and 2.6 for the slate. One calculates that the uppermost OH and Ah horizons (PPSD1) contain up to 90% and 50% of recent atmosphere-derived Sr and 95% and 50% of recent atmosphere-derived Nd, respectively. Such enrichments are rather surprising, suggesting that these elements have been transported over distances greater than 20 km. The closest active steel industrial parks are situated around 25 km southeast (Bissen, Luxembourg) and 120 km north-west (Liège, Belgium) of the studied site, and a historic mine of mainly Pb and Zn was located around 20 km north of the study site. Alternatively, these enrichments might be attributed to the heavy fighting nearby during the “Battle of the Bulge” in the vicinity of Bastogne during the Second World War (Cole, 1965).

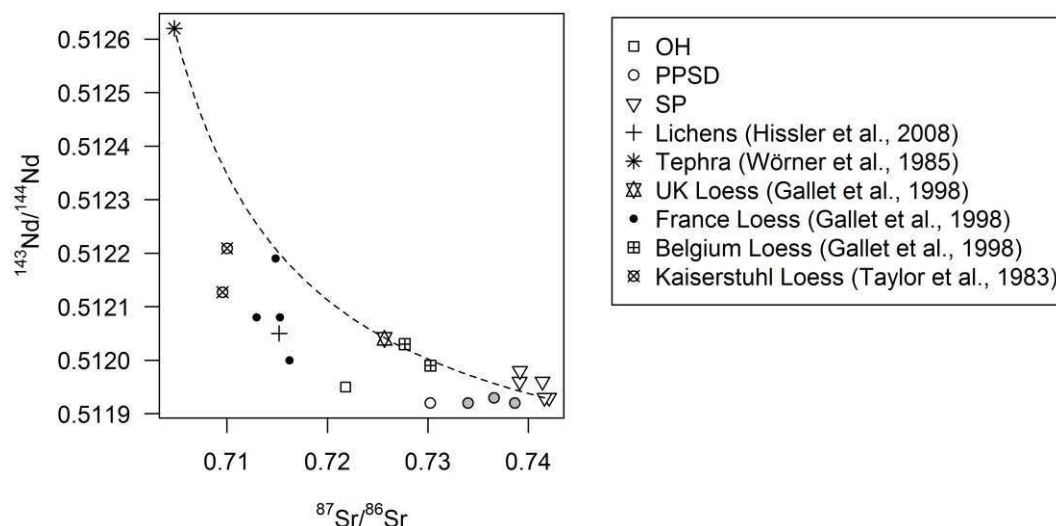


Figure 3.7. $^{87}\text{Sr}/^{86}\text{Sr}$ vs. $^{143}\text{Nd}/^{144}\text{Nd}$ diagram describing mixing hyperbolas between the unweathered slate sample of this study (SP5) as the continental crust end member (Sr: 98.2 ppm, $^{87}\text{Sr}/^{86}\text{Sr}$: 0.7416; Nd: 37.9 ppm, $^{143}\text{Nd}/^{144}\text{Nd}$: 0.51193) and a mantle representing end member according to the study of Wörner et al. (1985) (Sr: 500 ppm; $^{87}\text{Sr}/^{86}\text{Sr}$: 0.70477; Nd: 49 ppm; $^{143}\text{Nd}/^{144}\text{Nd}$: 0.51262); and between SP5 and the lichen representing the atmospheric derived anthropogenic end member (Sr: 1.17 ppm, $^{87}\text{Sr}/^{86}\text{Sr}$: 0.7152; Nd: 0.17 ppm, $^{143}\text{Nd}/^{144}\text{Nd}$: 0.51205, from Hissler et al., 2008). Included are the loess signatures from UK, France and Belgium from Gallet et al. (1998) and Kaiserstuhl (Germany) from Taylor et al. (1983) (grey circles: Nb enriched PPSD samples).

3.2.3 Impact of volcanic events on the PPSD

In central Europe, the upper layer of PPSD (UL) often presents a typical volcanic mineralogical composition related to the Laacher See Eruption in the late Pleistocene (12900 years BP) (Kleber and Terhorst, 2013; Pissart, 1995; Semmel and Terhorst, 2010; Wörner and Schmincke, 1984). Wörner and Schmincke (1984) and Wörner et al. (1985) also highlighted the very specific trace element and isotopical composition of the Laacher See tephra, which permits its identification and differentiation from other material contributions. These mineralogical and isotopical fingerprints allow us to use the Laacher See deposits as a stratigraphic marker (Schmincke et al., 1999). Nevertheless, relatively older volcanic events took place in the same region, such as the Rocourt (74-90.3 ka) and Eltville (16-30 ka) eruptions, whose tephra spread in the south east of Belgium, central Germany and north of Luxembourg (Poucllet et al., 2008; Poucllet and Juvigne, 2009). Poucllet et al. (2008) pointed out the potential of the Rocourt tephra as chronostratigraphic marker for the Upper Pleistocene loess deposits in these areas thanks to its glass fragment shape, chemical and mineral composition, which differs from the Laacher See tephra.

One of the principal questions raised in this study concerns the stratigraphic and pedogenetic evolution of the periglacial coverbeds (PPSD compartment) and, more specifically, the origin of their constituting mineral phases. Are these phases only derived from the underlying slate or do

some of them have other origins; e.g. originate from volcanic dust and ashes from the late-Pleistocene Laacher See eruption, and reached also the south-western edge of the Rhenish Massif. Indeed during solifluction processes the Laacher See tephra, which was already deposited, was admixed with other materials to become part of the upper covered (Kleber, 1997; Schmincke et al., 1999; Semmel and Terhorst, 2010; Stückrad et al., 2010; Terhorst, 2007). Previous studies have shown that Laacher See particles have been incorporated to the upper PPSD layer in central Europe (Kleber and Terhorst, 2013; Pissart, 1995; Semmel and Terhorst, 2010). At the same time, several tephra layers have been recognized in the Upper Pleistocene Loess deposits in Belgium, as the ones of the above mentioned Laacher See, Eltville and Rocourt (Pouclet and Juvigne, 2009). Among those tephra sequences, Wörner and Wright (1984) noticed that the Laacher See tephra has a phonolite-like mineral composition dominated by alkali feldspar, especially sanidine phenocrysts, followed by plagioclase (mainly albite), hauyne, amphibole, clinopyroxene, sphene, Ti-magnetite, apatite, phlogopite and traces of zircon phenocrysts. The abundance of the different observed mineral phases of the studied regolith vary along the profile but manifest specific mineral enrichments in the matrix of the basal layer of PPSD (PPSD3 and PPSD4), which might be related to a Pleistocene eruption (Fig.3.1).

In that regard, of great importance is the finding of chamosite as a main mineral phase (up to 20 vol.%) in the matrix of the basal layer of the PPSD compartment. It is significantly less present in the saprolitic material (SP, 10-13 vol.%). This mineral phase is the Fe-rich end-member of the chlorite group. Its presence explains the rather high Fe_2O_3 contents (7-11 wt.%) in the basal layer of PPSD. Chamosite is typically a replacement mineral phase and alteration product of ferromagnesian minerals such as pyroxenes and amphiboles (Lauf, 2014). However, also other mineral phases confirm the presence of tephra in the basal layer of PPSD, such as kaolinite, which results from feldspar alteration and reaches 20 vol % which represents a strong enrichment compared to the underlying saprolite (SP, 3-5 vol %). Primary feldspar minerals such as albite and orthoclase are also observable in smaller quantities in the PPSD. Orthoclase, respectively sanidine (a not distinguishable polymorph of orthoclase), occurs only in PPSD (up to 8 vol.% in the matrix and 14 vol.% in the coarse materials) and is not at all observable in SP.

In a similar way, one might suggest that the titanium enrichments observed for the same PPSD samples (Fig.3.2) result from sphene and Ti-magnetite. Indeed, the important presence of Ti-bearing minerals such as ilmenite, rutile and Ti-magnetite observed under the scanning electron microscope (SEM) confirm the presence of tephra-derived mineral constituents in the PPSD.

The deposited tephra dust particles caused elevated Nb concentrations in the samples (Haase et al., 2007; Schmincke et al., 1999) because the erupted tephra (Lower Laacher See Tephra deposits, LLST) is enriched in Nb with concentrations of more than 200 ppm (Wörner and Schmincke, 1984). The Nb concentrations of the studied covered matrix are well correlated

with TiO_2 (Table 3.1) indicating, as suggested (Bonjour and Dabard, 1991), that titaniferous mineral phases are the principal Nb carrying phases. Nb concentrations vary according to depth, being lowest close to the surface (10.28 ppm) (Fig.3.2 and Table 3.1). Between PPSD2 and PPSD4, the Nb concentrations range between 19.4 and 19.9 ppm and are higher than those of the underlying bedrock showing concentrations between 14 and 16 ppm. The Nb concentrations of coverbeds from two other sites of the studied plateau range, at same depths as PPSD2 to PPSD4, between 18.5 and 22.5 ppm (not shown). In the coarser materials (PPSDce) of these horizons and in the underlying bedrock, Nb concentrations decrease again to values below 11 and 16.6 ppm respectively. According to Taylor and McLennan (1985) the UCC Nb concentration is higher (25 ppm) and, therefore, the PPSD samples show Nb depletions similar to European loess studied by (Gallet et al., 1998). These authors provided plausible arguments that the depletions are artefacts resulting from an over-estimation of the UCC Nb concentration. Similarly (Condie, 1993) suggest that the Nb concentrations of clastic sediments are seldom higher than 15 ppm. This value is in agreement with the Nb concentrations found in the bedrock below the coverbed. Thus, the fact that the PPSD matrix shows slightly higher Nb concentrations than the PPSD coarse materials and the bedrock is suggested to be the result of deposition of Nb-enriched mineral phases from the late-Pleistocene Laacher See eruption.

The Nb contribution from this eruption to the loess component of the PPSD sediments can be estimated by using a two component mixing equation, a Nb concentration of the Laacher See tephra (100 ppm) (Wörner and Schmincke, 1984) for the volcanic mixing end-member and a Nb concentration of the underlying bedrock (15 ppm) for the PPSD end-member. This rough estimation indicates that the volcanic Nb contribution is less than 6% in the PPSD matrix. Mixing calculations can also be performed by using Nd concentrations and $^{143}\text{Nd}/^{144}\text{Nd}$ isotope ratios (see Faure, 1977). However, the Sr-Nd isotopic and concentration similarities between slate bedrock and PPSD samples and, thus, the resulting mixing relationships (Fig.3.7) suggest that the PPSD below 45 cm depth do not contain visible amounts of tephra-derived Sr and Nd. Nevertheless, Nb enriched PPSD samples plot close to the crust-mantle mixing hyperbola (Fig.3.7), pointing to a certain impact of the volcanic materials in their signature. Thus, in the case of our study only Nb enrichments and mineralogical composition allow the identification of tephra contributions in the lowermost PPSD horizons. Given the fractionation of some minerals and trace elements within the PPSD, we propose that the discontinuities observed from PPSD2 and PPSD3 respond both to the impact of volcanic depositions and pedogenetic processes such as diagenesis and neoformation of minerals.

3.2.4 Impact of the saprolite (SP) on PPSD

With the exception of the two uppermost soil horizons (OH and Ah), no impact of anthropogenic Sr and Nd is observable for the rest of the regolith compartments. Similarly we

have seen that neither Sr nor Nd isotope ratios are impacted by tephra depositions during Pleistocene volcanic eruption events. PPSD and SP material are isotopically very similar pointing to similar origins. This is confirmed by the major element concentrations of the saprolithic material (SP) and the coverbeds (PPSD) below the OH horizon, which scatter in nearly the same range (Fig.3.2) and show similar depletions and enrichments compared to the reference slate layer of SP (Fig.3.3). Only very few trace elements such as Nb and some redox-sensitive elements manifest, as discussed above, differences between PPSD and underlying saprolithic material. Consequently, if the PPSD profile contains, as suggested for other neighboured coverbeds (Stückrad et al., 2010), pre-industrial atmosphere-derived particles, then they have not travelled long distances but originate from the slate of the region. In Figure 3.8, the ϵNd (T) values of the Devonian slates of our study site (“initial” epsilon Nd values, calculated back to the stratigraphic age) are plotted versus their stratigraphic age and compared with other European phanerozoic shales. This type of diagram was first used by Michard et al. (1985) in order to show that during major orogenic events sediments have been impacted by mantle-derived material such as volcanogenic detrital material. One observes that the slates in this study show initial ϵNd (T) values very similar to those of other Devonian shales collected in Brittany and Wales. These sediments have been deposited in the same oceanic environment in a period between the Hercynian and Caledonian orogenesis and are not visibly impacted by volcanogenic detritus during their deposition. Volcanogenic deposits containing significant quantities of mantle-derived material are characterized by high $^{143}\text{Nd}/^{144}\text{Nd}$ isotope ratios and low $^{87}\text{Sr}/^{86}\text{Sr}$ isotope ratios, whereas crustal materials devoid of mantle-derived material have low $^{143}\text{Nd}/^{144}\text{Nd}$ isotope ratios and high $^{87}\text{Sr}/^{86}\text{Sr}$ isotope ratios (e.g. SP samples). Continental crust plots in function of the proportion of integrated mantle-derived Sr and Nd on a mixing hyperbola defined by the end-member compositions of continental crust and mantle (see hypothetical mixing hyperbola in Figure 3.7). Thus, when comparing the regolith data of this study with European loess and tephra data from the literature, one observes that each data set has a very particular isotopic signature. Each of these coordinates plot inside or on a mixing curve ranging from mantle or anthropogenic (low $^{87}\text{Sr}/^{86}\text{Sr}$ and $^{143}\text{Nd}/^{144}\text{Nd}$ ratios) materials to crustal materials (Fig.3.7). The tephra signature from Wörner et al. (1985) being the most mantle rich material. This indicates that the different loess deposits originate from very distinct rock units containing different proportions of mantle and crust material. In this context, our PPSD show Sr and Nd isotope signatures rather close to the studied slate regolith compartment than to other loesses (Fig.3.7), which we hypothesise reflects the genetic link of the materials of both compartments.

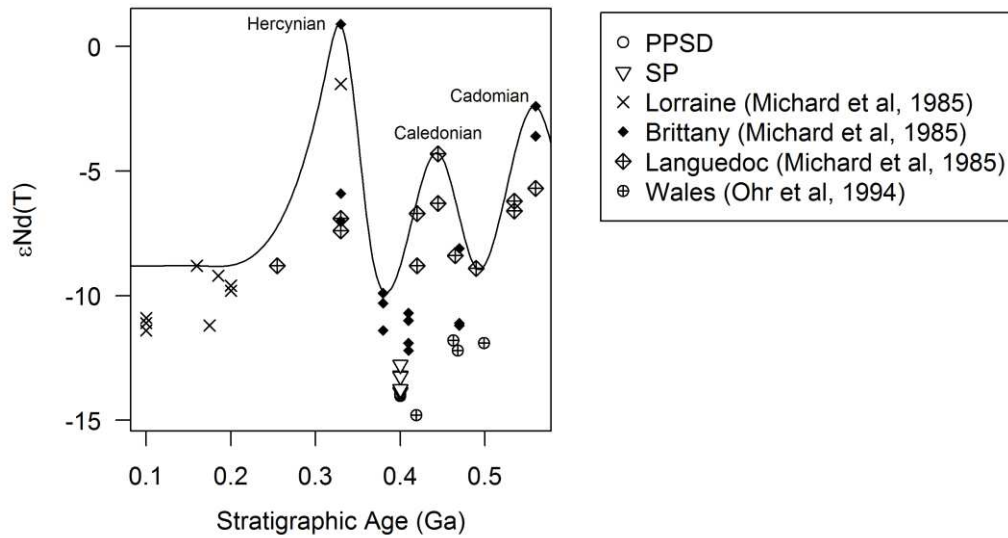


Figure 3.8. $\epsilon\text{Nd(T)}$ values vs. stratigraphic ages of the PSD and SP samples of this study and of rock materials which originated from similar palaeogeographic environments reported by Michard et al. (1985) and Ohr et al. (1994). Modified after Michard et al. (1985).

3.3 Conclusion

The study we performed on a typical polygenetic regolith profile from a remnant plateau from the western part of the Rhenish Massif allowed three distinct compartments to be distinguished. Their geochemical and mineralogical characteristics present contrasting evolutions, which can be related to different atmospheric deposition events and to the seasonal water saturation dynamics.

- 1) an uppermost PSD soil compartment (0-45 cm), enriched in organic matter and strongly impacted by anthropogenic atmospheric-derived depositions, as revealed by Pb, As, Hg, and Sb enrichments and low $^{87}\text{Sr}/^{86}\text{Sr}$, $^{143}\text{Nd}/^{144}\text{Nd}$ and $^{206}\text{Pb}/^{207}\text{Pb}$ isotopic compositions (0.714-0.722, ~0.51204 and 1.153-1.185 respectively). The estimations based on $^{87}\text{Sr}/^{86}\text{Sr}$ and $^{143}\text{Nd}/^{144}\text{Nd}$ ratios indicate that the recent atmospheric deposition contributes to about 50% of the Sr and Nd content in the organo-mineral part of the regolith (0-45 cm depth).
- 2) a lower PSD (45-140 cm depth) compartment characterized by the impact of old volcanic events, as evidenced by a refractory mineralogy (Ti-magnetite, chamosite, orthoclase) and Nb and Ti contributions/enrichments, and thus showing little potential as water interaction hot spot. However, REE-bearing minerals found in the lowermost PSD horizons like monazite and florencite were recognised as a pool of REE that appeared to be preserved from weathering.

- 3) the slate weathering profile (SP), strongly affected by seasonal water saturation dynamics, as indicated by REE patterns showing small positive Ce anomalies and $^{234}\text{U}/^{238}\text{U}$ activity ratios > 1 indicating the presence of a labile reservoir sensitive to redox processes.

Finally, we identified a close genetic link of both upper and lower subsolum materials. The fresh slate and the central European loess from the literature defines a mixing curve between crustal and mantle materials, in which our PPSD layers show signatures close to the studied slate compartment and continental crust rather than to other European loess with lower Sr and higher Nd isotopic compositions.

The combination of mineralogical, major and trace element pattern and Sr-Nd-Pb-U isotope ratio analyses appears to be an extremely powerful approach for understanding the evolution of the polygenetic regolith systems. This procedure offers the possibility of i) characterising and tracking the origin of the components that constitute the different compartments of the regolith; ii) identifying the genetic links between the different regolith compartments; and iii) doing further research on its great potential for the identification of important hydrological tracers, which are able to shed light on water pathways and water-rock interactions within the complex regolith system of the critical zone.

Chapter 4. Hydrological and geochemical characterization of the waters in the Weierbach catchment

Introduction

The hydrochemical profile of a catchment might be understood as the ensemble of geochemical compositions found in the different water reservoirs and stream outlet. In order to understand runoff generation processes, we must characterize not only the inputs and the stream, but also the potentially contributing water reservoirs, as all of these show an organized evolution in time according to varying hydrological connectivity (Fröhlich et al., 2008). At the small catchment scale, the geochemical composition of each “water pool” along space and time will be determined by the physico-chemical and mineralogical characteristics of the host environment itself, the mixing with waters from different pools and/or by the impact of other contributions such as atmospheric depositions. Therefore, reservoirs are here conceived as dynamic bodies of water *and* or *in* their physical environment.

In order to define the hydrochemical profile of the Weierbach catchment we propose to combine the use of stable isotopes of O and H and major and trace elements together with other physico-chemical parameters like pH, EC and alkalinity. Trace elements are particularly useful here because they are more mineral-specific, which is especially advantageous at the small catchment scale (Petelet-Giraud et al., 2016). Therefore, the full geochemical characterization of the different water pools allows linking them to their host environment, as previously described in regolith compartments, thereby enabling the understanding of the processes responsible for solutes release and transport. As a consequence, the combined use of these parameters allows a more precise differentiation of water pools and, therefore, water circulation dynamics. Indeed, their use in end member mixing analysis has been shown to enlarge the spectrum of potential

contribution to the stream, and thus, improve our understanding of catchments functioning (Barthold et al., 2011).

4.1 Results

Figure 4.1 shows the amount of data available (excluding those under the detection limit) for the different chemical parameters measured on the Weierbach waters from the biweekly sampling and the samplings carried out in the framework of this project. We decided to use all parameters with more than 70% values above the detection limit, which results in 39 chemical parameters for which we have 1173 complete observations (Figure 4.2).

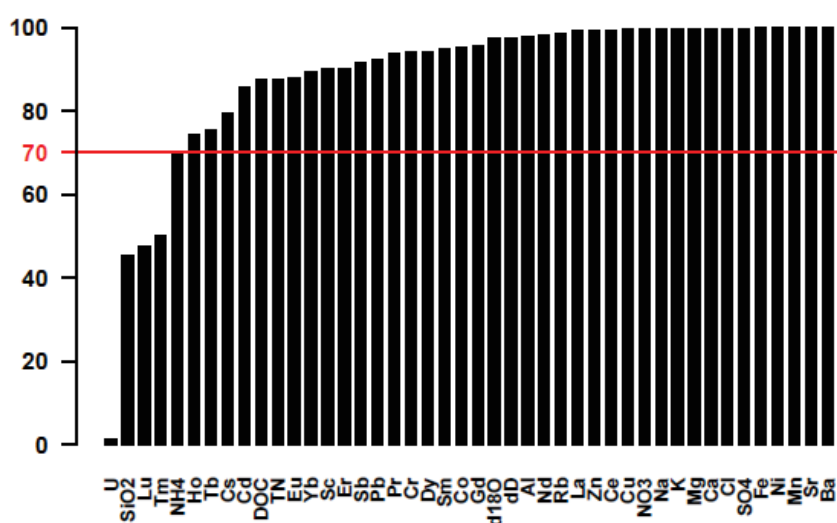


Figure 4.1. Bar plot showing the percentage of observations from the long term water dataset available for each chemical element and over the detection limit. The red bar indicates the boundary set for the parameters selection

The detection limit problem

The cleaned dataset contains a number of variables for which a percentage of the samples gave values under the detection limit. Since the data have been delivered through different series of laboratory measurements realized from 2009 to 2016, the detection limit value changed along the multiple ICPMS sessions, as it is expected with the change of instrument model and even users. In order to avoid neglecting these results in data processing (a value $< DL$ is a result), and to be able to carry out multivariate statistical studies, we decided to set, for each variable, the values $< DL$ to the half of the DL (we used the mode of the different DL, which generally happened to be the minima). At the same time, when studying central tendency and spread for the different variables, we used MEDIAN instead of MEAN, as the data are generally skewed and, thus, the former delivers a more reliable estimate (Reimann et al., 2008).

39 selected parameters / 1173 complete samples

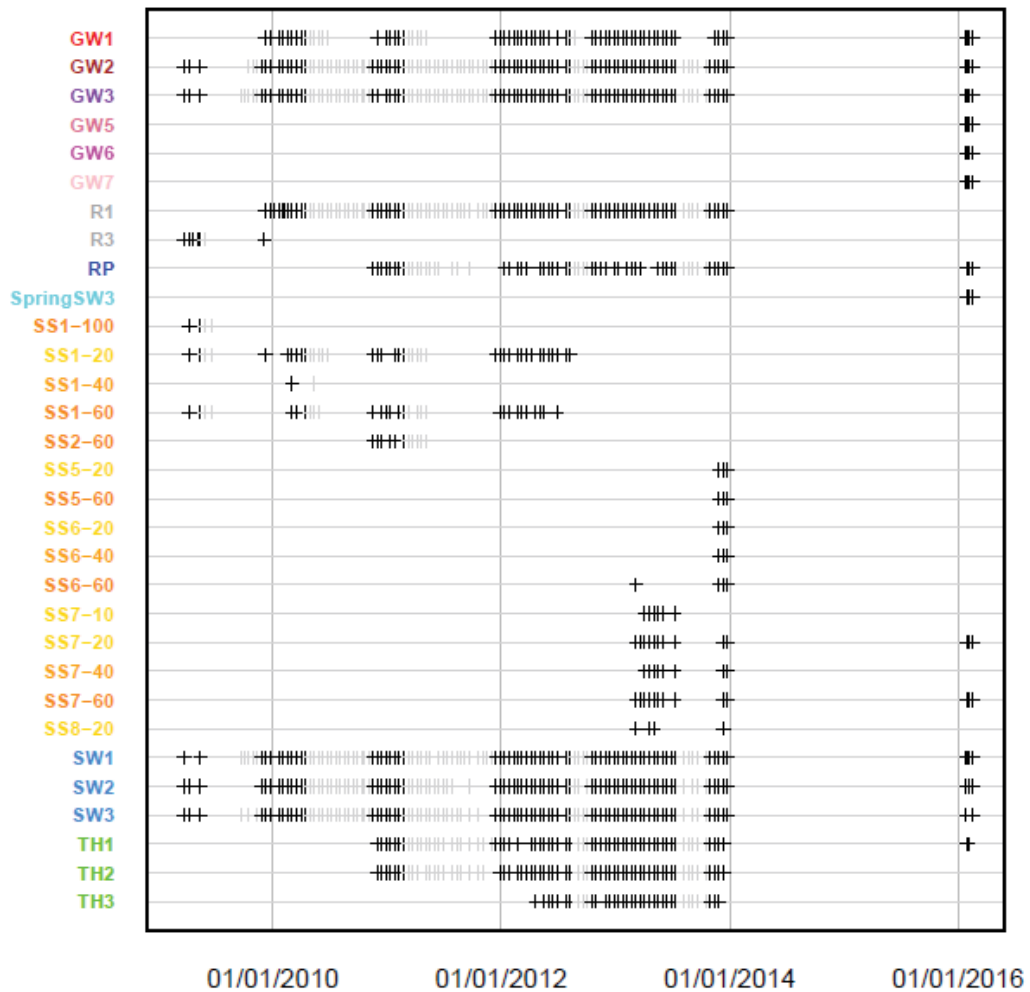


Figure 4.2. Distribution of the selected dataset through the bi-weekly samplings. The selection of 39 parameters accounted each more than 70 values and yielded 1173 complete observations including rain (R), throughfall (TH1-2-3), SS at 10, 20, 40 and 60 cm depth (SS10-20-40-60), groundwater collected from wells GW1, GW2, GW3, GW5, GW6 and GW7, riparian waters (RP), spring waters (SP), and stream water (SW) collected at the outlet (SW1) and tributaries SW2 and SW3 together.

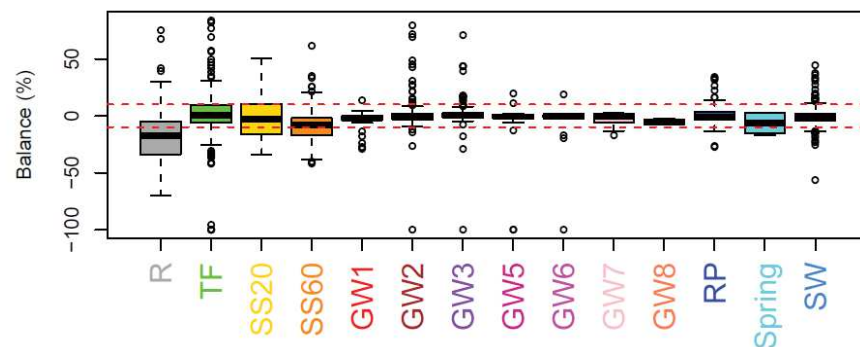


Figure 4.3. Boxplots of ionic balance percentage for the Weierbach waters. The red dashed lines indicate the $\pm 10\%$ limits. The black line in each box corresponds to the median of the data, the upper and lower limits of the boxes are the interquartile range (IQR), the whiskers are the first and third quantiles plus or minus 1.5 times the IQR, and points are outliers beyond the range of the whiskers.

The ionic balance problem

Figure 4.3 shows the ionic balance percentage for the waters collected in the Weierbach catchment. Generally, ground- and stream- waters fall inside the $\pm 10\%$ boundary, whereas the rain and soil solutions show, as expected, a larger proportion of observations being outside this threshold. It must be noted that the 10% threshold has been defined after streamwater data, generally more equilibrated than rain-, soil- and ground- waters. Thus, considering the additional “inconvenience” of the low alkalinity for the Weierbach catchment waters, which implies a greater difficulty to reach ionic balance, we have included in our study all ion composition data for all the water sample types.

4.1.1 Long term (2009-2016) characterization of the waters in the Weierbach catchment

Physico-chemical parameters: electrical conductivity, pH and alkalinity

In Figure 4.4 water electrical conductivity (EC), pH and alkalinity for the different waters of the Weierbach catchment are shown (see also Appendix 1). The EC medians range from 35.9 to 52.5 $\mu\text{S}/\text{cm}$ in all waters except GW3, 5 and 6 where the values are significantly higher, ranging between 111.0 and 185.5 $\mu\text{S}/\text{cm}$ (Fig.4.4-a). Compared to TF and R (median pH=5.8-6.2), SS20 and SS60 are on average more acid (pH=4.7), whereas GW1 is similar with a pH median of 5.8. All other GW, RP, SP and SW are relatively close to neutrality, with pH medians ranging from 6 to 6.8 (Fig.4.4-b). At the pH conditions of these waters (pH = 4-7), HCO_3^- is the dominant alkaline species. Bicarbonate concentrations are generally low in the waters of the Weierbach catchment with medians ranging between 0 and 1.5 meq/L. Significantly higher and more variable alkalinity values are found in GW2, GW3, GW5, and GW6. GW5 is the most alkaline water with 2.9 meq/L of HCO_3^- (Fig.4.4-c). We observed that the EC, pH and alkalinity of long time sampled GW1, GW2, GW3, RP and SW are generally higher during the dry periods and lower during wet periods (Appendix 4). More recent samples like GW5 and GW6 seem to show the same dynamic, but we lack data on the long term to corroborate this suggestion.

The geochemical and stable isotopic compositions ($\delta^{18}\text{O}$ and $\delta^2\text{H}$) of waters

Long term stable isotope and concentration data (median, max and min) of dissolved major and trace elements for the Weierbach waters as well as their sample size are reported in Appendices 1 to 3. In order to identify the chemical elements that characterize the best the hydrological system we performed a Hierarchical Cluster Analysis (HCA) similar to that performed on the major and trace element concentrations in the regolith (see section 3.4 and references therein).

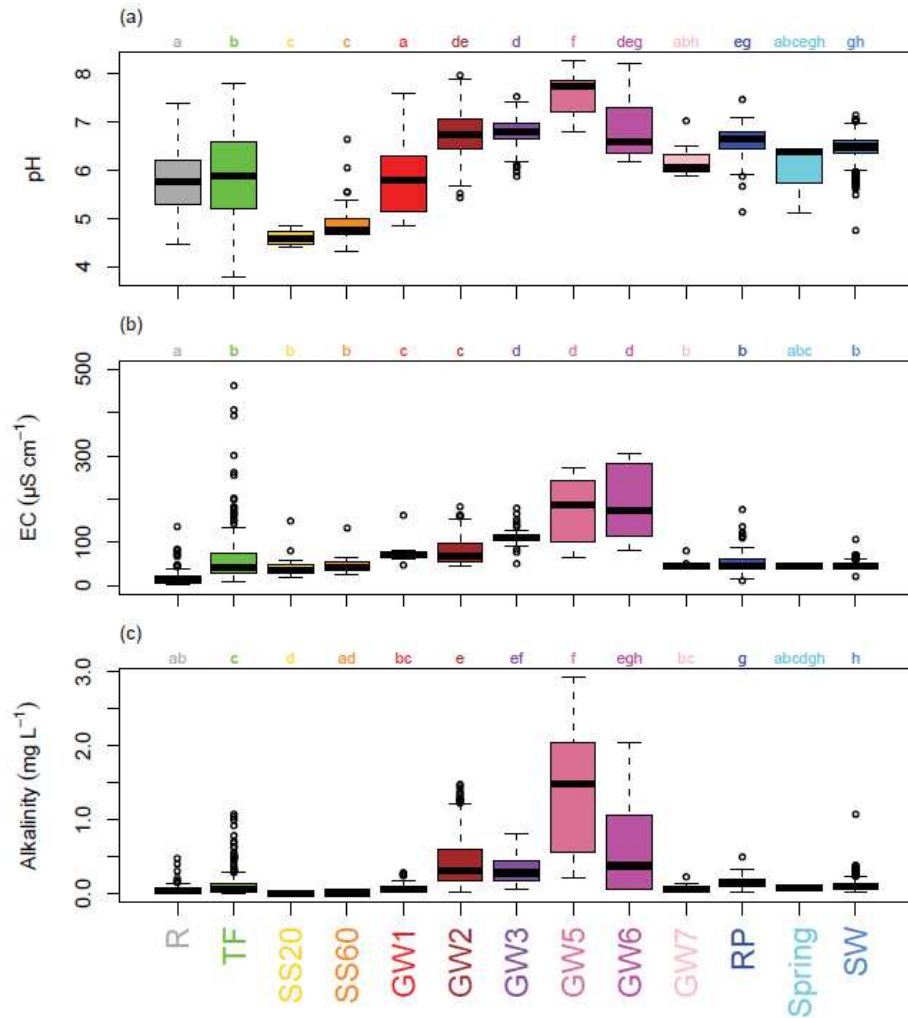


Figure 4.4. Boxplots of water pH (a), water electrical conductivity (b) and alkalinity (mg/L HCO_3^-) for the Weierbach waters. The black line in each box corresponds to the median of the data, the upper and lower limits of the boxes are the interquartile range (IQR), the whiskers are the first and third quantiles plus or minus 1.5 times the IQR, and points are outliers beyond the range of the whiskers. Letters above groups indicate statistically significant differences according to Kruskal-Wallis tests ($p\text{-value} < 2.2\text{e-}16$).

For the hydrochemical study, the clustering of both the chemical variables and the different water samples allowed to determine groups of waters with similar chemical compositions. While the clustering of the chemical variables delivers information on the relationships between major and trace elements and stable isotopes $\delta^{18}\text{O}$ and $\delta^2\text{H}$, the clustering of the different water samples allows detecting geochemical similarities between R, TF, SS, GW, RP, SP, SW.

As done for the regolith, we chose again the Ward's method (Ward, 1963) for the linkage rule. Here, we selected the Euclidian distance for the linkage distance because this is suitable for clustering both samples and variables (Reimann et al., 2008). Also, as the distributions of most chemical parameters are strongly positively skewed, all the data were log-transformed (Reimann et al., 2008). Finally, prior to the analysis, we applied a z-transformation of each parameter to ensure that each major and trace element is weighted equally (Reimann et al., 2008). As a result, two dendrograms illustrate the (dis)similarity of the parameters (top dendrogram) and the

samples (left dendrogram). The definition of the groups and subgroups of parameters and samples was done by retaining the phenon line heights of 8 and 6 respectively, which we found to visually summarise the best the results obtained in the dendrograms and the associated ordered log z-transformed concentrations matrix. An additional grey-black colour code was added to the left dendrogram to allow comparing the clustering to the proportion of observations from dry (grey) and wetness (black) conditions, according to average values respectively below or above a threshold of VWC > 28 %, GW level from surface < 2.1 at GW1, and Q > 1 mm/d.

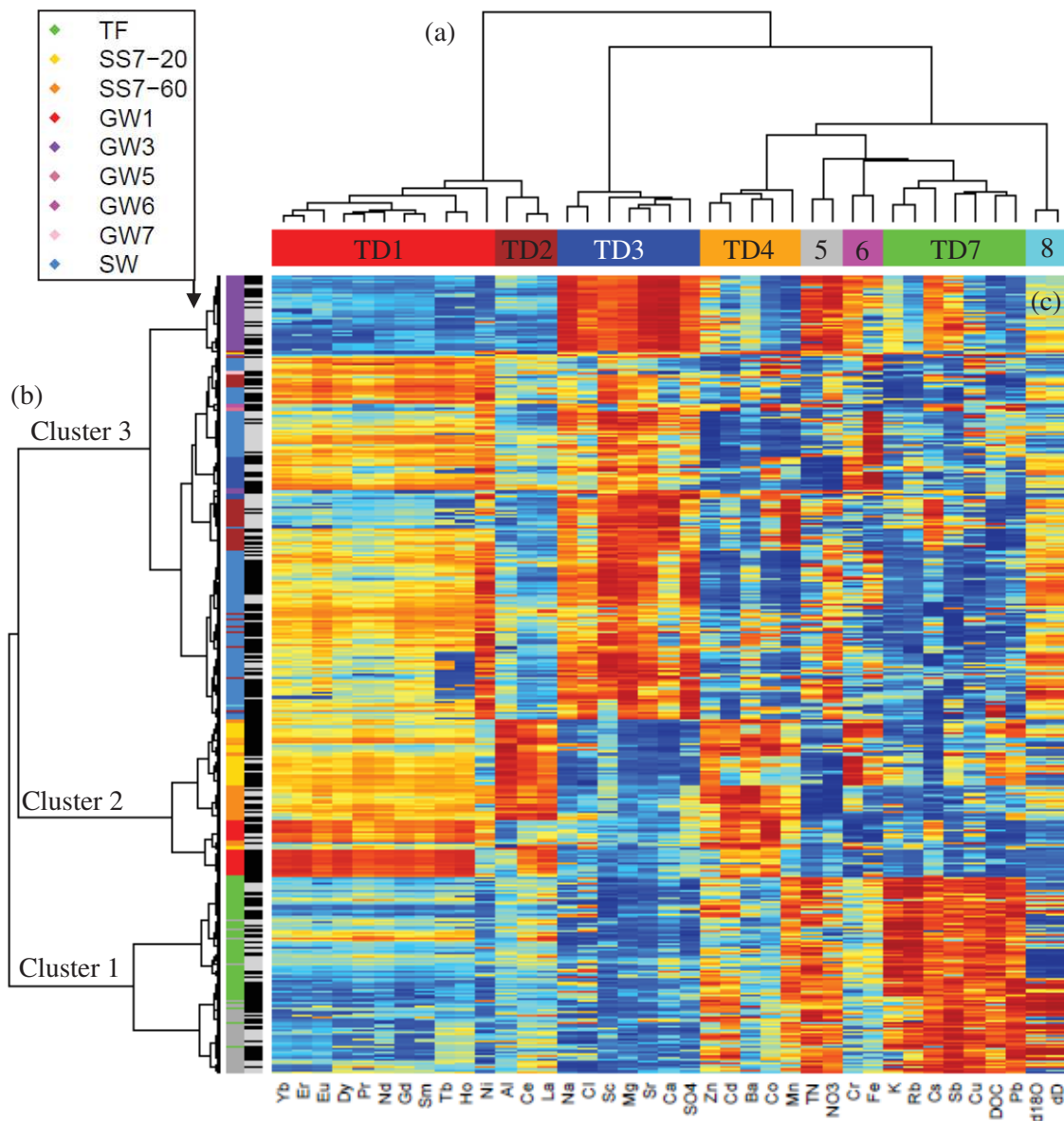


Figure 4.5. Hierarchical cluster analysis performed on water chemical variables (a, top dendrogram, colours correspond to geochemical groups) and catchment waters (b, left dendrogram, colours correspond to samples). The dendrograms (a,b) are defined using Euclidian distance as distance measure and Ward's method for the linkage rule; (c) is the coloured log z-transformed concentrations matrix (blue to red colours indicate weak to strong values).

The results of the HCA on the complete waters dataset are shown in Fig.4.5. Fig.4.6 shows the correlation matrix of the computed variables classified according to the HCA ordination. The cluster analysis indicated that there are 8 groups of geochemical variables according to the top dendrogram (TD1-8) that chemically define the following groups and subgroups of waters (left dendrogram):

- Cluster 1: TF and R are grouped together mainly characterized by common enrichments in K, Rb, Cs, Sb, Cu, DOC and Pb (TD7) as well as N components (TD5), Zn, Cd and Mn (TD4) and stable isotopes (TD8).
- Cluster 2: constituted by soil solutions (SS20-60) and GW1, which are dominated by REE and Al (TD1-2), Zn, Cd, Ba, Co and Mn (TD4) as well as Cr, Fe (TD6), DOC and Pb (TD7).
- Cluster 3: encompassing GW2, GW3, GW5, GW6, GW7, RP, SP and SW is defined by the common denominators Na^+ , Cl^- , Mg^{2+} , Ca^{2+} and SO_4^{2-} and the trace elements Sc and Sr (TD3). Cluster 3 may be classified in 3 subgroups:
 - Cluster 3.1: SW samples mostly collected in wetness conditions, which are also enriched in the TD1 REE and have a heavier $\delta^{18}\text{O}$ and $\delta^2\text{H}$ isotopic composition (TD8).
 - Cluster 3.2: SW samples mostly collected in dry conditions together with RP, GW2, GW5, GW6 and GW7, generally more influenced by the TD1 composition and less by the TD8.
 - Cluster 3.3: GW3 alone is completely depleted in TD1 and strongly enriched in TD3, TD5 and TD6 elements as well as influenced by Cs and Sb from TD7 and the stable isotopes from TD8.

In order to summarise and reduce all these informations to a few components, we have performed Principal Component Analysis (PCA) on the 39 variables of our *cleaned* waters dataset. PCA reduces the multi-dimensionality of the dataset to a new set of axes (or principal components, PC's) by calculating linear combinations of the original variables. The new axes or components are orthogonal (the covariance between each PC is 0) and successively account for the maximum variability in the multivariate space. In this space, all data points are plotted orthogonally against the PC's, resulting in new data points called *scores*. At the same time, the direction of each PC bears its relation to the original variables, which are expressed as positive or negative *loadings* that represent the importance of these variables for the *scores*. In fact, a PCA is the representation of the “eigenvectors” (or *loadings*) and “eigenvalues” (or variance of the *scores*) of the correlation matrix (Fig.4.6) (Reimann et al., 2008).

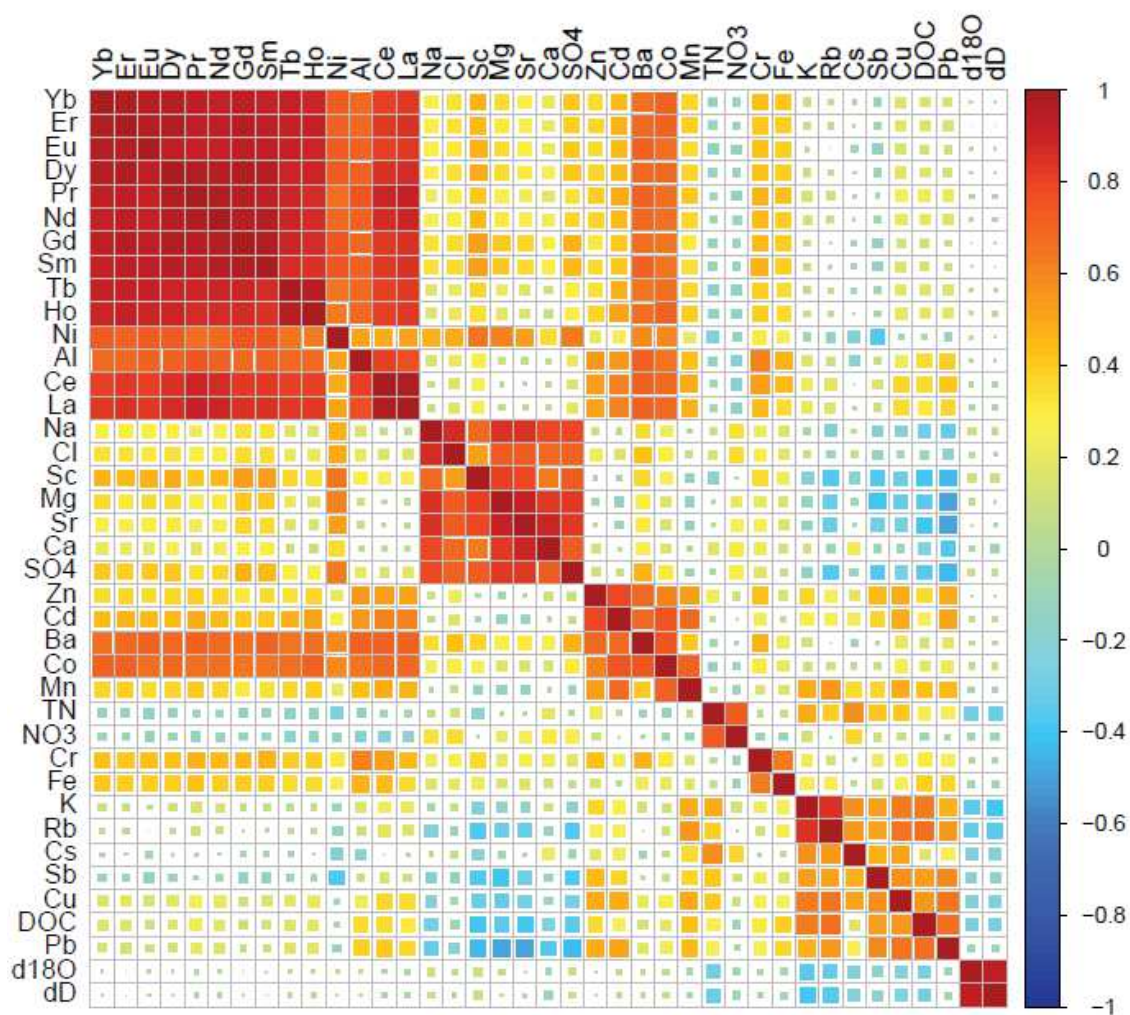


Figure 4.6. Correlation matrix for the parameters studied in the catchment waters.

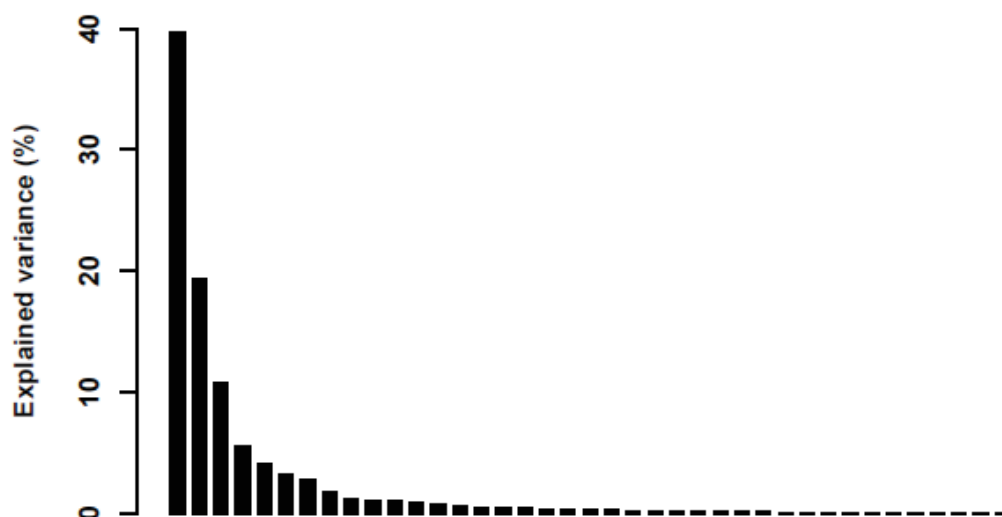


Figure 4.7. Histogram of eigenvalues representing the explained variance of each generated principal component.

In the study of our log z-transformed dataset, we retained firstly the components with eigenvalues > 1 based on the Kaiser criteria (Kaiser, 1958). This selection resulted in 7 components with eigenvalues > 1 explaining 86.1% of the total variance in the original scatter (Fig.4.7). The loadings and eigenvalues for these seven components are presented in Table 4.1. Loadings > 0.6 are marked in red bold digits and loadings < -0.6 in blue bold. The 5 first PC's present loadings > 0.6 and/or < -0.6 and the number of variables inside these limits as well as the variance explained decrease successively from PC1 to PC5. Given that the components PC4 and PC5 only explain about 5% of the variance each, accounting mainly for $\delta^{18}\text{O}$ - $\delta^2\text{H}$ and Cr-Fe respectively, we discarded them for the PCA graphic analysis. Similarly, although PC3 captures 10.9% of the variance explained, it affects only the Nitrogen components (TN and NO_3^-), Ca and Cs and, thus, its contribution to the visual separation of observations is minimal. Meanwhile, the 2 first PC's capture 59.2% of the variance and account for 28 variables out of the 39 computed. We therefore decided to keep PC1 and PC2 as the most relevant components and study separately the relationships between the aforementioned variables with loadings > 0.6 and/or < -0.6 from PC's 3 to 5.

PC1 explains the greatest percentage of variance (39.8%) and is dominated by highly negative loadings (< -0.6) of Al, Co, Ni, Ba and especially the REE (TD1, TD2 and TD4; Table 4.1). PC2 (19.4% of variance explained) is characterized by highly negative loadings of DOC, K, Cu, Rb, Pb and Sb (TD7) and highly positive loadings (> 0.6) of SO_4^{2-} , Na, Mg, Sr and Sc (TD3). Figure 4.8-a is the graphical representation of this information. The loadings (or variables) have been here coloured according to the geochemical groups (TD) previously identified in the HCA of the same dataset. This plot is efficient at reducing the geochemical groups delivered by the HCA from 8 to 3 but also at separating the variables inside TD1, TD4 and TD5 according to their inter-correlations with other TD's. Figure 4.8.b shows the (orthogonal) projection of the scores onto the PC's 1 and 2, which reflects the importance of the components for the water samples (Cloutier et al., 2008). The scores (or samples) have been here coloured according to the samples colour code reported all along this work and delimited according to the 3 main HCA water clusters. The PCA generally confirms the clustering defined by the HCA and brings additional insight. The relative geochemical composition of the different waters can now be better recognised according to the correlations identified: Cluster 1 (R/TF) composition seems to have a clearer impact on that of Cluster 2 soil solutions and, similarly, Cluster 2 composition shows a stronger link to that of the whole Cluster 3 but in particular SW, GW2, GW5, GW6 and GW7 (Cluster 3.1). Additionally, GW5 waters highlight now as a particular case, showing to be directly impacted by Cluster 1 precipitation composition. Further interpretation and discussion about the processes responsible for the distribution of the waters (and HCA water clusters) in the PCA environment are provided in section 5.2.1.

Table 4.1. Loadings and explained variance for the first 7 Principal Components (PC).

Parameters	PC1	PC2	PC3	PC4	PC5	PC6	PC7
DOC	-0.207	-0.728	0.143	-0.186	-0.284	0.054	0.028
TN	0.086	-0.310	0.709	-0.030	0.132	-0.380	-0.318
δ18O	0.004	0.258	-0.368	0.663	-0.243	-0.437	0.234
dD	0.013	0.245	-0.412	0.659	-0.232	-0.444	0.203
Cl	-0.438	0.459	0.552	0.189	-0.092	0.091	0.014
NO3	0.091	0.105	0.641	0.163	0.276	-0.397	-0.424
SO4	-0.476	0.696	0.335	0.122	0.043	0.084	-0.060
Na	-0.384	0.636	0.523	0.168	-0.111	0.030	0.065
K	-0.166	-0.623	0.558	-0.140	-0.044	0.018	0.247
Mg	-0.393	0.765	0.406	-0.048	-0.076	0.033	0.120
Ca	-0.323	0.535	0.663	0.047	-0.040	0.057	0.155
Al	-0.796	-0.201	-0.148	0.069	-0.268	0.154	-0.165
Cr	-0.548	-0.101	0.159	-0.052	-0.635	0.034	-0.190
Mn	-0.463	-0.526	0.129	0.278	0.170	0.225	0.403
Fe	-0.448	-0.166	0.135	-0.281	-0.651	-0.175	0.054
Co	-0.781	-0.150	-0.039	0.338	0.173	0.237	0.099
Ni	-0.760	0.368	-0.047	-0.073	0.034	0.153	0.097
Cu	-0.247	-0.726	0.315	0.042	0.021	-0.084	0.045
Zn	-0.511	-0.418	0.232	0.508	-0.040	0.225	-0.263
Rb	-0.086	-0.730	0.379	-0.192	-0.024	-0.020	0.392
Sr	-0.364	0.740	0.483	-0.015	-0.101	0.060	0.071
Cd	-0.575	-0.439	0.054	0.542	0.190	0.217	-0.057
Ba	-0.809	-0.018	0.036	0.299	0.006	0.262	-0.187
Pb	-0.197	-0.798	0.030	0.134	-0.238	-0.064	-0.096
Sc	-0.513	0.694	0.131	-0.076	-0.178	0.022	0.065
Sb	0.025	-0.689	0.362	0.182	-0.176	-0.014	-0.056
Cs	-0.002	-0.385	0.620	0.027	0.291	-0.296	0.279
La	-0.888	-0.264	-0.164	-0.019	0.066	-0.039	-0.086
Ce	-0.884	-0.299	-0.167	-0.016	-0.052	-0.029	-0.086
Pr	-0.948	-0.070	-0.114	-0.126	0.057	-0.101	-0.006
Nd	-0.943	-0.023	-0.107	-0.139	0.078	-0.124	-0.009
Sm	-0.945	0.083	-0.089	-0.133	0.051	-0.114	-0.002
Eu	-0.936	0.060	-0.159	-0.107	0.085	-0.090	-0.001
Gd	-0.946	0.105	-0.102	-0.151	0.083	-0.127	0.011
Tb	-0.895	-0.047	-0.230	-0.102	0.131	-0.126	0.002
Dy	-0.956	0.030	-0.099	-0.131	0.099	-0.119	0.018
Ho	-0.891	-0.076	-0.207	-0.059	0.143	-0.120	-0.007
Er	-0.945	0.008	-0.120	-0.104	0.119	-0.118	0.025
Yb	-0.941	0.028	-0.116	-0.127	0.099	-0.108	0.019
Explained variance	15.506	7.549	4.255	2.205	1.635	1.305	1.112
Explained variance %	39.8	19.4	10.9	5.7	4.2	3.3	2.9
Cumulative % variance	39.8	59.1	70.0	75.7	79.9	83.2	86.1

Bold red values: loadings > 0.6

Bold blue values: loadings < -0.6

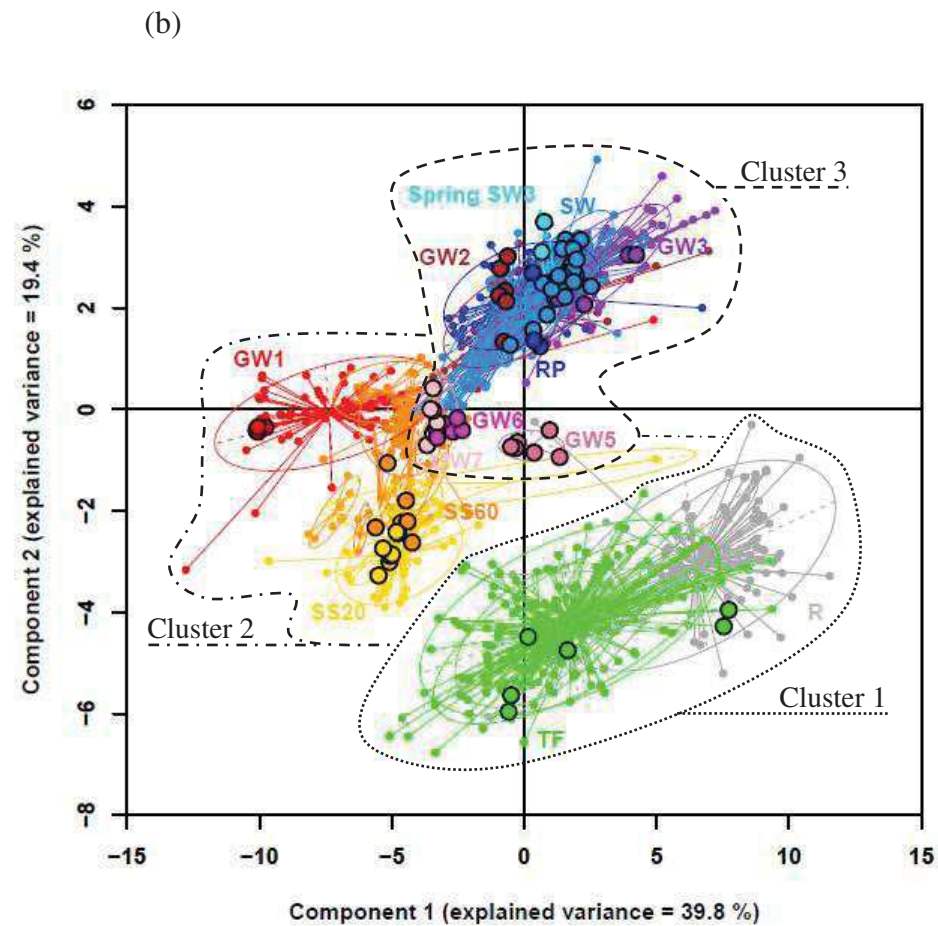
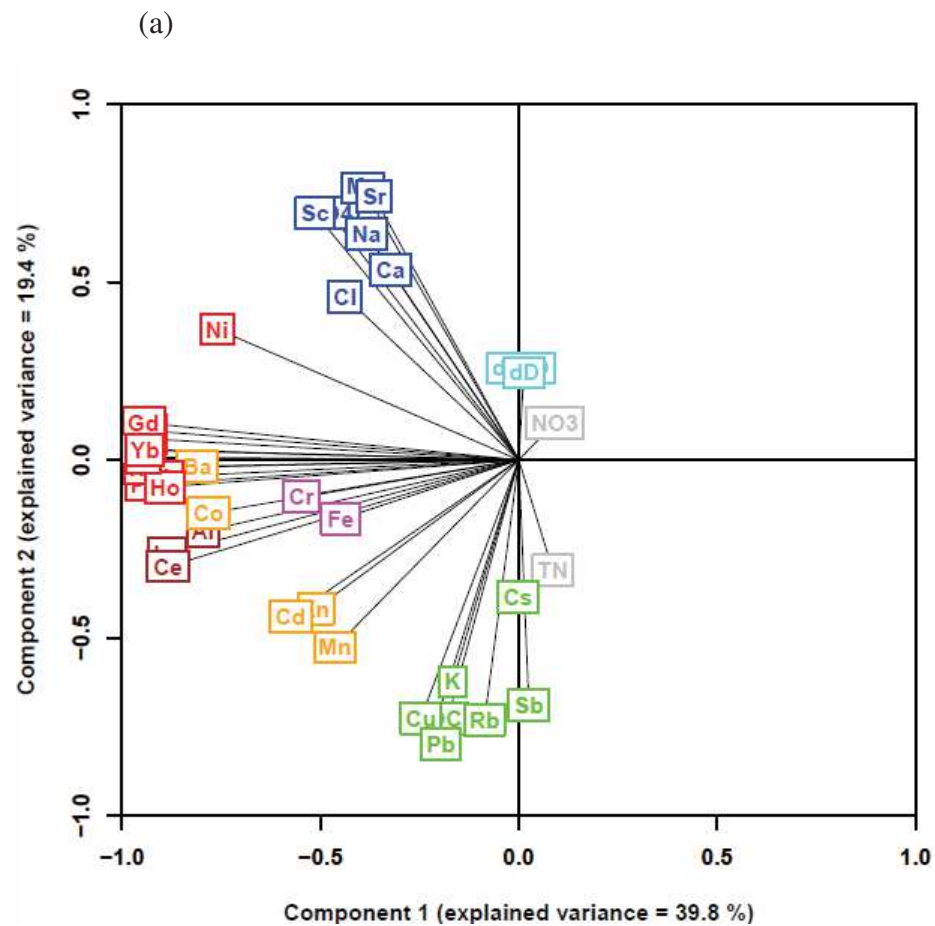


Figure 4.8. Projection on the components 1 and 2 space of (a) hydrochemical parameters (*loadings*) and (b) observations (*scores*), including envelopes corresponding to clusters identified in HCA. The colour code in (a) corresponds to the geochemical groups (TD) identified in the HCA (Fig.4.5) and in (b) to the water type. TF and R group all TF and R sampling points. SS20 groups soil solutions collected at 10 and to 20 cm depth and SS60 those collected at 40 and 60 cm depth. SW includes SW collected at the outlet (SW1) and the tributaries (SW2 and SW3).

Temporal dynamics

The time series of PC1 and PC2 scores are shown in Figure 4.9 and Appendices 5-6. They allow assessing the potential seasonal distribution of the scores in the PCA. PC1 and PC2 loadings are more positive for TF and SW during winter. GW1 and to a lesser extent SS tend to have lower negative PC1 loadings and higher positive PC2 loadings towards summer, when, due to dryness conditions these waters cannot be collected anymore (Fig.4.9-a and b). PC2 shows generally clearer time dependence than PC1 and allows a better identification of the time trends of GW2, GW3 and R similar to that of SW and TF (notably for 2010 and 2011). Additionally, PC2 shows slightly higher negative loadings in spring for SS (Fig.4.9-b).

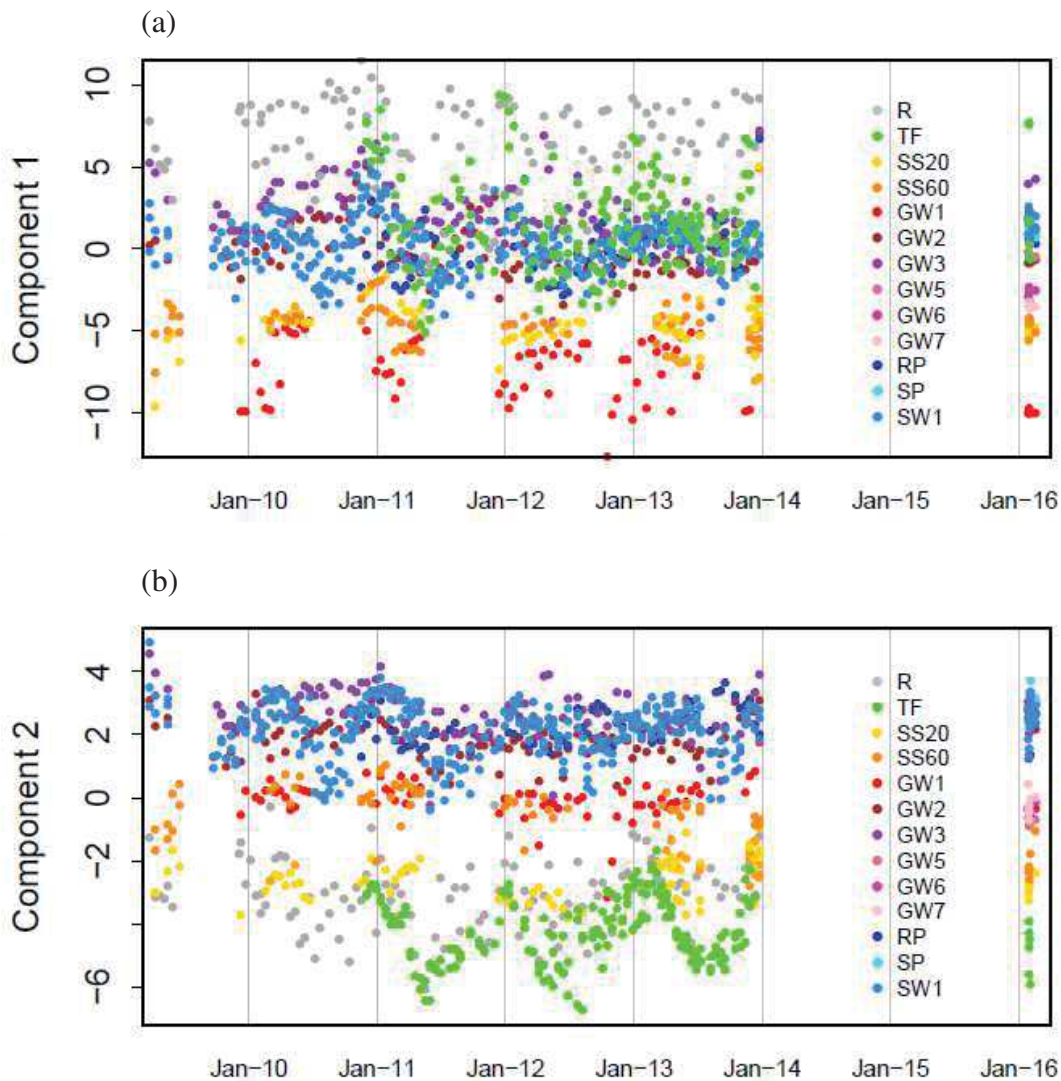


Figure 4.9. Time series of the waters *scores* of components 1 (a) and 2 (b).

In Figure 4.10 the scores of PC1 and PC2 are plotted against the logarithm of the discharge corresponding to their sampling date in order to link the clusters behaviour to the changing hydrological conditions. This plot shows that both PC1 and PC2 loadings distributions are generally not discharge dependent. However, it allows identifying a tendency towards more

negative PC1 loadings for GW1 and towards more positive PC2 loadings for TF and SW when discharge increases.

Hence, in the PCA we may generally identify a summer-winter trend from bottom-left (- PC2, - PC1) to top-right (+ PC2, + PC1) for clusters 1 and 3 and from right to left for cluster 2 (Fig.4.8). This temporal dynamics go along with the discharge dependent patterns observed for GW1, SW and TF. When looking at each of the individual water samples, SW and TF represent well the general time trend of their respective clusters because they are similarly influenced by PC1 and PC2. The situation is slightly different for other waters: SS (notably SS20) from cluster 2 and GW2 and GW3 from cluster 3 show a rather vertical gradient (bottom to top; Fig.4.8) as they are more influenced by PC2. GW5, GW6 and GW7 are excluded from these temporal patterns due to the lack of samples on the long term. However, it is interesting to note that they all have been collected in winter and fall between the PCA “summer” end members of cluster 2 and 3 (Fig.4.8).

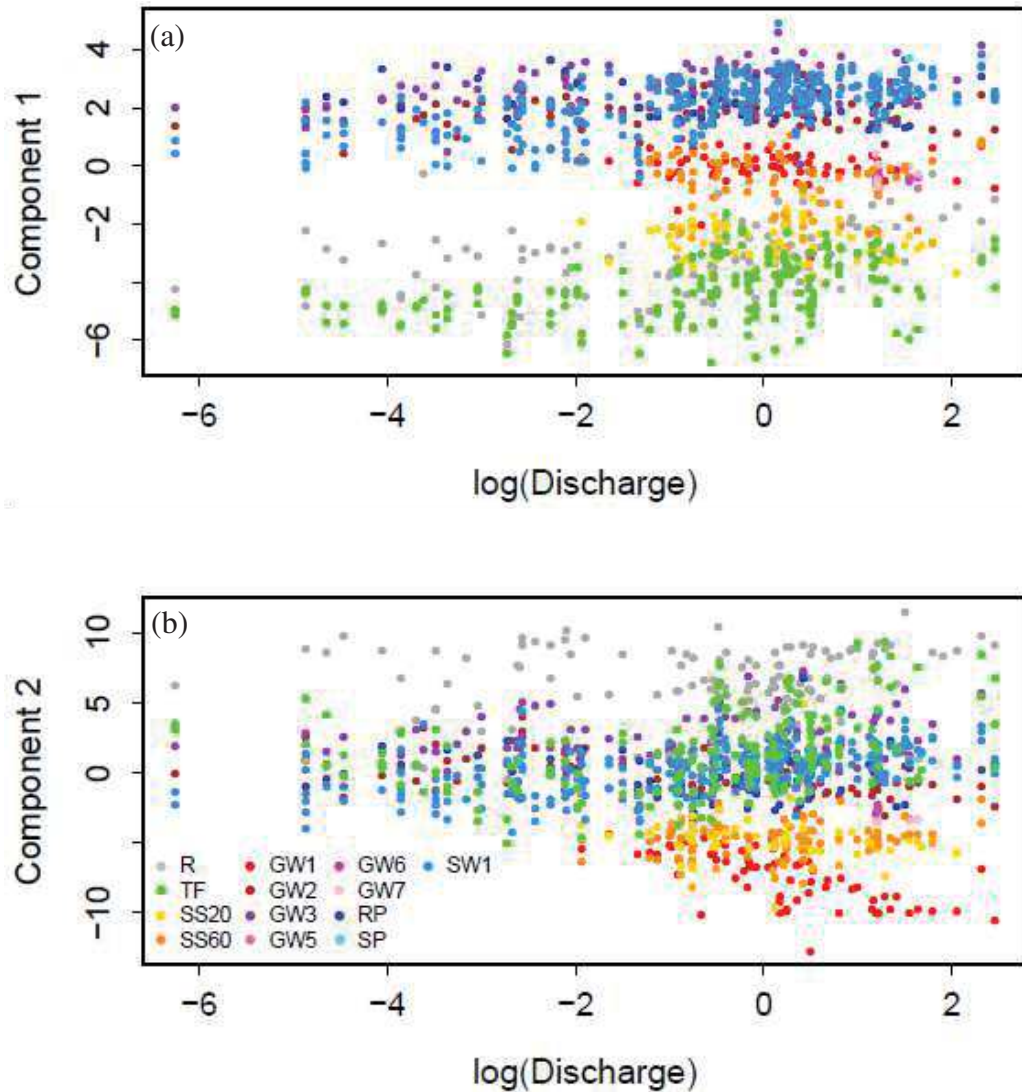


Figure 4.10. Scatterplot of the waters *scores* of components 1 (a) and 2 (b) against discharge (Q:mm/d).

REE distribution patterns of the waters

The Post Archean Australian Shales (PAAS) normalized REE distribution median patterns of the dissolved load of the Weierbach waters are shown in Figure 4.11. Soil solutions correspond to site 7, and have been found to be representative for the rest of the catchment sampling points at the same depths. Figure 4.12 shows the time series of the Ce anomalies of SS, GW1, GW2, GW3 and SW (1, 2, 3). Ce anomalies (CeN/CeN^*) are calculated as the enrichment of Ce with respect to other LREE (namely La and Pr) normalized to PAAS with the equation [$CeN/CeN^* = CeN/(0.5LaN+0.5PrN)$].

As deduced from the PCA, SS and notably GW1 are the most REE enriched waters. Among the SS, SS40 is the most enriched. TF and R are depleted in REE but, while R has rather flat REE

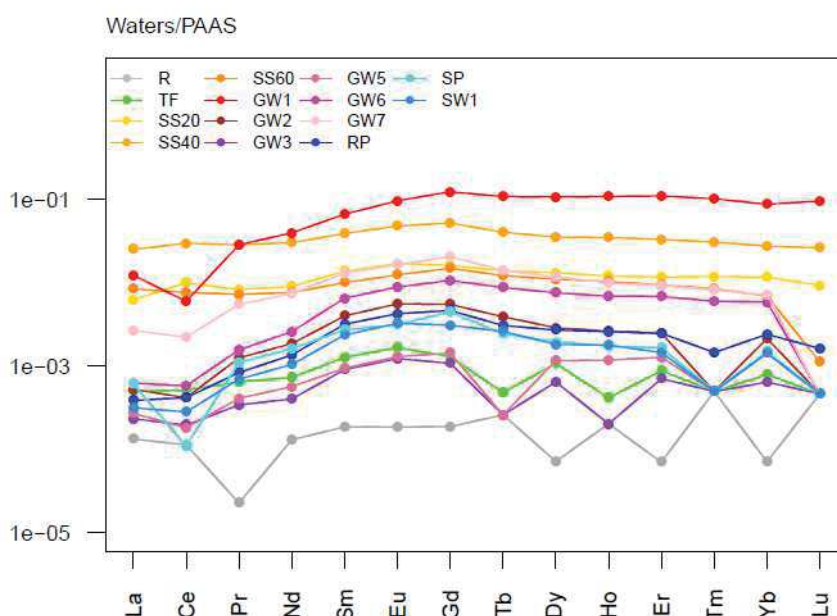


Figure 4.11. PAAS-normalized REE distribution patterns of the Weierbach waters.

patterns, TF is MREE enriched. All SS have PAAS like REE distributions with slight MREE and Ce enrichments. SS20 and SS40 show relatively stable (CeN/CeN^*) around 1.37 and 1.11 respectively along the years. On the other hand, SS60 shows variable Ce anomalies with time, ranging from 0.76 to 1.45. Conversely, GW1 is more enriched in MREE with respect to LREE and shows strong negative Ce anomalies fluctuating between 0.18 and 0.38 without a clear seasonal pattern. GW2, GW3, GW5, GW6 and GW7 are all more REE depleted, with GW5 and GW3 showing lowest REE concentrations similar to TF. All of them show similar patterns characterized by a more remarkable MREE enrichment and a smaller Ce anomaly than GW1. Indeed the Ce anomalies of these groundwaters range from 0.47 to 0.68 on median, but fluctuate slightly in time and sometimes reach balance or become positive for GW2 and notably for

GW3. The REE concentrations and patterns of RP, SP and SW resemble those of the groundwaters, with the exception of a stronger negative Ce anomaly and a slight Gd enrichment for SP (0.12). RP Ce anomalies fluctuate in time up to the unit without a clear seasonal trend, whereas those of SW are rather stable and show only punctual increases (less negative anomalies) mostly in dry conditions.

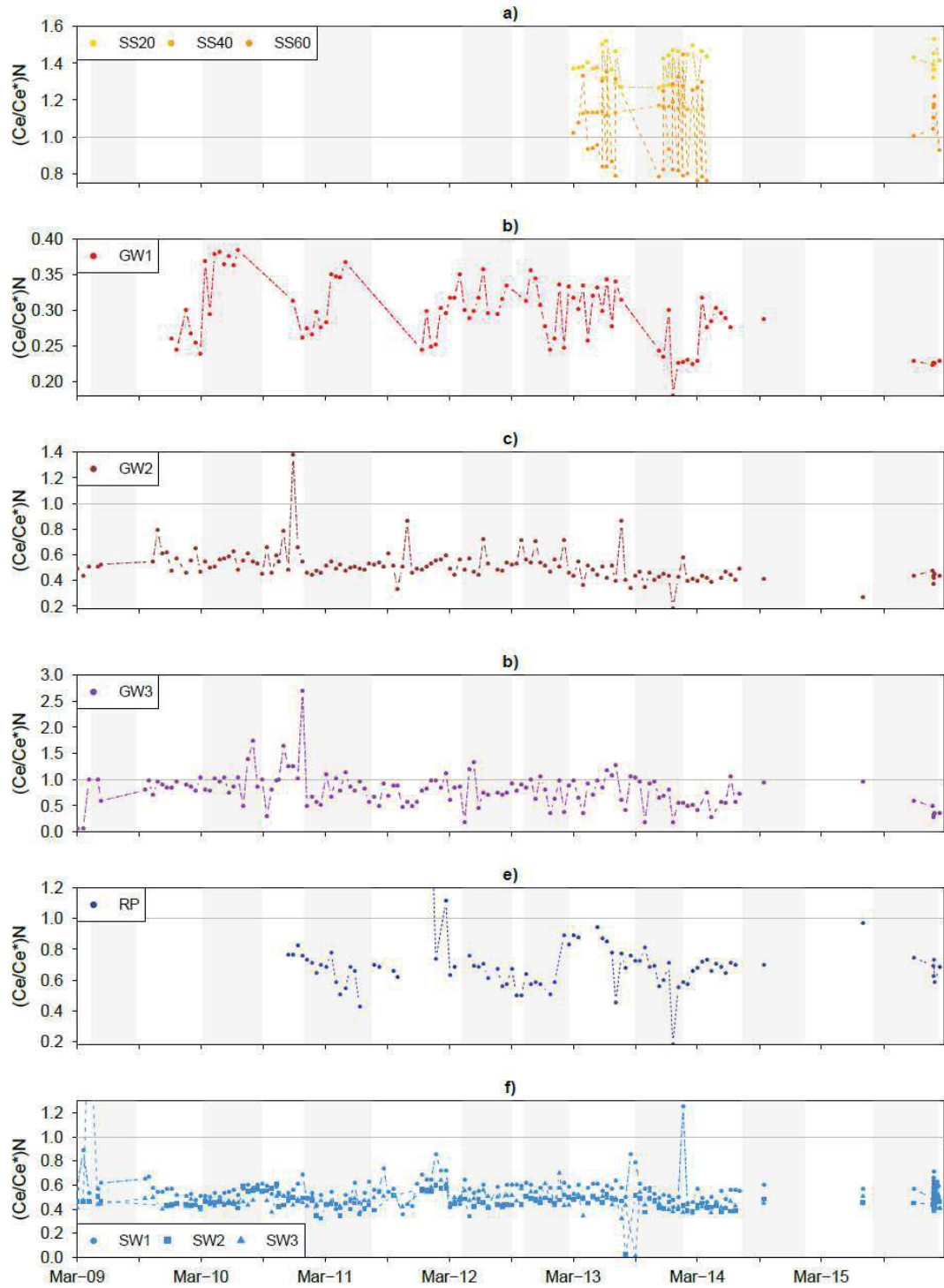


Figure 4.12. Time-series of the Ce anomalies ($(Ce/Ce^*)N$) for (a) soil solutions, (b) groundwaters from GW1 well, (c) groundwaters from GW2 well, (d) groundwaters from GW3 well, (e) riparian waters, and (f) streamwaters. Shaded areas represent wetness periods. Horizontal gray lines at $(Ce/Ce^*)N = 1$ indicate lack of anomaly.

REE correlations with pH, alkalinity and DOC

Total REE concentrations (ΣREE) are negatively correlated with pH for the GW samples, but not for SS or RP-SW samples (Fig.4.13). For the SW, a positive relationship might even be discerned. However, in nearly all cases, the trends look rather cloudy, indicating that other or additional factors than pH control these REE abundances. Indeed, the REE-pH trends in GW, RP and SW waters are in agreement with alkalinity levels (Fig.4.14), which seem to be of particular importance for the REE content of GW1. Additionally, DOC shows positive correlations with REE concentrations for SS20 and RP-SW waters (Fig.4.15). LREE enrichments, expressed as $(\text{La/Yb})/(\text{La/Yb}_{\text{PAAS}})$, seem to come along with higher pH for SS (mainly SS20) and notably for all GW samples, except GW1 which shows LREE enrichment with decreasing pH (Fig.4.16). The LREE enrichments with higher pH in SS are in agreement with slightly higher alkalinity values but GW1 shows no covariation with alkalinity and has lowest alkalinity values and LREE enrichments compared to the other GW samples (Fig.4.17). SS LREE enrichments seem to be importantly controlled by DOC (Fig.4.18-a). They show LREE depletions at highest DOC concentrations. GW samples present similar but rather cloudy distributions. LREE enrichments of SW show no clear trend as a function of pH, alkalinity or DOC. Finally, Ce anomalies seem to be pH controlled for GW1 samples, showing positive correlations between both variables (Fig.4.19-b and b-zoom GW1). Once again, alkalinity changes are positively correlated with Ce^* (and pH) for GW1, and to a lesser extent for SS20 (Fig.4.20-a,b,b-zoom GW1). DOC also seems to be correlated with the corresponding Ce anomalies of the SS, particularly of SS20 (Fig.4.21-a). At higher DOC concentrations, SS samples show more positive Ce anomalies. No clear correlation is visible for GW, RP and SW samples.

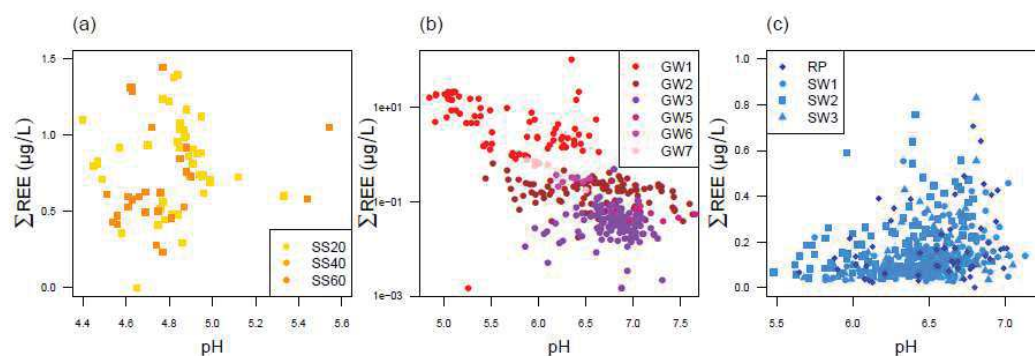


Figure 4.13. Total REE concentration against pH for (a) soil solutions, (b) groundwaters and (c) streamwaters.

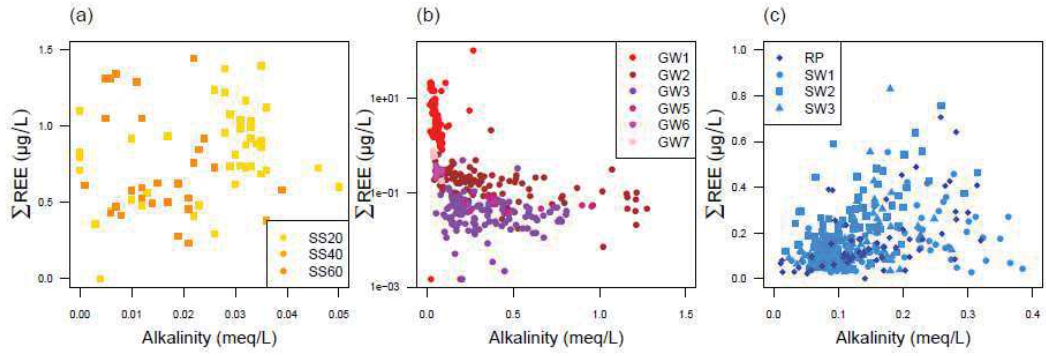


Figure 4.14. Total REE concentration against alkalinity for (a) soil solutions, (b) groundwaters and (c) streamwaters.

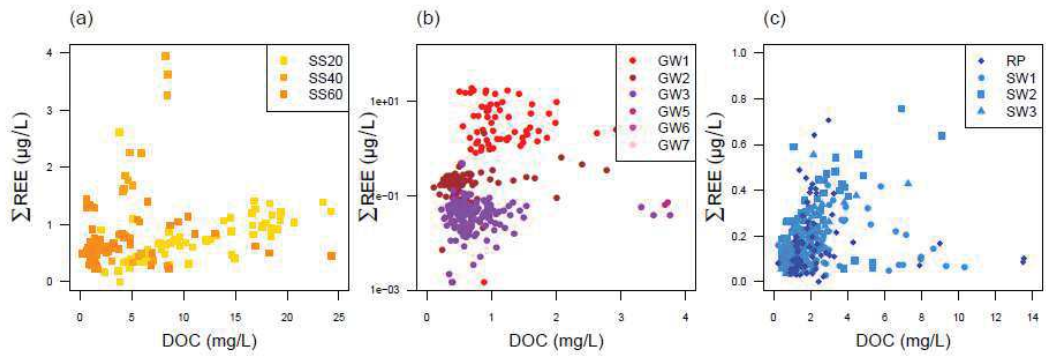


Figure 4.15. Total REE concentration against DOC for (a) soil solutions, (b) groundwaters and (c) streamwaters.

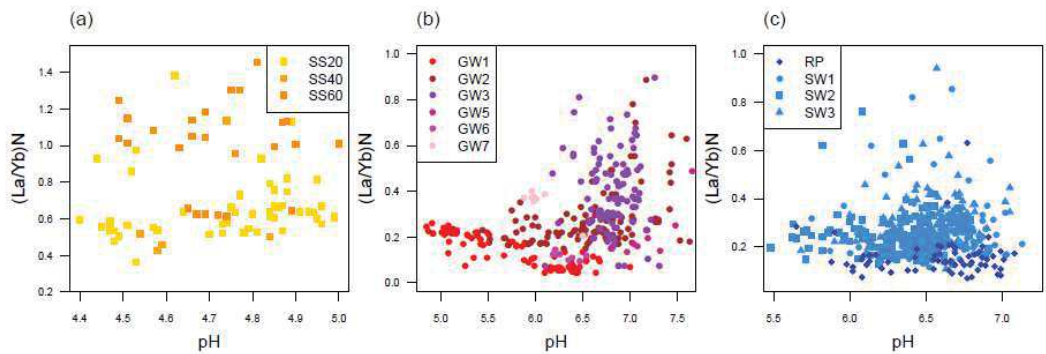


Figure 4.16. PAAS-normalized La/Yb ratios plotted against pH for (a) soil solutions, (b) groundwaters and (c) streamwaters.

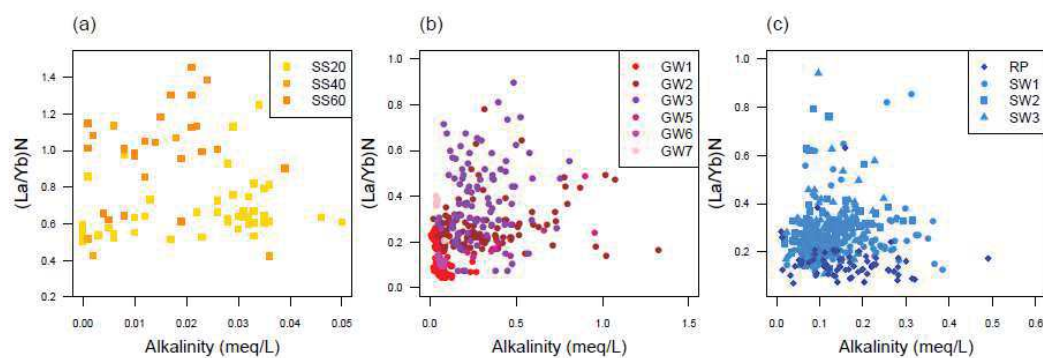


Figure 4.17. PAAS-normalized La/Yb ratios plotted against alkalinity for (a) soil solutions, (b) groundwaters and (c) streamwaters.

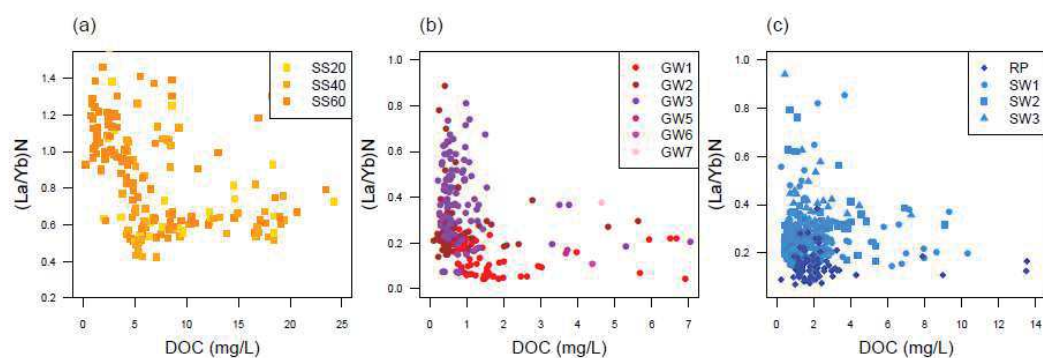


Figure 4.18. PAAS-normalized La/Yb ratios plotted against DOC for (a) soil solutions, (b) groundwaters and (c) streamwaters.

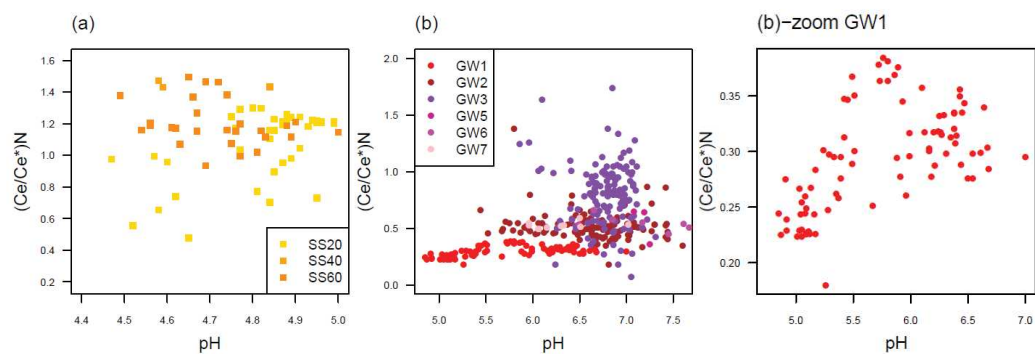


Figure 4.19. Ce anomaly ((Ce/Ce*)N) plotted against alkalinity for (a) soil solutions and (b) groundwaters. A zoom of GW1 in (b) is shown.

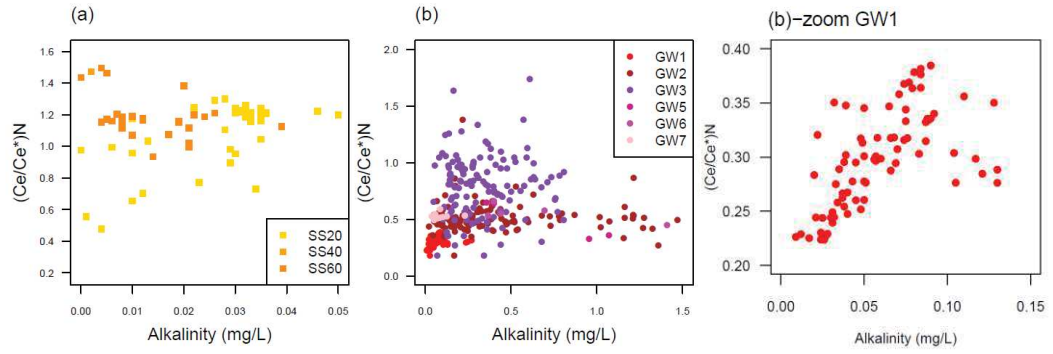


Figure 4.20. Ce anomaly ((Ce/Ce*)N) plotted against alkalinity for (a) soil solutions and (b) groundwaters. A zoom of GW1 in (b) is shown.

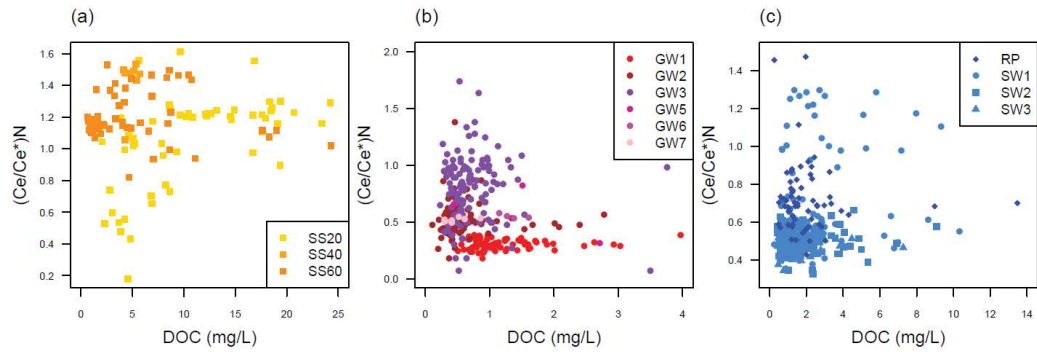


Figure 4.21. Ce anomaly ((Ce/Ce*)N) plotted against DOC for (a) soil solutions and (b) groundwaters. A zoom of GW1 in (b) is shown.

The O and H stable isotopic compositions of waters

The interaction of water with rock and plants, its evaporation, condensation, freezing and mixing leads to fractionation of O and H isotopes. Important seasonal variations of $\delta^{18}\text{O}$ and dD values related to air temperature have been observed especially for $\delta^{18}\text{O}$ in precipitation amounting to 12‰. However, subsurface storage consisting of reservoirs of different ages seems to have a major impact on the streamwater signatures (Pfister et al., 2017).

Figure 4.22 shows the standard dual isotope diagram for $\delta^{18}\text{O}$ and dD of the different waters collected through the catchment over 7 years as well as the Local Meteoric Water Line (LMWL) fitted to the measured rain data, where $\delta^2\text{H} = 5.3 \cdot \delta^{18}\text{O} + 7.3$. The different SS fall on the LMWL showing a large range of isotopic compositions.

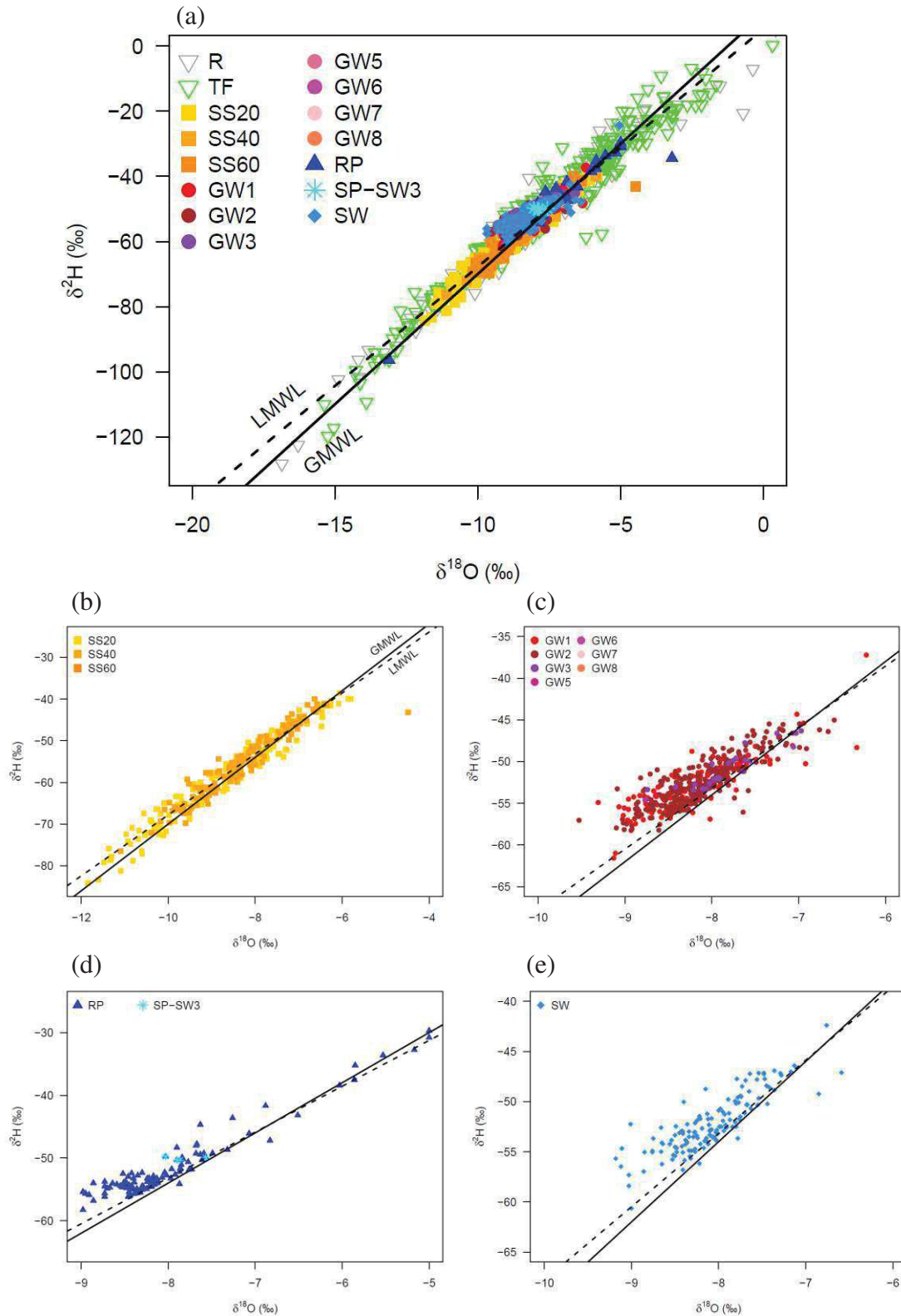


Figure 4.22 Stable isotope compositions of (a) the ensemble of the Weierbach waters and (b-e) of each water type relative to the LMWL (dashed line: $\delta^2\text{H} = 5.3 \cdot \delta^{18}\text{O} + 7.3$) and the GMWL (solid line: $\delta^2\text{H} = 8 \cdot \delta^{18}\text{O} + 10$).

The greatest variation is observed for SS20 ($\delta^{18}\text{O}$ from -12 to -6), whereas SS40 and SS60 are less variable but show higher values ($\delta^{18}\text{O}$ between -10 and -6). The GW samples lie above the

LMWL with a deviation to the left for the lower dD values, thus showing a different slope than the LMWL. GW isotopic compositions values are less variable and generally heavier than the average SS ($\delta^{18}\text{O} > -9$). Those of RP, SP and SW overlap with the GW values but spread less above the LMWL. RP values show a larger variance towards heavier compositions and SP isotopic compositions are slightly heavier than average compositions of the SW and RP.

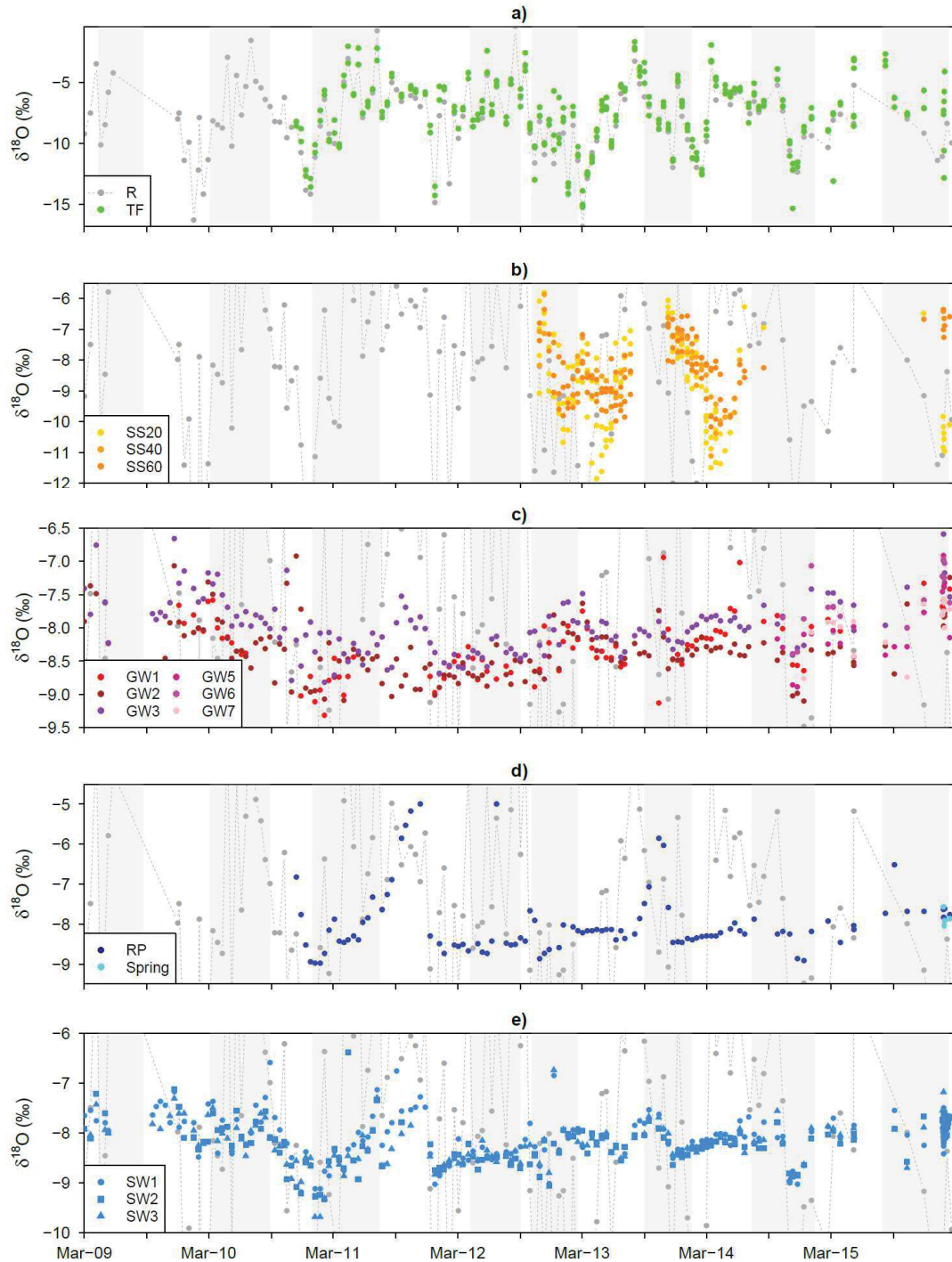


Figure 4.23. $\delta^{18}\text{O}$ time series for (a) rain and throughfall (R, TF), (b) soil solutions (SS), (c) groundwaters from GW1, GW2, GW3, GW5, GW6 and GW7 wells, (d) riparian and spring waters (RP, SP), and (e) streamwaters (SW1, SW2, SW3). Shaded areas represent wetness periods.

We analysed the $\delta^{18}\text{O}$ and $\delta^2\text{H}$ temporal dynamics for the Weierbach waters and observed that both isotopes present the same variability through the observation period. Therefore, only $\delta^{18}\text{O}$ time series are discussed here. Figure 4.23 shows the $\delta^{18}\text{O}$ time series of precipitation and of the different waters sampled in the catchment from March 2009 to February 2016. The wet periods are marked in grey. The $\delta^{18}\text{O}$ range of precipitation samples varied widely between wet and dry periods, but was very similar for both R and TF during the whole observation period. The $\delta^{18}\text{O}$ patterns of SS collected with porous cup lysimeters during the wet periods generally resemble those of precipitation, with an apparent slight delay visible e.g. around March 2013. Soil solution $\delta^{18}\text{O}$ values are most variable at 20 cm depth and generally increase at 40 and 60 cm depth, where the variability is smaller. GW samples show $\delta^{18}\text{O}$ values ranging between -10 and -6‰. At this scale, a seasonal trend parallel to the precipitation is observable, especially for GW3, pointing to a strong connectivity of the surface and groundwater systems. Waters collected in the riparian zone (RP) present $\delta^{18}\text{O}$ values varying between -10 and -5‰, with the higher values generally slightly delayed regarding precipitation $\delta^{18}\text{O}$ peaks. SP $\delta^{18}\text{O}$ resemble those of RP waters, but cannot be studied in a temporal sense because SP has only been sampled during 2016. The $\delta^{18}\text{O}$ time series of SW samples show similar patterns as that of RP in the values range of GW (ca. 7.5‰). The covariation between precipitation and all other waters points to a very fast connection of the surface and subsurface systems and, thus, manifests open system behaviour.

4.1.2 Event-scale evolution of the catchment waters

The physico-chemical, major, trace and rare earth element data for the different waters collected in the Weierbach catchment during the winter event sampling campaign is reported in Appendices 7 to 9. Two additional punctual samplings realized in July and December 2015 have been included in the appendix table as references for dry and winter conditions. It must be noted that for all these samplings, throughfall and soil solution were collected only under deciduous cover on the plateau site 7 (TF1). The prioritization of TF over R was done due to the greater importance of the former in the Weierbach catchment, whereas the site selection was done according to the location of the study regolith profile. The hydrometric time series of the flood event sampling are reported in chapter 1 (section 1.2, Fig.1.3.).

Physico-chemical dynamics at the event scale

Values of EC and pH of the waters sampled in the catchment during the event have, compared to the waters collected in summer, slightly lower EC, pH and alkalinity values, as it has been noted in previous sections for the wetter periods in general (Appendices 1 and 7 and Fig 4.24). While most waters show relatively constant EC, pH and alkalinity values during the event, GW2, GW5, SP and SW highlight for their physico-chemical dynamics around the rain episode. GW2 and GW5 show EC, pH and alkalinity peaks during the rain event. SP shows a strong pH

and alkalinity decrease during the second discharge peak but no EC variation, whereas SW values of all 3 variables strongly decrease during the first discharge peak (Fig 4.24).

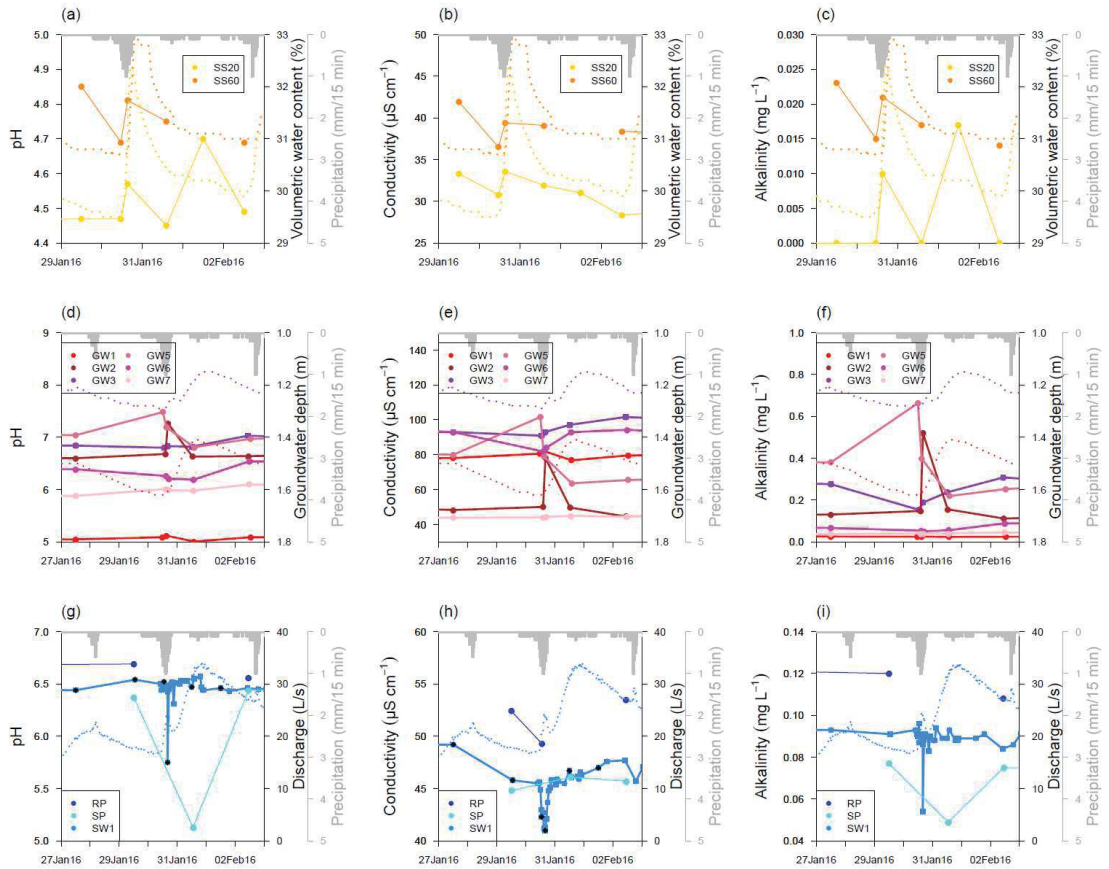


Figure 4.24. Temporal dynamics of pH, electrical conductivity ($\mu\text{S}/\text{cm}$) and alkalinity (HCO_3^- mg/L) for the studied storm event for (a-c) soil solutions at 20 and 60 cm depth (SS20, SS60), (d-f) groundwaters collected at the wells GW1, GW2, GW3, GW5, GW6 and GW7, and (g-i) streamwater collected at the outlet (SW1), riparian (RP) and spring water (SP). Grey histograms on top of the plots represent precipitation during the event. Dashed lines in the background of the plots represent soil volumetric water content at 20 and 60 cm depth (a-c), GW1 and GW3 depths (d-f), and SW1 discharge (g-i).

Dissolved major and trace element dynamics at the event scale

The composition of the waters collected during the event sampling compared to the long term data is highlighted in Fig.4.8. It can be observed that for the Cluster 1, the event TF samples generally represent the long term average. In Cluster 2 the same happens with the SS20 samples. However, SS60 collected during the event sampling are much closer to the SS20 long term average than to the SS60 one. Also, GW1 event waters plot all on the extreme left of the GW1 ellipse. GW5, GW6 and GW7 samples are all from the storm event. For Cluster 3 all GW2, GW3, RP, SP and SW plot inside the ellipses described by the long term data but show a certain vertical distribution. Thus, in general the event waters fall on the previously identified “winter” or “high discharge” areas of the clusters.

The event-scale concentration dynamics of major and trace elements (which explain the 3 main clusters identified in the HCA and PCA) in *all* waters might be classified in 2 main temporal patterns. This are defined according to elemental enrichment and depletion responses of the different waters to the starting of the rain event and/or the system saturation which leads to the first discharge peak (Fig.4.25.a). While most chemical elements, such like Ca, S, Sr and Ba become depleted in SW during the flood event, Mn, Fe, Co, Al, Pb, Rb, REE and U concentrations increase punctually during the first discharge peak. Any depletion occurring in SW may be attributed to simple dilution and, without further information on the fluxes, is difficult to link to a source. On the contrary, the increase in concentrations in SW must be due to greater contributions of specific water pools characterized by similar enrichments and are therefore studied here. Mn and Fe enrichments are observed in the GW1, GW2, GW5 and GW7 mostly when the system saturates, similar as in SW. Lead concentration peaks are observed also in the SS, GW1, GW2, GW5 and GW7 mostly as the rain event starts. Most of these waters are generally Mn and Fe enriched, and SS and the deep GW5 are additionally Pb enriched (Fig.4.25.b). Co and Al are typically enriched in the SS and GW1, and their concentrations increase mainly in GW5 during the first discharge peak likewise SW. Rubidium, typically enriched in TF, shows concentration peaks during the first and second discharge peaks in GW2, similar to SW, and SS respectively. The REE, which have been shown to be most abundant in GW1, are also punctually enriched in GW3 as the rain event starts and increasing concentrations are observed during the second discharge peak. Finally, even though U is generally under the detection limit for all waters, its slight increase (calculated by isotopic dilution) in the streamwaters during the first discharge peak comes along with an increase in SS (when soil moisture increases too).

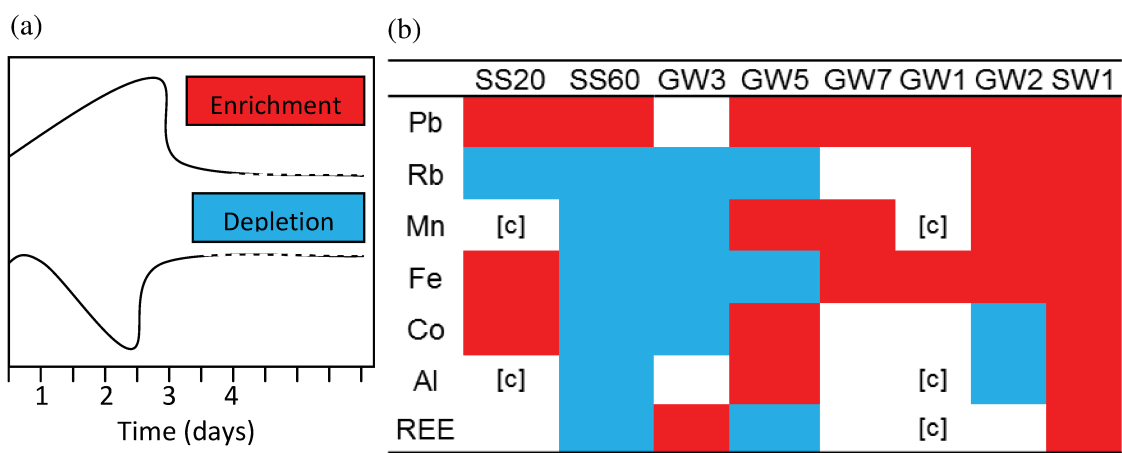


Figure 4.25. Temporal dynamics of major and trace element concentrations during the studied storm event. (a) Representation of the 2 main temporal concentration patterns before (day 1: 29/01/16) and during the event (2: 30/01/16 - 1st discharge peak; 3: 31/01/16; 4: 01/02/16 - 2nd discharge peak). (b) Representation of the temporal patterns of some elements (according to a) in soil solutions (SS20, SS60), groundwaters collected in GW3, GW5, GW7, and streamwater collected at the catchment outlet (SW1)

([c] indicates high concentrations in the long term). Elements shown are those enriched in SW1 at the first discharge peak.

O and H isotope dynamics at the event scale

Figure 4.26 shows the standard dual isotope diagram for the stable isotope composition of the waters collected in the Weierbach during the winter event sampling. The Local and Global Meteoric Water Lines (LMWL and GMWL respectively) fitted to the measured long term rain data in the Weierbach is also shown, LMWL: $\delta^2\text{H} = 5.3 \delta^{18}\text{O} + 7.3$; GMWL: $\delta^2\text{H} = 8 * \delta^{18}\text{O} + 10$. TF samples collected during the event are heavy compared to the long term TF average and also to the average isotopic compositions of all other event waters. Soil solutions from the event can be here more clearly differentiated than in the long term spread. While most SS60 event samples have similar compositions as TF, SS20 samples represent the lightest waters of all and fall above the LMWL. Ground, riparian, spring and stream waters (GW, RP, SP, SW) collected during the event generally plot in the field of heavier isotopic compositions of the long term data and show a trend towards lighter $\delta^{18}\text{O}$ compared to the LMWL.

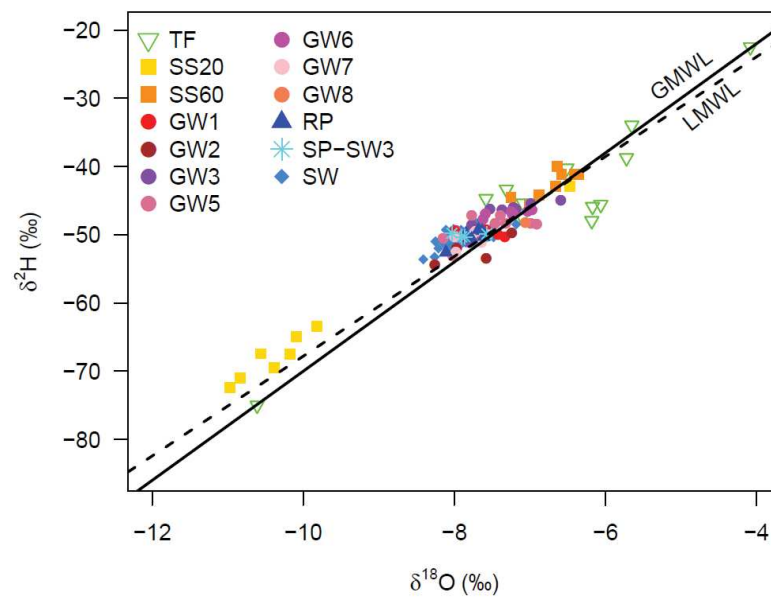


Figure 4.26. Stable isotope compositions of the ensemble of the Weierbach waters relative to the LMWL (dashed line: $\delta^2\text{H} = 5.3 * \delta^{18}\text{O} + 7.3$) and the GMWL (solid line: $\delta^2\text{H} = 8 * \delta^{18}\text{O} + 10$).

Figure 4.27 shows the $\delta^{18}\text{O}$ time series of precipitation and of the different waters sampled in the catchment during the flood event. SS samples show punctual $\delta^{18}\text{O}$ depletions at the beginning of the rain event and during the second discharge peak. Similarly, GW1, GW2 and GW7 $\delta^{18}\text{O}$ slightly decrease at the end of the rain event. On the contrary, GW3, GW5 and GW6 show $\delta^{18}\text{O}$ peaks during the rain event. RP, SP and SW show, similar to GW1, GW2 and GW7,

$\delta^{18}\text{O}$ depletions during the rain event. The $\delta^{18}\text{O}$ depletion is particularly remarkable for SW during the quick discharge response.

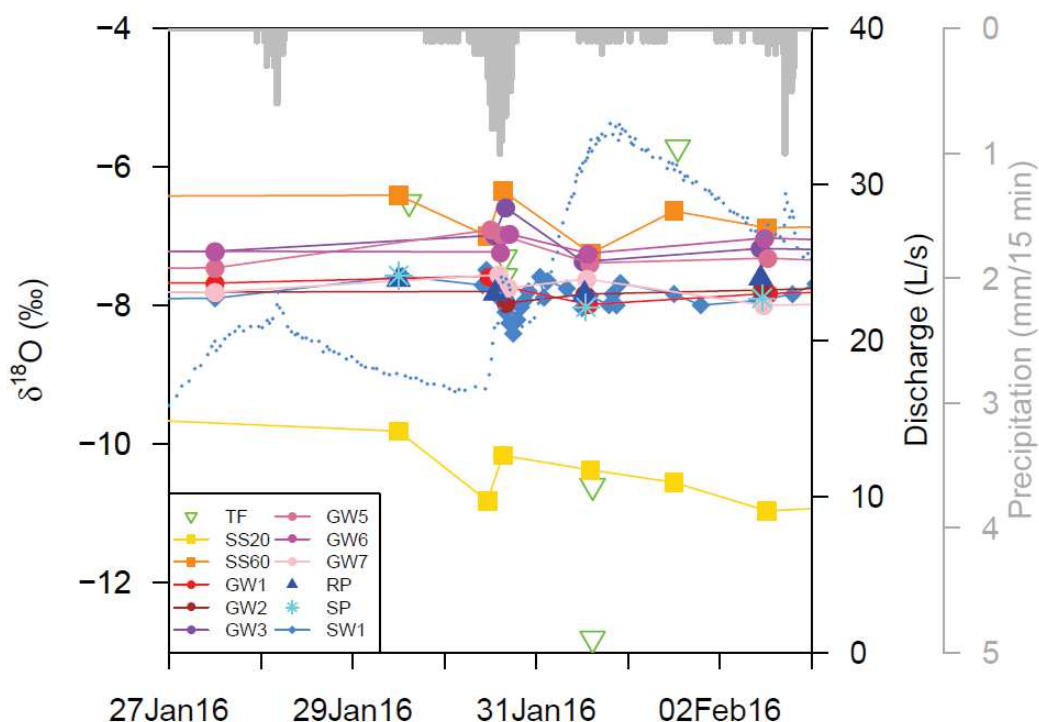


Figure 4.27. $\delta^{18}\text{O}$ time series for the Weierbach waters during the storm event. Top grey histogram represents the precipitation during the event and the blue dotted line in the background the discharge.

4.2 Interpretation and discussion

4.2.1 Hydrochemical classification according to major element concentrations

In order to compare the behaviour of the major cations and anions in the different waters of the catchment, we have plotted their proportions in a piper diagram (Fig.4.28). Envelopes delimiting the previously defined clusters are reported. Cluster 1 precipitation samples are characterized by a wide range of sodic-potassic carbonate and calcic chlorine compositions. Cluster 2 waters spread between the TF composition and a Ca/Mg- chloride and sulfate end member represented by GW1. Finally, Cluster 3 waters show a trend from GW1 compositions, where also most RP and SP waters fall, to a Ca- and Mg -carbonate end member represented by GW5.

TF samples (cluster 1) might be dominated by natural and anthropogenic components. According to previous observations (section 4.1.1), K^+ enrichments in TF are most likely related to the biological activity, as they go along with DOC enrichments. Nitrogen fixed forms, chloride and sodium contents might originate from cyclic (sea) salt or biologically fixed N_2 . For instance douglas fir trees are known to cycle a lot of N and excrete NO_3^- . However, fertilizers

are often also an important source for all of these elements. The greatest variability of chloride concentrations observed in TF might well represent a mixing range between chloride from wet or dry fallout of cyclic sea salt (correlated with Na^+) and chloride originating from pollution sources such as domestic and industrial sewage fertilizers, mining and road salt (Berner and Berner, 1996).

Among Cluster 2 waters, the soil solutions collected at 60 cm (SS60) are the most sulfate rich, similar to GW1, whereas the solutions collected at 40 and 20 cm depth show a more pronounced trend from sulfate to chloride based compositions. All of them are richer in Mg than TF but all tend, as TF, to Na^+ (and K^+) enrichments coupled with Ca depletions, pointing to the occurrence of Ca-Na ion exchange processes in Cluster 1 waters.

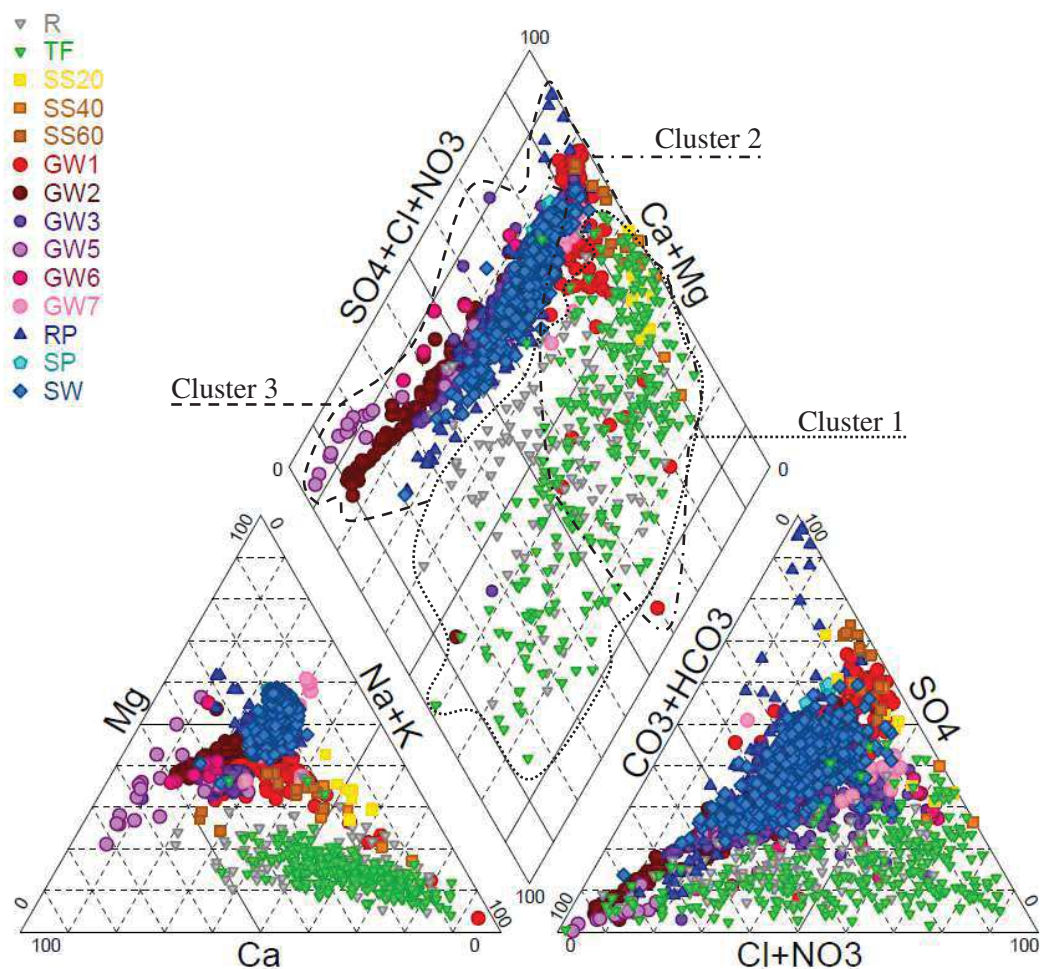


Figure 4.28. Piper diagram of the Weierbach waters. Envelopes correspond to clusters identified in HCA.

Cluster 3 waters are obviously affected by carbonate dissolution, which seems to be particularly important during the dryer periods. Since the rocks and soils of the catchment contain only small amounts of primary carbonates, and pollution represents generally a very small HCO_3^- contribution (no carbonates in the region), the most probable source of bicarbonate in the waters is the reaction of dissolved carbon dioxide released from bacterial decomposition with silicate

minerals: $2\text{CO}_2 + 11\text{H}_2\text{O} + 2\text{NaAlSi}_3\text{O}_8 \rightarrow 2\text{Na}^+ 2\text{HCO}_3^- + \text{Al}_2\text{Si}_2\text{O}_5(\text{OH})_4 + 4\text{H}_4\text{SiO}_4$ (Berner and Berner, 1996). Indeed, the enrichment of GW samples in Ca^{2+} , Na^+ and Mg^{2+} could be due to weathering of minerals such as albite (Na-plagioclase), anorthite (Ca-plagioclase) and/or Ca-phosphates like apatite, and illite and/or vermiculite respectively. Evidence for the strong impact of plagioclase and apatite alteration on the waters chemical compositions yield the Sr and Nd isotope data discussed in the following chapter 5. Nonetheless, an additional Ca source in the waters, such as atmosphere and notably vegetation nutrient cycles is probable, according to the observed seasonal trends and surface contributions.

When looking in detail the spread of Cluster 3 waters in the piper diagram, it is possible to identify chemistry dynamics related to the wetness conditions of the catchment (Appendices 10-12). GW2, GW3 and GW6 show bicarbonate compositions in dry conditions and a trend towards a chloride and sulfate composition in wetness conditions (Appendix 8-9). In these wells, depletion in bi-carbonate and enrichment in chlorides and nitrates take place as the system wets up, possibly linked to a greater impact from TF. Compared to chloride, nitrates dynamics with wetness conditions are more important in GW3 and GW6. All three wells generally present well mixed cation compositions (particularly for GW3) with a tendency to Ca and Mg enrichments. In GW2, water becomes more calcic as the system dries out, which would support the suggestion of greater impact of vegetation nutrient cycles, that are more important in summer (Appendix 10-a). Similarly, samples from GW5 fall in the range between Ca- and Mg – bicarbonate and chloride/sulfate regions (Appendix 11-a). However, in this case the samples collected during drier conditions represent the strongest Mg- bicarbonate end member (Ca to a lesser extend), which could be also due to very low concentrations of other anions. GW7 falls in the Mg-chloride region close to the other GW samples. With a reduced number of samples collected only during wetness conditions, enrichments in chloride and sulfate may be observed when passing from base to high flow (peaks).

Similarly, streamwater collected at the outlet (SW1) and the 2 tributaries (SW2 and SW3) show a trend similar to that of GW2, GW6 and notably GW3. SW samples have a rather Mg–bicarbonate composition in dry conditions and evolve towards a Mg- chloride and sulfate end member represented by the spring of SW3 as the system wets up (Appendix 12). SP waters have been sampled during wetness conditions only and, thus, a dry-wet composition trend is not observable. As it was mentioned before, SP, RP and SW waters mostly present well-mixed cations compositions, which points to their role as mixing spots of catchment waters. In the same way, the anions composition of the SW, even though dynamic, resembles that of SS and GW.

The Piper diagram efficiently represents the clusters previously identified in the HCA and PCA. Thanks to the integration of alkalinity, the piper diagram allows further understanding of the hydrological processes responsible for the clusters composition. The combination of HCA-PCA

and the Piper Diagram show that the hydrochemical classification of the catchment waters is strongly related to both the particular geological characteristics of their host environment and the hydrological conditions of the catchment.

The three identified sample clusters and the corresponding geochemical compositions can be characterized by 3 main processes identified in the 2 principal components of the PCA and in the diamond shape plot of the Piper diagram:

- (i) The atmospheric/vegetation inputs identified with TF and R compositions (Cluster 1) and characterized by the highly negative loadings of organic and atmosphere derived elements in PC2.
- (ii) The weathering and redox processes occurring in:
 - a. The upper-subsurface, represented by SS and GW1 (Cluster 2), with PC1 high negative loadings of REE, Al, Co, Ni and Ba, and a clear trend towards TF compositions in the Piper.
 - b. The deeper subsurface, represented by the waters of Cluster 3 (GW2, GW3, GW5, GW6 and GW7) characterized by highly positive major cation, Sr and Sc loadings in PC2 and by a range between carbonate and sulfate rich (cluster 2) compositions in the Piper plot.
- (iii) The reactivity and connectivity of the system and its impact in RP and SW (Cluster 3) under different hydrological conditions.

4.2.2 Hydrochemical processes at the Weierbach catchment

The atmosphere and vegetation cycling inputs

The distribution of Na, Cl, K, S and N components together with DOC, Pb, Rb and Sb in the catchment waters points to the importance of the TF as surface end member, characterized by atmospheric depositions and vegetation nutrient cycling (Figs. 4.8 and 4.28). The results suggest a preferential flowpath from the surface to the deeper regolith layers in the upper part of the plateau.

K^+ entering the system with TF can be found in SS as it migrates in the first layers of soil and is uptaken again by the roots. The concentrations observed in deep groundwaters suggest a preferential flowpath from the surface to the deeper regolith layers. Other than this, K^+ in ground and stream waters might come from the alteration of silicate minerals (potassium feldspar and micas). However, except in very acid ecosystems, K^+ leaching during rock weathering is slow compared to other elements (Na, Ca, Mg) and, thus, the concentrations remain low in the waters and higher in the residual mineral phases (Berner and Berner, 1996). The fact that Ca and Mg are more strongly enriched than K in our soil and ground waters

supports the suggestion that K originates from TF whereas Mg and notably Ca are principally related to weathering.

Similarly, the Pb and Rb enrichments together with abnormally high NO_3^- , DOC and SO_4^{2-} concentrations in the deep waters of GW5, GW6 and GW7 suggest the existence of preferential flowpaths. NO_3^- and NH_4^+ are the common fixed forms of nitrogen gas (N_2) found in the catchment waters and have three main sources (Berner and Berner, 1996):

- (i) OM (biologically fixed N_2) breakdown by bacteria first into NH_4^+ and then NO_3^- (ammonification and nitrification), which are mostly recycled by plants via photosynthesis but partially dissolved into soil water;
- (ii) precipitation and dry deposition of previously fixed nitrogen (directly from N_2O , or indirectly from NO_x), either natural or industrial;
- (iii) Industrially fixed nitrogen N_2 used in fertilizers which heavily pollute rain.

The very high nitrate concentrations in some wells (GW6 in the plateau and GW3 at the bottom of the catchment) contrast with the very low ones in the riparian and stream waters (RP, SW). NO_3^- may accumulate together with DOC and other atmosphere-derived elements in the groundwater, mobilize according to water table fluctuations and get reduced via denitrification processes in the riparian zone before to reach the stream.

Lastly, given that R and TF show the lowest SO_4^{2-} concentrations, recent cyclic salt or pollutive sulfate inputs into SS through wet or dry deposition might be neglected here. Nonetheless, older depositions might have accumulated at depth during “acidic rain times” and still show a great impact on the ground and stream waters as it is desorbed/“washed out” from the regolith. Otherwise, high sulfate concentrations in SS (increase with depth) and GW, might correspond to a natural source within the regolith, such as weathering of pyrite and gypsum (which are a priori scarce in our system but might be formed from atmospheric deposits) and other secondary minerals or organic matter decomposition, which content is very high in the catchments soils (see section 1.1.1.). However, the uncertainty about sulfate rich minerals formation and the limited OM mineralization expected in the saprolite suggest that old sulfate deposits of past acidic rains are the most probable source of SO_4^{2-} in our regolith and waters. Previous studies have shown that SO adsorbed in soils after strong episodes of acid rain are today in desorption phase due to the lower concentrations in R and TF (Heijden et al., 2011). In fact, nowadays the lower acidity of precipitation combined with the higher concentrations in soils allow the system to release part of the SO through a hysteretic desorption process (Heijden et al., 2011). In our case, sulfate might have initially accumulated in the soil and then, as it started desorbing, migrate to deeper saprolite layers. At this point it may accumulate and be newly released into the stream as the water table fluctuates and the connectivity between the subsurface compartments and the stream increases.

Weathering and redox processes in the light of REE

SS and shallow groundwaters (GW1) are characterized by chloride to sulfate compositions. These waters are clearly affected by TF and vegetation nutrient cycles (Fig.4.28 and 4.8). SS and GW1 have high REE concentrations but different PAAS distributions, indicating different processes are responsible for their geochemical composition (e.g.: vegetation nutrient cycles and weathering). While SS samples tend to present big MREE enrichments and positive Ce anomalies, GW1 shows a bit smaller MREE enrichments and strong negative Ce anomalies. It is well known that preferential mobilization of Ce from the soil particles to the solutions occurs under reducing conditions, which might be triggered in the organo-mineral soil horizons due to biological activity and/or micropore water saturation processes (Laveuf et al., 2012; Laveuf and Cornu, 2009). Indeed, the positive Ce anomaly found in the soil solution at 20 and 40 cm depth often disappears or even inverts at 60 cm depth (Fig.4.12). Below 60 cm depth, root density and biological activity significantly decrease. On the other hand, GW1 Ce negative anomalies might be due to Ce precipitation from the solution under oxidizing conditions in the form of cerianite (Ce(IV)O_2), on Fe and Mn (hydr)oxides (Braun et al., 1998; Dia et al., 2000; Gruau et al., 2004; Steinmann and Stille, 2006). Similarly, also suspended load and soil particles (e.g; clays) can be sites for the oxidation of Ce. Due to their high cation exchange capacity, these particles might easily adsorb Ce, which would then become depleted in the dissolved load (Braun et al., 1998; P. Stille et al., 2006). The saprolite at the GW1 depth level does not show Ce anomalies (see section 3.1.2) and, thus, an origin from the rock REE composition is not probable (Smedley, 1991). However, it must be noted that the strong REE enrichments described for the bottom of the PPSD in the regolith chapter (3) might be in general responsible for the high concentrations observed in GW1 -excepting Ce, which is depleted due to its particular redox behaviour and seems to be pH and alkalinity dependent (Gruau et al., 2004). Supportive is the fact that GW1 is the least alkaline water and has the most negative Ce anomaly, indicating that weathering reactions are not the major control.

LREE are known to be particularly sensitive to increases in pH, becoming more easily complexed or adsorbed in surfaces than HREE and, therefore, favouring HREE enrichments in solutions (Sholkovitz et al., 1994). While (La/Yb)N ratios of SS and most groundwaters show a weak positive relationship with pH, GW1 shows negative correlations, indicating that pH is a controlling factor for the REE concentrations and fractionation in these waters (Fig.4.16 and 4.19). Compared to major rivers of the world, with (La/Yb)N ratios between 1.2 and 0.4 for pH ranges of 4.5 to 7 respectively (Goldstein and Jacobsen, 1988a,b; Elderfield et al., 1990; Gaillardet et al., 1997), our GW1 waters plot at pH values between 5 and 6.5 in a subparallel trend with lower (La/Yb)N ratios between 0.2 and 0. These values are similar to the ones observed by Hissler et al. (2016) in industrialized Luxembourg rivers during low flow, and associated to soil water.

The higher abundance of cations, and Ca^{2+} and Mg^{2+} in particular, in the GW waters correlates with a higher content in bicarbonate, but also with silica, as well as with the higher electrical conductivity and pH, pointing to important weathering processes (Fig.4.28). However, GW2, GW3, GW5, GW6 and GW7 have lower REE concentrations and less pronounced negative Ce anomalies than GW1. This is probably due to slightly more reducing conditions (at least seasonally) which inhibit the massive Ce precipitation. GW7 and GW6 REE enrichments compared to the rest of the deep groundwaters might be due to the fact that these wells are located in the plateau landscape unit and drain weathering front zones, similar to GW1. Alternatively, the varying Ce anomaly in the different groundwaters might simply be the result of a relative immobile Ce compared to the more mobile other REE which are more or less enriched in function of the surrounding rock-aquifer (e.g. bottom of PPSD).

Higher REE concentrations along with high DOC values (Fig.4.15) might indicate the impact of greater bioactivity (mainly in summer) which enhances weathering activity, especially in the SS and the riparian area (Dia et al., 2000; Gruau et al., 2004). HREE tend to form more stable complexes with organic ligands than LREE due to higher stability constants (Byrne and Li, 1995). The decrease of (La/Yb)_N ratios and, thus, the increase of HREE with increasing DOC in the SS and GW1 samples (Fig.18-a-b) suggests that organic complexation is here responsible for LREE/HREE fractionation (Tricca et al., 1999). On the other hand the distribution observed for the SW samples excludes any relationship between HREE enrichment and DOC. The few spring waters (SP) sampled in winter show a very strong negative Ce anomaly, which might be explained either by a contribution from GW1-like oxidized aquifers and/or Ce precipitation at the spring, prior the exit to the stream, due to the oxidizing conditions. However, SW shows REE patterns similar to those of the “deep” GW and the RP, with a much smaller negative Ce anomaly than SP. This observation indicates that SW has a more important contribution from the waters with smaller negative Ce anomalies or even positive, as it is shown in the time series (Fig.4.12). Additionally, we may hypothesize that the riparian zone (RP) can buffer and homogenize the Ce anomaly signature of the different inputs to the stream, and give streamwater a rather stable Ce anomaly with only punctual positive or negative peaks. According to Dia et al. (2000), smaller negative or positive Ce anomalies can occur in swampy areas rich in OM like our riparian zone even under oxic conditions due to the complexation of Ce(IV) with OM and/or the adsorption of precipitating cerianite onto organic colloids. The importance of the colloidal phases for the REE behaviour in water would need to be further explored with different pore size filtration experiments. However, since we filtered at 0.45 μm , we may assume that our waters are strictly speaking not only dissolved load but also contain small particles like colloids (Davranche et al., 2013; Dia et al., 2000; Gaillardet et al., 2003).

Reactivity and connectivity of the system

According to stable isotope data, the Weierbach catchment behaves as an open and well-connected system, where rain or throughfall signatures are integrated by soil solutions and these quickly impact ground and stream waters. Other than this, the $\delta^{18}\text{O}$ signatures do not allow for a clear distinction of contributing end members. However, other parameters like pH, EC, alkalinity or the combined geochemical compositions do allow further assessment of the hydrological functioning of the system.

During the dry periods, groundwater alkalinity is more elevated, indicating a greater weathering activity which is probably related to longer residence times and smaller surface or upper-subsurface contributions (less dilution). Hence, groundwaters develop a higher resistance to pH changes and, consequently, greater buffering capacity. The buffering of any precipitation input in the deeper groundwaters (SP compartment) affects the mobility of ions in the subsurface and stream systems and implies greater differences of pH and EC between the surface/upper-subsurface waters and SW. This is particularly clear during the dryer periods, when RP, SW as well as the waters from the wells GW2 and GW3 at the bottom of the catchment become also more carbonated, similar to the deep plateau waters of GW5.

On the other hand, higher catchment connectivity triggered by wetness conditions may allow important contributions from the upper subsurface to the stream. This suggestion is supported not only by the changes in SW alkalinity, pH and EC but also in whole geochemical composition, which becomes more similar, under these conditions, to that of SS and the shallow GW1.

Finally, the event scale sampling allowed recognising important contributions of surface and upper-subsurface waters during peak flow conditions. Namely TF, SS and GW1 seemed to reach the bottom of the catchment through a quick-flow and yield enrichments of Pb, Rb and REE in SW during the first discharge peak. Since Pb is strongly enriched also in the deep groundwaters, we cannot decide whether a lateral subsurface flow or a vertical preferential flow is the responsible for the enrichments in the stream. However, REE are likely to originate from waters draining weathering front zones, as this has been shown to be extremely labile and only SS and GW1 show highest concentrations.

4.3 Conclusion

In this study, major and trace element data as well as the stable isotopes of O and H and physico-chemical parameters such as alkalinity, pH and electrical conductivity (EC) are used to characterize the waters of the Weierbach catchment. Throughfall, soil solutions, groundwaters and streamwaters are monitored during different hydrological conditions: low flow or dry

conditions, and high flow or wet conditions. The application of these tracers allows a first link to the geochemistry of the different regolith compartments and the identification of 3 to 4 geochemically different hydrological end members:

- 1) Precipitation (R, TF), characterized by mostly chlorinated compositions with enrichments in Pb and Sb linked to atmospheric inputs and in Rb, DOC and K among others, associated to vegetation nutrient cycling.
- 2) Shallow subsurface waters (SS, GW1), characterized by precipitation-like chlorinated to sulphate compositions with REE enrichments associated to the weathering of the PPSD horizons, notably in the lowermost part (PPSD4).
- 3) “Deep” groundwaters and riparian waters, which are characterized by chlorinated/sulphate to carbonated compositions and can at the same time be subdivided in:
 - a. the deep plateau and upper hillslope groundwaters (GW5, GW6, GW7), strongly dominated by the mineral weathering driven by the groundwater table fluctuation, but also by surface inputs, as evidenced by high DOC and Pb concentrations.
 - b. the catchment bottom groundwaters (GW2, GW3) and riparian waters (SP, RP) dominated by weathering products, but not necessarily linked to water table fluctuation processes.

The comparison of isotopic and geochemical results of waters on the long term- and storm event- time scales with hydrometrical and meteorological data suggests that riparian and stream waters chemical composition spreads between that of deep groundwaters in the plateau at dry conditions (also found in the groundwaters of the hillslope bottom) and that of the upper-subsurface waters (SS and GW1) during wetness conditions. This suggests the importance of seasonal subsurface flow contributions.

Chapter 5. Water-rock-atmosphere interactions and water circulation patterns at catchment scale

The work presented in this chapter is in preparation to be submitted as:

- Moragues-Quiroga, C., Hissler, C., Stille, P., (*in preparation*). Controls of atmospheric and mineral derived contributions on the hydrochemical profile of a natural small headwater catchment.
- Moragues-Quiroga, C., Hissler, C., Stille, P., (*in preparation*). Water circulation patterns at the small catchment scale: evidence from $\delta^{18}\text{O}$, Sr, U and Pb isotopes.

Major parts of the following are identical in word and content with the prepared drafts.

Introduction

Rain- and surface waters infiltrate the regolith system taking different flowpaths, resulting in shorter or longer interactions with organic matter and labile mineral phases it encounters along these pathways until it leaves this system and enters the stream. The scope of this chapter is to elucidate the main water-regolith interactions controlling the composition of the hydrological end member's and their eventual impact on the hydrochemistry of the stream. We will therefore combine the previously acquired information on the main regolith and hydrological end members and add Sr-Nd-Pb-U isotopic informations on a selection of waters in order to identify the labile mineral phases in play. The very fine grained slate of the Weierbach catchment does not allow clean mineral separation and, thus, the analysis of the chemical and isotopic compositions of its mineral constituents, the potential sources of major and trace elements in the waters. However, solid material, in the present study sediments and soils, can be considered to contain two major phases, a leachable phase and a residual, unleachable one (Sholkovitz et al., 1994). The leachable mobile phase includes all elements which participate in solid-liquid

interactions (Steinmann and Stille, 1997; Stille and Clauer, 1994). Therefore, leaching experiments allow imitating weathering and water-regolith exchange processes, where the leachates chemical composition might correspond roughly to that of the circulating waters and the residual phase that of the regoliths alteration products (Aubert et al., 2001; Stille and Shields, 1997). We therefore performed sequential leaching experiments on fresh bedrock, saprolite and soil materials in order to identify water-rock interaction processes and distinguish them from possible impacts of atmospheric deposition.

5.1 Results

5.1.1 Chemical characterization of the labile and residual pools of the system

Major and trace element data of the leachates and residues are shown in Appendix 13. The 0.05N HAc leachate (L1) desorbs and/or dissolves mainly Ca, particularly in the SP samples, as well as Mn, Co and Zn probably adsorbed on the surfaces of soil particles (Fig.5.1-a). The L1 step is also able to remove a significant amount of Pb from the SP5 bedrock sample. The 1N HCl leachate (L2) dissolves a Ca-P bearing phase enriched in MREE and Fe/Mn- secondary carbonates and/or oxides and hydroxides, hereafter grouped and abbreviated as oxides, and Pb (Fig.5.1-b). Compared to L1, L2 is also efficient on the recovery of Mg, Sr and U. The 2N HNO₃ (L3) leachate mainly attacks the transition elements Mn, Co and Cu, together with some LREE-enriched P-bearing phases (Fig.5.1-c). The fact that the L3 step presents the weakest yields can be explained by (i) the high leaching efficiency of the L2 step, (ii) the attack of a refractory OM- enriched phase and (Steinmann and Stille, 1997) (iii) the un-adaptation of the attack regarding the leachable phase of the regolith materials, by which L3 might have been too aggressive and already attacked the (residual/refractory) primary mineral phases.

The total content recovery is generally under 100%, but is nonetheless highly variable for the different elements and regolith samples (Fig.5.1-d). Only Ca total yield surpasses the 100% for SP4, SP5 and notable SP3. Duplicates of these bulk and leachate samples leached with different methods (acid/alkaline) yield the same results and, thus, allow excluding any analytical artefact. Hence, the higher recovery of Ca in these samples can be due to heterogeneities in the bulk sample aliquots. Interestingly, not only Ca but also P, “redox-sensitive” and rare earth elements have been more intensively leached in the SP compartment than in the PPSD. This is also true for Pb, which is on the other hand also enriched in the uppermost PPSD1 L2 samples.

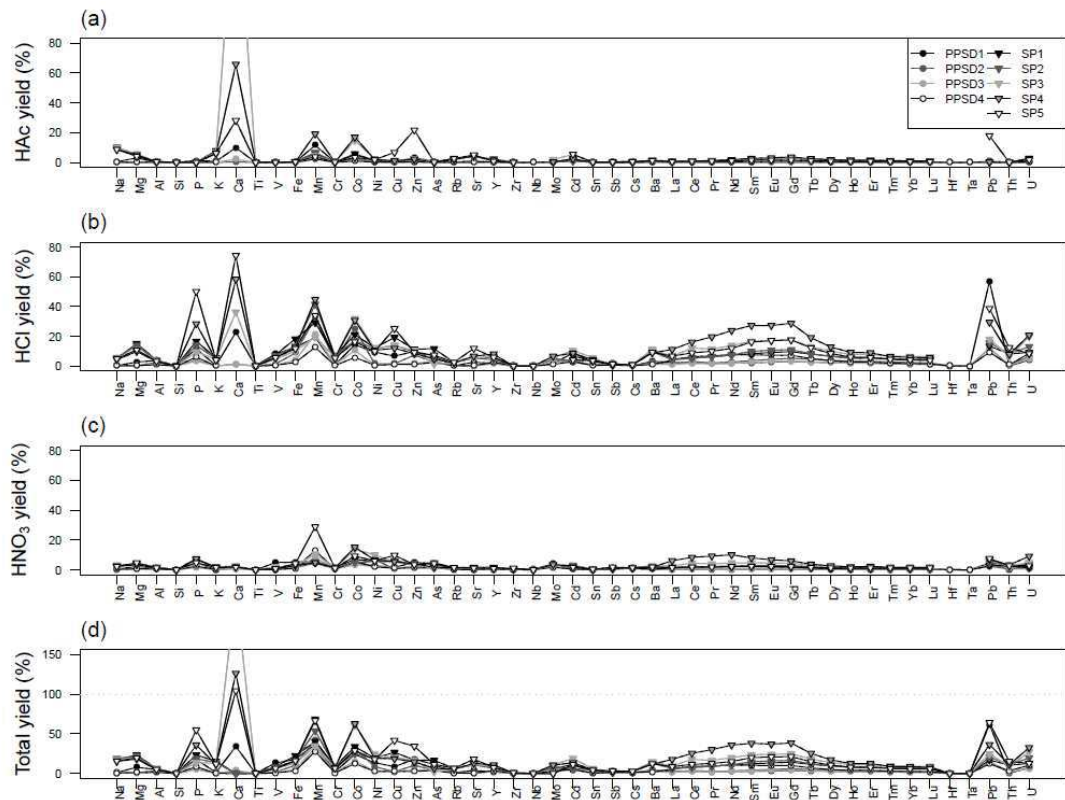


Figure 5.1. Major and trace element extraction yields (% of the total mass) for (a) L1 leachates (0.05N HAc), (b) L2 leachates (1N HCl) and (c) L3 leachates (2N HNO₃). (d) Total extraction yield.

REE fractionation

The Post Archean Australian Shales (PAAS) normalized REE distribution patterns of the regolith bulk and leachate samples are shown in Figure 5.2. Figure 5.3 shows the depth patterns of the corresponding LREE and MREE enrichments represented by PAAS normalized La/Yb and Eu/Yb ratios respectively, as well as those of the Ce anomalies, calculated as the enrichment of Ce with respect to other LREE (namely La and Pr) normalized to PAAS with the equation $[CeN/CeN^* = CeN/(0.5LaN + 0.5PrN)]$. As it was already shown in Moragues-Quiroga et al. (2017), the bulk sample patterns manifest LREE and notably MREE enrichments, especially in PPSD4 and in the redox zone SP3-4 samples, as well as a positive Ce-anomaly (1.05) in SP3 (Fig.5.2-a, 5.3 and Fig.3.4-Chapter 3). The patterns of L1 extracts show similar to the bulk ones, important enrichments in LREE for the PPSD samples and MREE for the whole profile. L1 extracts show notably stronger Ce anomalies in PPSD2 (1.26) and SP3 (1.45) samples than the bulk (0.97 and 1.05 respectively) (Fig.5.2-b and Fig.5.3). L2 patterns show greater LREE enrichments with respect to HREE in PPSD1, PPSD4 and SP samples (notably SP4 and SP5), and a stronger positive Ce anomaly for PPSD2 (1.75), PPSD3 (1.36) and SP3 (1.39) (Fig.5.2-c and Fig.5.3). Even stronger LREE enrichments with respect to HREE are observed in the L3 extracts of PPSD4 and SP samples (notably SP4). Also higher in this extract

are the previously observed Ce anomalies, reaching 3.58, 2.26 and 1.46 for PPSD2, PPSD3 and SP3 respectively (Fig.5.2-d and Fig.5.3). The residues generally show PAAS like REE patterns, with small Nd depletions and Eu enrichments (Fig.5.2-e and Fig.5.3). In summary, the extracts seem to show an evolution from MREE to LREE-enriched phases; particularly for the PPSD4 and SP samples, as well as towards increasing Ce anomalies for PPSD2, PPSD3 and SP4.

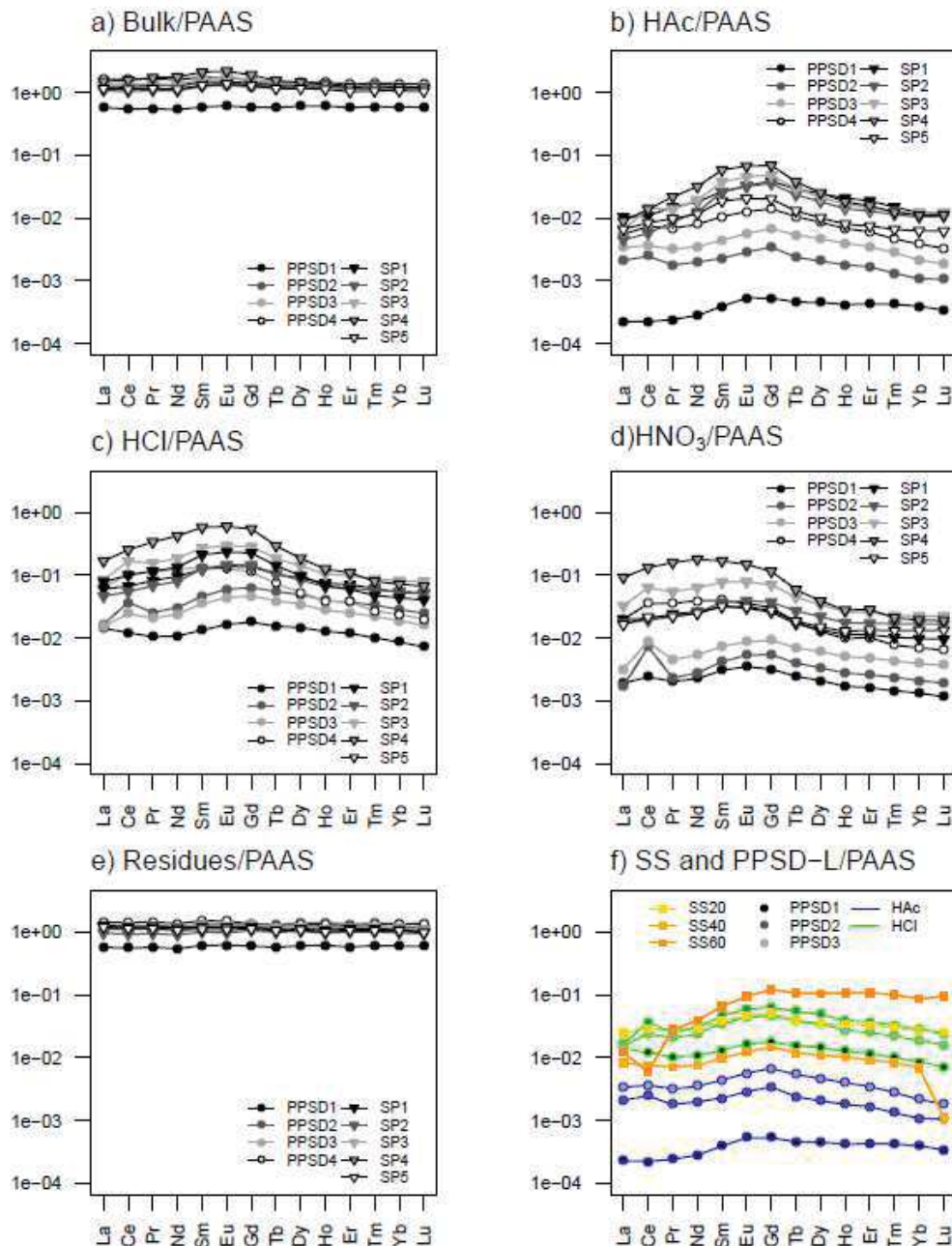


Figure 5.2. PAAS-normalized REE distribution patterns of (a) bulk regolith samples, (b) L1 leachates (0.05N HAc), (c) L2 leachates (1N HCl), (c) L3 leachates (2N HNO₃), (d) residues, and (e) soil solutions (SS20,SS60 and comparison with PPSD1-3 leachates).

The convex REE patterns characterized by high Sm/Nd ratios in the L1 and L2 extracts are similar to those found in marine and granite-derived apatites (Aubert et al., 2001; Shields and Stille, 2001). Distinctive is in the leachates case the tendency towards positive Ce anomalies, which were already perceptible in the whole rock samples.

The soil solutions collected at 20, 40 and 60 cm depth at the same site present, on average, very similar REE distribution patterns as the PPSD leachates, proving a good experimental performance of the natural soil (PPSD) leaching (Fig.5.2-f). SS20 and SS40 patterns are particularly similar to those of PPSD2 and PPSD3 L1-L2 extracts, whereas SS60 reproduce more closely the patterns of PPSD1 L1-L2. These similarities are not observable for the groundwaters collected from GW1 and GW5 wells (200 and 735 cm deep respectively) at the same site, nor for the ones collected at the other sampling sites of the catchment (Fig.4.11). All of them show rather negative Ce anomalies and MREE enrichments. Similar REE patterns can be observed for the RP, SP and SW (Fig.4.11).

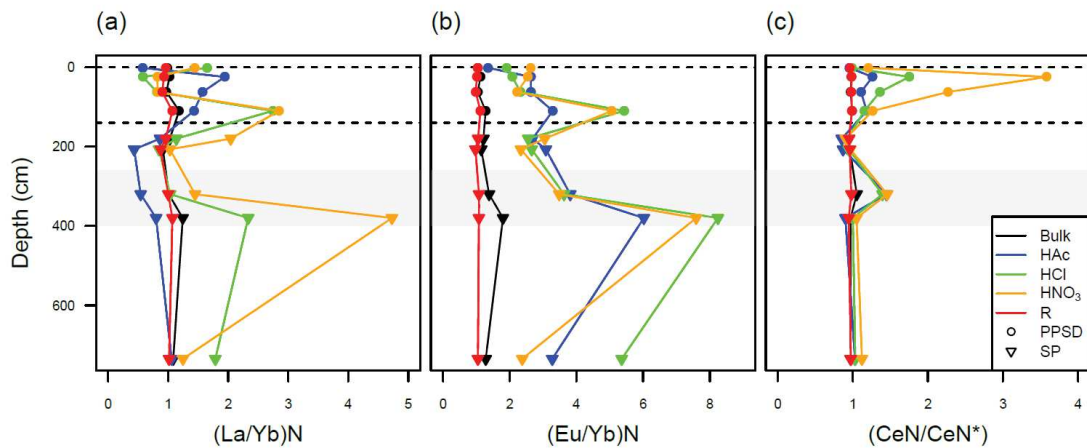


Figure 5.3. Depth dependent patterns of PAAS-normalized (a) LaN/YbN, (b) EuN/YbN ratios and (c) Ce anomaly (CeN/CeN^*) for bulk regolith samples (PPSD and SP), L1 (0.05N HAc), L2 (1N HCl) and L3 (2N HNO_3) leachates, and residue (R) samples (dashed lines: lithic discontinuities referred in Chapter 1; shaded area: redox sensitive horizons).

5.1.2 Sr and Nd isotopic characterization of leachates and comparison with the waters

$^{87}Sr/^{86}Sr$ isotopic compositions of leachates, residues and whole rocks are plotted against the corresponding Rb/Sr ratios (Fig. 5.4) and compared with those of waters (see also Appendix 14). L1 and L2 leachates of SP samples plot together on a mixing line which reaches with lower Rb/Sr ratios and comparatively low $^{87}Sr/^{86}Sr$ ratios the field of the studied water samples (Fig.5.4). The corresponding L3 leachates define closely associated a subparallel trend with higher Rb/Sr ratios. The bulk and residual SP and PPSD samples show comparatively higher Rb concentrations and, thus, higher Rb/Sr ratios similar to those of the L3 leachates of SP. No clear

mixing relationships are recognizable for the PPSD leachates. Nevertheless, they show an evolution from the waters field towards bulk and residual regolith samples, with respectively lower Sr concentrations and isotopic compositions.

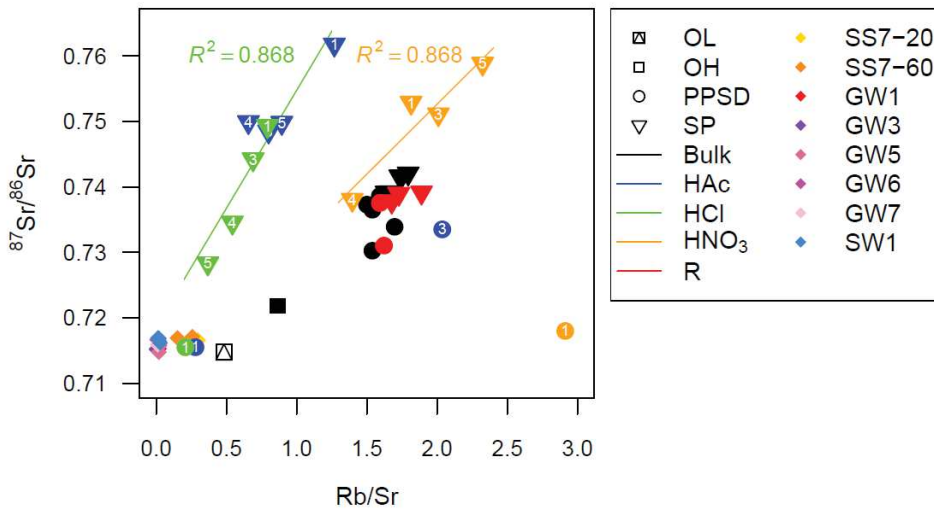


Figure 5.4. Sr isotopic composition of the organic horizons, bulk, leachate and residue regolith samples and a selection of waters. Numbers inside leachate symbols correspond to regolith sample number as reported in Chapter 3.

Similarly the Sr isotopic compositions and Rb/Sr ratios of some of the SP leachates are correlated with the corresponding Ca/P ratios. The Ca/P ratios of the SP L1 leachates range between 1000 and 4000 and are not correlated with the corresponding $^{87}\text{Sr}/^{86}\text{Sr}$ nor show a particular depth pattern (Fig.5.5-a). The very high Ca/P ratios indicate that the L1 leachates are dominated by Ca- rather than P- bearing mineral phases. The Ca/P ratios of the L2 and L3 SP leachates, however, are much lower ranging between 0.1 and 0.7 for L3 and 0.4 and 2.5 for L2 (Fig.5.5-b). Only the L2 SP leachates show a correlation with the Sr isotopic compositions, which is additionally depth dependent. From the top to the bottom of the SP profile the Ca/P ratios increase and the Sr isotopic composition decrease, showing highest Ca/P ratios of 1.36 and 2.44 at lowest $^{87}\text{Sr}/^{86}\text{Sr}$ ratios (0.73455 - 0.72832 respectively) for SP4 and SP5 (fresh bedrock). The PPSD leachates are contrarily to those of SP strongly scattered (**not shown**). Nevertheless, one recognizes that higher Ca/P ratios go along with lower $^{87}\text{Sr}/^{86}\text{Sr}$ and Rb/Sr ratios, which is generally the case for the uppermost (PPSD1) and lowermost (PPSD4) soil samples. For comparison, the Ca/P ratios of P bearing minerals such as monazite, Ca-rich florencite (crandallite) and apatite range between 0.14 and 0.34, 0.05 and 0.07, and 1.7 and 2 respectively (Berger et al., 2014; Lauf, 2014; Raynaud et al., 2001b; Uher et al., 2015).

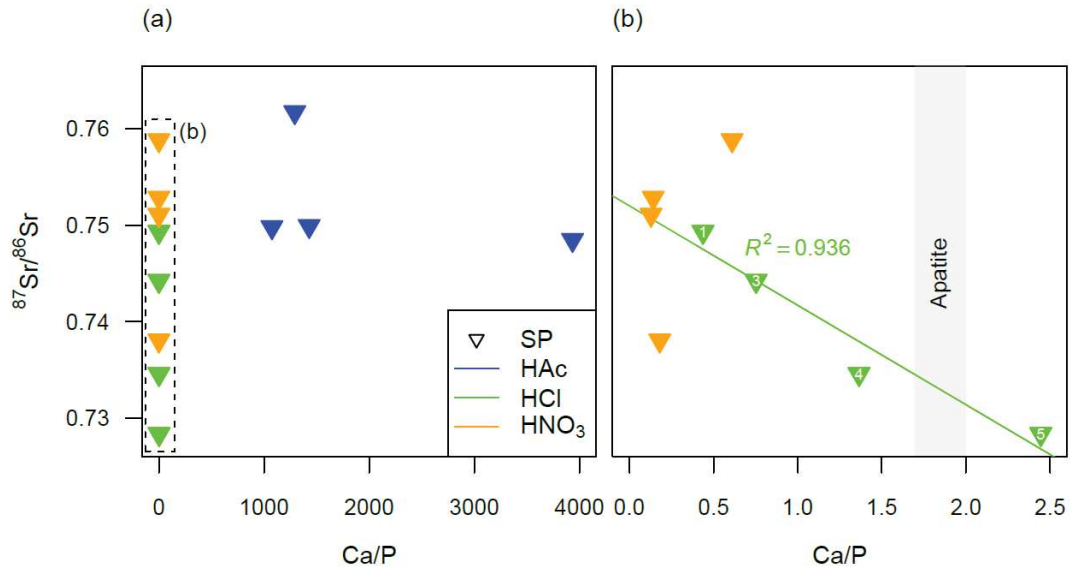


Figure 5.5. $^{87}\text{Sr}/^{86}\text{Sr}$ ratios as a function of Ca/P ratios for the SP leachates (a). (b) Zoom of L2 and L3 SP samples including apatite reference Ca/P ratios. Numbers inside leachate sample symbols correspond to regolith sample number as reported in Chapter 3.

In contrast to the Ca/P ratios, the Fe concentrations of the L2 and L3 leachates are positively correlated with their $^{87}\text{Sr}/^{86}\text{Sr}$ ratios (Fig.5.6-a). Thus, leachates with high Fe concentrations show higher $^{87}\text{Sr}/^{86}\text{Sr}$ than leachates with low Fe concentrations. While the composition of the L2 SP leachates is clearly depth dependent, L3 shows only a depth pattern from SP1 to SP4, being SP5 composition more similar to that of SP1. The Sr isotopic ratios of L2 SP samples show a similar but weaker –depth-dependent- positive correlation with Al concentrations (Fig.5.6-b). A clear correlation with Mg cannot be observed for L2 SP samples, but the increase in $^{87}\text{Sr}/^{86}\text{Sr}$ ratios with decreasing depth seems to come along with small Mg enrichments (Fig.5.6-c). Bulk and residue regolith samples show a stronger correlation between Fe, Al and Mg and the Sr isotope ratios than the leachates (not shown).

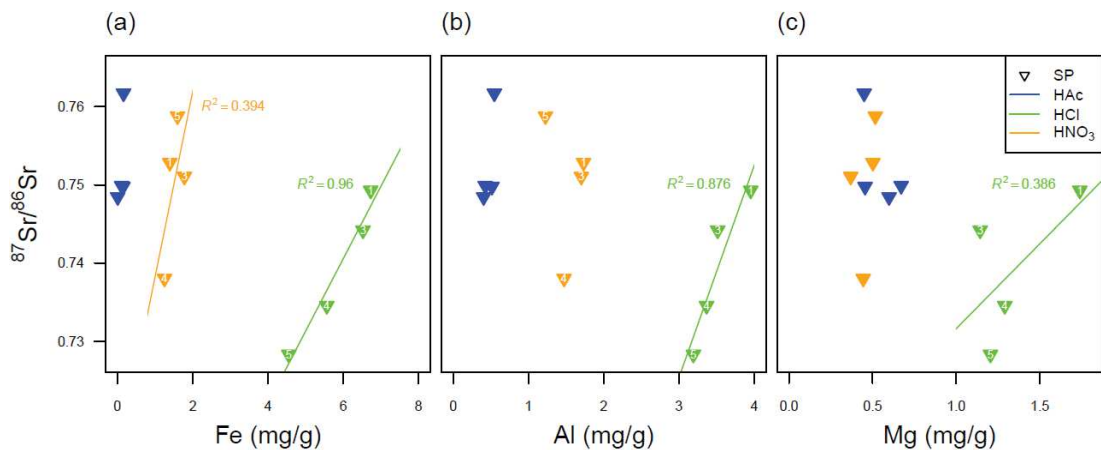


Figure 5.6. $^{87}\text{Sr}/^{86}\text{Sr}$ ratios of the SP leachates as a function of the corresponding concentrations in (a) Fe, (b) Al, and (c) Mg. Numbers inside leachate sample symbols correspond to regolith sample number as reported in Chapter 3.

$^{143}\text{Nd}/^{144}\text{Nd}$ isotopic compositions of leachates, residues, whole rocks and waters are plotted together against the corresponding Sm/Nd ratios (Fig.5.7). Lowest Sm/Nd ratios show the residues being closely associated to the whole rocks. The leachates have generally higher ratios and $^{143}\text{Nd}/^{144}\text{Nd}$ isotopic compositions. The waters are among the samples with the highest Sm/Nd ratios and $^{143}\text{Nd}/^{144}\text{Nd}$ isotopic compositions and are isotopically closest to L1 and L2 of SP samples and PPSD3 leachates. The PPSD1 leachates show generally lower Sm/Nd ratios and Nd isotopic compositions and plot closer to the L3 leachates of SP and the atmospheric dusts and the litter collected in the Weierbach. Compared to the dusts collected inside the forest, the atmospheric dusts collected outside the catchment in the agricultural land have much higher $^{143}\text{Nd}/^{144}\text{Nd}$ ratios, which are almost identical to those of the fertilizers studied by Aubert et al. (2002) (0.51243 vs. 0.51231-0.51234 respectively).

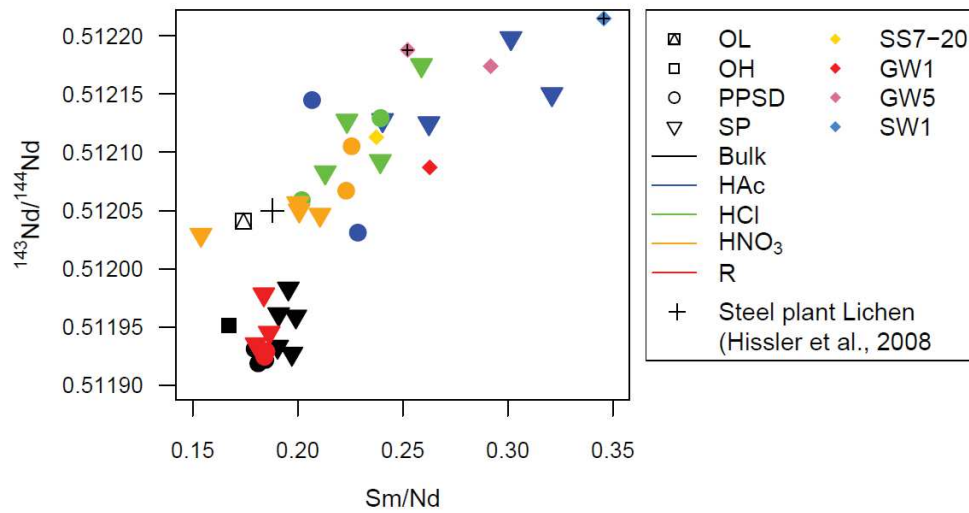


Figure 5.7. Nd isotopic composition of the organic horizons, bulk, leachate and residue regolith samples, a selection of waters, and a lichen sample from Hissler et al. (2008). Crosses inside water symbols indicate sampling in dry conditions.

Similar to the Sr isotopic compositions also the $^{143}\text{Nd}/^{144}\text{Nd}$ isotope ratios of the SP L2 leachates are correlated with the corresponding Ca/P ratios (Fig.5.8-a). However, they are not correlated with the corresponding Sm/Nd ratios but at least in the case of SP L2 leachates with their Rb/Sr ratios (**not shown**). Monazite, crandallite and apatite have, for reference, Sm/Nd ratios between 0.13 and 0.38, 0.02 and 0.26, and 0.3 and 0.5 respectively (Aubert et al., 2002b; Faure, 1977; Garçon et al., 2014; Henderson et al., 2010; McFarlane and McCulloch, 2007) and Rb/Sr ratios up to 0.88 for monazite and generally smaller than 0.05 for apatite and florencite/crandallite. L1 and L3 leachates of the SP samples do not show such a correlation. The Nd isotopic compositions of the PPSD leachates manifest no clear trends (Fig.5.8-b) since each leachate set consists of only two samples. Nevertheless, the data suggest that increasing P contents go along with decreasing $^{143}\text{Nd}/^{144}\text{Nd}$ isotopic compositions.

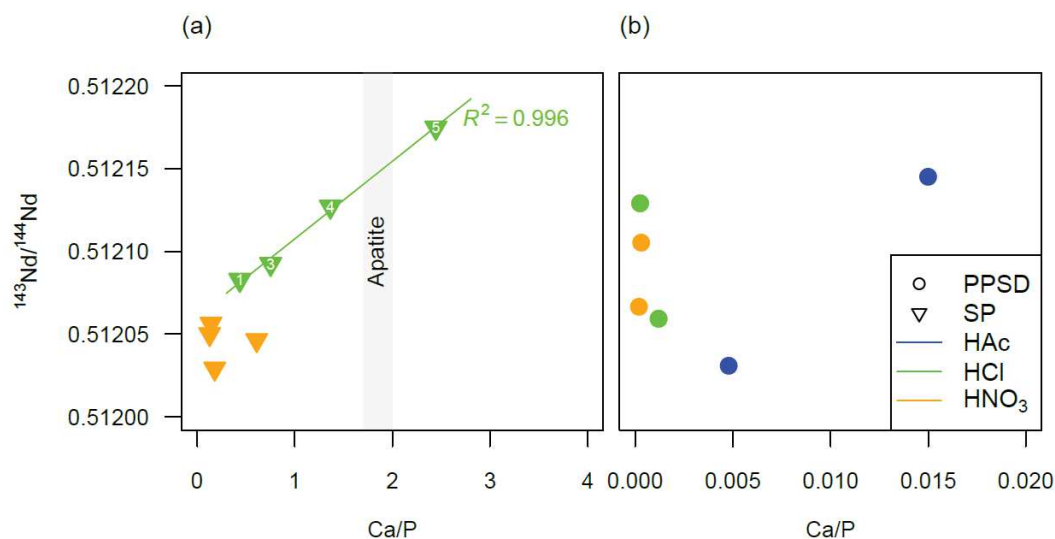


Figure 5.8. $^{143}\text{Nd}/^{144}\text{Nd}$ ratios as a function of Ca/P ratios for (a) the L2 and L3 SP leachates including apatite reference Ca/P ratios, and (b) PPSD leachates. Numbers inside leachate sample symbols correspond to regolith sample number as reported in Chapter 3.

5.1.3 Pb and U isotopic characteristics of leachates whole rocks and waters

The $^{208}\text{Pb}/^{204}\text{Pb}$ and $^{206}\text{Pb}/^{204}\text{Pb}$ isotope ratios of whole rock, residues, leachates and waters are shown in Fig.5.9 (see also Appendix 14). They define a mixing trend between the regolith whole rock and residue samples, with high $^{208}\text{Pb}/^{204}\text{Pb}$ and $^{206}\text{Pb}/^{204}\text{Pb}$ (higher than 38.6 and 18.72, respectively), and gasoline soot with low radiogenic values (36.72102 and 16.969, respectively; M. Lahd Geagea et al., 2008). The uppermost PPSD whole rock and leachate samples and the water samples (SS and SW) show Pb compositions similar to those of atmospheric dusts and lichens collected around the catchment and close to industrial areas respectively (Hissler et al., 2008).

The $^{206}\text{Pb}/^{207}\text{Pb}$ and $^{87}\text{Sr}/^{86}\text{Sr}$ isotope ratios of the same samples are shown together in Fig.5.10. Once again, two different fields are recognizable. Most of leachates, residues and WR manifest comparatively high $^{87}\text{Sr}/^{86}\text{Sr}$ ratios ranging between 0.728 and 0.76 and high $^{206}\text{Pb}/^{207}\text{Pb}$ scattering around 1.2. They define a so-called "natural" field according to previous studies (Lahd Geagea et al., 2008). Some of the PPSD leachates (uppermost soil horizon) and organic samples (OH, OL) plot together with the studied water samples in a field with much lower $^{87}\text{Sr}/^{86}\text{Sr}$ (<0.728) and $^{206}\text{Pb}/^{207}\text{Pb}$ (<1.2). They tend towards a field defined by anthropogenic emissions (traffic, industrial, urban) (Hissler et al., 2008; M. Lahd Geagea et al., 2008; Majdi Lahd Geagea et al., 2008).

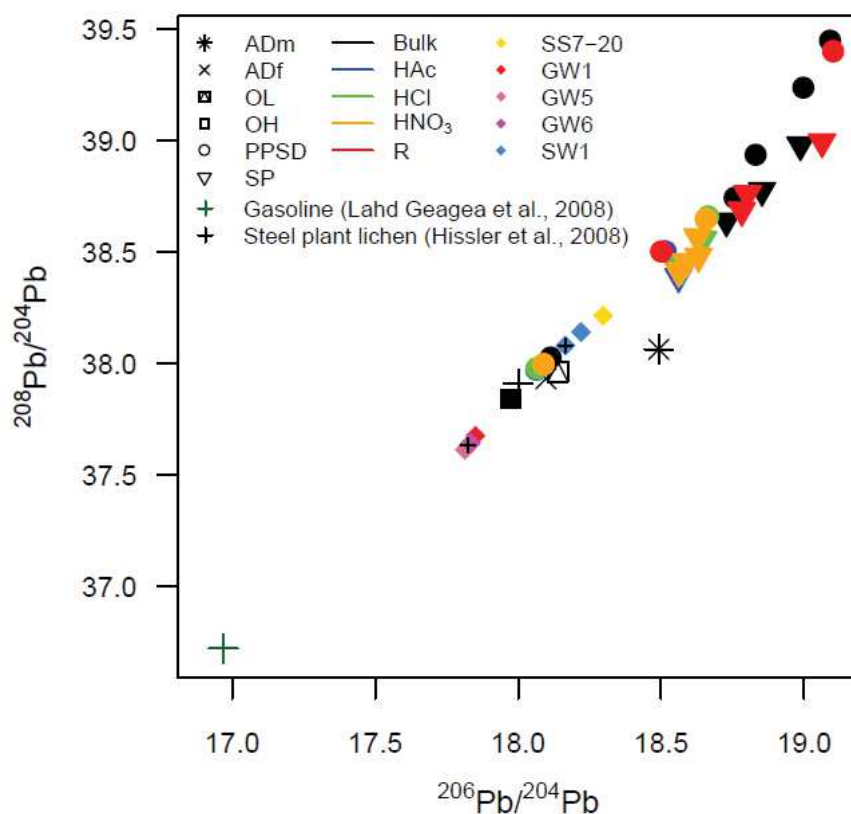


Figure 5.9. $^{208}\text{Pb}/^{204}\text{Pb}$ vs. $^{206}\text{Pb}/^{204}\text{Pb}$ for atmospheric dusts, organic horizons, bulk, leachate and residue regolith samples, a selection of waters, a lichen from Hissler et al. (2008) and gasoline soot reference from Lahd Geagea et al. (2008). Crosses inside water symbols indicate sampling in dry conditions.

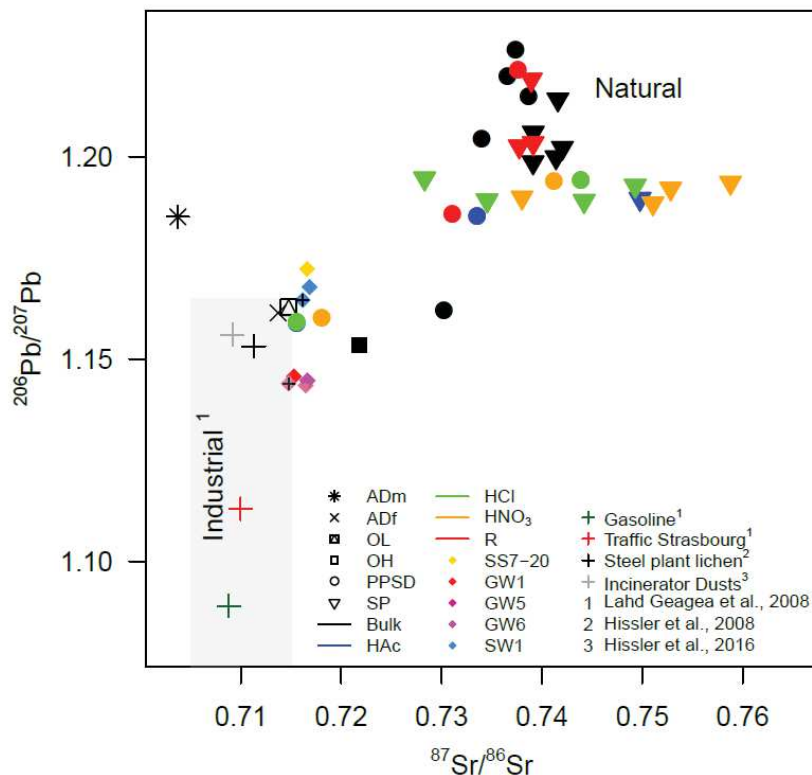


Figure 5.10. $^{206}\text{Pb}/^{207}\text{Pb}$ vs. $^{87}\text{Sr}/^{86}\text{Sr}$ for atmospheric dusts, organic horizons, bulk, leachate and residue regolith samples and a selection of waters. Industrial reference), gasoline soot and traffic isotopic signatures from Lahd Geagea et al. (2008), a lichen sample from Hissler et al. (2008) and incinerator dusts samples from Hissler et al (2016) are given for comparison. Crosses inside water symbols indicate sampling in dry conditions.

The $^{206}\text{Pb}/^{207}\text{Pb}$ isotope ratios are compared with the ($^{234}\text{U}/^{238}\text{U}$) activity ratios (Fig.5.11-a). WR and residues manifest at high $^{206}\text{Pb}/^{207}\text{Pb}$ ratios close to equilibrium $^{234}\text{U}/^{238}\text{U}$ activity ratios (= 1). Leachates with slightly lower $^{206}\text{Pb}/^{207}\text{Pb}$ (1.188-1.195) show a very important variation of their ($^{234}\text{U}/^{238}\text{U}$) activity ratios ranging between 0.7 and 1.7 indicating that ^{234}U can easily be mobilized. Even more disequilibrated are 2 water samples (GW1 and GW5 collected respectively during the event and in dry-base flow conditions) reaching at low $^{206}\text{Pb}/^{207}\text{Pb}$ a ($^{234}\text{U}/^{238}\text{U}$) activity ratio close to 2.3. Leachates of PPSD1 have $^{206}\text{Pb}/^{207}\text{Pb}$ ratios and ($^{234}\text{U}/^{238}\text{U}$) activity ratios between those of organic (OL, OH and Ah samples) and forest dust samples, SS and SW, and GW. This grouping is apparent also in Fig.5.11-b, where $^{87}\text{Sr}/^{86}\text{Sr}$ ratios are plotted against the U activity ratios. All SS samples plot in between the range of PPSD1 leachates, whereby decreasing $^{87}\text{Sr}/^{86}\text{Sr}$ ratios of all water samples are accompanied by increasing ($^{234}\text{U}/^{238}\text{U}$) activity ratios.

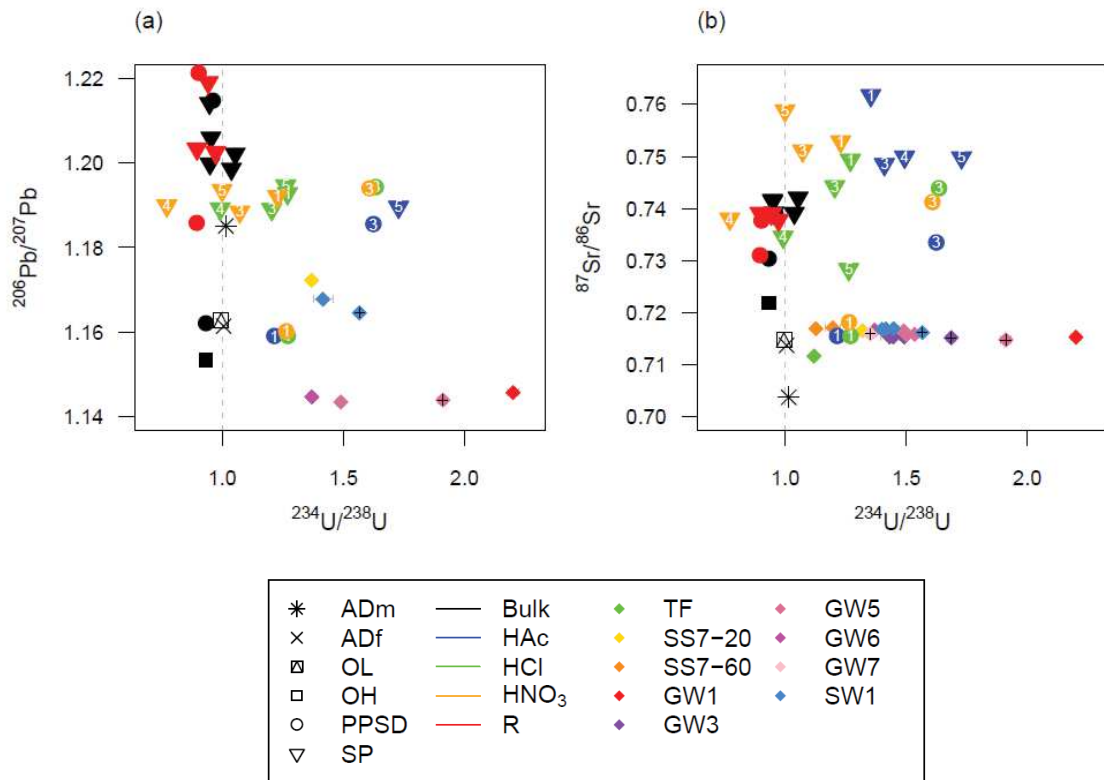


Figure 5.11. (a) $^{206}\text{Pb}/^{207}\text{Pb}$ vs. $^{234}\text{U}/^{238}\text{U}$ and (b) $^{87}\text{Sr}/^{86}\text{Sr}$ vs. $^{234}\text{U}/^{238}\text{U}$ for atmospheric dusts, organic horizons, bulk, leachate and residue regolith samples and a selection of waters. Numbers inside leachate sample symbols correspond to regolith sample number as reported in Chapter 3. Crosses inside water symbols indicate sampling in dry conditions.

5.2 Discussion

5.2.1 The chemical partitioning of Sr and Nd isotopes

In order to better understand the following discussion of the Sr and Nd isotopic compositions (IC) of the here studied rock system it is necessary and helpful to quickly recall a few basic informations on the behaviour of the Sr-Nd isotopes in a magmatic rock e.g. a granite, one of the potential sources of primary magmatic minerals and alteration products in sediments. Rb-Sr and Sm-Nd parent/daughter (P/D) systems show through the isochron diagrams that the respective Sr and Nd isotopic evolution of a granite and its minerals after formation from an isotopically homogeneous magma is time dependent (Fig.5.12a-b). Hence, a suite of cogenetic mineral phases which crystallized in this magma can be dated and their relative IC predicted according to their different parent/daughter (P/D) ratios (Faure, 1977). Different mineral phases crystallizing at the same time have the same Sr and Nd ICs but different P/D ratios. Then, as the time passes and assuming a closed system, the parents ^{87}Rb and ^{147}Sm decay in radioactive ^{87}Sr and ^{143}Nd daughters respectively. These decays gradually reduce the P/D ratios and increase the isotopic ratios, leading to the actual mineral phases which plot on the same line but have different IC and P/D ratios. The slope of the line is age-dependent and the line is called isochron, which indeed means that the minerals plotting on this line have the same age and initial IC. According to the Rb-Sr system, an isochron can be defined by a suite of principal rock-forming minerals with increasing Rb concentrations such as - in this order- apatites, feldspars and micas of the same initial rock ("Bulk"; Fig.5.12) leading with time to respectively higher $^{87}\text{Sr}/^{86}\text{Sr}$ ratios (Fig.5.12-a). In the Sm-Nd isochron diagram, on the other hand, these same minerals behave differently, being feldspars Sm depleted and thus closer to the initial rock $^{143}\text{Nd}/^{144}\text{Nd}$ ratio and apatites having very high Sm/Nd ratios and, consequently, comparatively high $^{143}\text{Nd}/^{144}\text{Nd}$ ratios (Fig.5.12-b).

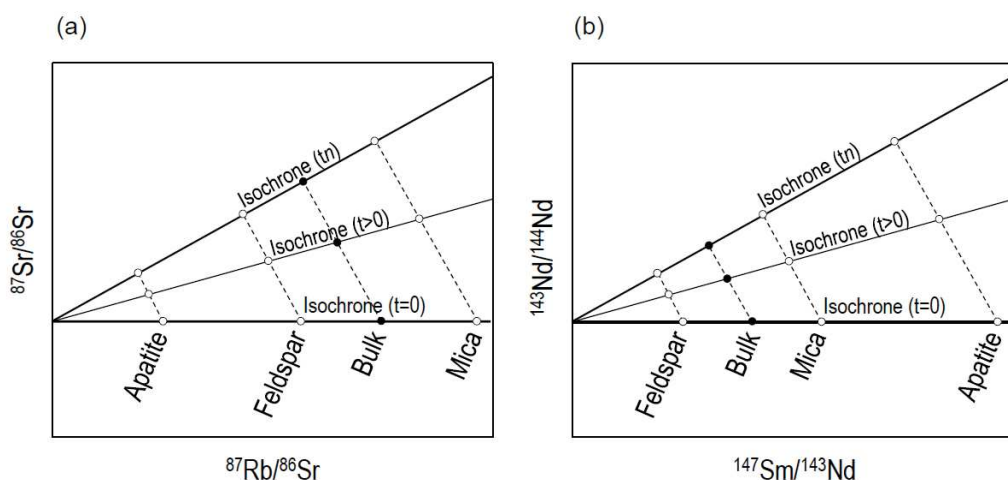


Figure 5.12. Schematic isochron diagrams for (a) Rb-Sr system and (b) Sm-Nd system for cogenetic apatite, feldspar and mica.

Relating the Sr and Nd isotope data of leachates with corresponding Rb/Sr, Sm/Nd, Ca/P ratios or element concentrations such as Ca, P, Fe or Al allows identifying labile adsorbed reservoirs and/or unstable, leachable mineral phases in the rock. Especially revealing in this respect are the L2 leachates of the SP samples. They plot on a mixing line with one mixing end-member at low $^{87}\text{Sr}/^{86}\text{Sr}$ (<0.728) and low Rb/Sr ratios (<0.37) (Fig.5.4). The correlations in Figs. 5.5 further suggest that this end-member is enriched in P and Ca and characterized by a high Ca/P ratio of 2.5 which is close to Ca-P-bearing mineral phases such as apatite (1.7-2) (Raynaud et al., 2001a). Since apatites contain only traces of Rb they carry very low Rb/Sr ratios, lower than those of other principal rock-forming minerals such as feldspars or micas of the same rock, and, thus, in a Rb-Sr isochron diagram they define the initial isotopic ratio of a rock. The L1 leachates of SP have in contrast to L2 very low P contents but at higher $^{87}\text{Sr}/^{86}\text{Sr}$ isotopic compositions and rather similar Ca concentrations, which results in high Ca/P ratios and thus L1 represents a labile adsorbed Ca reservoir (Fig.5.5a).

Apatites have very high Sm/Nd ratios (0.25-0.57) (Henderson et al., 2010) and, consequently, comparatively high $^{143}\text{Nd}/^{144}\text{Nd}$ isotope ratios compared to WR or principal rock-forming minerals. The L2 leachates of SP samples show Nd isotopic compositions which are similar to the Sr isotopic system correlated with Ca, P and Ca/P ratios. However, the Ca and P rich end-member show the highest $^{143}\text{Nd}/^{144}\text{Nd}$ isotopic composition (Fig. 5.8a) and, thus, confirm our suggestion that important quantities of at least Nd in the L2 leachates originate from the dissolution of apatite-like mineral phases.

Although apatite has not been directly identified in our system, it is known to be much dispersed and can be too small for direct observation (e.g. Stille et al., 2011, 2009). The detection of Ca-rich monazite and florencite (crandallite) in the regolith indicates that important quantities of P-(Ca)-REE bearing minerals exist. These mineral phases have much lower Ca/P ratios than apatite, and also lower Sm/Nd ratios, and thus do not represent the end member identified with the leachates. However, the observation of these primary minerals in the regolith gives evidence of the likely occurrence of dissiminated small grain secondary apatite, which matches with the identified low Sr and high Nd IC leachate end member.

Ca- and P- rich leachates (L1 and L2, respectively) have similar to the studied water samples highest Sm/Nd ratios and $^{143}\text{Nd}/^{144}\text{Nd}$ isotopic compositions (Fig.5.7). The WR samples, L3 leachates and residues have significantly lower Sm/Nd ratios and $^{143}\text{Nd}/^{144}\text{Nd}$ isotopic compositions. A similar sample distribution has been observed by Aubert and colleagues (2001) in a Sm-Nd isochron diagram of soils, bedrock (granite) and waters from the Strengbach catchment in the Vosges Mountains. In their study, the different samples define a scattered line with the waters showing the highest Nd isotopic compositions and Sm/Nd ratios and the soils the lowest. The Sm-Nd isotopic characteristics of their catchment waters are identical with those of apatites. It is interesting to note that in their study the leachate of (stream) suspended

loads carries also the isotopic signature of apatite and waters, whereas the residual phase tends to isotopic compositions of the bulk solid phases. In a similar way we suggest that our L1 and L2 leachates carry Nd isotopic signatures close to those of the circulating waters.

More information on the chemical partitioning at catchment scale yields the $^{143}\text{Nd}/^{144}\text{Nd}$ vs. $^{87}\text{Sr}/^{86}\text{Sr}$ isotope diagram (Fig.5.13). It allows elucidating the redistribution of Sr and Nd in the different rock-forming minerals and metastable phases like secondary carbonates (Aubert et al., 2002a; Stille et al., 2006). As it was explained before, Sr and Nd isotopic compositions of crustal rocks with granitic mineral composition are principally controlled by the presence of apatite, feldspars and micas. Apatite is for the Sr-Nd isotope system an important mineral phase since it is strongly enriched in Sr and REE (ca. 800 ppm and 1000 ppm, respectively; Aubert et al., 2001). Due to its comparatively high Sm/Nd and extremely low Rb/Sr ratios it is compared to other cogenetic mineral phases characterized by very high $^{143}\text{Nd}/^{144}\text{Nd}$ and very low $^{87}\text{Sr}/^{86}\text{Sr}$ ratios. Based on the results of our leaching experiments (Figs. 5.4, 5.5, 5.7, 5.8) we estimate an apatite-like Sr and Nd isotopic composition of <0.725 and >0.5122 , respectively. The stream water has the highest Nd isotopic composition. Therefore, we suggest, similar to previous observations in the Strengbach case studies (Aubert et al., 2001; Stille et al., 2006), slightly lower Sr and higher Nd isotopic compositions (0.715 and 0.51225 , respectively) for our apatite-like end member composition. Other important mineral constituents defining a granitic rock system are feldspars and micas. Micas have comparatively high Rb/Sr ratios but Sm/Nd ratios only slightly larger than those of corresponding WR. Thus, they are especially characterized by very high $^{87}\text{Sr}/^{86}\text{Sr}$ ratios and, therefore plot, as previously suggested (e.g. Aubert et al., 2001) to the right of the diagram. Feldspars have generally slightly lower Rb/Sr and Sm/Nd ratios than the corresponding WR and, therefore, in $^{143}\text{Nd}/^{144}\text{Nd}$ vs. $^{87}\text{Sr}/^{86}\text{Sr}$ isotope diagram, they would plot slightly to the left and below the isotope values of the WR samples.

Assuming arbitrarily the Nd and Sr concentration of a plagioclase feldspar (Aubert et al., 2001) and isotope ratios close to the WR ($^{143}\text{Nd}/^{144}\text{Nd}$: 0.5119 ; $^{87}\text{Sr}/^{86}\text{Sr}$: 0.739) and the above derived apatite isotopic compositions we can calculate the so-called "mixing curve of alteration products" (Aubert et al, 2001). All solid material derived from the same rock system and containing the three principal mineral phases but in different proportions plot somewhere within the apatite-, feldspar- , mica- triangle to the right of the "mixing curve of alteration products". This is also the case for our samples. All solid samples of the here studied rock system including SP leachates plot on this curve or to the right towards mica compositions.

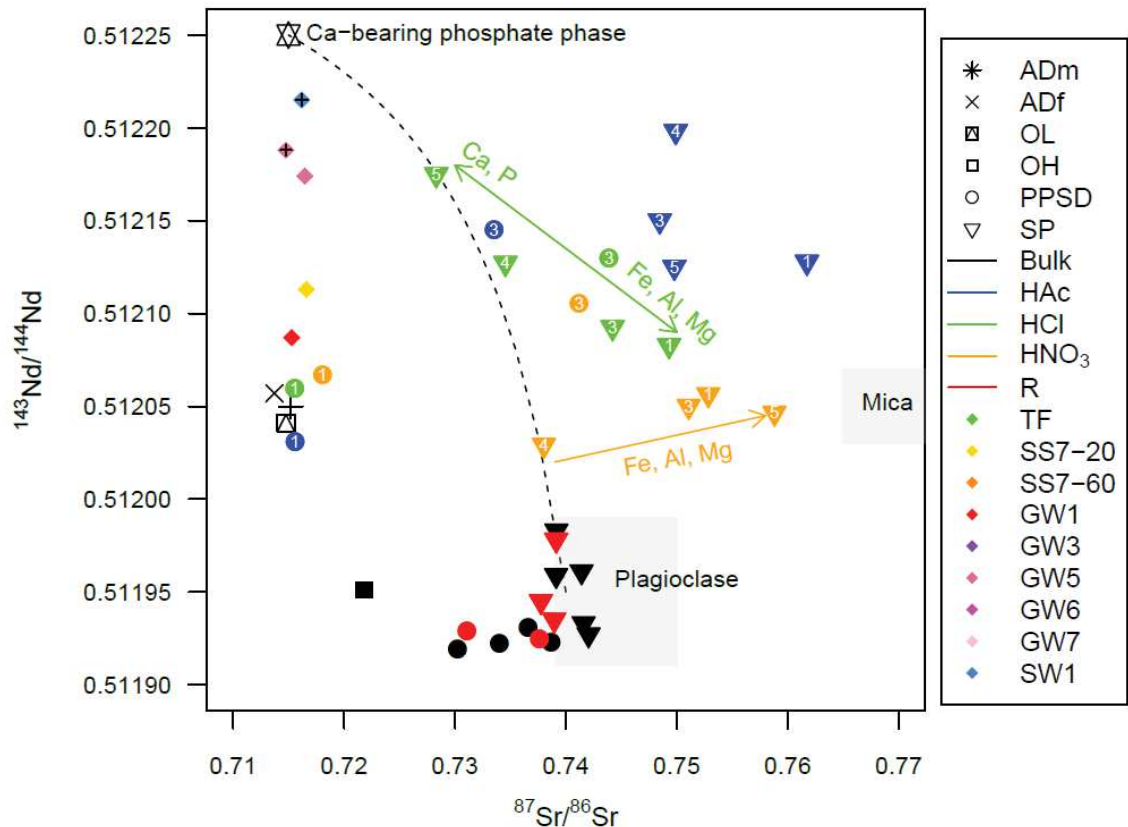


Figure 5.13. Relationship between Sr and Nd isotopic compositions of atmospheric dusts, organic horizons, bulk, leachate and residue regolith samples and a selection of waters. The diagram describes the mixing curve of alteration products between a Ca-bearing phosphate phase and a plagioclase end member. Arrows indicate elemental enrichments towards mica compositions. A lichen sample (+) from Hissler et al. (2008) is given as atmospheric reference. Numbers inside leachate sample symbols correspond to regolith sample number as reported in Chapter 3. Crosses inside water symbols indicate sampling in dry conditions.

In the case of previous studies one observed that waters and water suspended load, not contaminated by anthropogenic, atmosphere-derived depositions contain mainly Sr and Nd from apatite or other Ca-bearing P-phases and feldspar and plot on this curve of alteration products (Aubert et al., 2001; Stille et al., 2003).

It is interesting to note that the L2 leachates of SP define a slightly curved line from close to the apatite composition with highest $^{143}\text{Nd}/^{144}\text{Nd}$, lowest $^{87}\text{Sr}/^{86}\text{Sr}$ and, according to Figs.5.6, 5.6 and 5.8, highest P and lowest Fe, Al and Mg concentrations to another end member with lower Nd and higher Sr isotopic compositions and lower P but higher Fe, Al and to a lesser extent Mg concentrations. Thus, this end-member certainly contains mica-derived Sr and Nd. Compared to L2, the Sr and Nd isotopic compositions of the L3 leachate point to the presence of less phosphate- but more feldspar- and mica- derived Sr and Nd. As previously observed in separate Sr and Nd isotope diagrams, depth dependent patterns can also be here recognised for L2, with SP5 as the most apatite-like sample and SP1 the most mica-like one. We hypothesise that such distributions for the L2 SP leachates respond to the degree of alteration of the different SP

layers, such that the fresh bedrock is still rich in Ca-P bearing minerals compared to the saprolite layers that have already been intensively weathered and leached and in which mostly mica-like mineral phases remain. Similarly, L3 leachates show from SP4 to SP1 a tendency from plagioclase feldspar (and more bulk-like) towards more mica-like compositions, where also SP5 falls.

5.2.2 The impact of atmosphere-derived Sr, Nd and Pb on the waters chemical and isotopic compositions

Atmosphere-derived components have comparatively low Sr and Nd isotopic compositions, which are e.g. in the case of the Strengbach catchment in the Vosges mountains anthropogenic and lower than those of the granite rock forming mineral phases (Guéguen et al., 2012b; M. Lahd Geagea et al., 2008). Therefore, all solid and liquid samples containing these components tend to shift to the left of the above described "mixing curve of alteration products" (Aubert et al., 2002a, 2001; Stille et al., 2006). This is also the case for the here studied water samples and PPSD1 leachates. The $^{87}\text{Sr}/^{86}\text{Sr}$ ratios of these samples ranging between 0.712 and 0.717 are similar to those of our suggested apatite-like endmember (0.715) and atmospheric depositions represented by the organic and forest dust samples (between 0.714 and 0.722). However, the corresponding $^{143}\text{Nd}/^{144}\text{Nd}$ ratios (0.51203-0.51222) are significantly lower than that of the suggested Ca-bearing P-phase. Thus, only the combination of Sr and Nd isotope ratios allow discerning atmospheric and mineral contributions.

Anthropogenic atmosphere-derived components have generally low $^{206}\text{Pb}/^{207}\text{Pb}$, $^{206}\text{Pb}/^{204}\text{Pb}$, $^{207}\text{Pb}/^{204}\text{Pb}$ ratios (Carignan and Gariépy, 1995; Guéguen et al., 2012b; M. Lahd Geagea et al., 2008). $^{206}\text{Pb}/^{207}\text{Pb}$ isotope ratios of dusts and lichens collected in urban and industrial environments in the south of Luxembourg are low and scatter between 1.153 and 1.184 (Hissler et al., 2016, 2008). The here studied samples showing low Sr and Nd isotopic compositions manifest also lowest $^{206}\text{Pb}/^{207}\text{Pb}$ ratios and, thus, confirm the impact of atmosphere-derived components certainly impacted by some anthropogenic contributions (Fig.5.9). The $^{206}\text{Pb}/^{207}\text{Pb}$ ratios of the groundwaters are however even lower than those of the aforementioned anthropogenic compositions and closer to traffic and gasoline compositions reported for North-East France (M. Lahd Geagea et al., 2008).

The leaching experiments showed that in total between 20 and 60% of Pb was mobilized from the SP2 to SP5 samples, mainly by the L2 leaching step, together with some major and redox-sensitive elements. Surprisingly, the SP5 bedrock sample contains a very labile Pb fraction, as this is here recovered already in L1 leachate. Nonetheless, L1-SP5 $^{206}\text{Pb}/^{207}\text{Pb}$ isotopic ratios are similar to those of the other SP leachates and only slightly lower than those of the WR and R samples. Thus, significant amounts of anthropogenic Pb are not detectable for these samples.

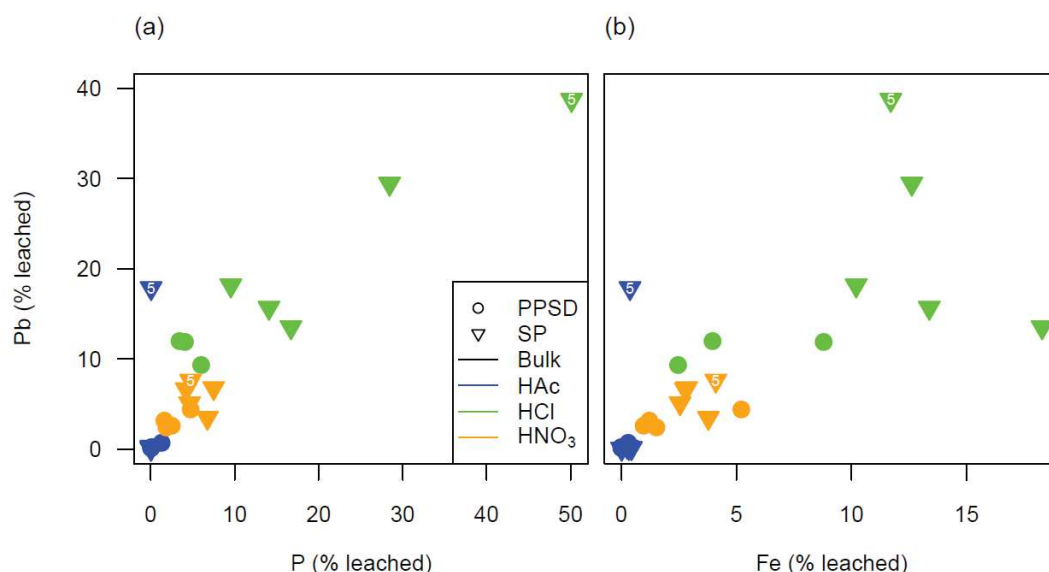


Figure 5.14. Relationship between leaching yields of Pb (%) and (a) P (%), and (b) Fe (%). The number 5 inside leachate sample symbols indicates SP5 regolith sample (as reported in Chapter 3).

Pb enrichments in L1 SP leachates come along with Ca (excluding SP3), Sr, Cd and Zn enrichments. Additionally, despite the L1 extraction is rather P and Fe depleted, when plotting the yields (% extraction respect to bulk) of Pb against those of P and Fe, we observe a trend reaching at SP5 highest Pb, P and Fe yields (Fig.5.14-a and -b). This trend is consistent in the other leachates (although not always SP5 is the most Pb, P and Fe enriched) and points to the existence of P(Ca)- and Fe-phases such as Fe-oxihydroxides or Ca-rich pyromorphites as Pb sinks in the whole regolith profile (Stille et al., 2011). Previous studies showed that pyromorphite forms when P and Pb are present in the system, is stable at $\text{pH} > 4$ and dissolves at $\text{pH} < 4$ (Zhang et al., 1998). Unfortunately, we do not count on SEM data for the SP samples, but we may hypothesize that fresh bedrock (SP5) and saprolite contain pyromorphite, which is stable under normal conditions (groundwater $\text{pH} > 6$) but is easily dissolved with the leaching experiments ($\text{pH} < 4$). Similarly, this Pb might naturally desorb from Fe and Ca/P-bearing mineral phases due to pH changes in function of saturation dynamics (Gangloff et al., 2014; Stille et al., 2011).

PPSD leachates plot in a field with Sr and Pb isotopic compositions distinct from those of “mineral” phase compositions but similar to those of anthropogenic atmospheric-derived isotopic compositions (Fig.5.10); this is also also true for soil solutions and streamwaters. Groundwaters have even significantly lower $^{206}\text{Pb}/^{207}\text{Pb}$ ratios. We assume that actual atmospheric Pb depositions with $^{206}\text{Pb}/^{207}\text{Pb}$ ratios similar to those of our collected dusts and organic samples (ADm, ADf and OL, OH) affected the catchment. These samples have low Pb isotopic ratios (1.153-1.185) in the exact range of lichens collected in industrial areas but significantly higher than those of the groundwaters (1.143-1.146) (Hissler et al., 2008; Moragues-Quiroga et al., 2017). Thus, anthropogenic atmosphere-derived contributions through

precipitations of *today* have and had certainly an important impact on the ecosystem, which is mostly observed in the surface and uppermost soil and water compartments.

On the other hand, the very low-anthropogenic $^{206}\text{Pb}/^{207}\text{Pb}$ ratios of groundwaters might represent an older industrial Pb component. Indeed GW $^{206}\text{Pb}/^{204}\text{Pb}$ ratios ranging between 17.814 and 17.581 are similar to those of Australian ore bodies (17.5-18) used for industrial purposes until mid-90's (Stille and Shields, 1997; and citations therein).

This means that older industrial emissions and gasoline Pb (Fig.5.9; Hissler et al., 2008; M. Lahd Geagea et al., 2008) have had a strong impact on the catchment system. These Pb fluxes decreased only with the ending of steel plant activities in the region and especially the ban of leaded gasoline in Europe in 2000 (Michelutti et al., 2009). Alternatively, these Pb signatures may correspond to the weapons of Second World War (Cole, 1965), option which then might be discarded for the surface signatures as hypothesized in chapter 3 (Moragues-Quiroga et al., 2017). Unfortunately, we do not count on data for this kind of war residues. Given the high DOC contents of groundwaters reported in the previous chapter, one may suggest that this old industrial Pb is bound on organic matter rich colloidal phases in the water and/or adsorbed with organic matter on the rockwalls of the aquifers and mobilized according to saturation-pH fluctuations (Gangloff et al., 2014 and references therein). Interestingly, GW5 presents lower values (17.825) than GW1 (17.851) and to a lesser extent GW6 (17.835) and, thus, is slightly more contaminated by old Pb. The mobilization of old Pb in GW5 seems to be more important during high flow conditions, since the $^{206}/^{204}\text{Pb}$ ratios decrease to lowest values of 17.814, which again might be linked to DOC and pH fluctuations.

Hence, the data point to the existence of two-to-three Pb reservoirs:

- (i) An anthropogenic Pb reservoir which can be differentiated in:
 - a. actual anthropogenic Pb with low $^{206}\text{Pb}/^{207}\text{Pb}$ (e.g.: atmospheric dusts), mainly deposited in the surface and upper subsurface compartments of the catchment;
 - b. older industrial Pb with very low $^{206}\text{Pb}/^{204}\text{Pb}$ (e.g; type Australian Pb) stored in the aquifer and probably complexed with labile organic phases.
- (ii) A leachable rock reservoir containing a rock Pb which is more stable and less mobilized in the groundwaters.

The slightly higher Pb isotopic ratios of soil solutions and streamwaters indicate that, due to their intermediate position, contain Pb from both reservoirs.

5.2.3 The origin and the chemical partitioning of U and the ^{234}U enrichments in the waters

The waters are similar to some of the leachates strongly enriched in ^{234}U . However, they are even more enriched and show even higher ($^{234}\text{U}/^{238}\text{U}$) activity ratios; e.g.: GW1 has the highest ratio of 2.2. The SP whole rock samples have ($^{234}\text{U}/^{238}\text{U}$) activity ratios scattering between 0.95 and 1.05 and are therefore close to secular equilibrium. The PPSD samples from closer to the surface appear to be slightly more ^{234}U depleted (0.93-0.96). Similarly, PPSD Leachates, and particularly the PPSD3 ones, are generally more ^{234}U enriched than those of SP. But one also observes that generally, among the three leachates L1 are the most and L3 the least enriched.

All the activity ratios are strongly fractionated due to chemical weathering. It has been shown in many previous studies that during water-rock interaction ^{234}U and ^{238}U manifest different mobilities. One observes that, compared to ^{238}U , ^{234}U is more easily released into solution due to the so-called alpha-recoil process (Osmond and Ivanovich, 1992 and references therein; Chabaux et al., 2003; 2008; DePaolo et al. 2006; 2012). These processes finally cause the preferential excess of ^{234}U with ($^{234}\text{U}/^{238}\text{U}$) activity ratios >1 in natural waters, and depletion of ^{234}U with ($^{234}\text{U}/^{238}\text{U}$) activity ratios <1 in the residual material of the soil or bedrock (Andrews and Kay, 1983; Camacho et al., 2010; Chabaux et al., 2008; François Chabaux et al., 2003; Dosseto et al., 2012, 2008; Osmond and Ivanovich, 1992; Pierret et al., 2014; Prunier et al., 2015). Thus, long periods of water saturation and intense weathering cause ^{234}U leaching from rock and soil minerals, causing ($^{234}\text{U}/^{238}\text{U}$) activity ratios >1 in the waters and <1 in the saprolithic source material. The very high ($^{234}\text{U}/^{238}\text{U}$) activity ratios of some of the groundwaters might especially be explained by high recoil effects reinforced by the small grain size of the minerals in the slates, which provide greater weathering surface (Vigier and Bourdon, 2012).

The released ^{234}U forms under oxidising conditions uranyl ions (U(VI)O_2^{+2}) which get released into the groundwater where it migrates; but it might also be readsorbed onto mineral surfaces or re-deposited during co-precipitation with Fe oxy-hydroxides at redox interfaces (e.g. SP3 and SP4) (Moragues-Quiroga et al., 2017). The high ($^{234}\text{U}/^{238}\text{U}$) activity ratios of the L1 leachates support the idea that some of the ^{234}U uranyl anions are readsorbed together with Ca (Fig.5.5) on mineral surfaces.

These results are also in agreement with the Ce anomalies investigated through the leaching experiment and in our previous study of the Weierbach waters (see REE sections 4.1.1 and 4.2.2). While the leaching experiment showed the abundance of labile Ce in PPSD (notably PPSD2) and in SP3, the waters study revealed positive Ce anomalies only in the 20 to 60 cm depth soil solutions. Negative Ce anomalies were found in all groundwaters, and were particularly strong for GW1. These results suggest that indeed, due to anoxic conditions in the biologically active soil horizons, soil solutions (SS) are able to mobilize U (preferably ^{234}U) and

Ce together with other light and middle REE. When migrating downward in the saprolite, they may become depleted in Ce as this precipitates with progressively oxidizing conditions until the level of GW1 and deeper in the “summer” redox interface (e.g. above and around SP3) with Fe and Mn oxides and other redox sensitive elements, which are found at these depths. In agreement are the positive Ce anomalies and high $^{234}\text{U}/^{238}\text{U}$ yielded by the laboratory leachates of these regolith samples, which proof the precipitation of ^{234}U and Ce. The deeper and “permanent” groundwater (GW5) table fluctuations will also slowly leach U and Ce, but here more reducing conditions –in particular under catchment saturation conditions- will reduce the Ce anomaly compared to GW1.

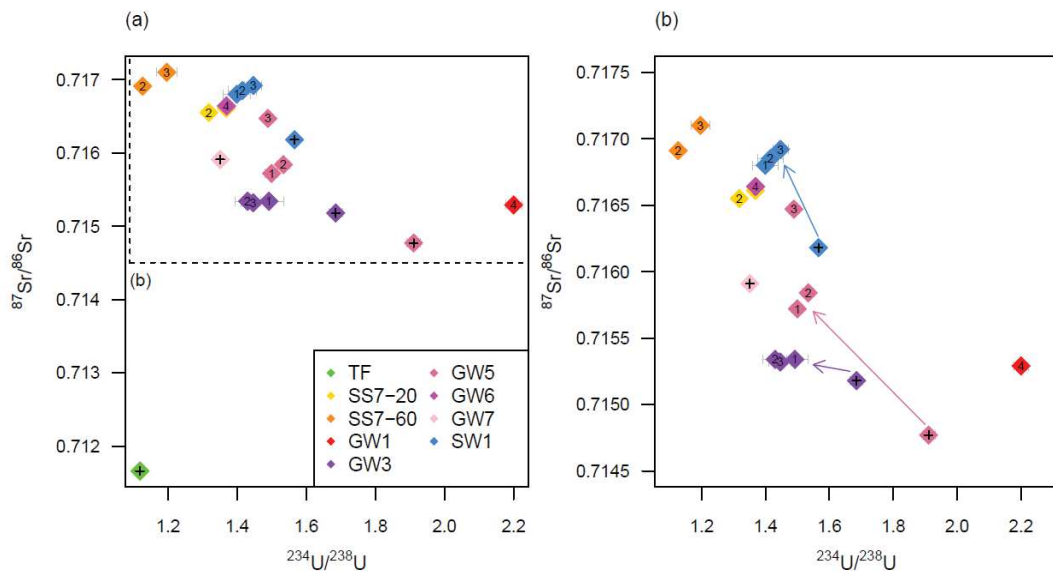


Figure 5.15. (a) $^{87}\text{Sr}/^{86}\text{Sr}$ vs. $^{234}\text{U}/^{238}\text{U}$ for a selection of waters. (b) Zoom excluding TF. Numbers inside water sample symbols correspond to sampling day (1: 29/01/16; 2: 30/01/16 - 1st discharge peak; 3: 31/01/16; 4: 01/02/16 - 2nd discharge peak). Crosses inside water symbols indicate sampling in dry conditions.

The ($^{234}\text{U}/^{238}\text{U}$) activity ratios of the waters are correlated with the corresponding Sr isotopic compositions (Fig.5.15). It is interesting to note that neither the forest dusts ($^{87}\text{Sr}/^{86}\text{Sr} = 0.713726$, $^{234}\text{U}/^{238}\text{U} = 1.0057$) nor throughfall ($^{87}\text{Sr}/^{86}\text{Sr} = 0.71166$, $^{234}\text{U}/^{238}\text{U} = 1.1192$) have a direct impact on the U and Sr isotopic compositions of the water samples (Fig.5.15). GW1 highflow waters and the baseflow groundwater samples have highest activity ratios. Based on the discussions above, their $^{87}\text{Sr}/^{86}\text{Sr}$ isotopic compositions are close to those of Ca-bearing phosphates such as apatite (0.715).

The GW and SW Sr isotopic compositions increase and the ($^{234}\text{U}/^{238}\text{U}$) activity ratios decrease from the summer baseflow conditions to the winter storm event (Fig.5.15). These changes of isotopic signatures come along with a decrease in Sr and U concentrations (Fig.5.16), pointing to mixing and dilution processes during wetness or highflow conditions. The very high ($^{234}\text{U}/^{238}\text{U}$) activity ratios of the baseflow groundwaters seem to respond to long interactions

with a labile reservoir strongly enriched in ^{234}U . ($^{234}\text{U}/^{238}\text{U}$) activity ratios of L1 and L2 leachates of SP support the suggestion of the presence of such reservoirs at depth. Under wetness conditions upper subsurface waters enter the saprolite and mix with the groundwaters. These upper subsurface waters are represented by the soil solutions which are characterized by highest $^{87}\text{Sr}/^{86}\text{Sr}$ isotopic compositions and U concentrations and lowest ($^{234}\text{U}/^{238}\text{U}$) activity ratios and Sr concentrations; their isotopic compositions are comparable with those of PPSD1 leachates and organic matter separated from the soil. One observes that as the connectivity between the soil and groundwater systems is reached, the SS enter the saprolite and lead to an increase of the $^{87}\text{Sr}/^{86}\text{Sr}$ ratios and a depletion of the ($^{234}\text{U}/^{238}\text{U}$) activity ratios in the newly mixed groundwaters. During the storm event GW5 shows slightly decreasing Sr concentrations (< 1 order of magnitude) and rather stable U concentrations, reinforcing the hypothesis of a SS contribution at these depths (Fig.5.16).

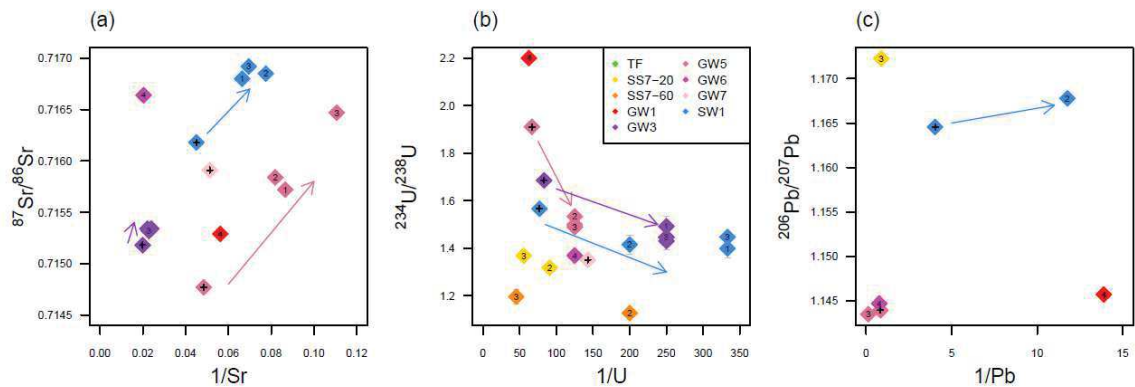


Figure 5.16. Mixing diagrams of (a) Sr, (b) U, and (c) Pb for the analysed waters. Numbers inside water sample symbols correspond to sampling day (1: 29/01/16; 2: 30/01/16 - 1st discharge peak; 3: 31/01/16; 4: 01/02/16 - 2nd discharge peak). Crosses inside water symbols indicate sampling in dry conditions.

Finally, the SW seems to mirror the chemical and isotopical compositions of the dominant highflow and baseflow sources. Under baseflow conditions, the stream is more importantly fed by the existing groundwaters and hence partially adopts their isotopic composition. On the contrary, during highflow conditions the SW Sr and U isotopic compositions rise towards those of SS and the concentrations generally decrease (Fig.5.15). During the storm event SW shows, for relatively stable Sr and U isotopic ratios, a U concentration peak during the first discharge response, pointing to a fast connection with a ^{234}U -rich pool. Both in base- and high- flow conditions GW7 –and potentially GW6- might be a SW counter-contribution, as it might characterize an end member with higher $^{87}\text{Sr}/^{86}\text{Sr}$ and lower $^{234}\text{U}/^{238}\text{U}$ activity ratios than observed for the other GWs.

5.2.4 The hydrological functioning of the system: evidence of O-Sr-Pb-U isotopes

The stable isotope data presented in Chapter 4 in combination with the newly reported geochemical observations allow further understanding of the hydrological functioning of the Weierbach catchment.

From summer base flow to winter storm event conditions, GW3 and GW5 show increasing $\delta^{18}\text{O}$ and $^{87}\text{Sr}/^{86}\text{Sr}$ values and decreasing ($^{234}\text{U}/^{238}\text{U}$) activity ratios (Fig.5.17 and Fig.5.18). On the contrary, SW shows decreasing $\delta^{18}\text{O}$ values and ($^{234}\text{U}/^{238}\text{U}$) activity ratios but, similar to the GW, increasing $^{87}\text{Sr}/^{86}\text{Sr}$ ratios (Fig.5.17 and Fig.5. 18).

During the storm event, GW samples show heavier $\delta^{18}\text{O}$ values during the first discharge peak and lighter ones before and after. The Sr isotopic ratios of GW5 tend to increase particularly during the second discharge peak, whereas those of GW3 remain rather stable (Fig.5.17-b). Similarly, the ($^{234}\text{U}/^{238}\text{U}$) activity ratios of both GW3 and GW5 show only little variations during the event (Fig.5.18-b).

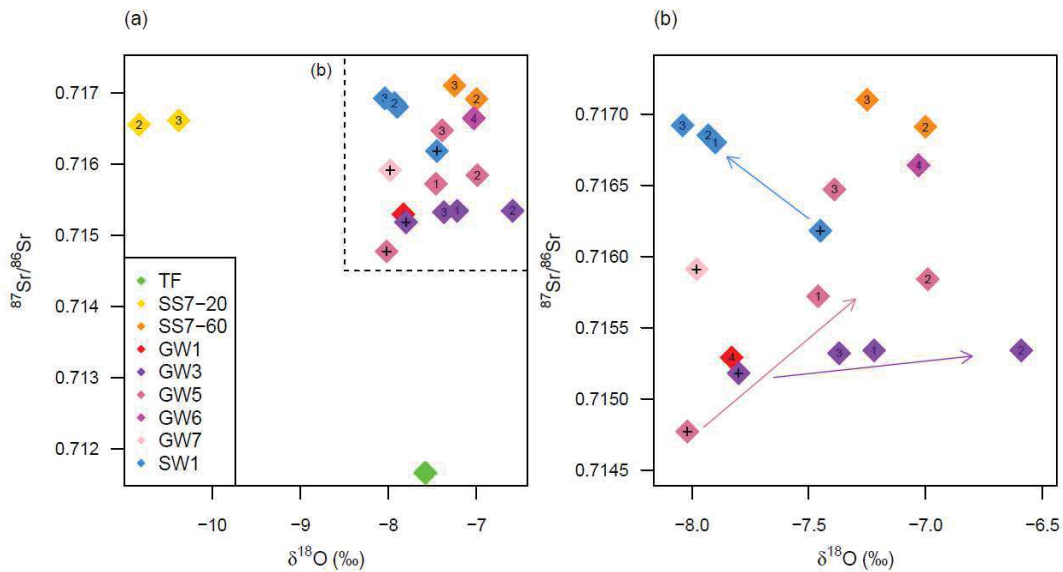


Figure 5.17. (a) $^{87}\text{Sr}/^{86}\text{Sr}$ vs. $\delta^{18}\text{O}$ for the analysed waters. (b) Zoom excluding TF and SS20. Numbers inside water sample symbols correspond to sampling day (1: 29/01/16; 2: 30/01/16 - 1st discharge peak; 3: 31/01/16; 4: 01/02/16 - 2nd discharge peak). Crosses inside water symbols indicate sampling in dry conditions.

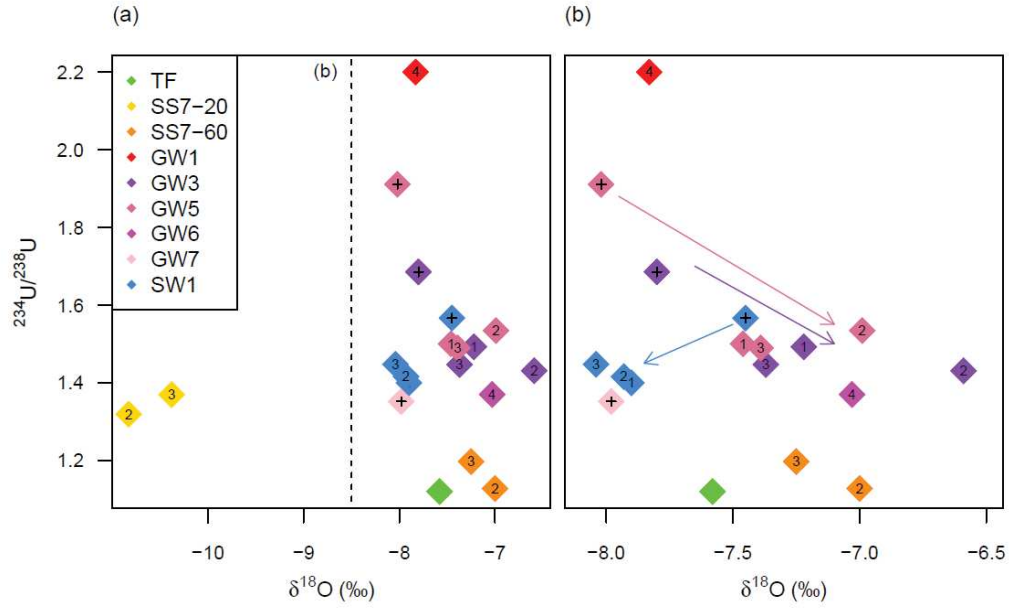


Figure 5.18. (a) $^{234}\text{U}/^{238}\text{U}$ vs. $\delta^{18}\text{O}$ for the analysed waters. (b) Zoom excluding TF and SS20. Numbers inside water sample symbols correspond to sampling day (1: 29/01/16; 2: 30/01/16 - 1st discharge peak; 3: 31/01/16; 4: 01/02/16 - 2nd discharge peak). Crosses inside water symbols indicate sampling in dry conditions.

The non-linear relationships between $\delta^{18}\text{O}$ values and the Sr and U isotopic ratios may show a hysteresis for these samples. Particularly in the case of GW5, an anticlockwise hysteretic loop might be expected, pointing to upper subsurface contributions. However, the few measurements available do not clearly allow such statement. Contrarily to the GW, the $\delta^{18}\text{O}$ values of SW samples decrease during the event while the corresponding Sr and U isotopic ratios increase. It is interesting to note that after the rain event both SS20 and SS60 become, like SW, more ^{87}Sr and ^{234}U enriched as well as $\delta^{18}\text{O}$ lighter (Fig.6.17a and b, and Fig. 5.16).

In Figure 18 the $\delta^{18}\text{O}$ and $^{234}\text{U}/^{238}\text{U}$ signatures of SS, GW and SW are combined to identify potential hydrological end members in high- and base- flow conditions. The conceptual model shows that, in base flow (dry) conditions, streamwater geochemically resembles the deep groundwaters of GW5 well in the plateau with low $^{87}\text{Sr}/^{86}\text{Sr}$ isotopic compositions (0.716) and high $^{234}\text{U}/^{238}\text{U}$ activity ratios (1.6). Conversely, in high (and peak) flow conditions, the streamwater signature is more similar to that of soil solutions and GW6 groundwaters, with higher $^{87}\text{Sr}/^{86}\text{Sr}$ isotopic compositions (0.717) and comparatively low $^{234}\text{U}/^{238}\text{U}$ activity ratios (1.4). Hence, a greater contribution of the upper subsurface compartments is to be expected in high-flow conditions through a sub-surface lateral flow or through the fractured bedrock. According to Martínez-Carreras et al. (2016), when the catchment storage surpasses an established threshold an upper subsurface reservoir contributes to the stream through the PPSD-SP interface or bedrock fractures. These findings are further supported by the work of Scaini et al. (2017a, 2017b) on artificial tracer transport, which points to the existence of lateral flow at the PPSD-SP interface and to the importance of bedrock cleavage orientation in fast flow

generation at the hillslope. In our study, the complete Sr and U isotopic tracing confirms these suggestions. Moreover, while the stable isotopes of oxygen show rather small variations and do not allow further understanding of the catchment end members, the incomplete water Pb isotopic composition data allow to better trace the aforementioned upper subsurface contributions. During wetness conditions $^{206}\text{Pb}/^{207}\text{Pb}$ and $^{206}\text{Pb}/^{204}\text{Pb}$ ratios are respectively 1.17 and 18.297 for SS, and 1.15 and 17.851 for GW1. The corresponding GW5 ratios are 1.144 and 17.825 at dry conditions and 1.143 and 17.814 at wetness conditions. GW6 waters collected during wetness conditions are in between GW1 and GW5 with ratios of 1.145 and 17.835 respectively. Finally, SW shows under dry situation slightly lower Pb ratios of 1.165 and 18.165 (but higher than all GWs) than during wet event with ratios of 1.168 and 18.22, indicating that during dry conditions SW contains more Pb from GW and during wet events more Pb from SS. Thus, Pb is rather coming from SS during high flow conditions than from the deep GW6.

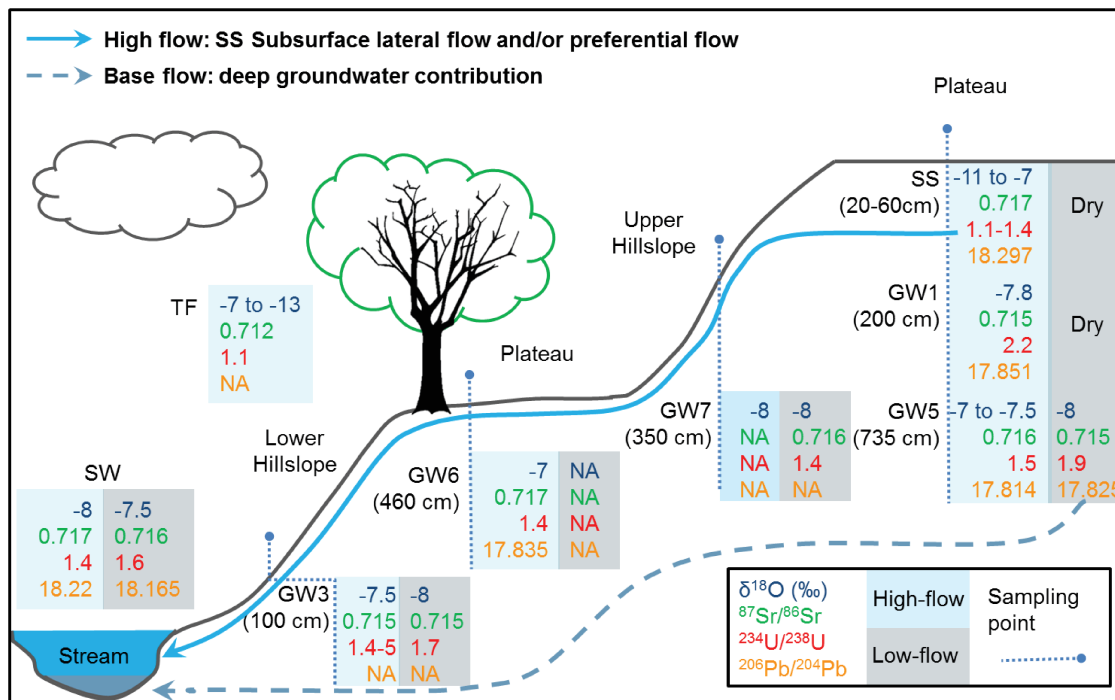


Figure 5.19. Conceptual model of water circulation dynamics at the Weierbach catchment under different hydrological conditions according to the $\delta^{18}\text{O}$, $^{87}\text{Sr}/^{86}\text{Sr}$, $^{234}\text{U}/^{238}\text{U}$ and $^{204}\text{Pb}/^{206}\text{Pb}$ signatures of the studied waters.

Also supportive are the pH and EC dynamics in the stream compared to SS and GWs. We saw in chapter 4 (see section 4.1.1) that pH is rather stable during the year, < 5 for SS20 and SS60, around 5 for GW1 and between 6.5 and 7.5 approximately for the other groundwaters. Streamwaters show a small depletion from around 7 to 6.5 between dry and wet conditions and, additionally, decrease to 5.5-6 during peak flow, suggesting a greater contribution from SS. Electrical conductivity (EC) shows similar or even more significant patterns: while EC is

between 30 and 40 $\mu\text{S}/\text{cm}$ for SS and 45-100 $\mu\text{S}/\text{cm}$ for GW1, SW decreases from ca. 60 $\mu\text{S}/\text{cm}$ at dry conditions to ~45 $\mu\text{S}/\text{cm}$ during wetness conditions. Similar to pH, an additional decrease of EC is observed during peak flow (~40 $\mu\text{S}/\text{cm}$), reinforcing the suggestion of a connection between stream and soil reservoirs under wet conditions.

5.3 Conclusion

This chapter deals with the comparison of the previously defined regolith and hydrological end members to precisely decipher the main interaction and solute transport mechanisms at both regolith profile- and catchment- scales. To facilitate this comparative study, O-Sr-Nd-Pb-U isotope compositions are here reported for a selection of water samples collected under low- and high- flow conditions. Additionally, the whole multi-tracer characterization is here applied on regolith leachates (and corresponding residues) obtained during laboratory leaching experiments. Leaching experiments are particularly useful to further understand water-rock interactions because they allow identifying labile atmospheric and mineral phases responsible for the hydrochemical profile of the catchment, even though they may not be recognisable through microscopic analyses.

Sr, Nd and Pb isotopes allowed elucidating 2 main contributions controlling the compositions of the Weierbach waters:

- (i) Most important are contributions from alteration of plagioclase ($^{87}\text{Sr}/^{86}\text{Sr}$: 0.739, $^{143}\text{Nd}/^{144}\text{Nd}$: 0.5119) and Ca rich phosphate phases ($^{87}\text{Sr}/^{86}\text{Sr}$: 0.715, $^{143}\text{Nd}/^{144}\text{Nd}$: 0.51225) which are particularly important in the SP compartment and have a great impact on the chemistry of deep groundwaters and the stream.
- (ii) Contributions from two different atmosphere-derived, anthropogenic reservoirs: one of *today* ($^{87}\text{Sr}/^{86}\text{Sr}$: 0.714-0.722, $^{143}\text{Nd}/^{144}\text{Nd}$: ~0.51204, $^{206}\text{Pb}/^{207}\text{Pb}$: 1.153-1.185), that impacts the uppermost soil layers and their drainage waters, as well as the stream; and an *old* one ($^{206}\text{Pb}/^{207}\text{Pb}$: 1.14-1.146) that impacts the deep groundwaters and only slightly the aquifer rocks.

Leaching experiments, and in particular L1 and L2 SP leachates, were extremely helpful to elucidate the role and impact of alteration of plagioclase and Ca-P mineral phases on the waters chemical composition which is suggested to be stronger at deeper regolith layers. Contrarily, the presence of mica in the regolith does not seem to have a visible impact on the water's dissolved load. Furthermore, the suggestion that Ca-bearing phosphate minerals greatly contribute to the chemistry of the waters is here supported by the correlation between higher U activity ratios with apatite-like Sr and Nd isotopic compositions, indicating strong weathering reactions with this mineral phase. The high U activity for the Weierbach waters (up to 2.3), particularly in the

GW1 and GW5 wells, are explained by long interactions (as is the case for baseflow samples) with labile Ca-bearing reservoirs, whose existence is corroborated by the high activity ratios of L1 and L2. We further suggest that the small grain size of the slate metastable minerals could reinforce recoil effects resulting in exceptional mobilization of ^{234}U (Vigier and Bourdon, 2012).

Finally, the combined use of Sr and Pb radiogenic isotopes with $^{234}\text{U}/^{238}\text{U}$ activity ratios on the water samples allows the identification of different water circulation dynamics during wet and dry periods. We show that in base flow (dry) conditions, streamwater is mainly fed by the “permanent” deep groundwaters of GW5 well in the plateau, with low $^{87}\text{Sr}/^{86}\text{Sr}$ and $^{206}\text{Pb}/^{204}\text{Pb}$ isotopic compositions (0.716 and 18.165, respectively) and highest $^{234}\text{U}/^{238}\text{U}$ activity ratios (1.6). Conversely, in high (and peak) flow conditions a greater contribution of the PPSD reservoir is to be expected, as suggested by a streamwater signature more similar to that of SS, with higher $^{87}\text{Sr}/^{86}\text{Sr}$ and $^{206}\text{Pb}/^{204}\text{Pb}$ isotopic compositions (0.717 and 18.22 respectively) and comparatively low $^{234}\text{U}/^{238}\text{U}$ activity ratios (1.4). It is thanks to the different impact of atmospheric inputs in the different reservoirs that we can recognise, through the Pb isotopic signatures, that SS and not other sources principally controls the chemical and isotopic compositions of the stream waters during wetness conditions. The results suggest that sub-surface lateral flow or preferential flowpaths through the fractured bedrock may connect the PPSD (SS) reservoir to the stream, as previously suggested by Martinez-Carreras et al. (2016) and Scaini et al. (2017a, 2017b). The extent to which these contributions originate specifically from the plateau or the hillslope areas cannot be here assessed due to the lack of SS isotopic data around the catchment. On the other hand, previous suggestions by these authors related to the *direct* impact of precipitation on the stream, are here contradicted according to the very different U and Sr isotopic compositions of our atmospheric end members ($^{87}\text{Sr}/^{86}\text{Sr} = 0.71166\text{--}0.7126$, $^{234}\text{U}/^{238}\text{U} = 1.0057\text{--}1.1192$) and the stream. The $\delta^{18}\text{O}$ composition does not allow in our study for further understanding of the system. We here stress the complementarity of the radiogenic isotopes and O and H stable isotope transit (/residence) time calculations in order to obtain more realistic assessments on catchment’s hydrological functioning.

Conclusions and Perspectives

In the present work we combined multiple geochemical tracers, namely major and trace elements and O-Sr-Nd-Pb-U isotopes, to shed light on the mechanisms responsible for regolith weathering and leaching processes that largely control the water chemistry dynamics at the small catchment scale. With this aim, we characterized different regolith compartments as potential “hot spots” of interaction with water circulating through the system, and the waters themselves.

In a first part, the mineralogical and geochemical study of the regolith brought useful information on the origin and behaviour of the potential “hot spots”. It then enabled a first approximation to the hydrochemistry of the catchment waters, by facilitating the association of regolith and water pools. However, it is with the final combined study of regolith and waters, through the use of leaching experiments and the whole tracer toolbox, that we could precisely identify two principal contributions controlling the catchment hydrochemical and isotopic characteristics, namely

- An atmosphere-derived anthropogenic contribution
- Contributions from alteration of the regolith’s mineral phases, mainly plagioclase and Ca rich phosphate phases

Knowing the geochemical and isotopic compositions of these sources, we could then assess water circulation dynamics at the catchment scale.

Atmospheric Contributions

The atmosphere-derived contributions were identified in atmospheric dusts, organic soil horizons (0-45 cm depth) and throughfall by enrichments in Pb, As, Hg, and Sb and $^{87}\text{Sr}/^{86}\text{Sr}$ ranging between 0.714-0.722, $^{143}\text{Nd}/^{144}\text{Nd}$ ranging between 0.51204 and 0.51208 and $^{206}\text{Pb}/^{207}\text{Pb}$ isotopic compositions ranging between 1.153 and 1.185, frequently associated to

high organic matter content. The “natural” background in the Weierbach slates was characterized by comparatively lower concentrations in Pb, As, Hg, and Sb, higher $^{87}\text{Sr}/^{86}\text{Sr}$ and $^{206}\text{Pb}/^{207}\text{Pb}$ ratios (~ 0.739 and ~ 1.2 respectively) and generally lower $^{143}\text{Nd}/^{144}\text{Nd}$ (~ 0.5119). Pb isotopes and the combination of Sr-Nd isotopes allowed distinguishing between atmospheric contributions and mineral signatures in the catchment waters.

Low $^{206}\text{Pb}/^{207}\text{Pb}$ found in atmospheric dusts and in the surface and upper subsurface compartments of the catchment (uppermost PPSD horizon) point to actual anthropogenic input to these compartments which are also enriched in Pb, Sb, As and Hg. On the other hand, older anthropogenic Pb was detected in the groundwaters (GW1, GW5, GW6) through even lower $^{206}\text{Pb}/^{207}\text{Pb}$ (1.14-1.146) and $^{206}/^{204}\text{Pb}$ ratios (17.581-17.814 for GW's compared to ratios > 18.72 for the slate) close to those of e.g. Pb from Australian ore bodies traditionally used as additive in gasoline before it was banned in the early 2000s. These signatures found in the groundwaters were not detectable in actually sampled dust and regolith (bulk, leachate or residue) samples. However, they came along with enrichments in Pb, Rb, SO_4^{2-} or DOC in the dissolved load, initially associated to acidic rains and/or rain inputs reaching the aquifer through preferential flowpaths. Given the high DOC contents reported for the groundwaters, we suggest that this Pb is bound in organic matter complexes in solution and/or on the rockwalls of the aquifers and mobilized according to saturation dynamics. The dissolved major and trace element composition of soil solutions and streamwaters also showed an important impact from throughfall. In this case, their isotopic ratios were intermediate between those of (actual and old) anthropogenic inputs and the natural background, pointing to a mixture of both components.

Contributions from mineral alterations

The lower part of the PPSD and the SP were found to contain negligible traces of atmospheric depositions, according to their “natural”-like chemical and isotopic compositions. Instead, they were defined by geogenic products.

The lower part of the PPSD (45-110 cm depth) was characterized by the impact of old volcanic events, as evidenced by a refractory mineralogy (Ti-magnetite, chamosite, orthoclase) and Nb and Ti enrichments. This mineralogy is not expected to greatly contribute to the waters chemistry, and thus shows little potential as water interaction “hot spot”. This suggestion was supported by the weak yields obtained for most of the chemical elements in the laboratory leachates of these horizons.

However, REE-bearing minerals found in the lowermost PPSD horizons like monazite and florencite were recognised as a labile pool of REE. Indeed, shallow subsurface waters around these depths (SS60, GW1), are not only impacted by throughfall and vegetation, as it was evidenced by their chloride to sulfate composition rich, but also by highest geogenic REE concentrations. Leaching experiments carried out on all of the PPSD samples further suggested

that the REE patterns of the soil solutions are indeed inherited from the PPSD. Both PPSD leachates and soil solutions (SS20 and SS60) were characterized by slight MREE enrichments and positive Ce anomalies, indicating that the PPSD horizons contain labile MREE and Ce, which can be mobilised under reducing or anoxia conditions probably triggered by biological activity. It is interesting to note that GW1 waters collected *only* during wetness conditions at the depth of the PPSD4 horizon (~108 cm) are the most REE-enriched and show a negative Ce anomaly. We suggest that this could be simply due to the higher concentrations and lability of all other REE compared to Ce in PPSD4; and/or a change to more oxidative environment (as evidenced by gleyic properties) at this depth, allowing for Ce precipitation.

PPSD4 and the whole slate weathering profile (SP) were found to be strongly affected by the seasonal water saturation dynamics. PAAS normalized REE patterns of the saprolite materials and the waters they host showed varying MREE enrichments and Ce anomalies associated to Fe, Mn oxides, indicating the impact of strong redox processes due to water table fluctuations. Similarly, very high U activity ratios (up to 2.2) in the waters stored and circulating through the saprolite indicated the occurrence of strong chemical weathering reactions, particularly in the GW1 and GW5 wells (close to 2.3). These high U activity ratios are explained by long interactions (as is the case for baseflow samples) with labile reservoirs, whose occurrence was corroborated by the high activity ratios of L1 and L2 SP samples. It is well known that the preferential leaching of ^{234}U compared to ^{238}U due to alpha-recoil results in waters with high U activity ratios and residual saprolites with lower ones. We further suggest that the recoil effect might be reinforced in the Weierbach slate due to the small grain size of the minerals in play, where a greater surface is available to react and, hence, produce very high U activity ratios.

Indeed, Sr and Nd isotope analysis applied on waters and regolith bulk and leachate samples allowed elucidating the two aforementioned mineral phases controlling the compositions of waters:

- (iii) Plagioclase, with an isotopic composition similar to that of the bulk regolith samples ($^{87}\text{Sr}/^{86}\text{Sr}$: 0.739, $^{143}\text{Nd}/^{144}\text{Nd}$: 0.5119)
- (iv) Ca-bearing phosphates, with low $^{87}\text{Sr}/^{86}\text{Sr}$ (0.715) and highest $^{143}\text{Nd}/^{144}\text{Nd}$ (0.51225)

It is only through the combined use of Sr and Nd isotopes, and with the help of the leaching experiments, that the Ca-bearing phosphate end member could be identified and distinguished from the atmospheric one, as these have very similar $^{87}\text{Sr}/^{86}\text{Sr}$ ratios. This information could not be deduced from our individual regolith and water studies, since these are metastable phases, hard to recognise by simple mineralogical or chemical analyses. Therefore, the leaching experiments and in particular L1 and L2 SP (and to a lesser extent PPSD4) leachates, were extremely useful to represent the natural weathering of plagioclase and Ca-P mineral phases by

waters, which is suggested to be higher at deeper regolith layers. Furthermore, the suggestion that Ca-bearing phosphate minerals greatly contribute to the chemistry of the waters was supported by the correlation between higher U activity ratios with apatite-like Sr and Nd isotopic compositions. Other minerals like mica ($^{87}\text{Sr}/^{86}\text{Sr} > 0.77$, $^{143}\text{Nd}/^{144}\text{Nd} \sim 0.51205$) were suggested to be important in the regolith isotopic composition, especially in the uppermost SP horizons, but not in the isotopic composition of the waters dissolved load.

Hydrological functioning according to the defined contributions controlling waters chemistry

Once defined the geochemical and isotopic characteristics of the mineral and atmospheric end members, we could follow the evolution of the O, Sr, Pb and U isotope ratios in waters collected under different hydrological conditions and assess the main water circulation and mixing dynamics at the profile and catchment scale.

We observed that, during base flow (dry) conditions, the PPSD reservoir is “dry” and the streamwater is mainly fed by the “permanent” deep groundwaters. Specifically, the GW5 well waters in the plateau were found to be the main contributing source to the stream, which presented similarly low $^{87}\text{Sr}/^{86}\text{Sr}$ (0.716) and $^{206}\text{Pb}/^{204}\text{Pb}$ isotopic compositions (18.165) compared to the other GW waters and highest $^{234}\text{U}/^{238}\text{U}$ activity ratios (1.6). This suggestion was supported by Ca- and Mg- bicarbonate compositions in the SW and bottom groundwaters (GW2, GW3) similar to those of GW5. During dry conditions, long residence times and the lack of dilution by new waters will result in strong weathering reactions in the permanently saturated aquifers (as evidenced by the high U activity ratios) involving Ca-rich minerals like plagioclase or apatites and dissolved CO₂ released by bacterial activity. Indeed, although no primary carbonate minerals are found in our system, the first leaching experiment clearly indicated the occurrence of very labile Ca-bearing phases such as secondary carbonates.

Contrarily, we showed that when the saturation increases in the catchment, and we pass from base- to high-flow conditions, ground- and stream-water isotopic compositions become closer to those of SS, indicating that a high connectivity of the system is reached. This was also observable in the trend of all ground- and stream-waters from bicarbonate to sulfate-chloride compositions like those of the upper subsurface compartments (SS and GW1 or GW6). Nonetheless, we could note that the different reservoirs (PPSD and deeper GW's) remain isotopically different even when connected. This allowed us to discriminate that, in high (and peak) flow conditions it is specifically the SS reservoir that contributes to the stream isotopic composition, which then adopts higher $^{87}\text{Sr}/^{86}\text{Sr}$ and $^{206}\text{Pb}/^{204}\text{Pb}$ ratios (0.717 and 18.22 respectively) and comparatively low $^{234}\text{U}/^{238}\text{U}$ activity ratios (1.4).

The variations observed in $\delta^{18}\text{O}$ point to the fact that the Weierbach catchment behaves as a rather open and well-connected system. However, in our study this tracer did not allow further

differentiation of the reservoirs contributing to the stream under different hydrological conditions. Here, the characterization of anthropogenic, atmosphere -derived end member, especially through the Pb isotopes, was particularly helpful to determine the contributing sources. However, it must be noted that neither the forest dusts ($^{87}\text{Sr}/^{86}\text{Sr} = 0.713726$, $^{234}\text{U}/^{238}\text{U} = 1.0057$) nor throughfall ($^{87}\text{Sr}/^{86}\text{Sr} = 0.71166$, $^{234}\text{U}/^{238}\text{U} = 1.1192$) were found to have a *direct* impact on the isotopic dynamics of the water samples, but an *indirect* one through the “contaminated” PPSD or SP reservoirs. Therefore, these isotopic results do not allow confirming previous assumptions on the direct contribution of precipitation on the Weierbach stream during storm events (Martínez-Carreras et al., 2016; Wrede et al., 2015).

On the other hand, the fact that the SS signatures are found in the stream indicates that part of these waters has travelled through a sub-surface lateral flow or through the fractured bedrock, by-passing the other reservoirs. These results do support previous findings by Martinez-Carreras et al. (2016) and Scaini et al. (2017), which suggested the contribution of PPSD reservoirs through the PPSD-SP interface or bedrock fractures under high saturation conditions in the Weierbach catchment. The extent to which these contributions originate specifically from the plateau or the hillslope areas, as suggested by Martinez-Carreras et al (2015), cannot be here assessed due to the lack of SS isotopic data around the catchment. An improved sampling set-up for the Weierbach catchment including hillslope transects would be ideal for such complementary radiogenic isotope assessment. Nonetheless, it must be considered that, in the case of the Weierbach catchment and for the hydrological conditions here considered, radiogenic isotopes do not seem to allow for storm-event time scale hydrological studies, but only “seasonal”.

Perspectives

To summarize, the concurrent study of the regolith (including atmospheric inputs) and the waters, through the combined use of isotopic and chemical data allowed better understanding the critical zone puzzle by informing on the mechanisms responsible for solutes release and transportation through the catchment. To our knowledge, this work targets the first ever tracing of an entire hydrological system with trace element concentrations and the Sr-Nd-Pb-U radiogenic isotopes, which are shown as a reliable complementary tool to major elements and O-H isotopes for the study of sub-surface hydrological processes.

As a perspective, this kind of study could be extended by developing on the characterization of microscopic features such as metastable mineral phases and (organic/inorganic) colloidal complexes, susceptible of controlling trace element behaviour during weathering and transport processes. In this sense, also the monitoring of the redox potential in the different reservoirs would be of interest to better understand the water chemistry of trace and rare earth elements.

On the other hand, the extension of field samplings towards more representative spatial scales, such as hillslope transects including sampling points of soil-, ground- and riparian- waters, would allow a more precise assessment of connectivity at catchment scale. This, together with the calculation of elemental fluxes and/or weathering rates, may allow the use of trace elements and isotopic ratios for the development of more realistic end member mixing analyses (EMMA) and hydrological models. The combination of trace elements and radiogenic isotopes as spatial hydrological tracers with O and H stable isotopes implemented in transit (/residence) time calculations shows great potential to improve our understanding on catchments functioning.

Naturally, the question rises whether the concentrations and temporal variability of radiogenic isotopes, as well as the analytical costs would be a limitation for hydrological studies in different catchments. Catchments of different sizes and subsurface properties, will offer different possibilities for this kind of studies. Finally, we must note that even for a same catchment, different flood typologies (according to precipitation intensity and antecedent wetness conditions) should be considered in order to assess the usefulness of radiogenic isotopes as hydrological tracers.

Bibliography

- Ad-hoc-Arbeitsgruppe Boden, 2005. Bodenkundliche Kartieranleitung. KA5. Schweizerbart Science Publishers, Stuttgart, Germany.
- Allègre, C.J., Dupré, B., Nègre, P., Gaillardet, J., All, C.J., Dupr, B., Philippe, N., Gaillardet, J., 1996. Sr-Nd-Pb isotope systematics in Amazon and Congo River systems : Constraints about erosion processes. *Chem. Geol.* 131, 93–112. doi:10.1016/0009-2541(96)00028-9
- Andrews, J.N., Kay, R.L.F., 1983. The U contents and $^{234}\text{U}/^{238}\text{U}$ activity ratios of dissolved uranium in groundwaters from some Triassic Sandstones in England. *Chem. Geol.* 41, 101–117. doi:10.1016/S0009-2541(83)80011-4
- Aubert, D., Probst, A., Stille, P., Viville, D., 2002a. Evidence of hydrological control of Sr behavior in stream water (Strengbach catchment, Vosges mountains, France). *Appl. Geochemistry* 17, 285–300. doi:10.1016/S0883-2927(01)00080-4
- Aubert, D., Stille, P., Probst, A., 2001. REE fractionation during granite weathering and removal by waters and suspended loads: Sr and Nd isotopic evidence. *Geochim. Cosmochim. Acta* 65, 387–406. doi:10.1016/S0016-7037(00)00546-9
- Aubert, D., Stille, P., Probst, A., Gauthier-Lafaye, F., Pourcelot, L., DelNero, M., 2002b. Characterization and migration of atmospheric REE in soils and surface waters. *Geochim. Cosmochim. Acta* 66, 3339–3350. doi:10.1016/S0016-7037(02)00913-4
- Banwart, S., Bernasconi, S.M., Bloem, J., Blum, W., Brandao, M., Brantley, S., Chabaux, F., Duffy, C., Kram, P., Lair, G., Lundin, L., Nikolaidis, N., Novak, M., Panagos, P., Ragnarsdottir, K.V., Reynolds, B., Rousseva, S., de Ruiter, P., van Gaans, P., van Riemsdijk, W., White, T., Zhang, B., 2011. Soil Processes and Functions in Critical Zone

Observatories: Hypotheses and Experimental Design. *Vadose Zo. J.* 10, 974.
doi:10.2136/vzj2010.0136

Barbier, F., 2012. Etude de paléoaaltération météorique (Crétacé Inférieur à Néogène) sur socle silicoclastique hétérogène: caractérisation et essai de cartographie d'altérites en Région Wallonne (Belgique). FUNDP Ecole doctorale en sciences.

Barthold, F.K., Tyralla, C., Schneider, K., Vaché, K.B., Frede, H.G., Breuer, L., 2011. How many tracers do we need for end member mixing analysis (EMMA)? A sensitivity analysis. *Water Resour. Res.* 47, 1–14. doi:10.1029/2011WR010604

Barthold, F.K., Wu, J., Vaché, K.B., Schneider, K., Frede, H.-G., Breuer, L., 2010. Identification of geographic runoff sources in a data sparse region: hydrological processes and the limitations of tracer-based approaches. *Hydrol. Process.* 24, 2313–2327. doi:10.1002/hyp.7678

Berger, A., Janots, E., Gnos, E., Frei, R., Bernier, F., 2014. Rare earth element mineralogy and geochemistry in a laterite profile from Madagascar. *Appl. Geochemistry* 41, 218–228. doi:10.1016/j.apgeochem.2013.12.013

Berner, E.K., Berner, R.A., 1996. Global environment: water, air, and geochemical cycles. Prentice Hall.

Berner, R.A., Maasch, K.A., 1996. Chemical weathering and controls on atmospheric O₂ and CO₂: Fundamental principles were enunciated by J.J. Ebelmen in 1845. *Geochim. Cosmochim. Acta* 60, 1633–1637. doi:10.1016/0016-7037(96)00104-4

Bini, C., Sartori, G., Wahsha, M., Fontana, S., 2011. Background levels of trace elements and soil geochemistry at regional level in NE Italy. *J. Geochemical Explor.* 109, 125–133. doi:10.1016/j.gexplo.2010.07.008

Biscaye, P.E., Grousset, F.E., Revel, M., Van der Gaast, S., Zielinski, G.A., Vaars, A., Kukla, G., 1997. Asian provenance of glacial dust (stage 2) in the Greenland Ice Sheet Project 2 Ice Core, Summit, Greenland. *J. Geophys. Res. Ocean.* 102, 26765–26781. doi:10.1029/97JC01249

Blum, J.D., Erel, Y., 2003. 5.12 - Radiogenic Isotopes in Weathering and Hydrology, in: Holland, H.D., Turekian, K.K. (Eds.), *Treatise on Geochemistry*. Pergamon, Oxford, pp. 365–392. doi:https://doi.org/10.1016/B0-08-043751-6/05082-9

Bonjour, J.-L., Dabard, M.-P., 1991. Ti/Nb ratios of clastic terrigenous sediments used as an

- indicator of provenance. *Chem. Geol.* 91, 257–267. doi:10.1016/0009-2541(91)90003-A
- Brantley, S.L., Goldhaber, M.B., Vala Ragnarsdottir, K., 2007. Crossing disciplines and scales to understand the critical zone. *Elements* 3, 307–314. doi:10.2113/gselements.3.5.307
- Brantley, S.L., White, T.S., White, A.F., Sparks, D., Richter, D., Pregitzer, K., Derry, L., Chorover, J., Chadwick, O., April, R., Anderson, S., Amundson, R., 2006. *Frontiers in Exploration of the Critical Zone: Report of a workshop sponsored by the National Science Foundation (NSF), October 24-26, 2005, Newark, DE*, 30p.
- Braun, J.-J., Pagel, M., Muller, J.-P., Bilong, P., Michard, A., Guillet, B., 1990. Cerium anomalies in lateritic profiles. *Geochim. Cosmochim. Acta* 54, 781–795. doi:10.1016/0016-7037(90)90373-S
- Braun, J.-J., Viers, J., Dupré, B., Polvé, M., Ndam, J., Muller, J.-P., 1998. Solid/Liquid REE Fractionation in the Lateritic System of Goyoum, East Cameroon: The Implication for the Present Dynamics of the Soil Covers of the Humid Tropical Regions. *Geochim. Cosmochim. Acta* 62, 273–299. doi:10.1016/S0016-7037(97)00344-X
- Brookins, D.G., 1989. Aqueous geochemistry of rare earth elements, in: Lippin, B.R., McKay, G.A. (Eds.), *Reviews in Mineralogy: Geochem- Istry and Mineralogy of Rare Earth Elements*, Vol. 21. Mineral Society of America, Washington, DC, p. 201–223.
- Brooks, J.R., Barnard, H.R., Coulombe, R., McDonnell, J.J., 2010. Ecohydrologic separation of water between trees and streams in a Mediterranean climate. *Nat. Geosci.* 3, 100–104. doi:10.1038/ngeo722
- Brooks, P.D., Chorover, J., Fan, Y., Godsey, S.E., Maxwell, R.M., McNamara, J.P., Tague, C., 2015. Hydrological partitioning in the critical zone: Recent advances and opportunities for developing transferable understanding of water cycle dynamics. *Water Resour. Res.* 51, 6973–6987. doi:10.1002/2015WR017039
- Bruno, J., De Pablo, J., Duro, L., Figuerola, E., 1995. Experimental study and modeling of the U(VI)-Fe(OH)₃ surface precipitation/coprecipitation equilibria. *Geochim. Cosmochim. Acta* 59, 4113–4123. doi:10.1016/0016-7037(95)00243-S
- Burns, D.A., McDonnell, J.J., Hooper, R.P., Peters, N.E., Freer, J.E., Kendall, C., Beven, K., 2001. Quantifying contributions to storm runoff through end-member mixing analysis and hydrologic measurements at the Panola Mountain Research Watershed (Georgia, USA). *Hydrol. Process.* 15, 1903–1924. doi:10.1002/hyp.246

- Byrne, R.H., Li, B., 1995. Comparative complexation behavior of the rare earths. *Geochim. Cosmochim. Acta* 59, 4575–4589. doi:10.1016/0016-7037(95)00303-7
- Camacho, A., Devesa, R., Vallés, I., Serrano, I., Soler, J., Blázquez, S., Ortega, X., Matia, L., 2010. Distribution of uranium isotopes in surface water of the Llobregat river basin (Northeast Spain). *J. Environ. Radioact.* 101, 1048–1054. doi:10.1016/j.jenvrad.2010.08.005
- Carignan, J., Gariépy, C., 1995. Isotopic composition of epiphytic lichens as a tracer of the sources of atmospheric lead emissions in southern Québec, Canada. *Geochim. Cosmochim. Acta* 59, 4427–4433. doi:10.1016/0016-7037(95)00302-G
- Carignan, J., Libourel, G., Cloquet, C., Le Forestier, L., 2005. Lead Isotopic Composition of Fly Ash and Flue Gas Residues from Municipal Solid Waste Combustors in France: Implications for Atmospheric Lead Source Tracing. *Environ. Sci. Technol.* 39, 2018–2024. doi:10.1021/es048693x
- Carignan, J., Simonetti, A., Gariépy, C., 2002. Dispersal of atmospheric lead in northeastern North America as recorded by epiphytic lichens. *Atmos. Environ.* 36, 3759–3766. doi:10.1016/S1352-2310(02)00294-7
- Catt, J.A., 1986. *Soils and Quaternary geology: a handbook for field scientists*. Oxford University Press, Oxford, UK.
- Chabaux, F., Blaes, E., Stille, P., di Chiara Roupert, R., Pelt, E., Dosseto, A., Ma, L., Buss, H.L., Brantley, S.L., 2013. Regolith formation rate from U-series nuclides: Implications from the study of a spheroidal weathering profile in the Rio Icacos watershed (Puerto Rico). *Geochim. Cosmochim. Acta* 100, 73–95. doi:10.1016/j.gca.2012.09.037
- Chabaux, F., Bourdon, B., Riotte, J., 2008. Chapter 3 U-Series Geochemistry in Weathering Profiles, River Waters and Lakes. Elsevier, pp. 49–104. doi:10.1016/S1569-4860(07)00003-4
- Chabaux, F., Dequincey, O., Lévêque, J.-J., Leprun, J.-C., Clauer, N., Riotte, J., Paquet, H., 2003. Tracing and dating recent chemical transfers in weathering profiles by trace-element geochemistry and ^{238}U – ^{234}U – ^{230}Th disequilibria: the example of the Kaya lateritic toposequence (Burkina-Faso). *Comptes Rendus Geosci.* 335, 1219–1231. doi:10.1016/j.crte.2003.10.007
- Chabaux, F., Riotte, J., Dequincey, O., 2003. U-Th-Ra Fractionation During Weathering and River Transport. *Rev. Mineral. Geochemistry* 52, 533–576. doi:10.2113/0520533

- Chabaux, F., Riotte, J., Schmitt, A.-D., Carignan, J., Herckes, P., Pierret, M.-C., Wortham, H., 2005. Variations of U and Sr isotope ratios in Alsace and Luxembourg rain waters: origin and hydrogeochemical implications. *Comptes Rendus Geosci.* 337, 1447–1456. doi:10.1016/j.crte.2005.07.008
- Chabaux, F., Unions, R.K., Cohen, A.S., Hein, J.R., 1997. $^{238}\text{U}/^{234}\text{U}$ disequilibrium in hydrogenous oceanic FeMn crusts: Palaeoceanographic record or diagenetic alteration? *Geochim. Cosmochim. Acta* 61, 3619–3632. doi:10.1016/S0016-7037(97)00187-7
- Chauvel, C., Garçon, M., Bureau, S., Besnault, A., Jahn, B., Ding, Z., 2014. Constraints from loess on the Hf–Nd isotopic composition of the upper continental crust. *Earth Planet. Sci. Lett.* 388, 48–58. doi:10.1016/j.epsl.2013.11.045
- Chorover, J., Troch, P.A., Rasmussen, C., Brooks, P.D., Pelletier, J.D., Breshears, D.D., Huxman, T.E., Kurc, S.A., Lohse, K.A., McIntosh, J.C., Meixner, T., Schaap, M.G., Litvak, M.E., Perdrial, J., Harpold, A., Durcik, M., 2011. How Water, Carbon, and Energy Drive Critical Zone Evolution: The Jemez–Santa Catalina Critical Zone Observatory. *Vadose Zo. J.* 10, 884. doi:10.2136/vzj2010.0132
- Christophersen, N., Hooper, R.P., 1992. Multivariate analysis of stream water chemical data: The use of principal components analysis for the end-member mixing problem. *Water Resour. Res.* 28, 99–107. doi:10.1029/91WR02518
- Cloutier, V., Lefebvre, R., Therrien, R., Savard, M.M., 2008. Multivariate statistical analysis of geochemical data as indicative of the hydrogeochemical evolution of groundwater in a sedimentary rock aquifer system. *J. Hydrol.* 353, 294–313. doi:10.1016/j.jhydrol.2008.02.015
- Cole, H.M., 1965. The Ardennes: Battle of the Bulge.
- Condie, K.C., 1993. Chemical composition and evolution of the upper continental crust: Contrasting results from surface samples and shales. *Chem. Geol.* 104, 1–37. doi:10.1016/0009-2541(93)90140-E
- Condie, K.C., 1991. Another look at rare earth elements in shales. *Geochim. Cosmochim. Acta* 55, 2527–2531. doi:https://doi.org/10.1016/0016-7037(91)90370-K
- Craig, M.A., Wilford, J.R., Tapley, I.J., 1999. Regolith-landform mapping in the Gawler Craton - an alternative approach.
- Davranche, M., Gérard Grau, Dia, A., Le Coz-Bouhnik, M., Marsac, R., Pédrot, M., Pourret, O.,

2013. Rare Earth Elements in Wetlands.

- Davranche, M., Grybos, M., Gruau, G., Pédrot, M., Dia, A., Marsac, R., 2011. Rare earth element patterns: A tool for identifying trace metal sources during wetland soil reduction. *Chem. Geol.* 284, 127–137. doi:10.1016/j.chemgeo.2011.02.014
- Debajyoti, P., White, W. M., Turcotte, D.L., 1967. Modelling isotopic evolution of Earth. *Br. Med. J.* 4, 438.
- Deckers, J., 1966. Contribution à l'étude de la composition et de la capacité de production des sols de l'Ardenne centrale et de la Famenne orientale, Société belge de Pédologie, Gand, Belgique.
- Demoulin, A., 2003. Paleosurfaces and residual deposits in Ardenne-Eifel: historical overview and perspectives. *Géologie la Fr.* n° 1, 17–21.
- Deniel, C., Pin, C., 2001. Single-stage method for the simultaneous isolation of lead and strontium from silicate samples for isotopic measurements. *Anal. Chim. Acta* 426, 95–103. doi:10.1016/S0003-2670(00)01185-5
- DePaolo, D.J., Lee, V.E., Christensen, J.N., Maher, K., 2012. Uranium comminution ages: Sediment transport and deposition time scales. *Comptes Rendus Geosci.* 344, 678–687. doi:10.1016/j.crte.2012.10.014
- DePaolo, D.J., Maher, K., Christensen, J.N., McManus, J., 2006. Sediment transport time measured with U-series isotopes: Results from ODP North Atlantic drift site 984. *Earth Planet. Sci. Lett.* 248, 394–410. doi:10.1016/j.epsl.2006.06.004
- Dequincey, O., Chabaux, F., Clauer, N., Sigmarsson, O., Liewig, N., Leprun, J.-C., 2002. Chemical mobilizations in laterites: evidence from trace elements and ^{238}U - ^{234}U - ^{230}Th disequilibria. *Geochim. Cosmochim. Acta* 66, 1197–1210. doi:10.1016/S0016-7037(01)00845-6
- Désiré-Marchand, J., 1985. Notice de la carte géomorphologique du Grand-Duché de Luxembourg. *Serv. Géologique Luxemb. Bulletin.*, (47 p).
- Dia, A., Gruau, G., Olivie-Lauquet, G., Riou, C., Molénat, J., Curmi, P., 2000. The distribution of rare earth elements in groundwaters: assessing the role of source-rock composition, redox changes and colloidal particles. *Geochim. Cosmochim. Acta* 64, 4131–4151. doi:10.1016/S0016-7037(00)00494-4
- Dietze, M., Kleber, A., 2010. Characterisation and prediction of thickness and material

- properties of periglacial cover beds, Tharandter Wald, Germany. *Geoderma* 156, 346–356. doi:10.1016/j.geoderma.2010.03.004
- Dosseto, A., Bourdon, B., Turner, S.P., 2008. Uranium-series isotopes in river materials: Insights into the timescales of erosion and sediment transport. *Earth Planet. Sci. Lett.* 265, 1–17. doi:10.1016/j.epsl.2007.10.023
- Dosseto, A., Buss, H.L., Suresh, P., 2012. Rapid regolith formation over volcanic bedrock and implications for landscape evolution. *Earth Planet. Sci. Lett.* 337–338, 47–55. doi:10.1016/j.epsl.2012.05.008
- Doucélance, R., Manhès, G., 2001. Reevaluation of precise lead isotope measurements by thermal ionization mass spectrometry: comparison with determinations by plasma source mass spectrometry. *Chem. Geol.* 176, 361–377. doi:10.1016/S0009-2541(00)00409-5
- Duff, M.C., Coughlin, J.U., Hunter, D.B., 2002. Uranium co-precipitation with iron oxide minerals. *Geochim. Cosmochim. Acta* 66, 3533–3547. doi:10.1016/S0016-7037(02)00953-5
- Dupré, B., Viers, J., Dandurand, J.L., Polve, M., Bénézech, P., Vervier, P., Braun, J.J., 1999. Major and trace elements associated with colloids in organic-rich river waters: Ultrafiltration of natural and spiked solutions. *Chem. Geol.* 160, 63–80. doi:10.1016/S0009-2541(99)00060-1
- Eggleton, R.A., 2001. The regolith glossary: surficial geology, soils, and landscapes. Cooperative Research Centre for Landscape Evolution and Mineral Exploration, Floreat Park, W.A.
- El Azzi, D., Probst, J.L., Teisserenc, R., Merlina, G., Baqu?, D., Julien, F., Payre-Suc, V., Guiesse, M., 2016. Trace Element and Pesticide Dynamics During a Flood Event in the Save Agricultural Watershed: Soil-River Transfer Pathways and Controlling Factors. *Water. Air. Soil Pollut.* 227. doi:10.1007/s11270-016-3144-0
- Elderfield, H., Upstill-Goddard, R., Sholkovitz, E.R., 1990. The rare earth elements in rivers, estuaries, and coastal seas and their significance to the composition of ocean waters. *Geochim. Cosmochim. Acta* 54, 971–991. doi:10.1016/0016-7037(90)90432-K
- Faure, G., 1977. Principles of isotope geology. John Wiley and Sons, Inc., New York, NY.
- Felix-Henningsen, P., 1994. Mesozoic-Tertiary weathering and soil formation on slates of the Rhenish Massif, Germany. *Catena* 21, 229–242. doi:10.1016/0341-8162(94)90014-0

- Field, J.P., Breshears, D.D., Law, D.J., Villegas, J.C., López-Hoffman, L., Brooks, P.D., Chorover, J., Barron-Gafford, G.A., Gallery, R.E., Litvak, M.E., Lybrand, R.A., McIntosh, J.C., Meixner, T., Niu, G.-Y., Papuga, S.A., Pelletier, J.D., Rasmussen, C.R., Troch, P.A., 2015. Critical Zone Services: Expanding Context, Constraints, and Currency beyond Ecosystem Services. *Vadose Zo. J.* 14, 0. doi:10.2136/vzj2014.10.0142
- Flegal, A.R., Nriagu, J.O., Niemeyer, S., Coale, K.H., 1989. Isotopic tracers of lead contamination in the Great Lakes. *Nature* 339, 455–458. doi:10.1038/339455a0
- Fröhlich, H.L., Breuer, L., Vach, K.B., Frede, H.G., 2008. Inferring the effect of catchment complexity on mesoscale hydrologic response. *Water Resour. Res.* 44, 1–15. doi:10.1029/2007WR006207
- Gabrielli, C.P., McDonnell, J.J., 2012. An inexpensive and portable drill rig for bedrock groundwater studies in headwater catchments. *Hydrol. Process.* 26, 622–632. doi:10.1002/hyp.8212
- Gaillardet, J., Viers, J., Dupré, B., 2003. 5.09 - Trace Elements in River Waters, in: Holland, H.D., Turekian, K.K. (Eds.), *Treatise on Geochemistry*. Pergamon, Oxford, pp. 225–272. doi:https://doi.org/10.1016/B0-08-043751-6/05165-3
- Gallet, S., Jahn, B., Van Vliet Lanoë, B., Dia, A., Rossello, E., 1998. Loess geochemistry and its implications for particle origin and composition of the upper continental crust. *Earth Planet. Sci. Lett.* 156, 157–172. doi:10.1016/S0012-821X(97)00218-5
- Gangloff, S., Stille, P., Pierret, M.C., Weber, T., Chabaux, F., 2014. Characterization and evolution of dissolved organic matter in acidic forest soil and its impact on the mobility of major and trace elements (case of the Strengbach watershed). *Geochim. Cosmochim. Acta* 130, 21–41. doi:10.1016/j.gca.2013.12.033
- Garçon, M., Chauvel, C., France-Lanord, C., Limonta, M., Garzanti, E., 2014. Which minerals control the Nd–Hf–Sr–Pb isotopic compositions of river sediments? *Chem. Geol.* 364, 42–55. doi:10.1016/j.chemgeo.2013.11.018
- Geagea, M.L., Stille, P., Millet, M., Perrone, T., 2007. REE characteristics and Pb, Sr and Nd isotopic compositions of steel plant emissions. *Sci. Total Environ.* 373, 404–19. doi:10.1016/j.scitotenv.2006.11.011
- Glaser, B., Klaus, J., Frei, S., Frentress, J., Pfister, L., Hopp, L., 2016. On the value of surface saturated area dynamics mapped with thermal infrared imagery for modeling the hillslope-riparian-stream continuum. *Water Resour. Res.* 52, 8317–8342.

doi:10.1002/2015WR018414

- Goldstein, S.L., O’Nions, R.K., Hamilton, P.J., 1984. A Sm-Nd isotopic study of atmospheric dusts and particulates from major river systems. *Earth Planet. Sci. Lett.* 70, 221–236. doi:10.1016/0012-821X(84)90007-4
- Gourdol, L., Hissler, C., Hoffmann, L., Pfister, L., 2013. On the potential for the Partial Triadic Analysis to grasp the spatio-temporal variability of groundwater hydrochemistry. *Appl. Geochemistry* 39, 93–107. doi:10.1016/j.apgeochem.2013.10.002
- Granet, M., Chabaux, F., Stille, P., Dosseto, A., France-Lanord, C., Blaes, E., 2010. U-series disequilibria in suspended river sediments and implication for sediment transfer time in alluvial plains: The case of the Himalayan rivers. *Geochim. Cosmochim. Acta* 74, 2851–2865. doi:10.1016/j.gca.2010.02.016
- Graustein, W.C., 1989. *⁸⁷Sr/⁸⁶Sr Ratios Measure the Sources and Flow of Strontium in Terrestrial Ecosystems*. Springer, New York, NY, pp. 491–512. doi:10.1007/978-1-4612-3498-2_28
- Grobéty, B., Gieré, R., Dietze, V., Stille, P., 2010. Airborne Particles in the Urban Environment. *Elements* 6, 229. doi:10.2113/gselements.6.4.229
- Grousset, F.E., Biscaye, P.E., 2005. Tracing dust sources and transport patterns using Sr, Nd and Pb isotopes. *Chem. Geol.* 222, 149–167. doi:10.1016/j.chemgeo.2005.05.006
- Gruau, G., Dia, A., Olivié-Lauquet, G., Davranche, M., Pinay, G., 2004. Controls on the distribution of rare earth elements in shallow groundwaters. *Water Res.* 38, 3576–3586. doi:10.1016/j.watres.2004.04.056
- Guéguen, F., Stille, P., Dietze, V., Gieré, R., 2012a. Chemical and isotopic properties and origin of coarse airborne particles collected by passive samplers in industrial, urban, and rural environments. *Atmos. Environ.* 62, 631–645. doi:10.1016/j.atmosenv.2012.08.044
- Guéguen, F., Stille, P., Lahd Geagea, M., Boutin, R., 2012b. Atmospheric pollution in an urban environment by tree bark biomonitoring--part I: trace element analysis. *Chemosphere* 86, 1013–9. doi:10.1016/j.chemosphere.2011.11.040
- Güler, C., Thyne, G.D., McCray, J.E., Turner, K. a., 2002. Evaluation of graphical and multivariate statistical methods for classification of water chemistry data. *Hydrogeol. J.* 10, 455–474. doi:10.1007/s10040-002-0196-6
- Haase, D., Fink, J., Haase, G., Ruske, R., Pécsi, M., Richter, H., Altermann, M., Jäger, K.D.,

2007. Loess in Europe-its spatial distribution based on a European Loess Map, scale 1:2,500,000. *Quat. Sci. Rev.* 26, 1301–1312. doi:10.1016/j.quascirev.2007.02.003
- Hartigan, J.A., 1975. *Clustering Algorithms*, 99th ed. John Wiley & Sons, Inc., New York, NY, USA.
- Heijden, G. van der, Legout, A., Nicolas, M., Ulrich, E., Johnson, D.W., Dambrine, E., 2011. Long-term sustainability of forest ecosystems on sandstone in the Vosges Mountains (France) facing atmospheric deposition and silvicultural change. *For. Ecol. Manage.* 261, 730–740.
- Henderson, A.L., Foster, G.L., Najman, Y., 2010. Testing the application of in situ Sm-Nd isotopic analysis on detrital apatites: A provenance tool for constraining the timing of India-Eurasia collision. *Earth Planet. Sci. Lett.* 297, 42–49. doi:10.1016/j.epsl.2010.06.001
- Hissler, C., Probst, J.-L., 2006. Impact of mercury atmospheric deposition on soils and streams in a mountainous catchment (Vosges, France) polluted by chlor-alkali industrial activity: the important trapping role of the organic matter. *Sci. Total Environ.* 361, 163–78. doi:10.1016/j.scitotenv.2005.05.023
- Hissler, C., Stille, P., Iffly, J.F., Guignard, C., Chabaux, F., Pfister, L., 2016. Origin and Dynamics of Rare Earth Elements during Flood Events in Contaminated River Basins: Sr–Nd–Pb Isotopic Evidence. *Environ. Sci. Technol.* 50, 4624–4631. doi:10.1021/acs.est.5b03660
- Hissler, C., Stille, P., Juilleret, J., Iffly, J.F., Perrone, T., Morvan, G., 2015. Elucidating the formation of terra fusca using Sr–Nd–Pb isotopes and rare earth elements. *Appl. Geochemistry* 54, 85–99. doi:10.1016/j.apgeochem.2015.01.011
- Hissler, C., Stille, P., Krein, A., Geagea, M.L., Perrone, T., Probst, J.L., Hoffmann, L., 2008. Identifying the origins of local atmospheric deposition in the steel industry basin of Luxembourg using the chemical and isotopic composition of the lichen *Xanthoria parietina*. *Sci. Total Environ.* 405, 338–344. doi:10.1016/j.scitotenv.2008.05.029
- Hooper, R.P., Christophersen, N., Peters, N.E., 1990. Modelling streamwater chemistry as a mixture of soilwater end-members — An application to the Panola Mountain catchment, Georgia, U.S.A. *J. Hydrol.* 116, 321–343. doi:10.1016/0022-1694(90)90131-G
- Huckle, D., Ma, L., McIntosh, J., Vázquez-Ortega, A., Rasmussen, C., Chorover, J., 2016. U-series isotopic signatures of soils and headwater streams in a semi-arid complex volcanic terrain. *Chem. Geol.* 445, 68–83. doi:10.1016/j.chemgeo.2016.04.003

- Huguet, F., 1998. Le Hunsrück : un jalon dans l'évolution géomorphologique de la chaîne varisque/Between Hohes Venn and Schwartzwald, geomorphological investigations in Hunsrück (Rhenish Massif). *Géomorphologie Reli. Process. Environ.* 4, 233–250. doi:10.3406/morfo.1998.957
- Inamdar, S., 2011. The Use of Geochemical Mixing Models to Derive Runoff Sources and Hydrologic Flow Paths. Springer Netherlands, pp. 163–183. doi:10.1007/978-94-007-1363-5_8
- Inamdar, S., Dhillon, G., Singh, S., Dutta, S., Levia, D., Scott, D., Mitchell, M., Van Stan, J., McHale, P., 2013. Temporal variation in end-member chemistry and its influence on runoff mixing patterns in a forested, Piedmont catchment. *Water Resour. Res.* 49, 1828–1844. doi:10.1002/wrcr.20158
- Juilleret, J., Iffly, J.F., Pfister, L., Hissler, C., 2011. Remarkable Pleistocene periglacial slope deposits in Luxem-bourg (Oesling): pedological implication and geosite potential. *Bull. la Société des Nat. Luxemb.* 112, 125–130.
- Kaiser, H.F., 1958. The varimax criterion for analytic rotation in factor analysis. *Psychometrika* 23, 187–200. doi:10.1007/BF02289233
- Kaufman, L., Rouseeuw, P.J., 1990. Finding Groups in Data. John Wiley and Sons Inc., NY.
- Klaus, J., McDonnell, J.J., 2013. Hydrograph separation using stable isotopes: Review and evaluation. *J. Hydrol.* 505, 47–64. doi:10.1016/j.jhydrol.2013.09.006
- Klaus, J., Wetzel, C.E., Martínez-Carreras, N., Ector, L., Pfister, L., 2015. A tracer to bridge the scales: on the value of diatoms for tracing fast flow path connectivity from headwaters to meso-scale catchments. *Hydrol. Process.* 29, 5275–5289. doi:10.1002/hyp.10628
- Kleber, A., 1997. Cover-beds as soil parent materials in midlatitude regions. *CATENA* 30, 197–213. doi:10.1016/S0341-8162(97)00018-0
- Kleber, A., Terhorst, B., 2013. Mid-Latitude Slope Deposits (Cover Beds), Developments in Sedimentology, Developments in Sedimentology. Elsevier. doi:10.1016/B978-0-444-53118-6.00001-5
- Kwaad, F.J.P.M., Mùcher, H.J., 1977. The evolution of soils and slope deposits in the Luxembourg Ardennes near wiltz. *Geoderma* 17, 1–37. doi:10.1016/0016-7061(77)90002-7
- Ladouche, B., Probst, A., Viville, D., Idir, S., Baqué, D., Loubet, M., Probst, J.-L., Bariac, T.,

2001. Hydrograph separation using isotopic, chemical and hydrological approaches (Strengbach catchment, France). *J. Hydrol.* 242, 255–274. doi:10.1016/S0022-1694(00)00391-7
- Lahd Geagea, M., Stille, P., Gauthier-lafaye, F., Millet, M., Centre, E., De, D.G., 2008. Tracing of industrial aerosol sources in an urban environment using Pb , Sr and Nd isotopes. *Environ. Sci. Technol.* 42, 692–698.
- Lahd Geagea, M., Stille, P., Gauthier-Lafaye, F., Perrone, T., Aubert, D., 2008. Baseline determination of the atmospheric Pb, Sr and Nd isotopic compositions in the Rhine valley, Vosges mountains (France) and the Central Swiss Alps. *Appl. Geochemistry* 23, 1703–1714. doi:10.1016/j.apgeochem.2008.02.004
- Lauf, R.J., 2014. An Introduction to the Rock-Forming Minerals, 3rd ed., by William A. Deer, Robert A. Howie, and Jack Zussman. The Mineralogical Society, London. 498 pages; 2013; £45 plus shipping (softbound). *Rocks Miner.* 89, 474–475. doi:10.1080/00357529.2014.926186
- Laveuf, C., Cornu, S., 2009. A review on the potentiality of Rare Earth Elements to trace pedogenetic processes. *Geoderma* 154, 1–12. doi:10.1016/j.geoderma.2009.10.002
- Laveuf, C., Cornu, S., Guilherme, L.R.G., Guerin, A., Juillot, F., 2012. The impact of redox conditions on the rare earth element signature of redoximorphic features in a soil sequence developed from limestone. *Geoderma* 170, 25–38. doi:10.1016/j.geoderma.2011.10.014
- Levitan, D.M., Zipper, C.E., Donovan, P., Schreiber, M.E., Seal, R.R., Engle, M. a., Chermak, J. a., Bodnar, R.J., Johnson, D.K., Aylor, J.G., 2015. Statistical analysis of soil geochemical data to identify pathfinders associated with mineral deposits: An example from the Coles Hill uranium deposit, Virginia, USA. *J. Geochemical Explor.* 154, 238–251. doi:10.1016/j.gexplo.2014.12.012
- Lin, X., Wang, X., Zhang, B., Yao, W., 2014. Multivariate analysis of regolith sediment geochemical data from the Jinwozi gold field, north-western China. *J. Geochemical Explor.* 137, 48–54. doi:10.1016/j.gexplo.2013.11.006
- Lorz, C., Phillips, J.D., 2006. Pedo-ecological consequences of lithological discontinuities in soils - Examples from Central Europe. *J. Plant Nutr. Soil Sci.* 169, 573–581. doi:10.1002/jpln.200521872
- Martínez-Carreras, N., Hissler, C., Gourdol, L., Klaus, J., Juilleret, J., Iffly, J.F., Pfister, L., 2016. Storage controls on the generation of double peak hydrographs in a forested

- headwater catchment. *J. Hydrol.* 543, 255–269. doi:10.1016/j.jhydrol.2016.10.004
- Martínez-Carreras, N., Udelhoven, T., Krein, A., Gallart, F., Iffly, J.F., Ziebel, J., Hoffmann, L., Pfister, L., Walling, D.E., 2010. The use of sediment colour measured by diffuse reflectance spectrometry to determine sediment sources: Application to the Attert River catchment (Luxembourg). *J. Hydrol.* 382, 49–63. doi:10.1016/j.jhydrol.2009.12.017
- Martínez-Carreras, N., Wetzel, C.E., Frentress, J., Ector, L., McDonnell, J.J., Hoffmann, L., Pfister, L., 2015. Hydrological connectivity inferred from diatom transport through the riparian-stream system. *Hydrol. Earth Syst. Sci.* 19, 3133–3151. doi:10.5194/hess-19-3133-2015
- McClain, M.E., Boyer, E.W., Dent, C.L., Gergel, S.E., Grimm, N.B., Groffman, P.M., Hart, S.C., Harvey, J.W., Johnston, C.A., Mayorga, E., McDowell, W.H., Pinay, G., 2003. Biogeochemical Hot Spots and Hot Moments at the Interface of Terrestrial and Aquatic Ecosystems. *Ecosystems* 6, 301–312. doi:10.1007/s10021-003-0161-9
- McFarlane, C.R.M., McCulloch, M.T., 2007. Coupling of in-situ Sm-Nd systematics and U-Pb dating of monazite and allanite with applications to crustal evolution studies. *Chem. Geol.* 245, 45–60. doi:10.1016/j.chemgeo.2007.07.020
- McGuire, K.J., McDonnell, J.J., 2006. A review and evaluation of catchment transit time modeling. *J. Hydrol.* 330, 543–563. doi:10.1016/j.jhydrol.2006.04.020
- Michard, A., Gurriet, P., Soudant, M., Albarede, F., 1985. Nd isotopes in French Phanerozoic shales: external vs. internal aspects of crustal evolution. *Geochim. Cosmochim. Acta* 49, 601–610. doi:10.1016/0016-7037(85)90051-1
- Michelutti, N., Simonetti, A., Briner, J.P., Funder, S., Creaser, R.A., Wolfe, A.P., 2009. Temporal trends of pollution Pb and other metals in east-central Baffin Island inferred from lake sediment geochemistry. *Sci. Total Environ.* 407, 5653–5662. doi:10.1016/j.scitotenv.2009.07.004
- Monna, F., Lancelot, J., Croudace, I.W., Cundy, A.B., Lewis, J.T., 1997. Pb Isotopic Composition of Airborne Particulate Material from France and the Southern United Kingdom: Implications for Pb Pollution Sources in Urban Areas. *Environ. Sci. Technol.* 31, 2277–2286. doi:10.1021/es960870
- Moragues-Quiroga, C., Juilleret, J., Gourdol, L., Pelt, E., Perrone, T., Aubert, A., Morvan, G., Chabaux, F., Legout, A., Stille, P., Hissler, C., 2017. Genesis and evolution of regoliths: Evidence from trace and major elements and Sr-Nd-Pb-U isotopes. *CATENA* 149, 185–

198. doi:10.1016/j.catena.2016.09.015

Müller, E.H., 1954. Die Bedeutung des eiszeitlichen Bodenfließens (Solifluktion) für die Bodenbildung im nördlichen Teil des Rheinischen Schiefergebirges. *Zeitschrift für Pflanzenernährung, Düngung, Bodenkd.* 65, 52–61. doi:10.1002/jpln.19540650107

National Research Council, 2001. Basic Research Opportunities in Earth Science. The National Academies Press, Washington, DC. doi:10.17226/9981

Négrel, P., Petelet-Giraud, E., 2005. Strontium isotopes as tracers of groundwater-induced floods: the Somme case study (France). *J. Hydrol.* 305, 99–119. doi:10.1016/j.jhydrol.2004.08.031

Ohr, M., Halliday, A.N., Peacor, D.R., 1994. Mobility and fractionation of rare earth elements in argillaceous sediments: Implications for dating diagenesis and low-grade metamorphism. *Geochim. Cosmochim. Acta* 58, 289–312. doi:10.1016/0016-7037(94)90465-0

Osmond, J.K., Ivanovich, M., 1992. Uranium-series mobilization and surface hydrology, in: Harmon, M.I. and R.S. (Ed.), *Uranium Series Disequilibrium: Application to the Earth, Marine and Environmental Sciences*. Oxford University press, pp. 259–288.

P, I.S., 2011. Forest Hydrology and Biogeochemistry. *For. Hydrol. Biogeochem. Synth. past Res. Futur. Dir.* 216, xxii, 740. doi:10.1007/978-94-007-1363-5

Paces, J.B., Wurster, F.C., 2014. Natural uranium and strontium isotope tracers of water sources and surface water–groundwater interactions in arid wetlands – Pahrnagat Valley, Nevada, USA. *J. Hydrol.* 517, 213–225. doi:https://doi.org/10.1016/j.jhydrol.2014.05.011

Paepe, R., Sommé, J., 1931. Les Loess et la stratigraphie du Pléistocène récent dans le Nord de la France et en Belgique. *Imp. Centrale du Nord*.

Pelt, E., Chabaux, F., Innocent, C., Navarre-Sitchler, A.K., Sak, P.B., Brantley, S.L., 2008. Uranium–thorium chronometry of weathering rinds: Rock alteration rate and paleo-isotopic record of weathering fluids. *Earth Planet. Sci. Lett.* 276, 98–105. doi:10.1016/j.epsl.2008.09.010

Petelet-Giraud, E., Luck, J.-M., Ben Othman, D., Joseph, C., Négrel, P., 2016. Chemical and isotopic fingerprinting of small ungauged watershed: How far the hydrological functioning can be understood? *Comptes Rendus Geosci.* 348, 379–386. doi:10.1016/j.crte.2016.03.001

- Pfister, L., Martínez-Carreras, N., Hissler, C., Klaus, J., Carrer, G.E., Stewart, M.K., McDonnell, J.J., 2017. Bedrock geology controls on catchment storage, mixing, and release: A comparative analysis of 16 nested catchments. *Hydrol. Process.* 31, 1828–1845. doi:10.1002/hyp.11134
- Pfister, L., Wagner, C., Vansuypeene, E., Drogue, G., Hoffmann, L., 2005. Atlas climatique du grand-duché de Luxembourg. Musée national d'histoire naturelle, Société des naturalistes luxembourgeois, Centre de recherche public Gabriel Lippmann, Administration des services techniques de l'agriculture, Luxembourg.
- Pierret, M.C., Stille, P., Prunier, J., Viville, D., Chabaux, F., 2014. Chemical and U–Sr isotopic variations in stream and source waters of the Strengbach watershed (Vosges mountains, France). *Hydrol. Earth Syst. Sci.* 18, 3969–3985. doi:10.5194/hess-18-3969-2014
- Pin, C., Zalduegui, J.S., 1997. Sequential separation of light rare-earth elements, thorium and uranium by miniaturized extraction chromatography: Application to isotopic analyses of silicate rocks. *Anal. Chim. Acta* 339, 79–89. doi:10.1016/S0003-2670(96)00499-0
- Pissart, A., 1995. L'Ardenne sous le joug du froid. Le modelé périglaciaire du massif ardennais. L'Ardenne, essai de Géographie physique. Département de Géographie physique, Uni. De Liège.
- Pouclet, A., Juvigne, E., 2009. The Eltville tephra, a late Pleistocene widespread tephra layer in Germany, Belgium and The Netherlands; symptomatic compositions of the minerals. *Geol. Belgica*.
- Pouclet, A., Juvigné, E., Pirson, S., 2008. The Rocourt Tephra, a widespread 90–74 ka stratigraphic marker in Belgium. *Quat. Res.* 70, 105–120. doi:10.1016/j.yqres.2008.03.010
- Pourret, O., Dia, A., Davranche, M., Gruau, G., Hénin, O., Angée, M., 2007. Organo-colloidal control on major- and trace-element partitioning in shallow groundwaters: Confronting ultrafiltration and modelling. *Appl. Geochemistry* 22, 1568–1582. doi:10.1016/j.apgeochem.2007.03.022
- Prunier, J., Chabaux, F., Stille, P., Gangloff, S., Pierret, M.C., Viville, D., Aubert, A., 2015. Geochemical and isotopic (Sr, U) monitoring of soil solutions from the Strengbach catchment (Vosges mountains, France): Evidence for recent weathering evolution. *Chem. Geol.* 417, 289–305. doi:10.1016/j.chemgeo.2015.10.012
- Raynaud, S., Champion, E., Bernache-assollant, D., Laval, J., 2001a. Determination of Calcium / Phosphorus Atomic Ratio of Apatites Using X-ray Diffractometry. *J. Am. Ceram. Soc.*

84, 359–366. doi:10.1111/j.1151-2916.2001.tb00663.x

Raynaud, S., Champion, E., Bernache-Assollant, D., Laval, J.-P., 2001b. Determination of Calcium/Phosphorus Atomic Ratio of Calcium Phosphate Apatites Using X-ray Diffractometry. *J. Am. Ceram. Soc.* 84, 359–66. doi:10.1111/j.1151-2916.2001.tb00663.x

Redon, P.-O., Bur, T., Guiresse, M., Probst, J.-L., Toiser, A., Revel, J.-C., Jolivet, C., Probst, A., 2013. Modelling trace metal background to evaluate anthropogenic contamination in arable soils of south-western France. *Geoderma* 206, 112–122. doi:10.1016/j.geoderma.2013.04.023

Reimann, C., Filzmoser, P., Garrett, R., Dutter, R., 2008. *Statistical data analysis explained : applied environmental statistics with R*. John Wiley & Sons.

Riotte, J., Chabaux, F., 1999. (234U/238U) activity ratios in freshwaters as tracers of hydrological processes: the Strengbach watershed (Vosges, France). *Geochim. Cosmochim. Acta* 63, 1263–1275. doi:10.1016/S0016-7037(99)00009-5

Rousseau, D.-D., Chauvel, C., Sima, A., Hatté, C., Lagroix, F., Antoine, P., Balkanski, Y., Fuchs, M., Mellett, C., Kageyama, M., Ramstein, G., Lang, A., 2014. European glacial dust deposits: Geochemical constraints on atmospheric dust cycle modeling. *Geophys. Res. Lett.* 41, 7666–7674. doi:10.1002/2014GL061382

Rousseau, D.D., Ghil, M., Kukla, G., Sima, a., Antoine, P., Fuchs, M., Hatté, C., Lagroix, F., Debret, M., Moine, O., 2013. Major dust events in Europe during marine isotope stage 5 (130–74 ka): A climatic interpretation of the “markers.” *Clim. Past* 9, 2213–2230. doi:10.5194/cp-9-2213-2013

Sauer, D., 2002. *Genese, Verbreitung und Eigenschaften periglaziärer Lagen im Rheinischen Schiefergebirge- anhand von Beispielen aus Westerwald, Hunsrück und Eifel*. Philipps-Universität Marburg.

Sauer, D., Felix-Henningsen, P., 2006. Saprolite, soils, and sediments in the Rhenish Massif as records of climate and landscape history. *Quat. Int.* 156–157, 4–12. doi:10.1016/j.quaint.2006.05.001

Scaini, A., Audebert, M., Hissler, C., Fenicia, F., Gourdol, L., Pfister, L., Beven, K.J., 2017a. Velocity and celerity dynamics at plot scale inferred from artificial tracing experiments and time-lapse ERT. *J. Hydrol.* 546, 28–43. doi:10.1016/J.JHYDROL.2016.12.035

Scaini, A., Hissler, C., Fenicia, F., Juilleret, J., Iffly, J.F., Pfister, L., Beven, K., 2017b.

- Hillslope response to sprinkling and natural rainfall using velocity and celerity estimates in a slate-bedrock catchment. *J. Hydrol.* doi:10.1016/J.JHYDROL.2017.12.011
- Schaffhauser, T., Chabaux, F., Ambroise, B., Lucas, Y., Stille, P., Reuschlé, T., Perrone, T., Fritz, B., 2014. Geochemical and isotopic (U, Sr) tracing of water pathways in the granitic Ringelbach catchment (Vosges Mountains, France). *Chem. Geol.* 374–375, 117–127. doi:10.1016/j.chemgeo.2014.02.028
- Schmincke, H.-U., Park, C., Harms, E., 1999. Evolution and environmental impacts of the eruption of Laacher See Volcano (Germany) 12,900 a BP. *Quat. Int.* 61, 61–72. doi:10.1016/S1040-6182(99)00017-8
- Schot, P.P., van der Wal, J., 1992. Human impact on regional groundwater composition through intervention in natural flow patterns and changes in land use. *J. Hydrol.* 134, 297–313. doi:10.1016/0022-1694(92)90040-3
- Schwab, M., 2017. Long-term, high-frequency analysis on the interplay between rainfall-runoff processes, discharge, DOC and nitrate. Albert-Ludwigs-Universität Freiburg im Breisgau, Germany.
- Schwab, M., Klaus, J., Pfister, L., Weiler, M., 2016. Diel discharge cycles explained through viscosity fluctuations in riparian inflow. *Water Resour. Res.* 52, 8744–8755. doi:10.1002/2016WR018626
- Scott, K.M., Pain, C.F., 2008. *Regolith Science.*, Scott, K.M. ed. Springer Science and CSIRO, Dordrecht, The Netherlands, and Collingwood, Australia.
- Semlali, R.M., Dessogne, J.B., Monna, F., Bolte, J., Azimi, S., Navarro, N., Denaix, L., Loubet, M., Chateau, C., Van Oort, F., 2004. Modeling Lead Input and Output in Soils Using Lead Isotopic Geochemistry. *Environ. Sci. Technol.* 38, 1513–1521. doi:10.1021/es0341384
- Semmel, A., Terhorst, B., 2010. The concept of the Pleistocene periglacial cover beds in central Europe: A review. *Quat. Int.* 222, 120–128. doi:10.1016/j.quaint.2010.03.010
- Shields, G., Stille, P., 2001. Diagenetic constraints on the use of cerium anomalies as palaeoseawater redox proxies: an isotopic and REE study of Cambrian phosphorites. *Chem. Geol.* 175, 29–48. doi:10.1016/S0009-2541(00)00362-4
- Sholkovitz, E.R., 1995. The aquatic chemistry of rare earth elements in rivers and estuaries. *Aquat. Geochemistry* 1, 1–34. doi:10.1007/BF01025229
- Sholkovitz, E.R., Landing, W.M., Lewis, B.L., 1994. Ocean particle chemistry: The

fractionation of rare earth elements between suspended particles and seawater. *Geochim. Cosmochim. Acta* 58, 1567–1579. doi:10.1016/0016-7037(94)90559-2

Smedley, P.L., 1991. The geochemistry of rare earth elements in groundwater from the Carnmenellis area, southwest England. *Geochim. Cosmochim. Acta* 55, 2767–2779. doi:[https://doi.org/10.1016/0016-7037\(91\)90443-9](https://doi.org/10.1016/0016-7037(91)90443-9)

Soil Science Glossary Terms Committee (SSGT), 2008, 2008. Internet glossary of soil science terms <https://www.soils.org/publications/soils-glossary> (accessed 17.08.2015). [WWW Document]. URL <https://dl.sciencesocieties.org/publications/books/tocs/acsesspublicati/glossaryofsoils> (accessed 12.18.15).

Steinmann, M., Stille, P., 2006. Rare earth element transport and fractionation in small streams of a mixed basaltic–granitic catchment basin (Massif Central, France). *J. Geochemical Explor.* 88, 336–340. doi:10.1016/j.gexplo.2005.08.071

Steinmann, M., Stille, P., 1997. Rare earth element behavior and Pb, Sr, Nd isotope systematics in a heavy metal contaminated soil. *Appl. Geochemistry* 12, 607–623. doi:10.1016/S0883-2927(97)00017-6

Stille, P., Clauer, N., 1994. The process of glauconitization: chemical and isotopic evidence. *Contrib. to Mineral. Petrol.* 117, 253–262. doi:10.1007/BF00310867

Stille, P., Gauthier-Lafaye, F., Jensen, K.A., Salah, S., Bracke, G., Ewing, R.C., Louvat, D., Million, D., 2003. REE mobility in groundwater proximate to the natural fission reactor at Bangombé (Gabon). *Chem. Geol.* 198, 289–304. doi:10.1016/S0009-2541(03)00035-4

Stille, P., Pierret, M.C., Steinmann, M., Chabaux, F., Boutin, R., Aubert, D., Pourcelot, L., Morvan, G., 2009. Impact of atmospheric deposition, biogeochemical cycling and water–mineral interaction on REE fractionation in acidic surface soils and soil water (the Strengbach case). *Chem. Geol.* 264, 173–186. doi:10.1016/j.chemgeo.2009.03.005

Stille, P., Pourcelot, L., Granet, M., Pierret, M.C., Guéguen, F., Perrone, T., Morvan, G., Chabaux, F., 2011. Deposition and migration of atmospheric Pb in soils from a forested silicate catchment today and in the past (Strengbach case): Evidence from ²¹⁰Pb activities and Pb isotope ratios. *Chem. Geol.* 289, 140–153. doi:10.1016/j.chemgeo.2011.07.021

Stille, P., Shields, G., 1997. Radiogenic Isotope Geochemistry of Sedimentary and Aquatic Systems, Lecture Notes in Earth Sciences. Springer Berlin Heidelberg, Berlin, Heidelberg.

doi:10.1007/BFb0117747

- Stille, P., Steinmann, M., Pierret, M.-C., Gauthier-Lafaye, F., Aubert, D., Probst, A., Viville, D., Chabaux, F., 2006. The impact of vegetation on fractionation of rare earth elements (REE) during water–rock interaction. *J. Geochemical Explor.* 88, 341–344. doi:10.1016/j.gexplo.2005.08.070
- Stille, P., Steinmann, M., Pierret, M.-C., Gauthier-Lafaye, F., Chabaux, F., Viville, D., Pourcelot, L., Matera, V., Aouad, G., Aubert, D., 2006. The impact of vegetation on REE fractionation in stream waters of a small forested catchment (the Strengbach case). *Geochim. Cosmochim. Acta* 70, 3217–3230. doi:10.1016/j.gca.2006.04.028
- Stückerad, S., Sabel, K.-J., Wilcke, W., 2008. Periglacial transport distance of Pb derived from small-scale ore veins in the Rhenish Slate Mountains. *Geoderma* 148, 232–239. doi:10.1016/j.geoderma.2008.10.011
- Stückerad, S., Sabel, K.J., Wilcke, W., 2010. Contributions of different parent materials in soils developed from periglacial cover-beds. *Eur. J. Soil Sci.* 61, 844–853. doi:10.1111/j.1365-2389.2010.01288.x
- Stumpp, C., Maloszewski, P., Stichler, W., Maciejewski, S., 2007. Quantification of the heterogeneity of the unsaturated zone based on environmental deuterium observed in lysimeter experiments. *Hydrol. Sci. J.* 52, 748–762. doi:10.1623/hysj.52.4.748
- Taylor, G., Eggleton, R.A., 2001. *Regolith geology and geomorphology*. John Wiley & Sons Ltd, Chichester, UK.
- Taylor, S., McLennan, S., McCulloch, M., 1983. Geochemistry of loess, continental crustal composition and crustal model ages. *Geochim. Cosmochim. Acta* 47, 1897–1905. doi:10.1016/0016-7037(83)90206-5
- Taylor, S.R., McLennan, S.M., 1985. *The continental crust: Its composition and evolution*. Blackwell Scientific Pub., Palo Alto, CA, United States.
- Taylor, S.R., McLennan, S.M., 1981. The composition and evolution of the continental crust: rare earth element evidence from sedimentary rocks. *Phil. Trans. R. Soc. Lond.* A301, 381–399.
- Templ, M., Filzmoser, P., Reimann, C., 2008. Cluster analysis applied to regional geochemical data: Problems and possibilities. *Appl. Geochemistry* 23, 2198–2213. doi:10.1016/j.apgeochem.2008.03.004

- Terhorst, B., 2007. Periglacial cover beds and soils in landslide areas of SW-Germany. *CATENA* 71, 467–476. doi:10.1016/j.catena.2007.03.021
- Tricca, A., Stille, P., Steinmann, M., Kiefel, B., Samuel, J., Eikenberg, J., 1999. Rare earth elements and Sr and Nd isotopic compositions of dissolved and suspended loads from small river systems in the Vosges mountains (France), the river Rhine and groundwater. *Chem. Geol.* 160, 139–158. doi:10.1016/S0009-2541(99)00065-0
- Uher, P., Ondrejka, M., Bačík, P., Broska, I., Konečný, P., 2015. Britholite, monazite, REE carbonates, and calcite: Products of hydrothermal alteration of allanite and apatite in A-type granite from Stupn??, Western Carpathians, Slovakia. *Lithos* 236–237, 212–225. doi:10.1016/j.lithos.2015.09.005
- Vázquez-Ortega, A., Huckle, D., Perdrial, J., Amistadi, M.K., Durcik, M., Rasmussen, C., McIntosh, J., Chorover, J., 2016. Solid-phase redistribution of rare earth elements in hillslope pedons subjected to different hydrologic fluxes. *Chem. Geol.* 426, 1–18. doi:10.1016/j.chemgeo.2016.01.001
- Vázquez-Ortega, A., Perdrial, J., Harpold, A., Zapata-Ríos, X., Rasmussen, C., McIntosh, J., Schaap, M., Pelletier, J.D., Brooks, P.D., Amistadi, M.K., Chorover, J., 2015. Rare earth elements as reactive tracers of biogeochemical weathering in forested rhyolitic terrain. *Chem. Geol.* 391, 19–32. doi:10.1016/j.chemgeo.2014.10.016
- Viers, J., Dupré, B., Polvé, M., Schott, J., Dandurand, J.-L., Braun, J.-J., 1997. Chemical weathering in the drainage basin of a tropical watershed (Nsimi-Zoetele site, Cameroon) : comparison between organic-poor and organic-rich waters. *Chem. Geol.* 140, 181–206. doi:10.1016/S0009-2541(97)00048-X
- Vigier, N., Bourdon, B., 2012. Constraining Rates of Chemical and Physical Erosion Using U-Series Radionuclides, in: *Handbook of Environmental Isotope Geochemistry*. Springer Berlin Heidelberg, Berlin, Heidelberg, pp. 553–571. doi:10.1007/978-3-642-10637-8_27
- Völkel, J., Huber, J., Leopold, M., 2011. Significance of slope sediments layering on physical characteristics and interflow within the Critical Zone – Examples from the Colorado Front Range, USA. *Appl. Geochemistry* 26, S143–S145. doi:10.1016/J.APGEOCHEM.2011.03.052
- Ward, J.H., 1963. Hierarchical grouping to optimize an objective function. *J. Am. Stat. Assoc.* doi:10.1080/01621459.1963.10500845
- Wenninger, J., Uhlenbrook, S., Tilch, N., Leibundgut, C., 2004. Experimental evidence of fast

- groundwater responses in a hillslope/floodplain area in the Black Forest Mountains, Germany. *Hydrol. Process.* 18, 3305–3322. doi:10.1002/hyp.5686
- West, N., Kirby, E., Bierman, P., Slingerland, R., Ma, L., Rood, D., Brantley, S., 2013. Regolith production and transport at the Susquehanna Shale Hills Critical Zone Observatory, Part 2: Insights from meteoric ¹⁰Be. *J. Geophys. Res. Earth Surf.* 118, 1877–1896. doi:10.1002/jgrf.20121
- Wörner, G., Schmincke, H.-U., 1984. Mineralogical and Chemical Zonation of the Laacher See Tephra Sequence (East Eifel, W. Germany). *J. Petrol.* 25, 805–835. doi:10.1093/petrology/25.4.805
- Wörner, G., Staudigel, H., Zindler, A., 1985. Isotopic constraints on open system evolution of the Laacher See magma chamber (Eifel, West Germany). *Earth Planet. Sci. Lett.* 75, 37–49. doi:10.1016/0012-821X(85)90048-2
- Wörner, G., Wright, T.L., 1984. Evidence for magma mixing within the Laacher See magma chamber (East Eifel, Germany). *J. Volcanol. Geotherm. Res.* 22, 301–327. doi:10.1016/0377-0273(84)90007-6
- Wrede, S., Fenicia, F., Martínez-Carreras, N., Juilleret, J., Hissler, C., Krein, A., Savenije, H.H.G., Uhlenbrook, S., Kavetski, D., Pfister, L., 2015. Towards more systematic perceptual model development: a case study using 3 Luxembourgish catchments. *Hydrol. Process.* 29, 2731–2750. doi:10.1002/hyp.10393
- Yokoyama, T., Makishima, A., Nakamura, E., 1999. Evaluation of the coprecipitation of incompatible trace elements with fluoride during silicate rock dissolution by acid digestion. *Chem. Geol.* 157, 175–187. doi:10.1016/S0009-2541(98)00206-X
- Zanella, A., Jabiol, B., Ponge, J.F., Sartori, G., De Waal, R., Van Delft, B., Graefe, U., Cools, N., Katzensteiner, K., Hager, H., Englisch, M., 2011. A European morpho-functional classification of humus forms. *Geoderma* 164, 138–145. doi:10.1016/j.geoderma.2011.05.016
- Zhang, P., Ryan, J.A., Yang, J., 1998. In Vitro Soil Pb Solubility in the Presence of Hydroxyapatite. *Environ. Sci. Technol.* 32, 2763–2768. doi:10.1021/es971065d

Appendices

Appendix 1. Long term waters pH, EC, alkalinity, DOC, TN, major elements, $\delta^{18}\text{O}$ and dD data used in this study (includes values D.L./2).

Sample	Value	pH	EC	HCO_3^-	DOC	TN	$\delta^{18}\text{O}$	$\delta^2\text{H}$	Cl^-	NO_3^-	SO_4^{2-}	Na^+	K^+	Mg^{2+}	Ca^{2+}	Al^{3+}	Mn^{2+}	Fe^{2+}
			($\mu\text{S/cm}$)	(meq/L)	(mg/L)				(mg/L)							(μg/L)		
TH1	N	63	72	68	76	78	78	78	80	80	80	80	80	80	80	80	80	80
	ME	5.8	35.45	0.044	10.7	2.9	-6.97	-45.30	2.29	0.96	1.73	1.31	1.71	0.35	0.98	25.26	146.63	13.99
	AVG	5.7	60.14	0.076	23.3	5.2	-7.47	-48.56	3.07	1.83	2.97	1.75	5.15	0.73	1.74	40.94	350.83	19.29
	MAX	6.9	460.00	0.912	259.0	34.4	-2.26	-6.77	42.75	10.56	25.60	20.14	88.40	7.93	10.96	329.79	3774.97	104.80
	MIN	3.8	7.10	0.007	2.4	0.2	-15.04	-117.35	0.01	0.00	0.02	0.02	0.00	0.00	0.02	1.02	5.26	1.15
TH2	N	65	71	66	70	71	72	72	75	75	75	75	75	75	75	75	75	75
	ME	6.2	39.20	0.068	12.1	3.2	-7.33	-46.84	2.34	0.84	1.86	1.24	3.38	0.31	0.91	24.55	167.14	16.49
	AVG	6.1	62.76	0.132	22.2	6.0	-7.48	-48.11	3.43	1.46	3.16	1.56	6.27	0.58	1.59	36.35	281.40	19.80
	MAX	7.4	394.00	0.790	250.0	32.7	-2.02	-8.11	22.55	10.99	16.01	8.95	60.90	4.74	13.78	193.23	2808.17	125.58
	MIN	4.5	10.00	0.002	1.7	0.2	-14.12	-109.40	0.28	0.01	0.16	0.28	0.33	0.09	0.18	2.08	16.44	2.73
TH3	N	38	39	38	40	40	39	39	41	41	41	41	41	41	41	41	41	41
	ME	5.2	47.20	0.044	21.9	3.5	-7.79	-51.15	3.02	0.86	1.63	1.42	1.67	0.39	1.31	34.18	403.15	22.98
	AVG	5.5	54.74	0.092	24.6	4.9	-7.96	-52.69	3.30	1.06	2.50	1.58	2.28	0.50	1.47	39.94	436.48	22.66
	MAX	7.3	115.30	0.618	84.9	25.5	-1.65	-11.89	7.25	6.09	14.70	3.37	7.89	1.49	4.50	140.89	1263.80	57.78
	MIN	4.4	22.50	0.006	3.1	0.8	-15.25	-119.76	0.49	0.15	0.39	0.02	0.00	0.00	0.02	6.89	27.21	5.11
SS7-20	N	37	43	43	70	77	86	86	87	87	87	87	87	87	87	87	87	87
	ME	4.9	26.40	0.029	10.3	0.7	-8.51	-57.65	2.24	0.26	3.09	1.31	0.95	0.71	0.99	1147.73	130.94	62.50
	AVG	4.9	34.11	0.024	11.6	1.1	-8.60	-56.73	2.96	0.68	3.57	1.78	0.95	0.83	1.30	1270.89	248.24	88.60
	MAX	5.3	120.00	0.050	31.9	3.9	-6.06	-37.09	18.50	6.13	9.19	10.60	5.67	2.40	9.40	6601.30	2253.90	1008.27
	MIN	4.5	20.30	0.000	2.1	0.2	-12.67	-85.86	0.27	0.01	1.30	0.65	0.10	0.30	0.22	0.67	23.06	10.14
SS7-40	N	1	1	1	13	13	15	15	15	15	15	15	15	15	15	15	15	15
	ME	6.6	32.20	0.036	5.1	0.4	-8.30	-54.87	2.72	0.11	6.03	1.84	0.68	0.61	0.92	759.34	324.36	31.89
	AVG	6.6	32.20	0.036	5.5	0.7	-7.93	-52.64	3.38	0.53	6.00	2.58	1.21	0.79	1.14	765.31	404.01	31.21

	MAX	6.6	32.20	0.036	8.5	2.2	-6.61	-42.95	7.20	4.06	8.91	6.60	6.05	1.90	3.10	1294.45	914.14	66.02
	MIN	6.6	32.20	0.036	3.1	0.2	-10.16	-67.80	1.66	0.02	4.00	0.94	0.40	0.44	0.60	161.15	156.08	17.83
SS7-60	N	24	36	28	72	72	84	84	84	84	84	84	84	84	84	84	84	84
	ME	4.7	49.10	0.013	1.6	0.2	-8.58	-57.07	2.91	0.05	9.24	1.59	0.29	0.95	1.34	515.77	254.73	7.79
	AVG	4.8	53.77	0.015	3.6	0.3	-8.62	-56.24	3.69	0.20	9.79	2.27	0.46	1.01	1.90	608.75	348.37	14.06
	MAX	6.4	149.20	0.039	24.3	1.8	-6.35	-35.66	15.20	1.75	23.20	10.20	2.62	2.70	10.10	1614.05	1695.19	158.90
	MIN	4.5	32.70	0.001	0.2	0.0	-13.90	-96.67	0.01	0.00	0.02	0.02	0.00	0.00	0.02	0.67	28.32	0.64
GW1	N	67	71	74	65	74	73	73	76	76	76	76	76	76	76	76	76	76
	ME	5.8	70.60	0.050	1.1	1.5	-8.42	-54.39	4.15	1.13	14.47	3.09	0.66	2.55	3.26	89.02	165.87	8.27
	AVG	5.8	70.51	0.061	1.3	1.7	-8.32	-53.90	4.21	1.25	14.75	3.55	0.74	2.46	3.42	167.65	200.87	30.05
	MAX	6.6	82.10	0.270	6.9	5.0	-6.33	-48.32	6.79	2.81	24.48	14.58	2.16	3.04	5.91	1083.44	904.85	506.03
	MIN	4.9	45.70	0.020	0.5	0.6	-9.31	-60.99	2.30	0.37	10.13	1.90	0.39	0.28	0.43	26.34	49.39	0.77
GW2	N	109	117	114	111	117	120	120	123	123	123	123	123	123	123	123	123	123
	ME	6.6	63.70	0.287	0.5	0.8	-8.43	-54.35	2.96	0.62	7.01	2.78	0.30	3.10	3.78	20.74	199.14	5.04
	AVG	6.6	73.17	0.387	0.6	0.9	-8.34	-53.94	3.01	0.66	6.88	2.95	0.34	3.49	4.99	38.71	310.59	19.53
	MAX	7.8	143.90	1.275	5.5	2.8	-6.92	-48.08	5.68	3.41	13.41	5.12	0.71	6.90	14.78	1551.04	1266.75	1351.70
	MIN	5.4	43.60	0.043	0.1	0.1	-9.53	-58.23	2.23	0.01	4.00	1.97	0.16	1.71	1.31	0.67	4.63	0.07
GW3	N	110	118	114	112	119	121	121	125	125	125	125	125	125	125	125	125	125
	ME	6.8	109.50	0.282	0.6	3.2	-8.06	-51.65	5.12	2.64	13.38	5.14	0.46	4.18	7.90	11.93	2.28	9.52
	AVG	6.8	107.91	0.342	0.9	3.8	-7.99	-51.19	5.12	2.73	13.05	5.16	0.49	4.34	8.35	40.01	26.14	17.16
	MAX	7.3	124.00	0.808	8.0	48.1	-6.59	-45.02	9.20	4.98	18.63	10.43	1.82	20.54	62.01	2822.04	671.21	332.72
	MIN	5.9	49.50	0.055	0.2	0.0	-8.82	-55.65	0.01	0.00	0.02	0.02	0.00	0.00	0.02	0.15	0.02	0.14
GW5	N	1	7	9	6	6	8	8	9	9	9	9	9	9	9	9	9	9
	ME	6.8	78.90	0.400	10.7	0.5	-7.43	-48.33	4.29	0.43	8.62	3.62	0.36	3.22	6.43	14.38	168.36	7.11
	AVG	6.8	88.51	0.511	11.6	0.5	-7.50	-48.93	4.56	0.51	8.50	3.52	0.42	3.79	7.94	13.50	198.02	8.46
	MAX	6.8	132.00	0.955	25.9	0.9	-6.91	-47.15	5.98	1.30	14.29	4.16	1.04	7.65	13.41	27.69	382.90	24.25
	MIN	6.8	63.60	0.219	3.7	0.3	-8.15	-53.13	3.84	0.08	4.09	2.68	0.22	2.26	3.95	2.90	148.45	1.68
GW6	N	1	5	7	6	6	7	7	7	7	7	7	7	7	7	7	7	7

	ME	6.2	84.10	0.062	10.3	4.3	-7.23	-46.93	5.05	5.22	11.24	4.44	0.43	4.24	3.73	91.36	129.24	5.07
	AVG	6.2	95.42	0.066	11.7	4.3	-7.27	-46.90	5.36	5.12	12.65	4.35	0.44	4.45	3.65	87.53	131.36	5.67
	MAX	6.2	136.70	0.089	18.8	5.2	-6.97	-46.32	7.39	6.60	18.42	5.05	0.52	5.18	4.27	96.30	153.79	13.27
	MIN	6.2	81.60	0.051	4.4	3.8	-7.62	-47.74	4.29	3.89	9.38	3.79	0.39	4.18	3.09	70.55	106.79	1.89
GW7	N	1	5	8	6	6	8	8	8	8	8	8	8	8	8	8	8	8
	ME	6.0	44.70	0.041	9.5	1.1	-7.74	-50.06	3.20	1.04	6.28	2.22	0.24	2.46	0.70	60.13	44.17	9.13
	AVG	6.0	44.74	0.046	10.7	1.1	-7.76	-50.43	3.57	1.08	7.46	2.28	0.27	2.45	0.92	56.03	46.20	14.86
	MAX	6.0	45.60	0.086	20.8	1.1	-7.56	-49.56	5.28	1.55	10.13	2.59	0.50	2.59	2.51	65.38	74.75	52.61
	MIN	6.0	44.10	0.038	4.7	1.0	-8.00	-52.58	3.09	0.45	5.63	2.20	0.20	2.23	0.66	23.89	19.04	2.19
RP	N	51	46	56	62	67	67	67	70	70	70	70	70	70	70	70	70	70
	ME	6.7	43.95	0.144	1.7	0.1	-8.24	-53.26	2.62	0.02	6.28	2.23	0.22	2.22	1.77	21.37	14.85	28.46
	AVG	6.5	55.34	0.158	2.0	0.2	-8.06	-51.68	2.52	0.07	12.74	2.36	0.27	3.00	2.43	28.30	33.27	81.52
	MAX	7.5	175.50	0.320	9.0	1.5	-5.00	-30.76	3.84	0.74	90.70	4.33	1.05	15.13	11.18	103.29	311.66	1092.93
	MIN	5.7	32.40	0.011	0.3	0.1	-8.98	-58.28	0.01	0.00	0.02	0.02	0.00	0.00	0.02	3.99	1.05	0.46
SP	N	1	2	4	4	4	4	4	4	4	4	4	4	4	4	4	4	4
	ME	5.1	45.45	0.074	11.8	0.2	-7.88	-50.09	3.50	0.23	12.18	1.81	0.22	2.66	1.46	23.85	2.59	1.98
	AVG	5.1	45.45	0.074	11.8	0.2	-7.88	-50.09	3.50	0.23	12.18	1.81	0.22	2.66	1.46	23.85	2.59	1.98
	MAX	5.1	45.45	0.074	11.8	0.2	-7.88	-50.09	3.50	0.23	12.18	1.81	0.22	2.66	1.46	23.85	2.59	1.98
	MIN	5.1	45.45	0.074	11.8	0.2	-7.88	-50.09	3.50	0.23	12.18	1.81	0.22	2.66	1.46	23.85	2.59	1.98
SW1	N	108	155	152	124	127	157	157	163	163	163	163	163	163	163	163	163	163
	ME	6.6	48.80	0.098	1.6	0.7	-7.95	-51.18	3.22	0.65	8.28	2.43	0.25	2.55	1.92	18.57	2.91	13.71
	AVG	6.6	50.69	0.137	2.4	0.9	-7.99	-51.31	3.45	0.67	8.85	2.57	0.30	2.60	2.16	22.74	11.41	23.46
	MAX	7.1	69.50	0.384	16.4	2.7	-5.04	-24.36	16.80	1.45	13.00	3.80	1.35	3.72	4.40	110.18	544.91	112.22
	MIN	5.8	20.70	0.028	0.2	0.3	-9.18	-57.32	2.33	0.00	0.90	1.97	0.15	1.74	1.44	0.67	0.69	2.69
SW2	N	120	137	135	103	103	139	139	142	142	142	142	142	142	142	142	142	142
	ME	6.4	41.80	0.077	1.1	0.8	-8.08	-52.28	2.97	0.72	7.00	2.20	0.20	2.28	1.27	28.10	9.23	4.89
	AVG	6.3	43.68	0.101	1.7	1.0	-8.15	-52.28	3.07	0.72	7.47	2.23	0.23	2.32	1.44	32.43	31.05	10.90
	MAX	6.9	69.00	0.315	9.1	2.5	-6.39	-47.73	7.30	1.53	10.38	2.90	1.04	3.03	3.17	101.58	758.26	120.46

	MIN	5.5	38.40	0.019	0.4	0.4	-9.32	-56.96	1.93	0.12	5.00	1.68	0.11	1.35	0.92	0.67	0.49	0.62
SW3	N	137	144	140	108	108	145	145	149	149	149	149	149	149	149	149	149	149
	ME	6.5	45.85	0.095	1.0	0.7	-8.05	-51.86	2.71	0.41	8.55	2.16	0.21	2.57	1.48	15.92	3.29	9.60
	AVG	6.5	46.95	0.111	1.3	0.8	-8.13	-52.13	2.86	0.45	8.51	2.22	0.27	2.64	1.57	19.22	4.90	14.65
	MAX	7.1	107.10	0.275	7.3	3.5	-6.74	-46.41	10.10	1.21	13.35	3.03	0.89	3.66	2.86	98.35	68.94	114.79
	MIN	4.8	39.60	0.024	0.4	0.1	-9.68	-57.60	2.23	0.03	4.66	1.80	0.15	1.95	1.08	0.67	0.34	1.85

Appendix 2. Long term waters trace element data used in this study (includes values D.L./2).

Sample	Value	Cr	Co	Ni	Cu	Zn	Rb	Sr	Cd	Ba	Pb	Sc	Sb	Cs
		(µg/L)												
TH1	N	80	80	80	80	80	80	80	80	80	80	80	80	80
	ME	0.16	0.08	0.57	2.01	11.28	3.88	2.00	0.06	2.18	0.508	0.04	0.186	0.0175
	AVG	0.20	0.20	1.42	3.30	21.38	17.38	3.90	0.12	3.96	0.651	0.11	0.215	0.0536
	MAX	0.70	5.27	20.11	22.04	181.14	386.53	26.89	3.19	24.56	3.265	1.67	0.830	1.1140
	MIN	0.01	0.00	0.10	0.45	1.13	0.51	0.25	0.00	0.18	0.031	0.00	0.040	0.0002
TH2	N	75	75	75	75	75	75	75	75	75	75	75	75	75
	ME	0.18	0.09	0.88	2.90	11.24	11.02	2.00	0.04	1.65	0.614	0.10	0.167	0.0350
	AVG	0.21	0.18	1.73	3.59	15.15	18.78	3.10	0.06	2.38	0.775	0.13	0.202	0.0774
	MAX	1.32	0.95	21.96	19.82	99.96	222.66	10.09	0.34	9.21	2.499	0.60	0.557	0.9460
	MIN	0.01	0.01	0.04	0.36	1.49	0.81	0.50	0.01	0.16	0.100	0.00	0.055	0.0044
TH3	N	41	41	41	41	41	41	41	41	41	41	41	41	41
	ME	0.20	0.18	1.06	2.66	17.58	9.29	3.26	0.09	3.06	0.824	0.04	0.179	0.0597
	AVG	0.21	0.23	1.17	3.14	21.37	10.03	3.48	0.11	5.24	0.863	0.05	0.190	0.0661
	MAX	0.42	0.58	3.19	8.03	64.59	32.29	9.41	0.30	36.26	1.642	0.17	0.464	0.2772
	MIN	0.05	0.05	0.17	0.95	5.29	0.70	0.75	0.01	0.80	0.194	0.00	0.010	0.0086

	MAX	1.28	5.27	6.50	5.46	53.37	0.76	75.65	0.09	7.33	0.682	2.76	0.478	0.1050
	MIN	0.00	0.00	0.00	0.02	0.17	0.00	0.00	0.00	0.02	0.001	0.02	0.002	0.0002
GW5	N	9	9	9	9	9	9	9	9	9	9	9	9	9
	ME	0.02	7.36	7.35	0.53	14.44	0.28	12.21	0.32	2.98	5.627	0.27	0.611	0.0132
	AVG	0.42	7.70	6.72	0.51	13.33	0.31	14.47	0.35	3.15	5.017	0.20	0.907	0.0152
	MAX	3.60	19.50	8.12	0.78	17.13	0.64	26.40	0.54	3.68	8.420	0.33	1.701	0.0221
	MIN	0.02	2.18	3.14	0.28	8.27	0.20	9.04	0.22	2.79	0.710	0.02	0.361	0.0075
	N	7	7	7	7	7	7	7	7	7	7	7	7	7
GW6	ME	0.21	3.03	11.17	1.36	20.64	0.41	45.03	0.14	2.23	0.936	0.58	0.182	0.0358
	AVG	0.20	3.09	11.14	1.37	20.70	0.42	43.84	0.14	2.21	0.919	0.50	0.198	0.0337
	MAX	0.24	4.15	11.86	1.57	22.43	0.48	49.10	0.16	2.41	1.469	0.62	0.383	0.0419
	MIN	0.12	2.43	10.25	1.14	18.07	0.37	38.59	0.12	1.93	0.474	0.02	0.096	0.0193
GW7	N	8	8	8	8	8	8	8	8	8	8	8	8	8
	ME	0.14	2.95	7.89	0.95	11.44	0.23	6.79	0.03	7.45	0.069	0.29	0.035	0.0072
	AVG	0.21	3.08	7.54	0.95	10.91	0.23	8.32	0.03	6.86	0.087	0.22	0.027	0.0068
	MAX	0.55	6.84	8.21	1.29	14.49	0.28	19.47	0.04	7.95	0.173	0.30	0.054	0.0103
	MIN	0.02	0.37	5.48	0.45	3.52	0.21	5.80	0.00	2.05	0.026	0.02	0.002	0.0002
RP	N	70	70	70	70	70	70	70	70	70	70	70	70	70
	ME	0.26	0.33	5.82	0.30	2.95	0.57	18.24	0.01	1.32	0.026	1.47	0.016	0.0020
	AVG	0.34	0.47	7.20	0.44	4.37	0.94	25.65	0.02	2.35	0.046	1.37	0.058	0.0046
	MAX	1.03	2.12	34.73	5.85	21.55	27.39	126.62	0.13	11.98	1.016	2.85	1.158	0.1679
	MIN	0.10	0.03	2.26	0.06	0.02	0.12	3.02	0.00	0.58	0.002	0.02	0.001	0.0002
SP	N	4	4	4	4	4	4	4	4	4	4	4	4	4
	ME	0.14	0.00	9.76	0.14	4.62	0.13	10.54	0.00	1.65	0.004	0.30	0.041	0.0002
	AVG	0.14	0.00	9.76	0.14	4.62	0.13	10.54	0.00	1.65	0.004	0.30	0.041	0.0002
	MAX	0.14	0.00	9.76	0.14	4.62	0.13	10.54	0.00	1.65	0.004	0.30	0.041	0.0002
	MIN	0.14	0.00	9.76	0.14	4.62	0.13	10.54	0.00	1.65	0.004	0.30	0.041	0.0002
SW1	N	163	163	163	163	163	163	163	163	163	163	163	163	163

	ME	0.13	0.04	3.72	0.30	3.50	0.22	14.28	0.01	2.80	0.051	1.20	0.015	0.0016
	AVG	0.14	0.05	3.70	0.42	3.79	0.31	15.99	0.03	3.08	0.070	1.08	0.044	0.0017
	MAX	0.43	0.56	10.24	3.74	19.38	2.00	49.00	2.17	30.93	0.409	4.09	3.920	0.0230
	MIN	0.01	0.00	1.11	0.08	0.17	0.00	6.63	0.00	1.06	0.004	0.02	0.002	0.0002
SW2	N	142	142	142	142	142	142	142	142	142	142	142	142	142
	ME	0.11	0.18	5.57	0.41	6.21	0.19	10.53	0.02	4.32	0.037	1.07	0.011	0.0020
	AVG	0.12	0.52	5.52	0.68	6.25	0.26	10.91	0.02	4.45	0.054	0.92	0.017	0.0019
	MAX	0.50	13.00	10.20	3.22	15.95	2.05	17.04	0.10	14.33	0.306	2.37	0.083	0.0200
	MIN	0.01	0.02	2.00	0.08	1.56	0.00	5.01	0.00	1.25	0.004	0.02	0.002	0.0002
SW3	N	149	149	149	149	149	149	149	149	149	149	149	149	149
	ME	0.11	0.02	5.16	0.26	3.27	0.18	10.51	0.01	1.57	0.047	1.06	0.014	0.0018
	AVG	0.12	0.03	5.00	0.42	3.42	0.26	11.10	0.01	1.71	0.069	0.95	0.023	0.0017
	MAX	0.50	1.15	10.48	3.36	13.25	1.09	29.43	0.15	9.79	0.469	2.07	0.151	0.0070
	MIN	0.02	0.00	1.23	0.02	0.17	0.00	4.51	0.00	0.70	0.004	0.02	0.001	0.0002

Appendix 3. Long term waters Rare Earth Element (REE) data used in this study (includes values D.L./2).

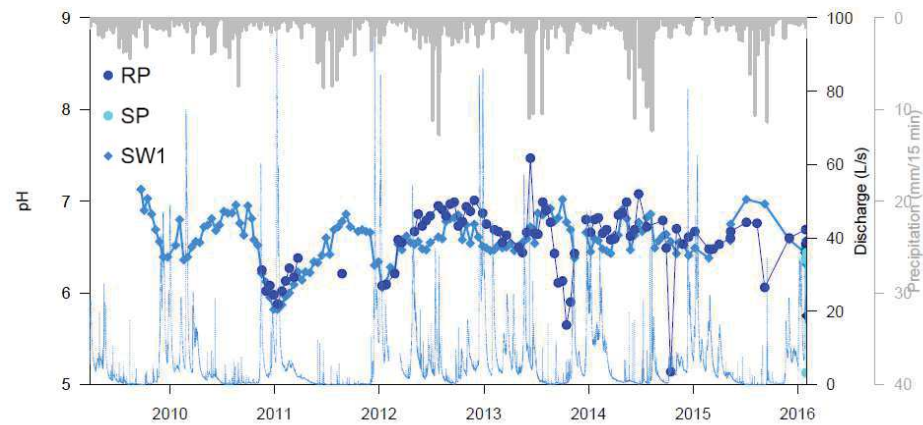
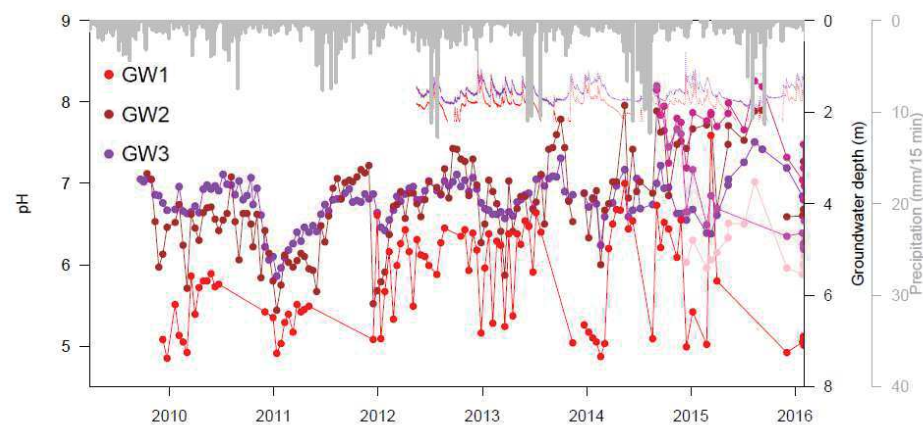
Sample	Value	La	Ce	Pr	Nd	Sm	Eu	Gd	Tb	Dy	Ho	Er	Tm	Yb
		(µg/L)												
TH1	N	80	80	80	80	80	80	80	80	80	80	80	80	80
	ME	0.0218	0.0425	0.0062	0.0250	0.0071	0.0020	0.0068	0.0006	0.0050	0.0006	0.0030	0.0002	0.0024
	AVG	0.0750	0.0721	0.0162	0.0662	0.0136	0.0034	0.0152	0.0020	0.0111	0.0019	0.0055	0.0005	0.0040
	MAX	1.7092	1.0277	0.3213	1.2548	0.2092	0.0514	0.2342	0.0283	0.1568	0.0279	0.0675	0.0079	0.0423
	MIN	0.0025	0.0050	0.0002	0.0002	0.0002	0.0002	0.0002	0.0000	0.0002	0.0001	0.0002	0.0000	0.0001

TH2	N	75	75	75	75	75	75	75	75	75	75	75	75	75
	ME	0.0190	0.0372	0.0050	0.0250	0.0061	0.0016	0.0066	0.0006	0.0050	0.0007	0.0030	0.0002	0.0022
	AVG	0.0431	0.0574	0.0106	0.0457	0.0101	0.0025	0.0112	0.0014	0.0083	0.0015	0.0044	0.0004	0.0035
	MAX	0.5628	0.3734	0.1124	0.4425	0.0763	0.0192	0.0992	0.0129	0.0669	0.0124	0.0307	0.0033	0.0182
	MIN	0.0019	0.0038	0.0002	0.0002	0.0002	0.0001	0.0002	0.0000	0.0002	0.0000	0.0002	0.0000	0.0001
TH3	N	41	41	41	41	41	41	41	41	41	41	41	41	41
	ME	0.0215	0.0502	0.0072	0.0332	0.0082	0.0021	0.0075	0.0010	0.0055	0.0011	0.0031	0.0005	0.0030
	AVG	0.0428	0.0616	0.0114	0.0495	0.0111	0.0030	0.0115	0.0016	0.0086	0.0017	0.0047	0.0007	0.0038
	MAX	0.2790	0.2190	0.0660	0.2870	0.0610	0.0140	0.0690	0.0090	0.0500	0.0100	0.0270	0.0030	0.0190
	MIN	0.0039	0.0088	0.0010	0.0046	0.0010	0.0003	0.0011	0.0001	0.0009	0.0001	0.0006	0.0000	0.0001
SS7-20	N	87	87	87	87	87	87	87	87	87	87	87	87	87
	ME	0.2235	0.7042	0.0700	0.3024	0.0770	0.0190	0.0810	0.0107	0.0566	0.0105	0.0293	0.0040	0.0270
	AVG	0.2569	0.7495	0.0768	0.3304	0.0833	0.0211	0.0882	0.0117	0.0619	0.0115	0.0319	0.0044	0.0290
	MAX	0.8910	2.7680	0.2430	1.0920	0.2820	0.0710	0.3370	0.0430	0.2070	0.0380	0.0970	0.0120	0.0810
	MIN	0.0002	0.0002	0.0002	0.0002	0.0002	0.0002	0.0002	0.0002	0.0002	0.0002	0.0002	0.0002	0.0002
SS7-40	N	15	15	15	15	15	15	15	15	15	15	15	15	15
	ME	0.7236	1.7516	0.1718	0.7262	0.1549	0.0382	0.1732	0.0229	0.1150	0.0243	0.0689	0.0089	0.0520
	AVG	0.7134	1.8351	0.1896	0.7856	0.1636	0.0411	0.1801	0.0222	0.1239	0.0254	0.0694	0.0093	0.0574
	MAX	2.0285	5.6216	0.5982	2.4876	0.4790	0.1126	0.5351	0.0627	0.3598	0.0737	0.1952	0.0257	0.1612
	MIN	0.1298	0.3270	0.0370	0.1536	0.0358	0.0108	0.0361	0.0050	0.0240	0.0050	0.0130	0.0020	0.0100
SS7-60	N	84	84	84	84	84	84	84	84	84	84	84	84	84
	ME	0.2919	0.4221	0.0541	0.2170	0.0640	0.0210	0.0692	0.0092	0.0479	0.0099	0.0243	0.0030	0.0160
	AVG	0.3969	0.5463	0.0678	0.2711	0.0686	0.0200	0.0751	0.0097	0.0501	0.0097	0.0255	0.0030	0.0185
	MAX	1.9290	1.6720	0.2120	0.9015	0.1905	0.0450	0.2219	0.0279	0.1569	0.0311	0.0851	0.0114	0.0702
	MIN	0.0720	0.1000	0.0190	0.0782	0.0193	0.0058	0.0180	0.0020	0.0130	0.0030	0.0090	0.0002	0.0050
GW1	N	76	76	76	76	76	76	76	76	76	76	76	76	76
	ME	0.3545	0.3835	0.2080	1.1617	0.3538	0.0936	0.5081	0.0705	0.4024	0.0866	0.2712	0.0381	0.2357
	AVG	0.9321	0.8411	0.4815	2.5310	0.7073	0.1944	1.0983	0.1608	0.9427	0.2016	0.5724	0.0737	0.4393

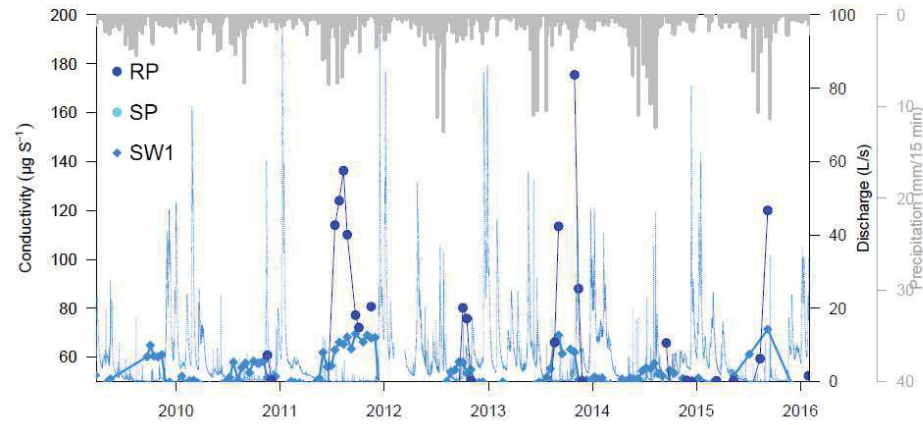
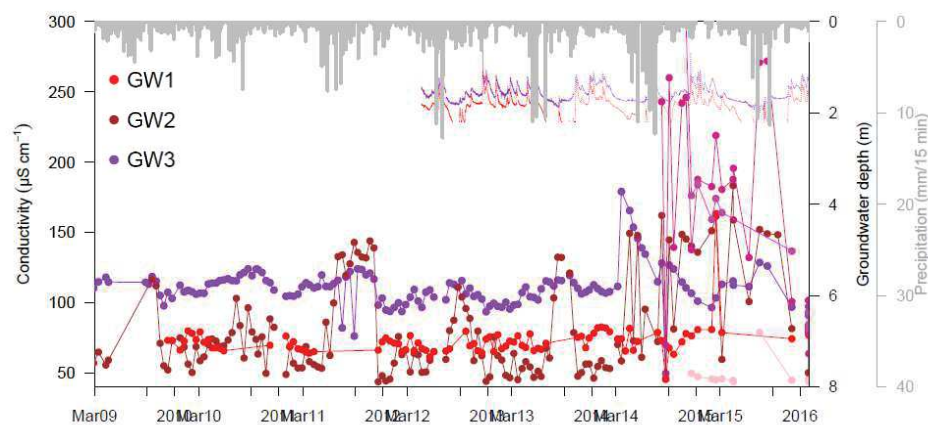
	ME	0.0123	0.0286	0.0061	0.0354	0.0146	0.0039	0.0172	0.0020	0.0102	0.0020	0.0061	0.0006	0.0060
	AVG	0.0176	0.0401	0.0091	0.0558	0.0215	0.0058	0.0266	0.0030	0.0158	0.0030	0.0089	0.0010	0.0087
	MAX	0.0730	0.1550	0.0360	0.2260	0.0930	0.0240	0.1180	0.0130	0.0690	0.0130	0.0370	0.0050	0.0330
	MIN	0.0002	0.0002	0.0002	0.0002	0.0002	0.0002	0.0002	0.0002	0.0002	0.0002	0.0002	0.0002	0.0002
SP	N	4	4	4	4	4	4	4	4	4	4	4	4	4
	ME	0.0243	0.0088	0.0106	0.0587	0.0179	0.0036	0.0218	0.0021	0.0100	0.0018	0.0047	0.0002	0.0044
	AVG	0.0243	0.0088	0.0106	0.0587	0.0179	0.0036	0.0218	0.0021	0.0100	0.0018	0.0047	0.0002	0.0044
	MAX	0.0243	0.0088	0.0106	0.0587	0.0179	0.0036	0.0218	0.0021	0.0100	0.0018	0.0047	0.0002	0.0044
	MIN	0.0243	0.0088	0.0106	0.0587	0.0179	0.0036	0.0218	0.0021	0.0100	0.0018	0.0047	0.0002	0.0044
SW1	N	163	163	163	163	163	163	163	163	163	163	163	163	163
	ME	0.0120	0.0226	0.0061	0.0353	0.0130	0.0035	0.0141	0.0020	0.0080	0.0017	0.0040	0.0002	0.0040
	AVG	0.0173	0.0302	0.0082	0.0457	0.0159	0.0042	0.0184	0.0020	0.0107	0.0018	0.0054	0.0004	0.0049
	MAX	0.1040	0.1500	0.0370	0.2100	0.0710	0.0180	0.0830	0.0100	0.0460	0.0072	0.0230	0.0030	0.0200
	MIN	0.0040	0.0080	0.0020	0.0090	0.0002	0.0002	0.0002	0.0002	0.0020	0.0002	0.0002	0.0002	0.0002
SW2	N	142	142	142	142	142	142	142	142	142	142	142	142	142
	ME	0.0180	0.0277	0.0090	0.0520	0.0189	0.0053	0.0226	0.0026	0.0130	0.0021	0.0060	0.0002	0.0058
	AVG	0.0266	0.0385	0.0190	0.0800	0.0240	0.0065	0.0292	0.0033	0.0164	0.0029	0.0080	0.0006	0.0068
	MAX	0.1220	0.1580	0.9894	1.7399	0.0900	0.0240	0.1200	0.0164	0.1356	0.0120	0.0320	0.0030	0.0230
	MIN	0.0047	0.0076	0.0022	0.0173	0.0002	0.0015	0.0065	0.0002	0.0041	0.0002	0.0023	0.0002	0.0020
SW3	N	149	149	149	149	149	149	149	149	149	149	149	149	149
	ME	0.0129	0.0209	0.0070	0.0387	0.0130	0.0034	0.0148	0.0017	0.0070	0.0013	0.0040	0.0002	0.0036
	AVG	0.0184	0.0286	0.0138	0.0576	0.0162	0.0041	0.0185	0.0018	0.0098	0.0015	0.0046	0.0003	0.0042
	MAX	0.2489	0.1980	0.7155	1.1841	0.1114	0.0256	0.1288	0.0145	0.0810	0.0117	0.0298	0.0037	0.0240
	MIN	0.0035	0.0055	0.0020	0.0117	0.0002	0.0002	0.0053	0.0002	0.0025	0.0002	0.0002	0.0001	0.0002

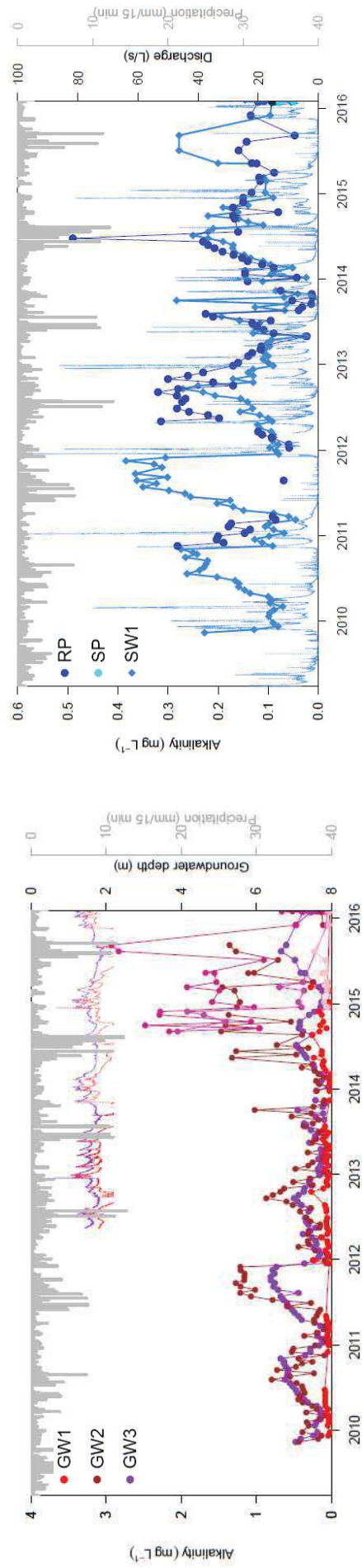
Appendix 4. Long term time series of (a) pH, (b) electrical conductivity and (c) Alkalinity for ground- and stream- water.

(a)



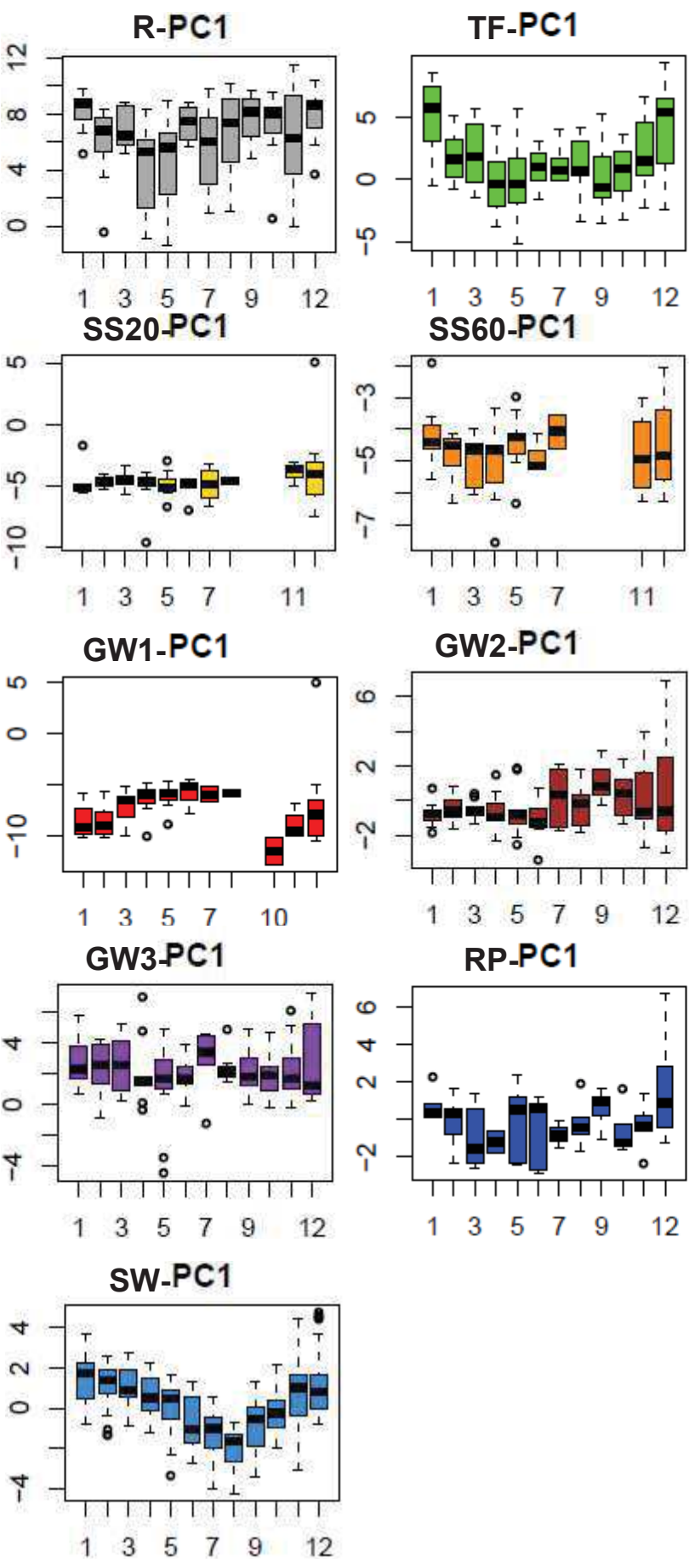
(b)



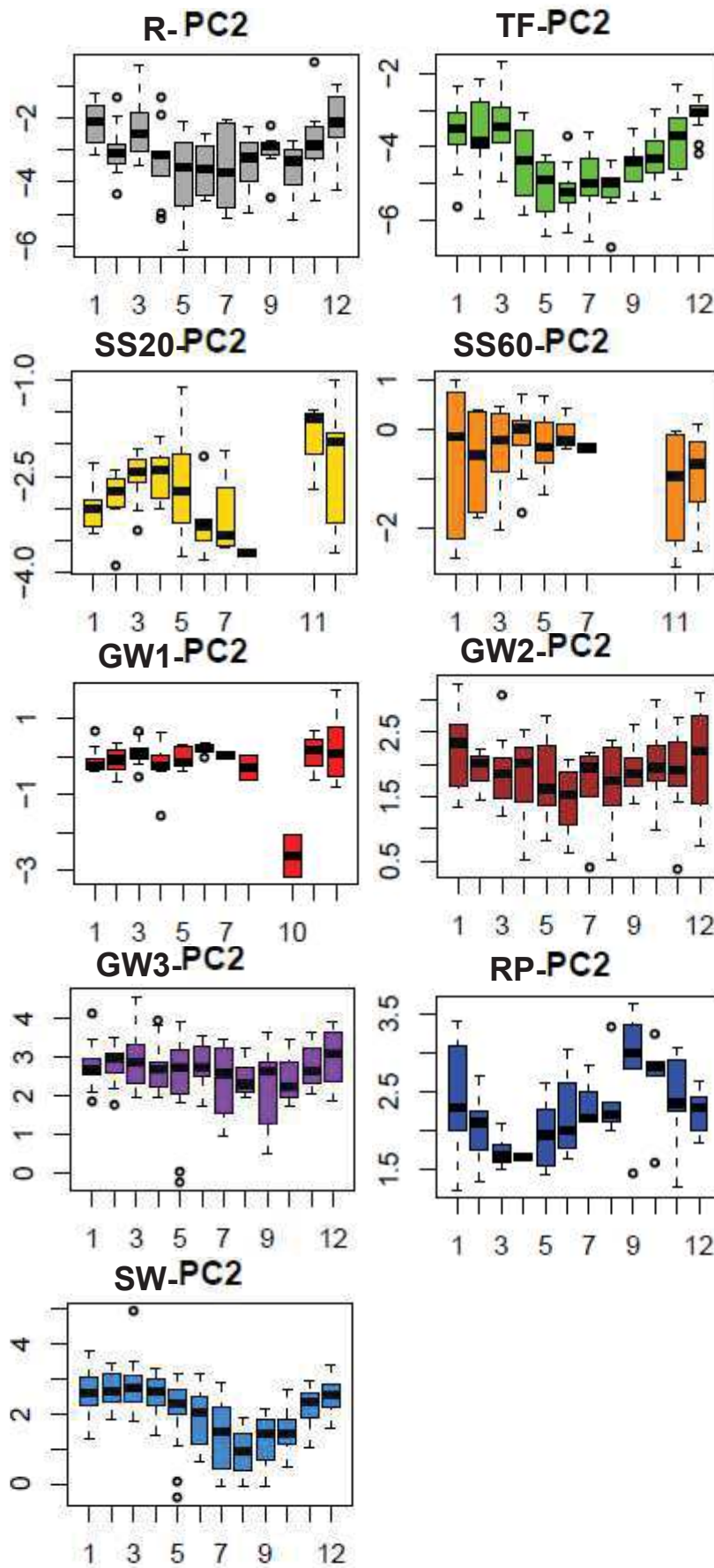


(c)

Appendix 5. Boxplots of PC1 water scores in function of the month (1-12).



Appendix 6. Boxplots of PC2 water scores in function of the month (1-12).



Appendix 7. Stable isotope, physico-chemical and major element data for water samples collected during punctual and event samplings of this project. DL: Detection Limit.

Sample	Sampling date	$\delta^{18}\text{O}$	$\delta^2\text{H}$	pH	EC	HCO_3^-	Cl^-	NO_3^-	SO_4^{2-}	Na^+	K^+	Mg^{2+}	Ca^{2+}	NH_4^+	Al^{3+}	Mn^{2+}	Fe^{2+}
					($\mu\text{S/cm}$)	(meq/L)	(mg/L)								(μg/L)		
TF1	06/07/2015 11:30	-6.17	-45.87	7.8	115.0	0.91	2.67	0.04	4.24	1.19	10.14	0.91	3.35	0.02	18.57	83.35	1.15
	30/01/2016 15:45	-6.51	-40.25	-	-	-	-	-	-	-	-	-	-	-	7.02	95.41	6.30
	31/01/2016 14:45	-7.58	-44.72	6.2	9.5	0.05	0.52	0.03	0.19	0.78	0.82	0.10	0.27	0.02	11.53	12.42	2.79
	01/02/2016 13:00	-12.82	-93.34	5.6	15.9	0.04	1.25	0.01	0.32	0.92	1.28	0.24	0.82	0.02	42.63	70.83	8.76
TF2	30/01/2016 15:45	-5.72	-38.74	6.1	7.1	0.05	0.30	0.02	0.09	0.51	0.63	0.08	0.30	0.02	14.29	10.70	3.20
	31/01/2016 14:45	-7.31	-43.35	5.4	20.1	0.06	0.82	0.01	0.20	0.82	3.82	0.16	0.96	0.02	29.70	83.27	13.85
	02/02/2016 13:00	-10.61	-75	6.0	21.3	0.05	4.61	0.17	0.42	1.77	1.51	0.17	0.61	0.03	47.41	103.49	23.03
	31/01/2016 14:45	-4.08	-22.47	5.2	34.5	0.06	2.86	0.01	0.30	1.80	4.08	0.33	2.12	0.02	79.63	244.02	45.79
SS7-20	03/12/2015 00:00	-6.47	-42.93	4.4	33	0.00	3.22	0.04	2.34	1.31	0.13	0.66	0.67	0.02	1368.09	189.57	75.65
	29/01/2016 00:00	-9.82	-63.39	4.5	33.3	0.00	2.50	0.56	2.23	1.52	0.17	0.62	0.45	0.02	1045.23	167.71	83.62
	30/01/2016 11:15	-10.83	-70.96	4.5	30.8	0.00	2.50	0.42	2.30	1.46	0.18	0.57	0.41	0.02	1151.50	180.63	79.24
	30/01/2016 11:30	-10.17	-67.52	4.6	33.6	0.01	2.97	0.36	2.64	1.74	0.23	0.65	0.44	0.02	1235.84	197.92	113.08
	31/01/2016 14:00	-10.38	-69.45	4.5	31.9	0.00	2.40	0.33	2.50	1.43	0.16	0.56	0.44	0.02	1147.73	176.85	85.78
	01/02/2016 00:00	-10.97	-72.44	4.7	31.9	0.02	3.25	0.26	3.33	1.86	0.29	0.71	0.50	0.02	885.36	229.32	40.04
	02/02/2016 12:00	-10.56	-67.44	4.5	28.3	0.00	3.41	0.42	3.47	1.46	0.13	0.51	0.34	0.02	1044.50	149.47	72.86

SS7-60	03/12/2015 00:00	-6.66	-42.91	-	34.6	-	2.80	0.02	6.85	1.62	0.10	0.62	0.99	0.12	656.73	144.98	6.51
	29/01/2016 00:00	-6.41	-41.11	4.9	41.9	0.02	3.52	0.28	7.06	1.66	0.37	0.99	1.30	0.09	730.82	626.03	21.64
	30/01/2016 15:15	-7	-45.72	4.7	36.5	0.02	3.10	0.18	6.30	1.59	0.20	0.67	0.71	0.02	830.67	326.82	8.38
	30/01/2016 15:30	-6.35	-41.2	4.8	39.4	0.02	3.02	0.11	7.57	1.48	0.31	0.71	0.93	0.04	787.96	431.97	6.14
	31/01/2016 14:15	-7.25	-44.56	4.8	39.1	0.02	3.00	0.26	7.42	1.57	0.32	0.79	0.97	0.06	738.29	496.46	6.50
	01/02/2016 00:00	-6.88	-44.15	-	-	-	-	-	-	-	-	-	-	-	89.56	1390.07	5.03
	02/02/2016 12:15	-6.64	-39.98	4.7	38.4	0.01	4.64	0.20	10.96	1.52	0.22	0.69	0.71	0.02	803.37	445.55	6.10
GW1	03/12/2015 13:00	-7.33	-50.29	4.9	74.2	0.03	3.64	1.37	14.26	2.25	0.49	2.11	4.02	0.01	332.70	100.02	7.43
	27/01/2016 00:00	-7.68	-49.75	5.1	78.1	0.03	4.33	1.74	15.82	2.56	0.52	2.31	4.75	0.02	372.77	98.77	5.04
	30/01/2016 11:45	-7.58	-49.24	5.1	80.6	0.03	4.41	1.81	16.24	2.61	0.49	2.36	4.80	0.02	361.76	94.43	3.42
	30/01/2016 15:00	-7.72	-49.65	5.1	82.1	0.03	4.42	1.80	16.65	2.86	0.50	2.36	4.77	0.02	369.44	93.17	6.22
	31/01/2016 13:45	-7.99	-49.38	5.0	76.8	0.02	3.93	1.54	15.58	2.41	0.48	2.21	4.54	0.02	355.72	95.95	1.98
	02/02/2016 12:45	-7.83	-49.95	5.1	79.6	0.03	6.15	2.66	24.16	2.25	0.46	2.13	4.47	0.02	386.45	100.27	1.62
GW2	06/07/2015 12:30	-8.26	-54.37	7.5	100.7	0.71	2.96	0.14	5.60	3.22	0.43	4.58	8.33	0.02	<D.L.	516.18	<D.L.
	03/12/2015 11:10	-7.58	-53.49	6.6	81.4	0.11	2.40	0.33	7.44	2.17	0.21	2.26	1.85	0.02	41.93	39.42	6.26
	27/01/2016 00:00	-7.81	-50.81	6.6	48.3	0.13	2.55	0.54	7.40	2.26	0.25	2.48	2.19	0.02	46.66	57.39	3.68
	30/01/2016 14:15	-7.8	-50.48	6.7	50.1	0.15	2.59	0.45	7.61	2.22	0.23	2.51	2.38	0.02	40.12	67.55	2.91
	30/01/2016 16:10	-7.97	-51.98	7.3	78.2	0.52	2.70	0.12	6.39	2.80	0.37	3.92	6.38	0.02	12.04	317.31	4.42

	31/01/2016 12:37	-7.84	-50.47	6.6	49.7	0.16	2.67	0.46	7.53	2.24	0.30	2.52	2.43	0.02	43.92	62.93	2.52
	02/02/2016 11:00	-7.78	-50.34	6.6	44.6	0.11	3.40	0.61	10.40	2.15	0.20	2.40	2.04	0.02	46.43	43.41	2.77
GW3	06/07/2015 12:00	-7.80	-51.13	7.3	111.4	0.49	5.14	1.60	12.20	5.58	0.48	4.50	8.44	0.02	<D.L.	14.26	0.77
	03/12/2015 03:36	-7.77	-48.58	7.2	96.8	0.48	5.74	2.10	10.76	5.03	1.28	4.92	8.19	0.02	<D.L.	671.21	49.55
	27/01/2016 00:00	-7.22	-46.07	6.8	93.0	0.28	5.67	2.22	12.42	4.57	0.67	4.06	6.43	0.02	<D.L.	375.82	102.30
	30/01/2016 13:00	-6.99	-45.47	6.8	90.9	0.15	5.19	2.88	12.52	4.29	0.45	3.65	5.52	0.02	<D.L.	66.19	4.91
	30/01/2016 16:00	-6.59	-45.02	6.8	93.0	0.19	4.98	2.78	12.67	4.32	0.56	3.71	5.96	0.02	<D.L.	218.59	6.40
	31/01/2016 12:15	-7.37	-46.42	6.8	97.1	0.24	5.39	2.45	12.66	4.49	0.67	3.88	6.21	0.02	<D.L.	344.48	21.33
	02/02/2016 10:30	-7.18	-46.27	7.0	101.6	0.31	7.24	3.17	15.55	4.71	0.72	4.27	6.90	0.02	<D.L.	490.72	37.19
GW5	06/07/2015 10:50	-8.02	-53.13	7.7	132.0	0.90	3.84	1.30	4.09	2.68	0.57	5.50	12.88	0.02	6.77	240.75	24.25
	03/12/2015 13:05	-7.77	-47.21	7.3	100.7	0.47	5.08	0.08	9.25	4.16	0.40	3.70	6.91	0.02	4.05	153.65	10.02
	27/01/2016 00:00	-7.46	-48.34	7.0	80.0	0.38	4.01	0.32	8.62	3.62	0.39	3.00	5.83	0.02	15.77	175.25	10.38
	30/01/2016 12:00	-6.91	-48.45	7.5	101.6	0.66	4.01	0.76	6.91	3.30	0.36	3.38	11.50	0.02	7.36	164.43	1.68
	30/01/2016 15:00	-6.99	-48.3	7.2	78.9	0.40	4.29	0.54	7.83	3.47	0.31	3.22	6.43	0.02	14.38	181.44	3.21
	31/01/2016 14:00	-7.39	-47.15	6.8	63.6	0.22	3.87	0.18	9.68	3.77	0.22	2.26	3.95	0.02	27.69	148.45	4.46
	02/02/2016 12:30	-7.32	-48.31	7.0	65.5	0.25	5.98	0.43	14.29	3.67	0.23	2.50	4.17	0.02	23.76	168.36	7.11
GW6	03/12/2015 13:50	-7.59	-46.93	6.4	136.7	0.06	5.06	5.87	11.24	5.05	0.52	5.18	4.07	0.02	95.22	151.22	2.68
	27/01/2016 00:00	-7.22	-47	6.4	93.0	0.07	5.05	5.22	10.75	4.54	0.49	4.81	3.92	0.02	96.30	129.24	6.24

	30/01/2016 14:40	-7.23	-47.09	6.3	81.8	0.05	4.30	4.31	9.40	3.82	0.39	4.21	3.13	0.02	91.36	106.79	4.89
	30/01/2016 17:00	-6.97	-46.32	6.2	84.1	0.05	4.29	4.33	9.38	3.79	0.40	4.18	3.09	0.02	83.39	110.45	5.64
	31/01/2016 13:30	-7.25	-46.6	6.2	92.9	0.06	4.93	3.89	13.17	4.90	0.48	4.24	3.31	0.02	96.20	151.42	5.07
	02/02/2016 11:40	-7.03	-46.59	6.5	94.3	0.09	7.39	6.60	18.42	4.44	0.43	4.34	4.27	0.02	79.70	153.79	13.27
GW7	06/07/2015 00:00	-7.98	-52.58	6.5	60.2	0.09	3.23	0.45	10.13	2.59	0.50	2.23	2.51	0.02	23.89	19.04	8.96
	03/12/2015 12:20	-7.64	-51.20	6.0	44.7	0.04	3.17	1.01	5.63	2.23	0.29	2.32	0.70	0.03	51.91	74.75	52.61
	27/01/2016 00:00	-7.81	-50.18	5.9	43.9	0.04	3.28	0.98	6.20	2.22	0.24	2.44	0.66	0.02	65.17	37.02	2.19
	30/01/2016 14:15	-7.56	-49.94	6.0	44.1	0.04	3.16	1.07	6.26	2.22	0.27	2.48	0.70	0.02	64.59	45.56	12.67
	30/01/2016 16:45	-7.75	-49.84	6.0	44.4	0.04	3.14	1.07	6.30	2.22	0.23	2.49	0.67	0.02	65.38	38.98	4.08
	31/01/2016 13:15	-7.62	-49.84	6.0	44.9	0.04	3.09	0.98	6.24	2.20	0.22	2.44	0.68	0.02	59.07	42.79	7.09
	02/02/2016 11:30	-8	-50.29	6.1	44.5	0.05	5.28	1.55	9.54	2.33	0.20	2.59	0.71	0.02	57.03	62.05	22.02
RP	06/07/2015 12:40	-8.11	-52.59	6.8	44.7	0.16	2.16	0.01	7.07	2.32	0.25	2.27	2.04	0.02	41.21	311.66	34.64
	03/12/2015 00:00	-7.68	-49.27	6.6	47.6	0.14	2.75	0.20	7.68	2.42	0.17	2.45	2.07	0.02	35.27	17.33	14.19
	29/01/2016 00:00	-7.63	-49.44	6.7	52.4	0.12	2.29	0.41	11.01	2.17	0.27	2.87	2.43	0.02	18.16	14.97	12.34
	30/01/2016 13:15	-7.83	-50.17	-	49.3	-	-	-	-	-	-	-	-	-	13.52	14.74	7.18
	31/01/2016 12:37	-7.84	-49.9	-	-	-	-	-	-	-	-	-	-	-	19.94	13.74	4.03
	02/02/2016 10:40	-7.61	-50.29	6.6	53.5	0.11	3.84	0.71	16.84	2.26	0.28	2.90	2.50	0.02	15.47	14.35	5.60
Spring	29/01/2016 00:00	-7.57	-49.88	6.4	44.8	0.08	2.75	0.16	9.72	1.83	0.23	2.72	1.49	0.02	24.18	2.72	1.60

	31/01/2016 13:00	-8.03	-49.77	5.1	46.1	0.05	2.82	0.22	9.65	1.79	0.23	2.58	1.36	0.02	23.51	2.43	2.22
	02/02/2016 11:00	-7.9	-50.31	6.4	45.7	0.08	4.17	0.26	14.63	1.78	0.20	2.60	1.42	0.02	23.38	2.54	2.29
SW1	06/07/2015 12:00	-7.45	-48.45	7.0	61.2	0.28	3.37	0.18	7.12	3.23	0.53	3.09	3.53	0.02	51.04	29.85	91.26
	03/12/2015 09:00	-8.25	-50.98	6.6	48.5	0.10	2.50	0.57	7.45	2.25	0.31	2.45	1.98	0.02	24.16	2.56	13.64
	27/01/2016 00:00	-7.9	-50.11	6.4	49.2	0.09	2.92	0.61	8.21	2.32	0.25	2.57	2.00	0.02	15.12	1.65	6.48
	29/01/2016 13:00	-7.65	-49.07	6.5	45.8	0.09	2.64	0.54	7.98	2.15	0.25	2.43	1.82	0.02	11.07	4.19	5.99
	30/01/2016 13:00	-7.93	-51.3	6.5	42.3	0.09	2.55	0.50	7.17	2.07	0.26	2.32	1.74	0.02	23.35	1.75	13.74
	30/01/2016 16:00	-8.04	-49.52	5.8	41.0	0.05	2.64	0.53	6.86	2.01	0.31	2.14	1.61	0.02	43.07	1.96	27.81
	31/01/2016 12:00	-7.93	-49.76	6.5	46.7	0.09	2.69	0.59	8.32	2.16	0.26	2.46	1.84	0.02	16.06	2.50	6.81
	01/02/2016 12:00	-7.58	-49.22	6.5	46.98	0.09	2.70	0.63	8.43	2.22	0.25	2.56	1.92	0.02	15.27	2.14	6.46
	02/02/2016 10:05	-7.84	-49.65	6.5	47.7	0.08	4.34	0.85	13.00	2.18	0.22	2.53	1.86	0.02	12.08	2.23	4.83
SW2	06/07/2015 12:20	-7.61	-50.82	6.8	44.6	0.16	2.41	0.12	7.43	2.34	0.36	2.80	1.90	0.02	29.31	12.68	40.92
	03/12/2015 11:00	-7.67	-50.49	6.5	40.4	0.07	2.28	0.50	6.67	1.97	0.26	2.19	1.18	0.02	54.88	11.58	4.33
	27/01/2016 00:00	-7.74	-50.97	6.4	40.3	0.08	2.43	0.56	6.48	2.01	0.19	2.24	1.20	0.02	29.60	9.41	2.75
SW3	06/07/2015 12:25	-7.48	-50.35	6.8	47.8	0.18	2.29	0.25	4.66	2.38	0.28	2.35	2.10	0.02	98.35	68.94	114.79
	03/12/2015 11:05	-7.89	-51.15	6.6	42.2	0.09	2.42	0.20	8.20	1.99	0.24	2.48	1.39	0.02	22.54	5.35	10.55
	27/01/2016 00:00	-7.55	-50.24	6.5	44.0	0.09	2.68	0.22	8.60	1.97	0.21	2.56	1.39	0.02	15.44	3.69	5.69
D.L.															1.33	0.03	0.33

Appendix 8. Trace element data for water samples collected during the punctual and event samplings of this project. DL: Detection Limit.

Sample	Sampling date	Sc	Cr	Co	Ni	Cu	Zn	Rb	Sr	Cd	Sb	Cs	Ba	Pb	U
(µg/L)															
TF1	06/07/2015 11:30	<D.L.	0.17	5.27	5.38	1.66	38.95	0.67	10.91	<D.L.	0.046	0.0144	2.74	0.03	-
	30/01/2016 15:45	<D.L.	<D.L.	0.03	0.26	0.80	3.52	1.53	1.07	<D.L.	0.195	0.0061	0.79	0.31	-
	31/01/2016 14:45	<D.L.	<D.L.	<D.L.	0.15	0.75	3.47	1.98	0.38	<D.L.	0.233	<D.L.	0.25	0.14	0.002
	01/02/2016 13:00	<D.L.	<D.L.	0.06	0.44	1.75	10.83	3.29	1.42	0.05	0.222	0.0111	2.29	0.71	-
TF2	30/01/2016 15:45	<D.L.	0.22	0.03	0.24	0.77	6.98	1.42	0.54	0.03	0.402	<D.L.	0.44	0.16	-
	31/01/2016 14:45	<D.L.	0.18	0.06	0.59	1.78	9.55	9.72	1.81	0.07	0.323	0.0201	3.46	0.70	-
	02/02/2016 13:00	<D.L.	0.19	0.11	0.49	1.73	18.15	3.45	1.46	0.03	0.397	<D.L.	1.19	0.61	-
	31/01/2016 14:45	<D.L.	0.24	0.15	0.90	2.83	19.63	11.44	4.23	0.12	0.222	0.0223	7.05	1.22	-
SS7-20	03/12/2015 00:00	0.21	1.54	3.06	5.17	0.87	36.51	0.23	2.35	0.19	0.169	<D.L.	13.67	1.50	-
	29/01/2016 00:00	0.52	1.53	5.24	4.92	0.73	40.40	0.73	2.54	0.29	0.167	<D.L.	9.94	1.09	-
	30/01/2016 11:15	0.54	1.50	4.91	4.76	0.78	38.11	0.71	2.40	0.26	0.220	<D.L.	9.77	1.16	0.011
	30/01/2016 11:30	0.55	1.64	6.31	5.10	1.00	40.32	0.58	2.82	0.31	0.852	<D.L.	9.76	1.50	0.029
	31/01/2016 14:00	0.49	1.43	4.26	4.72	0.70	36.76	0.66	2.23	0.26	0.206	<D.L.	9.38	1.12	0.018
	01/02/2016 00:00	0.54	1.20	7.29	4.72	0.87	40.73	0.83	2.77	0.32	0.594	<D.L.	9.08	0.43	-
	02/02/2016 12:00	0.51	1.44	3.74	4.46	0.48	34.31	0.49	2.02	0.23	0.149	<D.L.	8.52	0.95	-
SS7-60	03/12/2015 00:00	<D.L.	0.38	2.58	4.79	0.57	23.46	0.20	3.68	0.26	0.073	<D.L.	16.94	0.13	-
	29/01/2016 00:00	0.40	0.45	10.46	6.91	0.81	47.48	1.38	5.89	0.56	0.213	<D.L.	20.92	0.17	-
	30/01/2016 15:15	0.30	0.28	7.86	6.45	0.53	39.20	0.61	4.02	0.46	0.424	<D.L.	17.80	0.20	0.005
	30/01/2016 15:30	0.24	0.22	7.58	6.05	0.64	33.71	0.87	4.69	0.46	1.204	<D.L.	18.81	0.15	-
	31/01/2016 14:15	0.30	0.22	7.76	6.52	0.43	40.05	1.18	4.57	0.49	0.341	<D.L.	19.02	0.16	0.022
	01/02/2016 00:00	0.37	0.26	12.34	5.91	1.59	39.14	3.73	10.65	0.48	1.333	0.0058	20.21	0.09	-
	02/02/2016 12:15	0.28	0.19	8.85	6.89	0.48	41.92	0.86	3.86	0.54	0.192	<D.L.	18.18	0.21	-
GW1	03/12/2015 13:00	<D.L.	0.23	5.00	7.96	0.74	13.93	0.39	14.17	0.32	0.034	0.0267	29.20	0.09	-
	27/01/2016 00:00	0.26	0.24	4.86	8.29	0.79	14.44	0.41	16.86	0.35	0.030	0.0255	32.01	0.07	-
	30/01/2016 11:45	0.24	0.24	4.74	8.27	0.82	14.06	0.40	17.04	0.32	0.035	0.0244	31.41	0.06	-
	30/01/2016 15:00	0.25	0.26	4.69	8.23	0.83	13.81	0.40	16.64	0.32	0.035	0.0222	30.85	0.10	-
	31/01/2016 13:45	0.23	0.25	4.93	8.29	0.76	13.75	0.39	16.42	0.33	0.034	0.0221	30.09	0.05	-
	02/02/2016 12:45	0.24	0.22	4.46	8.33	0.72	14.04	0.37	17.79	0.37	0.032	0.0253	30.50	0.07	0.016

GW2	06/07/2015 12:30	<D.L.	0.11	0.06	0.97	<D.L.	1.12	0.56	32.05	<D.L.	<D.L.	0.0179	0.46	<D.L.	-
	03/12/2015 11:10	<D.L.	0.22	0.36	4.47	0.23	3.56	0.20	12.53	0.03	0.030	<D.L.	3.01	0.03	-
	27/01/2016 00:00	0.37	0.18	0.29	4.73	0.18	3.47	0.21	14.26	<D.L.	<D.L.	<D.L.	3.21	<D.L.	-
	30/01/2016 14:15	0.37	0.39	0.26	4.58	0.29	4.45	0.22	14.73	<D.L.	0.042	0.0055	2.96	0.03	-
	30/01/2016 16:10	0.54	0.15	0.13	2.83	0.19	2.13	0.35	26.23	<D.L.	<D.L.	0.0108	1.63	<D.L.	0.027
	31/01/2016 12:37	0.36	0.15	0.26	4.58	0.26	3.69	0.22	15.22	<D.L.	0.043	<D.L.	2.95	<D.L.	-
	02/02/2016 11:00	0.34	0.15	0.29	4.83	0.27	3.73	0.18	14.18	<D.L.	0.028	<D.L.	3.12	<D.L.	-
GW3	06/07/2015 12:00	<D.L.	0.26	0.07	0.33	<D.L.	7.47	0.16	50.21	<D.L.	<D.L.	0.0059	2.13	<D.L.	0.012
	03/12/2015 03:36	<D.L.	0.25	5.27	4.79	0.14	53.37	0.76	52.68	0.03	0.060	0.0071	6.34	<D.L.	-
	27/01/2016 00:00	0.52	<D.L.	2.68	2.00	<D.L.	13.10	0.44	45.11	<D.L.	0.052	0.0066	3.88	<D.L.	0.004
	30/01/2016 13:00	0.47	0.25	0.32	1.04	0.18	9.57	0.27	40.58	<D.L.	0.030	0.0053	1.90	<D.L.	-
	30/01/2016 16:00	0.50	0.31	1.04	1.51	0.18	12.70	0.39	41.74	<D.L.	0.038	0.0068	3.10	<D.L.	0.004
	31/01/2016 12:15	0.47	0.17	2.26	1.93	0.15	12.73	0.43	43.73	<D.L.	0.056	0.0060	3.75	<D.L.	0.004
	02/02/2016 10:30	0.51	0.17	3.16	2.63	0.17	14.31	0.48	49.38	<D.L.	0.039	0.0075	3.75	<D.L.	-
GW5	06/07/2015 10:50	<D.L.	<D.L.	2.18	3.14	0.34	9.88	0.40	20.61	0.45	1.701	0.0220	2.98	1.18	0.015
	03/12/2015 13:05	<D.L.	<D.L.	2.62	6.00	0.28	8.27	0.34	13.62	0.30	1.265	0.0221	2.79	7.56	-
	27/01/2016 00:00	0.29	<D.L.	7.45	7.10	0.44	14.44	0.26	11.54	0.34	0.611	0.0150	2.85	5.92	0.008
	30/01/2016 12:00	0.33	<D.L.	5.21	7.35	0.50	15.81	0.29	14.74	0.54	1.110	0.0122	3.50	8.42	-
	30/01/2016 15:00	0.32	<D.L.	7.22	7.43	0.59	13.77	0.28	12.21	0.32	0.574	0.0132	2.87	5.63	0.008
	31/01/2016 14:00	0.24	0.12	9.47	8.12	0.78	17.13	0.20	9.04	0.29	0.393	0.0115	2.94	7.66	0.008
	02/02/2016 12:30	0.27	<D.L.	8.26	7.70	0.53	16.95	0.20	10.27	0.30	0.361	0.0075	3.15	3.13	-
GW6	03/12/2015 13:50	<D.L.	0.24	4.15	11.86	1.48	22.43	0.48	47.25	0.14	0.182	0.0419	2.32	0.47	-
	27/01/2016 00:00	0.62	0.15	3.03	11.66	1.14	21.27	0.46	47.74	0.14	0.180	0.0358	2.32	1.47	-
	30/01/2016 14:40	0.60	0.23	2.45	10.79	1.57	20.01	0.39	38.59	0.12	0.097	0.0303	2.19	0.96	-
	30/01/2016 17:00	0.58	0.24	2.57	10.91	1.30	20.64	0.39	38.91	0.14	0.096	0.0193	2.41	0.94	-
	31/01/2016 13:30	0.60	0.21	3.74	11.17	1.43	22.09	0.41	45.03	0.13	0.210	0.0385	2.23	0.80	-
	02/02/2016 11:40	0.56	0.12	3.24	11.38	1.36	20.40	0.42	49.10	0.16	0.383	0.0323	2.08	1.29	0.008
GW7	06/07/2015 00:00	<D.L.	0.36	0.37	5.48	0.45	3.52	0.21	19.47	<D.L.	<D.L.	<D.L.	2.05	0.03	0.007
	03/12/2015 12:20	<D.L.	<D.L.	6.84	7.09	0.99	10.44	0.28	5.80	0.03	<D.L.	0.0103	7.23	0.03	-
	27/01/2016 00:00	0.30	0.13	3.17	7.87	1.06	12.05	0.23	6.57	0.04	<D.L.	0.0071	7.95	0.04	-
	30/01/2016 14:15	0.29	0.55	3.13	8.21	1.29	14.49	0.25	6.84	0.03	0.054	0.0073	7.60	0.17	-
	30/01/2016 16:45	0.29	0.20	3.10	8.01	1.17	12.89	0.25	6.85	0.03	0.045	0.0078	7.71	0.13	-
	31/01/2016 13:15	0.29	0.14	2.70	7.91	0.91	11.64	0.21	6.59	0.04	0.038	0.0065	7.41	0.17	-

	02/02/2016 11:30	0.28	0.12	2.81	7.93	0.90	11.23	0.23	7.74	0.03	0.032	0.0084	7.46	0.10	-
RP	06/07/2015 12:40	<D.L.	0.29	0.30	2.74	5.85	15.59	27.39	3.02	0.06	0.140	0.1679	0.65	1.02	-
	03/12/2015 00:00	<D.L.	0.21	0.31	5.65	0.96	3.62	0.12	19.80	<D.L.	<D.L.	<D.L.	1.79	0.07	-
	29/01/2016 00:00	0.37	0.10	0.36	6.22	0.46	4.73	0.41	24.68	<D.L.	0.369	<D.L.	2.22	0.03	-
	30/01/2016 13:15	0.34	0.13	0.36	5.89	0.55	5.03	0.61	24.30	<D.L.	0.923	<D.L.	2.11	0.04	-
	31/01/2016 12:37	0.35	0.17	0.27	5.67	0.39	4.04	0.69	27.19	<D.L.	1.158	<D.L.	2.08	0.03	-
	02/02/2016 10:40	0.35	0.21	0.29	6.26	0.48	5.00	0.43	26.03	<D.L.	0.383	<D.L.	2.10	0.04	-
Spring	29/01/2016 00:00	0.31	0.14	0.03	9.90	0.22	4.88	0.16	10.10	<D.L.	0.048	0.0061	1.80	0.03	-
	31/01/2016 13:00	0.28	0.18	<D.L.	9.65	0.14	4.45	0.14	10.41	<D.L.	0.057	<D.L.	1.64	<D.L.	-
	02/02/2016 11:00	0.31	0.14	<D.L.	9.86	<D.L.	4.57	0.13	10.67	<D.L.	0.034	<D.L.	1.66	<D.L.	-
SW1	06/07/2015 12:00	<D.L.	<D.L.	0.18	7.24	0.78	5.04	0.61	22.20	<D.L.	0.035	<D.L.	3.55	0.25	0.013
	03/12/2015 09:00	<D.L.	0.16	0.03	3.16	0.19	3.41	0.25	13.41	<D.L.	0.043	<D.L.	2.80	0.05	-
	27/01/2016 00:00	0.36	0.11	<D.L.	3.90	0.13	4.20	0.21	15.06	<D.L.	0.054	<D.L.	5.64	0.03	0.003
	29/01/2016 13:00	0.33	0.11	0.05	3.71	0.61	3.77	0.16	13.44	<D.L.	<D.L.	<D.L.	2.73	0.05	-
	30/01/2016 13:00	0.31	0.12	0.03	4.06	0.32	4.04	0.24	13.14	<D.L.	0.032	<D.L.	2.80	0.07	-
	30/01/2016 16:00	0.29	0.16	0.04	4.17	0.30	3.97	0.25	12.90	<D.L.	0.068	<D.L.	2.65	0.08	0.005
	31/01/2016 12:00	0.34	0.13	0.03	4.09	0.17	4.27	0.19	14.39	<D.L.	0.033	<D.L.	2.86	0.03	0.003
	01/02/2016 12:00	0.35	0.11	0.03	4.30	0.18	4.52	0.20	14.63	<D.L.	0.038	<D.L.	3.11	0.03	-
	02/02/2016 10:05	0.34	<D.L.	0.03	4.52	0.17	4.72	0.18	14.96	<D.L.	0.041	<D.L.	3.14	<D.L.	-
SW2	06/07/2015 12:20	<D.L.	0.25	0.17	5.33	0.58	1.56	0.46	11.37	<D.L.	<D.L.	<D.L.	1.25	0.23	-
	03/12/2015 11:00	<D.L.	0.14	0.28	5.26	0.19	8.08	0.21	9.55	<D.L.	0.046	<D.L.	4.66	0.04	-
	27/01/2016 00:00	0.31	0.10	0.22	5.76	0.15	5.98	0.18	10.20	<D.L.	0.046	<D.L.	4.66	0.03	-
SW3	06/07/2015 12:25	<D.L.	0.50	1.15	5.12	1.34	3.63	0.55	12.06	<D.L.	<D.L.	<D.L.	3.01	0.47	-
	03/12/2015 11:05	<D.L.	0.17	<D.L.	5.19	0.12	3.19	0.22	9.27	<D.L.	0.034	<D.L.	1.51	0.04	-
	27/01/2016 00:00	0.32	0.10	<D.L.	6.10	0.10	3.42	0.17	10.14	<D.L.	0.030	<D.L.	1.68	0.03	-
D.L.		0.03	0.03	0.01	0.01	0.03	0.33	0.01	0.01	0.01	0.003	0.0003	0.03	0.025	(I.D.)

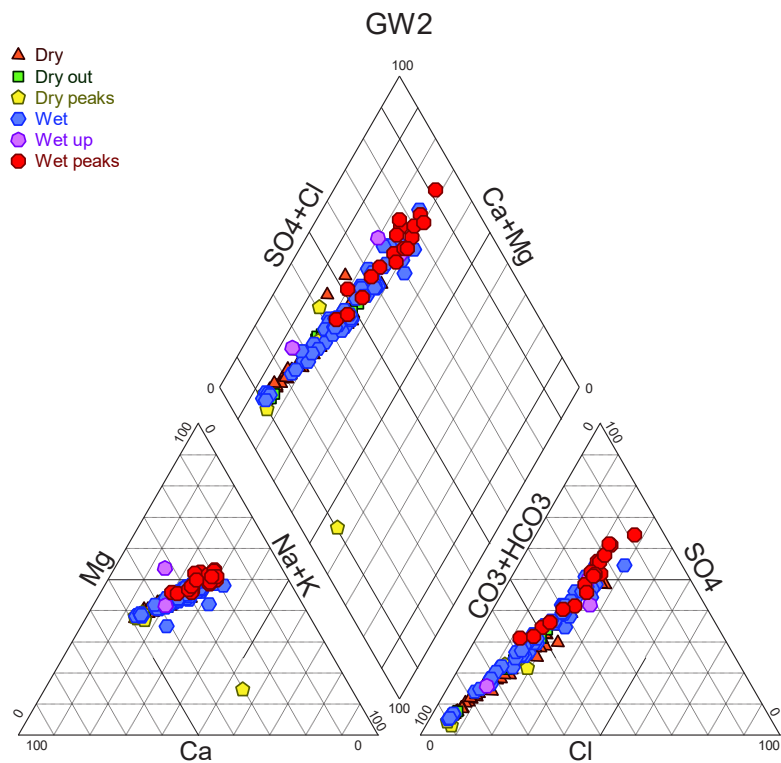
Appendix 9. Rare Earth Element (REE) data for water samples collected during the punctual and event samplings of this project. DL: Detection Limit.

Sample	Sampling date	La	Ce	Pr	Nd	Sm	Eu	Gd	Tb	Dy	Ho	Er	Tm	Yb	Lu
(µg/L)															
TF1	06/07/2015 11:30	0.0056	0.0121	0.0027	0.0180	<D.L.	0.0014	0.0065	<D.L.	0.0053	<D.L.	0.0024	<D.L.	0.0028	<D.L.
	30/01/2016 15:45	0.0134	0.0208	0.0038	0.0189	<D.L.	<D.L.	0.0059	<D.L.	0.0043	<D.L.	0.0019	<D.L.	0.0019	<D.L.
	31/01/2016 14:45	0.0063	0.0103	0.0013	0.0074	<D.L.	<D.L.	<D.L.	<D.L.	0.0018	<D.L.	<D.L.	<D.L.	<D.L.	<D.L.
	01/02/2016 13:00	0.0291	0.0454	0.0090	0.0383	0.0076	0.0018	0.0111	0.0015	0.0095	0.0021	0.0053	<D.L.	0.0034	<D.L.
TF2	30/01/2016 15:45	0.0044	0.0096	0.0012	0.0057	<D.L.	<D.L.	<D.L.	<D.L.	<D.L.	<D.L.	<D.L.	<D.L.	<D.L.	<D.L.
	31/01/2016 14:45	0.0753	0.0762	0.0248	0.1078	0.0307	0.0065	0.0398	0.0058	0.0334	0.0060	0.0155	0.0019	0.0079	<D.L.
	02/02/2016 13:00	0.0309	0.0513	0.0131	0.0691	0.0153	0.0040	0.0222	0.0026	0.0160	0.0035	0.0096	0.0011	0.0072	<D.L.
	31/01/2016 14:45	0.0438	0.0965	0.0134	0.0636	0.0124	0.0029	0.0137	0.0020	0.0092	0.0016	0.0044	<D.L.	0.0040	<D.L.
SS7-20	03/12/2015 00:00	0.3702	1.2704	0.1118	0.4750	0.1096	0.0253	0.1075	0.0143	0.0872	0.0165	0.0452	0.0065	0.0461	0.0061
	29/01/2016 00:00	0.2576	0.8911	0.0823	0.3563	0.0781	0.0183	0.0827	0.0108	0.0609	0.0118	0.0339	0.0051	0.0341	<D.L.
	30/01/2016 11:15	0.2417	0.8337	0.0796	0.3500	0.0789	0.0186	0.0870	0.0120	0.0691	0.0124	0.0372	0.0051	0.0334	<D.L.
	30/01/2016 11:30	0.2685	0.9088	0.0906	0.3925	0.0874	0.0217	0.1000	0.0131	0.0732	0.0144	0.0409	0.0056	0.0357	<D.L.
	31/01/2016 14:00	0.2487	0.8952	0.0790	0.3428	0.0814	0.0187	0.0815	0.0107	0.0619	0.0122	0.0335	0.0048	0.0329	<D.L.
	01/02/2016 00:00	0.2488	0.9944	0.0867	0.4003	0.0950	0.0193	0.0960	0.0125	0.0771	0.0138	0.0406	0.0054	0.0370	<D.L.
	02/02/2016 12:00	0.2121	0.7320	0.0699	0.2897	0.0682	0.0161	0.0749	0.0103	0.0628	0.0119	0.0330	0.0043	0.0305	<D.L.
SS7-60	03/12/2015 00:00	0.3565	0.6645	0.0644	0.2540	0.0467	0.0128	0.0649	0.0090	0.0556	0.0106	0.0280	0.0033	0.0179	<D.L.
	29/01/2016 00:00	0.3855	0.8379	0.0891	0.3562	0.0747	0.0187	0.0950	0.0126	0.0715	0.0142	0.0356	0.0050	0.0286	<D.L.
	30/01/2016 15:15	0.3275	0.6973	0.0645	0.2658	0.0500	0.0129	0.0695	0.0094	0.0553	0.0103	0.0265	0.0035	0.0204	<D.L.
	30/01/2016 15:30	0.2947	0.6014	0.0468	0.1845	0.0325	0.0096	0.0514	0.0077	0.0447	0.0088	0.0210	0.0024	0.0149	<D.L.
	31/01/2016 14:15	0.2922	0.6446	0.0542	0.2092	0.0411	0.0107	0.0551	0.0080	0.0432	0.0089	0.0234	0.0028	0.0165	<D.L.
	01/02/2016 00:00	0.1189	0.2941	0.0315	0.1252	0.0245	0.0068	0.0307	0.0039	0.0232	0.0044	0.0121	0.0016	0.0097	<D.L.
	02/02/2016 12:15	0.3047	0.6844	0.0541	0.1927	0.0436	0.0105	0.0571	0.0082	0.0464	0.0084	0.0238	0.0026	0.0164	<D.L.
GW1	03/12/2015 13:00	2.5772	1.7808	1.1282	5.4649	1.4064	0.3775	2.3099	0.3543	2.2358	0.4572	1.2502	0.1574	0.8763	0.1341
	27/01/2016 00:00	3.0149	2.0102	1.2968	6.4215	1.6414	0.4516	2.7485	0.4189	2.5297	0.5332	1.4830	0.1813	0.9999	0.1530
	30/01/2016 11:45	2.9597	1.9940	1.2749	6.3230	1.6015	0.4351	2.6825	0.4078	2.4639	0.5261	1.4467	0.1777	0.9986	0.1459
	30/01/2016 15:00	2.9186	1.9923	1.2784	6.3867	1.6273	0.4476	2.7301	0.4101	2.4931	0.5283	1.4693	0.1786	1.0084	0.1506
	31/01/2016 13:45	2.7427	1.8200	1.1698	5.8163	1.4563	0.3985	2.4879	0.3759	2.2789	0.4909	1.3436	0.1643	0.9247	0.1376
	02/02/2016 12:45	3.0806	2.0793	1.3282	6.3171	1.6606	0.4408	2.7253	0.4169	2.5091	0.5342	1.4799	0.1821	0.9997	0.1587

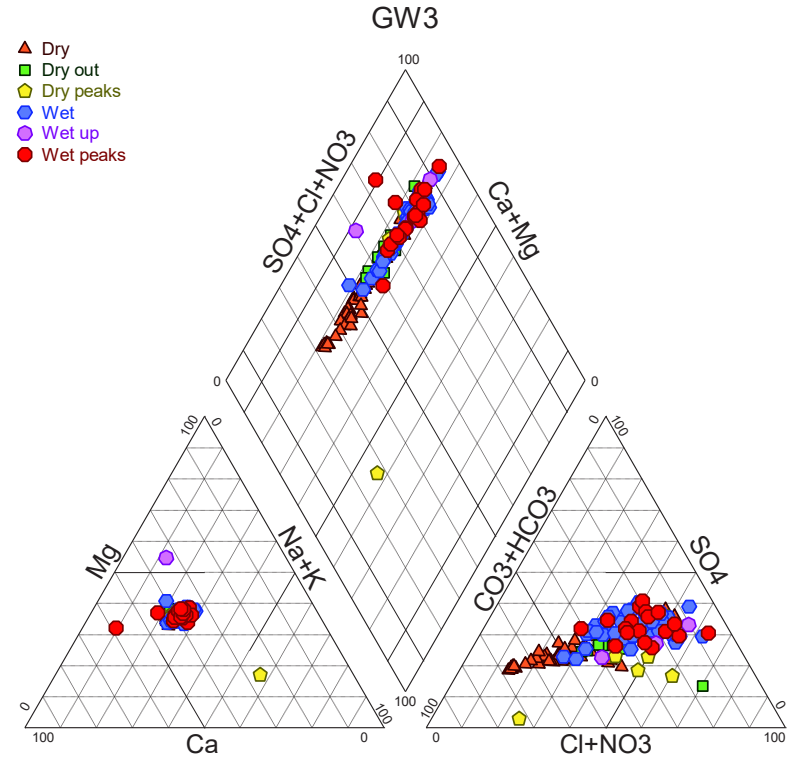
GW2	06/07/2015 12:30	0.0051	0.0050	0.0030	0.0146	<D.L.	0.0013	0.0055	<D.L.	0.0051	<D.L.	0.0017	<D.L.	0.0020	<D.L.
	03/12/2015 11:10	0.0378	0.0582	0.0208	0.1169	0.0409	0.0111	0.0485	0.0051	0.0264	0.0041	0.0113	0.0017	0.0103	<D.L.
	27/01/2016 00:00	0.0318	0.0498	0.0159	0.0945	0.0326	0.0081	0.0395	0.0042	0.0220	0.0036	0.0104	0.0012	0.0087	<D.L.
	30/01/2016 14:15	0.0301	0.0392	0.0131	0.0758	0.0209	0.0062	0.0287	0.0036	0.0174	0.0034	0.0102	0.0013	0.0075	<D.L.
	30/01/2016 16:10	0.0284	0.0375	0.0160	0.0911	0.0301	0.0083	0.0371	0.0041	0.0196	0.0036	0.0090	0.0012	0.0074	<D.L.
	31/01/2016 12:37	0.0317	0.0446	0.0161	0.0936	0.0305	0.0076	0.0370	0.0043	0.0188	0.0036	0.0078	0.0013	0.0078	<D.L.
	02/02/2016 11:00	0.0348	0.0520	0.0175	0.0880	0.0315	0.0084	0.0381	0.0042	0.0203	0.0035	0.0101	0.0014	0.0083	<D.L.
GW3	06/07/2015 12:00	0.0024	0.0033	<D.L.	0.0053	<D.L.	<D.L.	<D.L.	<D.L.	0.0051	<D.L.	<D.L.	<D.L.	<D.L.	<D.L.
	03/12/2015 03:36	0.0032	0.0062	0.0016	0.0112	<D.L.	<D.L.	<D.L.	<D.L.	0.0051	<D.L.	0.0012	<D.L.	0.0024	<D.L.
	27/01/2016 00:00	0.0033	0.0050	0.0015	0.0067	<D.L.	<D.L.	<D.L.	<D.L.	0.0015	<D.L.	0.0016	<D.L.	0.0013	<D.L.
	30/01/2016 13:00	0.0085	0.0070	0.0038	0.0164	0.0060	0.0013	0.0085	0.0011	0.0068	0.0012	0.0043	<D.L.	0.0032	<D.L.
	30/01/2016 16:00	0.0059	0.0061	0.0030	0.0146	0.0065	0.0011	0.0065	<D.L.	0.0052	<D.L.	0.0033	<D.L.	0.0027	<D.L.
	31/01/2016 12:15	0.0076	0.0061	0.0023	0.0153	<D.L.	<D.L.	0.0058	<D.L.	0.0048	0.0011	0.0023	<D.L.	0.0027	<D.L.
	02/02/2016 10:30	0.0093	0.0082	0.0031	0.0163	0.0052	<D.L.	0.0065	<D.L.	0.0056	0.0010	0.0034	<D.L.	0.0026	<D.L.
GW5	06/07/2015 10:50	0.0131	0.0229	0.0049	0.0206	0.0052	0.0014	0.0060	<D.L.	0.0051	<D.L.	0.0035	<D.L.	0.0020	<D.L.
	03/12/2015 13:05	0.0059	0.0111	0.0025	0.0138	<D.L.	0.0011	0.0053	<D.L.	0.0051	<D.L.	0.0027	<D.L.	0.0031	<D.L.
	27/01/2016 00:00	0.0103	0.0166	0.0040	0.0254	0.0070	0.0020	0.0092	0.0012	0.0073	0.0017	0.0054	<D.L.	0.0045	<D.L.
	30/01/2016 12:00	0.0123	0.0123	0.0032	0.0157	<D.L.	<D.L.	0.0067	<D.L.	0.0056	0.0012	0.0039	<D.L.	0.0037	<D.L.
	30/01/2016 15:00	0.0117	0.0136	0.0033	0.0191	0.0054	0.0016	0.0079	<D.L.	0.0054	0.0012	0.0036	<D.L.	0.0044	<D.L.
	31/01/2016 14:00	0.0096	0.0143	0.0037	0.0208	0.0061	0.0017	0.0090	0.0012	0.0070	0.0012	0.0043	<D.L.	0.0045	<D.L.
	02/02/2016 12:30	0.0074	0.0133	0.0028	0.0144	<D.L.	0.0010	0.0063	<D.L.	0.0042	0.0011	0.0032	<D.L.	0.0040	<D.L.
GW6	03/12/2015 13:50	0.0224	0.0460	0.0145	0.0900	0.0414	0.0108	0.0537	0.0068	0.0374	0.0074	0.0207	0.0027	0.0171	<D.L.
	27/01/2016 00:00	0.0237	0.0469	0.0137	0.0871	0.0359	0.0100	0.0492	0.0067	0.0353	0.0070	0.0193	0.0023	0.0164	<D.L.
	30/01/2016 14:40	0.0240	0.0413	0.0130	0.0736	0.0272	0.0081	0.0428	0.0058	0.0317	0.0064	0.0166	0.0024	0.0140	<D.L.
	30/01/2016 17:00	0.0224	0.0329	0.0093	0.0650	0.0211	0.0060	0.0359	0.0045	0.0241	0.0048	0.0117	0.0017	0.0114	<D.L.
	31/01/2016 13:30	0.0312	0.0553	0.0163	0.1044	0.0398	0.0118	0.0606	0.0072	0.0432	0.0079	0.0217	0.0028	0.0184	<D.L.
	02/02/2016 11:40	0.0304	0.0508	0.0149	0.0875	0.0361	0.0095	0.0519	0.0067	0.0351	0.0068	0.0203	0.0028	0.0185	<D.L.
GW7	06/07/2015 00:00	0.0184	0.0505	0.0098	0.0598	0.0239	0.0061	0.0274	0.0024	0.0169	0.0029	0.0064	0.0012	0.0067	<D.L.
	03/12/2015 12:20	0.0814	0.1548	0.0422	0.2154	0.0638	0.0151	0.0800	0.0092	0.0489	0.0089	0.0218	0.0029	0.0149	<D.L.
	27/01/2016 00:00	0.1062	0.1988	0.0544	0.3023	0.0903	0.0213	0.1126	0.0124	0.0629	0.0112	0.0274	0.0036	0.0212	<D.L.
	30/01/2016 14:15	0.1013	0.1746	0.0482	0.2513	0.0700	0.0170	0.0951	0.0106	0.0569	0.0100	0.0276	0.0036	0.0204	<D.L.
	30/01/2016 16:45	0.1006	0.1786	0.0496	0.2678	0.0735	0.0193	0.0984	0.0119	0.0563	0.0104	0.0272	0.0033	0.0209	<D.L.
	31/01/2016 13:15	0.1011	0.1770	0.0480	0.2471	0.0741	0.0177	0.0944	0.0111	0.0530	0.0096	0.0258	0.0033	0.0198	<D.L.

Appendix 10. Distribution in the Piper diagram of (a) GW2 samples and (b) GW3 samples according to wetness conditions.

(a)

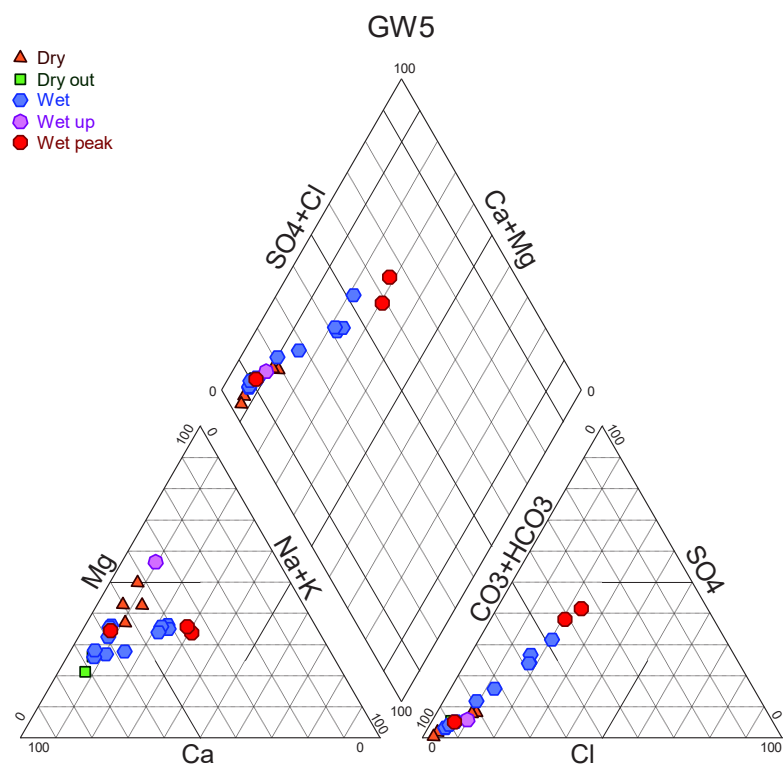


(b)

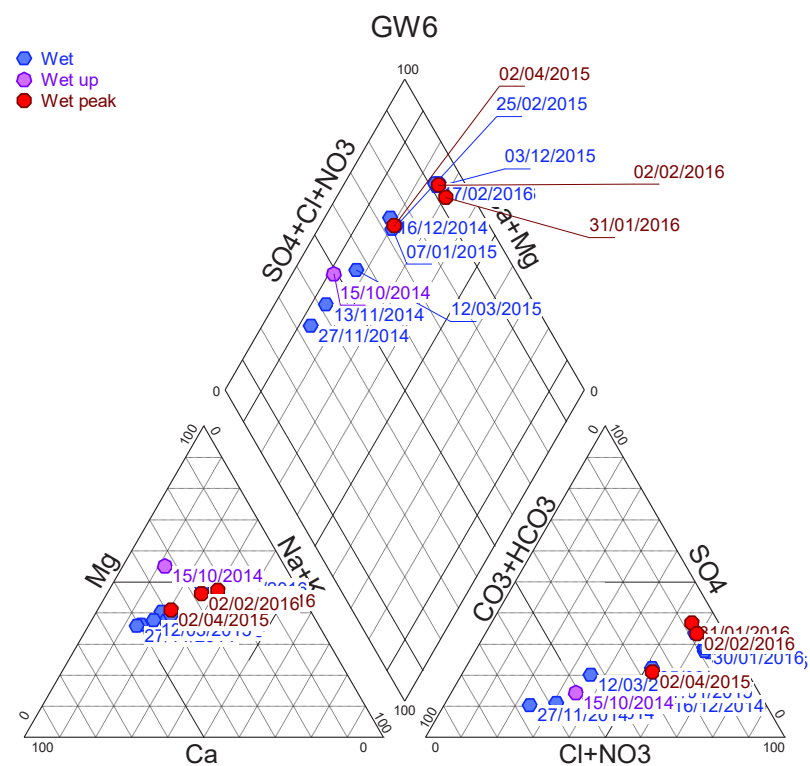


Appendix 11. Distribution in the Piper diagram of (a) GW5 samples and (b) GW6 samples according to wetness conditions

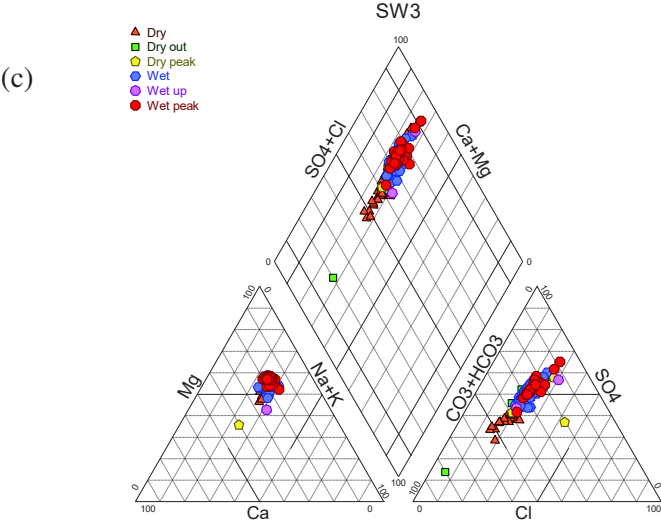
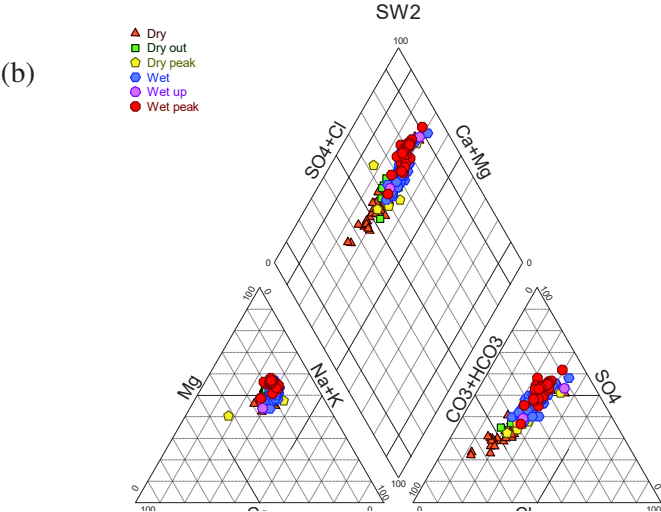
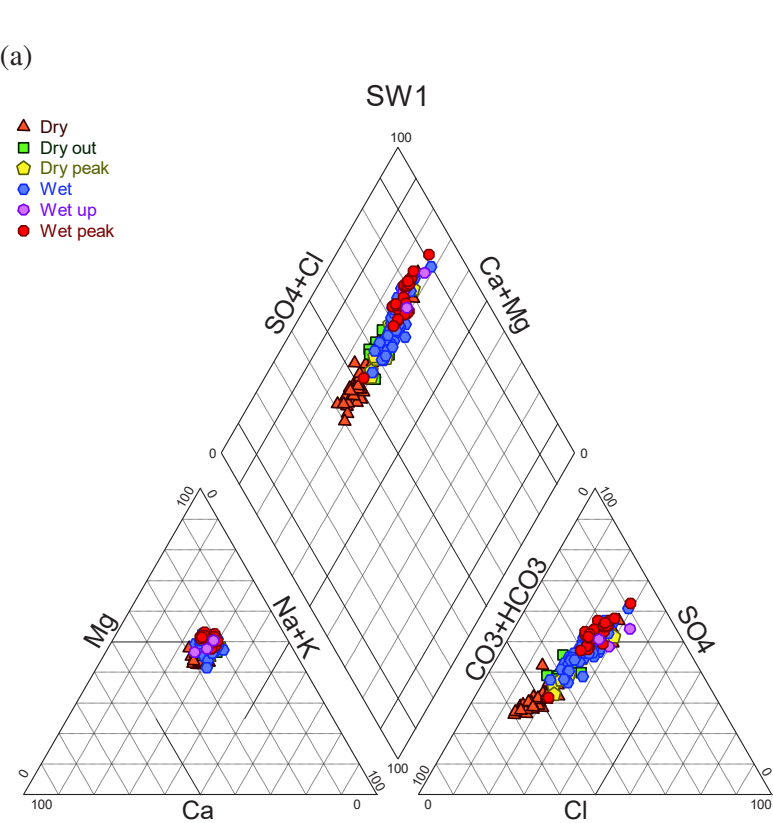
(a)



(b)



Appendix 12. Distribution in the Piper diagram of (a) SW1 samples, as well as (b) SW2 samples and (c) SW3 samples according to wetness conditions.



Appendix 13. Major and trace element concentrations in leachates (a) L1: 0.05 N HAc, (b) L2: 1 N HCl, (c) L3: 2 N HNO₃ and (d) residues (R) of the regolith (PPSD and SP) samples.

(a)

L1		PPSD1	PPSD2	PPSD3	PPSD4	SP1	SP2	SP3	SP4	SP5
Depth	(cm)	1.5	24.5	62.5	110	180	207	320	380	735
Na	(mg/g bulk)	0.01	0.01	0.01	0.01	0.22	0.16	0.18	0.17	0.17
Mg		0.05	0.00	0.00	0.01	0.45	0.48	0.60	0.67	0.45
Al		0.06	0.32	0.19	0.20	0.55	0.54	0.40	0.43	0.52
Si		0.02	0.02	0.02	0.02	0.07	0.07	0.10	0.09	0.11
P		0.02	0.00	0.00	0.00	0.00	0.00	0.00	0.00	0.00
K		0.08	0.01	0.01	0.02	2.38	1.80	2.06	2.01	1.92
Ca		0.07	0.00	0.01	0.01	0.21	0.12	0.48	0.29	0.30
Ti		0.00	0.00	0.00	0.00	0.00	0.00	0.00	0.00	0.00
Fe		0.07	0.00	0.00	0.00	0.16	0.16	0.01	0.11	0.15
Mn		0.03	0.03	0.01	0.02	0.01	0.01	0.33	0.07	0.01
V	(µg/g bulk)	0.19	0.01	0.01	0.01	0.01	0.02	0.01	0.02	0.02
Cr		0.13	0.11	0.07	0.05	0.32	0.29	0.22	0.24	0.25
Co		0.25	0.37	0.30	0.18	0.92	0.39	29.64	10.48	0.52
Ni		0.31	0.16	0.13	0.19	0.91	1.18	3.23	1.57	1.24
Cu		0.04	0.02	0.07	0.10	0.22	0.42	0.56	0.38	2.99
Zn		2.67	0.76	0.48	0.57	1.87	2.18	4.37	2.50	21.94
As		0.08	0.01	0.00	0.00	0.01	0.01	0.01	0.00	0.02
Rb		0.13	0.10	0.08	0.09	4.53	3.62	3.79	3.35	4.43
Sr		0.48	0.02	0.04	0.08	3.57	3.33	4.73	5.10	4.95
Y		0.01	0.07	0.14	0.21	0.79	0.35	0.39	0.47	0.20
Zr		0.03	0.03	0.02	0.01	0.00	0.01	0.01	0.01	0.01
Nb		0.01	0.00	0.00	0.00	-	-	-	-	-
Mo		0.01	0.00	0.00	0.00	0.00	0.00	0.02	0.00	0.00
Cd		0.01	0.00	0.00	0.00	0.00	0.00	0.02	0.00	0.01
Sn		0.01	0.00	0.00	0.00	0.00	0.00	0.01	0.00	0.01
Sb		0.01	0.00	0.00	0.00	0.00	0.00	0.00	0.00	0.00
Cs		0.00	0.00	0.00	0.00	0.03	0.02	0.06	0.04	0.03
Ba		0.63	1.81	1.74	1.99	5.51	5.05	3.87	4.54	5.35
La		0.01	0.08	0.13	0.21	0.40	0.17	0.25	0.34	0.25
Ce		0.02	0.20	0.29	0.59	0.87	0.46	1.16	1.10	0.67
Pr		0.00	0.02	0.03	0.06	0.13	0.08	0.12	0.19	0.09
Nd		0.01	0.07	0.12	0.27	0.61	0.42	0.65	1.08	0.40
Sm		0.00	0.01	0.02	0.06	0.15	0.14	0.21	0.32	0.10
Eu		0.00	0.00	0.01	0.01	0.04	0.03	0.05	0.07	0.02
Gd		0.00	0.02	0.03	0.07	0.18	0.17	0.23	0.32	0.09
Tb		0.00	0.00	0.00	0.01	0.02	0.02	0.02	0.03	0.01
Dy		0.00	0.01	0.02	0.04	0.11	0.09	0.10	0.12	0.05
Ho		0.00	0.00	0.00	0.01	0.02	0.01	0.02	0.02	0.01
Er		0.00	0.00	0.01	0.02	0.05	0.04	0.04	0.04	0.02
Tm		0.00	0.00	0.00	0.00	0.01	0.00	0.01	0.01	0.00
Yb		0.00	0.00	0.01	0.01	0.03	0.03	0.03	0.03	0.02
Lu		0.00	0.00	0.00	0.00	0.01	0.00	0.01	0.00	0.00
Hf		0.00	0.00	0.00	0.00	-	-	-	-	-
Ta		0.00	0.00	0.00	0.00	-	-	-	-	-
Pb		0.87	0.03	0.04	0.02	0.03	0.03	0.01	0.06	3.18
Th		0.01	0.00	0.00	0.00	0.01	0.01	0.00	0.01	0.02
U		0.00	0.01	0.01	0.02	0.06	0.10	0.13	0.16	0.07

(b)

L2		PPSD1	PPSD2	PPSD3	PPSD4	SP1	SP2	SP3	SP4	SP5
Depth	(cm)	1.5	24.5	62.5	110	180	207	320	380	735
Na	(mg/g bulk)	0.01	0.01	0.01	0.01	0.11	0.09	0.09	0.09	0.10
Mg		0.05	0.02	0.03	0.04	1.74	1.52	1.14	1.29	1.21
Al		1.56	2.10	1.19	1.19	3.95	3.54	3.51	3.37	3.19
Si		0.04	0.15	0.10	0.09	0.37	0.28	0.26	0.32	0.30
P		0.14	0.03	0.02	0.06	0.05	0.10	0.12	0.19	0.33
K		0.05	0.04	0.04	0.05	1.66	1.25	1.42	1.43	1.29
Ca		0.17	0.01	0.00	0.00	0.02	0.03	0.09	0.25	0.80
Ti		0.00	0.01	0.00	0.00	0.02	0.01	0.01	0.01	0.01
Fe		3.04	3.55	1.84	1.38	6.73	6.69	6.53	5.56	4.55
Mn		0.04	0.16	0.08	0.09	0.04	0.08	1.42	0.17	0.13
V	(μg/g bulk)	6.08	1.75	1.05	0.91	10.05	8.07	6.00	7.90	7.46
Cr		0.67	3.86	1.54	0.77	11.60	10.52	8.49	8.48	7.19
Co		0.71	3.87	1.84	1.23	3.39	2.36	64.05	18.99	2.49
Ni		1.91	0.95	0.46	0.51	9.08	8.60	15.73	8.55	6.73
Cu		1.31	0.33	0.33	0.44	3.36	5.76	9.32	4.31	11.16
Zn		8.34	10.70	1.91	1.69	10.95	10.99	18.57	9.88	9.23
As		1.01	0.24	0.32	0.36	0.97	0.68	0.24	0.60	0.56
Rb		0.26	0.87	0.53	0.36	4.18	3.53	3.94	4.11	4.31
Sr		1.25	0.10	0.07	0.51	5.27	4.46	5.72	7.58	11.73
Y		0.29	0.93	0.67	0.91	1.99	1.37	2.05	2.72	1.64
Zr		0.03	0.72	0.68	0.56	0.91	0.26	0.28	0.10	0.13
Nb		0.02	0.10	0.02	0.01	-	-	-	-	-
Mo		0.03	0.02	0.02	0.01	0.02	0.04	0.05	0.05	0.04
Cd		0.03	0.01	0.01	0.01	0.02	0.01	0.03	0.02	0.01
Sn		0.27	0.03	0.02	0.02	0.13	0.16	0.24	0.19	0.15
Sb		0.05	0.01	0.00	0.00	0.00	0.01	0.00	0.00	0.01
Cs		0.01	0.03	0.04	0.05	0.04	0.05	0.13	0.12	0.06
Ba		6.12	10.06	5.51	5.21	45.00	36.01	45.81	40.32	40.30
La		0.54	0.63	0.59	2.47	2.32	1.77	3.21	6.41	2.97
Ce		0.97	2.93	1.94	8.16	5.27	4.30	13.26	20.08	7.94
Pr		0.09	0.22	0.18	1.00	0.73	0.60	1.37	2.98	1.02
Nd		0.36	1.03	0.81	4.23	3.22	2.68	6.28	14.27	4.51
Sm		0.07	0.26	0.19	0.73	0.69	0.70	1.50	3.19	1.17
Eu		0.02	0.06	0.05	0.14	0.15	0.16	0.32	0.64	0.25
Gd		0.08	0.30	0.22	0.52	0.63	0.67	1.32	2.54	1.05
Tb		0.01	0.04	0.03	0.06	0.08	0.08	0.14	0.23	0.11
Dy		0.07	0.23	0.16	0.25	0.42	0.39	0.65	0.87	0.46
Ho		0.01	0.04	0.03	0.04	0.07	0.06	0.10	0.12	0.07
Er		0.03	0.11	0.07	0.11	0.20	0.18	0.28	0.31	0.17
Tm		0.00	0.01	0.01	0.01	0.02	0.02	0.04	0.03	0.02
Yb		0.02	0.08	0.05	0.07	0.15	0.15	0.23	0.20	0.12
Lu		0.00	0.01	0.01	0.01	0.02	0.02	0.03	0.03	0.02
Hf		0.00	0.03	0.02	0.02	-	-	-	-	-
Ta		0.00	0.00	0.00	0.00	-	-	-	-	-
Pb		73.15	2.32	1.75	1.36	4.09	3.80	6.12	7.22	6.89
Th		0.01	0.07	0.10	0.15	1.20	1.10	0.94	1.21	1.70
U		0.08	0.21	0.16	0.30	0.28	0.50	1.03	1.21	0.32

(c)

L3		PPSD1	PPSD2	PPSD3	PPSD4	SP1	SP2	SP3	SP4	SP5
Depth	(cm)	1.5	24.5	62.5	110	180	207	320	380	735
Na	(mg/g bulk)	0.01	0.01	0.01	0.01	0.05	0.05	0.04	0.05	0.04
Mg		0.04	0.04	0.06	0.08	0.50	0.42	0.37	0.44	0.52
Al		0.44	0.79	0.65	0.66	1.73	1.49	1.70	1.47	1.23
Si		0.05	0.09	0.07	0.08	0.13	0.10	0.13	0.11	0.10
P		0.06	0.01	0.01	0.02	0.02	0.03	0.05	0.05	0.03
K		0.03	0.02	0.03	0.04	0.62	0.49	0.56	0.59	0.51
Ca		0.01	0.01	0.00	0.00	0.00	0.00	0.01	0.01	0.02
Ti		0.00	0.00	0.00	0.00	0.00	0.00	0.00	0.00	0.00
Fe		1.27	0.62	0.57	0.54	1.39	1.28	1.78	1.25	1.60
Mn		0.01	0.02	0.03	0.09	0.01	0.01	0.76	0.02	0.11
V	(μg/g bulk)	3.57	0.52	0.34	0.36	1.41	1.37	2.60	1.07	0.97
Cr		1.04	1.25	0.76	0.62	2.91	2.45	2.03	1.96	1.52
Co		0.23	0.55	0.60	1.20	1.12	0.70	27.47	9.40	1.41
Ni		0.57	4.21	1.64	1.56	4.41	4.13	13.19	5.29	4.15
Cu		0.34	0.11	0.32	0.41	1.09	2.25	3.58	2.00	4.31
Zn		4.24	3.60	2.20	1.94	3.63	3.80	6.92	4.68	3.53
As		0.62	0.10	0.14	0.18	0.40	0.29	0.17	0.22	0.31
Rb		0.45	1.14	0.74	0.52	2.38	2.02	2.62	2.72	2.58
Sr		0.15	0.10	0.07	0.25	1.31	1.14	1.30	1.95	1.11
Y		0.03	0.06	0.12	0.22	0.27	0.34	0.48	0.57	0.27
Zr		0.02	0.19	0.25	0.26	1.44	1.00	0.79	0.88	1.61
Nb		0.04	0.06	0.02	0.01	-	-	-	-	-
Mo		0.08	0.01	0.01	0.01	0.01	0.03	0.03	0.02	0.03
Cd		0.00	0.00	0.00	0.00	0.00	0.00	0.01	0.00	0.00
Sn		0.01	0.01	0.01	0.01	0.01	0.01	0.01	0.02	0.02
Sb		0.04	0.00	0.00	0.00	0.00	0.00	0.01	0.00	0.01
Cs		0.04	0.07	0.12	0.17	0.06	0.07	0.20	0.20	0.08
Ba		0.71	6.39	2.91	1.90	8.70	7.45	11.33	8.07	8.18
La		0.07	0.07	0.12	0.76	0.76	0.66	1.24	3.52	0.62
Ce		0.19	0.57	0.70	2.78	1.59	1.51	5.02	10.45	1.71
Pr		0.02	0.02	0.04	0.31	0.21	0.19	0.48	1.40	0.19
Nd		0.08	0.09	0.18	1.33	0.88	0.85	2.14	6.05	0.83
Sm		0.02	0.02	0.04	0.22	0.18	0.21	0.43	0.93	0.18
Eu		0.00	0.01	0.01	0.04	0.03	0.04	0.08	0.16	0.03
Gd		0.01	0.03	0.04	0.14	0.12	0.17	0.33	0.54	0.13
Tb		0.00	0.00	0.01	0.01	0.01	0.02	0.03	0.05	0.01
Dy		0.01	0.02	0.03	0.06	0.06	0.10	0.16	0.18	0.07
Ho		0.00	0.00	0.01	0.01	0.01	0.02	0.03	0.03	0.01
Er		0.00	0.01	0.01	0.03	0.03	0.05	0.07	0.08	0.04
Tm		0.00	0.00	0.00	0.00	0.00	0.01	0.01	0.01	0.01
Yb		0.00	0.01	0.01	0.02	0.03	0.05	0.06	0.05	0.04
Lu		0.00	0.00	0.00	0.00	0.00	0.01	0.01	0.01	0.01
Hf		0.00	0.01	0.01	0.01	-	-	-	-	-
Ta		0.00	0.00	0.00	0.00	-	-	-	-	-
Pb		5.73	0.48	0.47	0.38	1.05	1.23	2.24	1.66	1.35
Th		0.01	0.08	0.23	0.46	0.35	0.37	0.37	0.50	0.37
U		0.06	0.02	0.03	0.05	0.05	0.15	0.26	0.53	0.11

(d)

R		PPSD1	PPSD2	PPSD3	PPSD4	SP1	SP2	SP3	SP4	SP5
Depth	(cm)	1.5	24.5	62.5	110	180	207	320	380	735
Na	(mg/g bulk)	1.84	2.89	2.82	2.98	1.48	1.26	1.53	1.74	1.67
Mg		1.73	6.49	10.48	11.85	8.89	8.70	8.27	10.98	9.06
Al		41.38	86.70	101.35	121.79	88.71	78.31	90.50	99.77	89.98
Si		187.89	308.44	290.96	253.99	309.47	312.69	282.87	284.55	307.08
P		0.96	0.52	0.44	0.70	0.17	0.70	1.09	0.17	0.17
K		11.66	23.15	29.59	33.84	25.55	22.09	27.36	31.38	27.78
Ca		0.29	0.49	0.24	0.00	0.21	0.21	0.21	0.21	0.21
Ti		3.58	6.32	6.56	6.92	6.04	5.41	5.84	5.98	5.34
Fe		19.59	36.92	44.99	54.91	27.92	43.35	57.43	38.12	32.74
Mn		0.11	0.20	0.20	0.42	0.07	0.08	4.22	0.11	0.10
V	(μg/g bulk)	64.86	115.00	131.50	151.00	120.98	103.51	123.74	130.69	123.80
Cr		71.62	123.10	147.90	170.80	153.52	133.47	136.57	143.13	124.60
Co		3.53	9.32	13.92	17.54	8.95	9.49	62.17	19.11	10.69
Ni		16.75	56.57	69.69	75.95	54.45	57.10	89.79	64.93	55.45
Cu		11.72	16.65	23.68	33.83	8.39	29.33	46.59	26.82	22.24
Zn		72.23	124.60	104.70	101.80	65.02	84.22	117.91	86.47	74.38
As		12.91	8.22	8.78	13.07	6.14	13.88	17.65	11.09	5.79
Rb		78.88	160.20	171.70	194.70	159.09	135.51	146.99	168.43	162.06
Sr		48.62	96.65	107.70	125.30	84.22	70.64	87.64	97.48	80.26
Y		15.96	32.73	37.99	34.98	31.77	29.42	28.62	29.81	26.27
Zr		142.50	280.80	275.80	274.40	279.46	211.69	191.14	187.93	150.37
Nb		10.62	19.95	18.88	19.36	15.96	14.87	15.48	16.16	13.93
Mo		1.63	0.63	0.62	0.73	0.50	0.83	0.90	0.62	0.50
Cd		0.15	0.27	0.25	0.29	0.04	0.04	0.05	0.04	0.03
Sn		10.52	4.15	4.71	5.16	4.23	3.58	3.89	4.06	4.09
Sb		2.70	0.56	0.43	0.51	0.41	0.70	0.89	0.77	0.48
Cs		4.74	7.75	9.35	12.88	5.69	4.98	12.01	12.35	5.89
Ba		187.90	408.30	431.70	455.60	354.40	319.21	373.65	424.74	384.61
La		21.92	42.46	47.18	54.23	45.31	37.25	44.18	47.57	38.78
Ce		44.01	87.90	97.43	112.90	90.05	73.52	87.09	90.26	77.13
Pr		5.07	10.06	11.15	12.83	10.56	8.41	9.52	10.20	8.62
Nd		18.43	36.99	40.39	46.29	38.93	30.99	35.12	37.41	31.22
Sm		3.41	6.78	7.44	8.39	7.16	5.75	6.55	6.74	5.49
Eu		0.67	1.32	1.45	1.61	1.40	1.18	1.34	1.35	1.13
Gd		2.80	5.55	6.20	6.33	5.80	5.00	5.52	5.46	4.53
Tb		0.44	0.90	1.02	1.00	0.94	0.85	0.89	0.89	0.76
Dy		2.85	5.78	6.65	6.29	5.94	5.46	5.53	5.63	4.83
Ho		0.61	1.25	1.44	1.34	1.24	1.15	1.16	1.18	1.03
Er		1.65	3.40	3.86	3.64	3.44	3.16	3.19	3.24	2.82
Tm		0.25	0.50	0.57	0.54	0.50	0.47	0.47	0.48	0.41
Yb		1.69	3.37	3.86	3.75	3.48	3.16	3.25	3.28	2.82
Lu		0.26	0.53	0.59	0.59	0.51	0.47	0.49	0.49	0.42
Hf		3.94	7.46	7.47	7.42	7.55	5.84	5.36	5.22	4.27
Ta		0.90	1.67	1.61	1.67	1.46	1.29	1.35	1.40	1.25
Pb		13.59	14.75	11.15	11.43	25.06	18.45	25.09	14.87	8.93
Th		6.99	13.94	15.09	17.46	12.06	10.54	12.84	13.06	10.39
U		1.54	2.72	2.72	2.91	2.78	3.06	4.09	4.14	3.19

Appendix 14. Sr, Nd, Pb and U isotopic compositions of regolith leachates and residues and water samples (2SE: 2*Standard Error; SEcorr: SE corrected according to blank).

Sample type/date		87Sr/86Sr	2SE	143Nd/144Nd	2SE	206Pb/204Pb	2SE	206Pb/207Pb	2SE	234U/238U	2SE	SEcorr
PPSD1	L1	0.71557	0.00001	0.51203	0.00010	18.0645	0.0005	1.15893	0.00001	1.214	0.012	0.17
PPSD3	L1	0.73353	0.00002	0.51215	0.00000	18.5155	0.0005	1.18540	0.00001	1.623	0.007	0.03
SP1	L1	0.76173	0.00000	0.51213	0.00001	NA	NA	NA	NA	1.353	0.002	NA
SP3	L1	0.74846	0.00000	0.51215	0.00001	NA	NA	NA	NA	1.410	0.002	NA
SP4	L1	0.74990	0.00000	0.51220	0.00001	NA	NA	NA	NA	1.493	0.002	NA
SP5	L1	0.74978	0.00001	0.51213	0.00000	18.5612	0.0005	1.18958	0.00001	1.728	0.003	NA
PPSD1	L2	0.71555	0.00000	0.51206	0.00001	18.0657	0.0006	1.15902	0.00001	1.270	0.001	NA
PPSD3	L2	0.74388	0.00001	0.51213	0.00000	18.6649	0.0004	1.19422	0.00001	1.634	0.002	NA
SP	L2	0.74930	0.00000	0.51208	0.00000	18.6399	0.0004	1.19280	0.00001	1.269	0.001	NA
SP3	L2	0.74421	0.00000	0.51209	0.00001	18.5723	0.0004	1.18905	0.00001	1.204	0.001	NA
SP4	L2	0.73454	0.00000	0.51213	0.00001	18.5775	0.0004	1.18919	0.00001	#REF!	0.001	NA
SP5	L2	0.72832	0.00000	0.51217	0.00001	18.6461	0.0004	1.19460	0.00001	1.262	0.002	NA
PPSD1	L3	0.71807	0.00001	0.51207	0.00001	18.0889	0.0004	1.16021	0.00001	1.264	0.001	0.002
PPSD3	L3	0.74119	0.00002	0.51211	0.00001	18.6569	0.0006	1.19387	0.00001	1.608	0.002	0.01
SP	L3	0.75284	0.00001	0.51206	0.00001	18.6272	0.0004	1.19210	0.00001	1.229	0.001	0.001
SP3	L3	0.75107	0.00000	0.51205	0.00001	18.5611	0.0002	1.18845	0.00001	1.072	0.001	NA
SP4	L3	0.73802	0.00001	0.51203	0.00001	18.5890	0.0002	1.18989	0.00001	0.771	0.001	NA
SP5	L3	0.75880	0.00001	0.51205	0.00001	18.6311	0.0004	1.19356	0.00001	0.999	0.001	NA
PPSD1	R	0.73107	0.00002	0.51193	0.00000	18.5002	0.0003	1.18582	0.00000	0.895	0.001	NA
PPSD3	R	0.73761	0.00001	0.51193	0.00001	19.1015	0.0004	1.22132	0.00001	0.902	0.001	NA
SP1	R	0.73913	0.00000	0.51198	0.00001	18.8025	0.0004	1.20334	0.00001	0.896	0.001	NA
SP3	R	0.73775	0.00000	0.51195	0.00001	18.7826	0.0004	1.20252	0.00001	0.973	0.001	NA
SP4	R	0.73895	0.00000	0.51194	0.00001	19.0631	0.0005	1.21902	0.00001	0.942	0.001	NA
TF	30/01/2016 15:45	0.71166	0.00001	NA	NA	NA	NA	NA	NA	1.119	0.003	0.01
SS20	30/01/2016 11:15	0.71655	0.00001	NA	NA	NA	NA	NA	NA	1.319	0.003	0.01
SS60	31/01/2016 14:00	0.71691	0.00001	NA	NA	NA	NA	NA	NA	1.127	0.004	0.01
SS20	30/01/2016 15:15	0.71661	0.00001	0.51211	0.00001	18.2972	0.0001	1.17226	0.00003	1.369	0.002	0.01
SS60	31/01/2016 14:15	0.71710	0.00001	NA	NA	NA	NA	NA	NA	1.197	0.007	0.03
GW1	02/02/2016 12:45	0.71529	0.00001	0.51209	0.00000	17.8506	0.0002	1.14571	0.00004	2.200	0.003	0.02

GW3	06/07/2015 12:00	0.71518	0.00001	NA	NA	NA	NA	NA	NA	1.686	0.003	0.02
GW3	27/01/2016 00:00	0.71534	0.00001	NA	NA	NA	NA	NA	NA	1.492	0.003	0.04
GW3	30/01/2016 16:00	0.71534	0.00001	NA	NA	NA	NA	NA	NA	1.431	0.003	0.04
GW3	31/01/2016 12:15	0.71532	0.00001	NA	NA	NA	NA	NA	NA	1.447	0.004	0.03
GW5	06/07/2015 10:50	0.71477	0.00001	0.51219	0.000010	17.8248	0.0009	1.14395	0.00003	1.911	0.003	0.02
GW5	27/01/2016 00:00	0.71572	0.00001	NA	NA	NA	NA	NA	NA	1.500	0.003	0.02
GW5	30/01/2016 15:00	0.71584	0.00002	NA	NA	NA	NA	NA	NA	1.534	0.002	0.02
GW5	31/01/2016 14:00	0.71647	0.00001	0.51217	0.000014	17.8141	0.0008	1.14349	0.00004	1.489	0.003	0.02
GW6	02/02/2016 11:40	0.71664	0.00001	NA	NA	17.8352	0.0009	1.14470	0.00003	1.369	0.003	0.01
GW7	06/07/2015 00:00	0.71591	0.00001	NA	NA	NA	NA	NA	NA	1.351	0.003	0.01
SW1	06/07/2015 12:00	0.71618	0.00001	0.51222	0.000016	18.1653	0.0001	1.16456	0.00005	1.566	0.004	0.01
SW1	27/01/2016 00:00	0.71680	0.00001	NA	NA	NA	NA	NA	NA	1.399	0.004	0.04
SW1	30/01/2016 16:00	0.71685	0.00001	NA	NA	18.2201	0.0002	1.16778	0.00005	1.415	0.005	0.04
SW1	31/01/2016 12:00	0.71692	0.00001	NA	NA	NA	NA	NA	NA	1.447	0.002	0.02

Summary in French

Introduction

La zone critique (ZC) est la section de la surface terrestre externe qui s'étend du sommet de la canopée de la végétation jusqu'aux zones de régolithe saturée les plus profondes (National Research Council, 2001). Les flux d'eau relient les différents compartiments de la ZC et participent aux processus physiques et biogéochimiques responsables de leur formation et de leur altération, tels que l'altération et le cycle des éléments nutritifs de la végétation. La ZC est en outre contrôlée par des facteurs climatiques, tectoniques et humains tels que, par exemple, des sédiments transportés ou des dépôts atmosphériques d'origine naturelle ou anthropique peuvent modifier de manière importante sa structure et ses flux (Brantley et al., 2006). L'hétérogénéité des différents compartiments et flux de la ZC, et plus particulièrement la production et la transformation de régolithe, entraîne la production de « points chauds » qui déterminent la réponse hydrochimique dans l'eau du cours d'eau (Chorover et al., 2011 ; McClain et al., 2003 ; West et al., 2013). Par conséquent, la caractérisation géochimique spatiale et temporelle des compartiments de régolithe et des eaux qu'ils accueillent présente un intérêt particulier pour l'hydrologie des bassins hydrographiques afin d'évaluer la connectivité hydrologique et de comprendre les fluctuations hydrochimiques des cours d'eau (Brantley et al., 2007; Brooks et al., 2015; Chorover et al., 2011).

Depuis les années 1960, les principaux éléments géochimiques (Na^+ , K^+ , Ca^{2+} , Mg^{2+} , H_4SiO_4 , SO_4^{2-} , Cl^- , NO_3^- , alcalinité et COD), les isotopes stables de O et H, la température et la conductivité électrique dans l'eau sont couramment utilisés pour les études de génération de ruissellement à l'échelle de pente et de bassin versant (Barthold et al., 2010, Burns et al., 2001, Christophersen et Hooper, 1992, Hooper et al., 1990, Inamdar, 2011, Wenninger et al., 2004). Bien que ces

paramètres soient devenus de plus en plus populaires dans les études sur les processus hydrologiques, les hypothèses fondamentales liées à leur application en tant que traceurs ont été rarement rencontrées (Klaus et McDonnell, 2013). Par exemple, les modèles de mélange hydrologique supposent que les traceurs doivent donner des compositions significativement différentes à chacun des membres finaux étudiés et doivent avoir un comportement conservateur, c.-à-d. que les concentrations ne doivent pas changer à cause des processus biogéochimiques (Hooper et al. 1990, Inamdar et al., 2013). Dans la nature, cependant, les principaux éléments sont omniprésents et participent à divers processus tels que l'altération chimique et les processus de précipitation et le cycle des éléments nutritifs de la végétation. De même, les isotopes stables de l'eau sont sensibles au fractionnement dû aux changements de température ou de pression. Par conséquent, bien que des progrès considérables aient été réalisés pour déterminer le temps de transit de l'eau à l'échelle des bassins versants (Brooks et al., 2010, McGuin et McDonnell, 2006 ; Stumpp et al., 2007), leur utilisation comme traceurs de processus hydrologiques est plutôt limitée et peut conduire à de fausses conclusions sur le fonctionnement des bassins versants (Barthold et al., 2011). De plus, nous manquons encore de compréhension de ce qui finit par déclencher la dynamique temporelle complexe de la physico-chimie des eaux souterraines.

Jusqu'à présent, les études de recherche dans les compartiments et les processus hydrologiques de la ZC sont restées largement découplées - empêchant ainsi l'identification des bassins d'eau et des voies d'écoulement dans la recherche hydrologique. Des travaux récents ont montré qu'il existe un besoin urgent de recherche interdisciplinaire sur ce sujet (Brooks et al., 2015). En effet, si nous voulons apporter une nouvelle compréhension aux fonctions fondamentales de la collecte, du mélange, du stockage et de la libération de l'eau, nous devons nous concentrer sur les relations entre (au moins) les propriétés du régolithe et la dynamique hydrochimique. Une telle approche nécessite l'application d'une boîte à outils de traceurs hydrologiques plus large qui permet la caractérisation et la comparaison des phases solide / organo- minérale et liquide / aqueuse. Au cours des dernières décennies, les éléments traces et certains de leurs rapports isotopiques radiogéniques ont été présentés comme des traceurs prometteurs des processus pédogénétiques et éco-hydrologiques.

Les éléments traces ont souvent été écartés des études sur les solides dissous totaux en raison de leur faible masse combinée naturelle (concentrations inférieures à 1 mg / L) comparativement aux ions majeurs et du fait que seules les avancées technologiques récentes ont permis de les mesurer avec précision (Gaillardet et al., 2003). Cependant, les mécanismes d'altération / précipitation et de transport de soluté peuvent être mieux compris avec l'utilisation supplémentaire d'éléments traces parce qu'ils deviennent plus fractionnés que les éléments majeurs au cours de ces processus. Ce n'est pas seulement parce qu'ils sont très liés à la minéralogie, mais aussi parce que certains d'entre eux sont sensibles aux fluctuations du COD, du pH et de l'oxydoréduction. Par conséquent,

différentes lithologies et même des horizons / couches de régolithe peuvent fournir différentes compositions d'éléments traces en solutions. De plus, étant donné leur utilisation prolongée à des fins industrielles, les métaux traces sont également très utiles pour suivre l'impact des activités anthropiques dans les écosystèmes. Les travaux de Ladouche et al. (2001) et El Azzi et al. (2016) montre comment les éléments traces peuvent être de bons outils complémentaires pour différencier les zones contribuant à la génération d'écoulement et au transfert des polluants dans différentes conditions d'écoulement.

Parmi les éléments traces, les terres rares (REE, abrégée en anglais) se comportent comme un groupe plutôt homogène en raison de leur configuration électronique trivalente. Une diminution graduelle des rayons ioniques REE avec un nombre atomique croissant entraîne une réponse légèrement différente (fractionnement) de REE léger (LREE, La-Sm) et de REE lourd (HREE, Dy-Lu) aux processus de lixiviation, de précipitation, d'adsorption ou de complexation (Brookins, 1989). Des comportements exceptionnels sont observés pour Ce, qui est tétravalent dans les conditions oxydantes, et Eu, qui est bivalent dans les conditions réductrices telles que celles trouvées dans le manteau et la croûte inférieure. Les concentrations de REE et les schémas de distribution sont donc particulièrement sensibles aux changements dans les conditions redox, au pH et à l'abondance des ligands complexes (organiques / inorganiques) impliqués dans les interactions eau-roche et les processus de transport (Aubert et al. 1998, Condie, 1991, Dupré et al., 1999, Elderfield et al., 1990, Goldstein et al., 1984, Hissler et al., 2015, Pourret et al., 2007, Sholkovitz, 1995, Smedley, 1991, Stille. et al., 2009, Taylor et McLennan, 1981, Tricca et al., 1999, Viers et al., 1997). En effet, les cartographies des terres rares et la surveillance physico-chimique des eaux souterraines et souterraines et de leurs roches encaissantes à l'échelle des (sous-) bassins et à différentes échelles temporelles s'avèrent utiles pour distinguer les sources d'eau et les voies d'écoulement (Davranche et al. 2011, Dia et al., 2000, Gruau et al., 2004, Vázquez-Ortega et al., 2016).

La connaissance et la prédiction de la dynamique d'origine spécifique des éléments traces (et des éléments majeurs associés) dans la ZC sont améliorées par l'étude des rapports isotopiques comme $^{87}\text{Sr}/^{86}\text{Sr}$, $^{143}\text{Nd}/^{144}\text{Nd}$, $^{206}\text{Pb}/^{207}\text{Pb}$ et $^{234}\text{U}/^{238}\text{U}$. Les systèmes isotopiques Sr, Nd, Pb et U sont des outils utilisés depuis longtemps par les géochronologues et les pétrologues avant d'être appliqués aux études d'altération et d'hydrologie. Leur intérêt réside dans leur stabilité - à l'inverse de $\delta^{18}\text{O}$ et $\delta^2\text{H}$, ils ne se fractionnent pas lors des processus bio-géo-physico-chimiques dans l'environnement - et sur leurs grandes variations entre les sources. Ces caractéristiques permettent l'attribution d'une empreinte digitale pour des interactions spécifiques eau-roche. Connaissant les caractéristiques de la source isotopique dans le système, elles peuvent être utilisées pour caractériser les processus d'altération, évaluer les sources d'eau et les voies d'écoulement, et

quantifier les contributions naturelles et anthropiques (Aubert et al., 2002a ; 2014, Schaffhauser et al., 2014, Stille et al., 2011, 2009).

Les calculs de mélange impliquant ces traceurs reposent également sur des hypothèses telles que l'inclusion de toutes les sources potentielles et leur bonne différenciation isotopique. Afin de résoudre ce problème, la combinaison de divers systèmes isotopiques et d'éléments chimiques est fortement recommandée. Cette approche fournit des informations contrastées qui augmentent la précision sur la compréhension des mécanismes contrôlant le comportement des traceurs et sur la détermination du membre final (Blum et Erel, 2003, Graustein, 1989). Plusieurs études pédologiques et hydrologiques ont couplé efficacement l'utilisation de concentrations d'éléments traces et de deux systèmes isotopiques dans les mêmes échantillons ; souvent Sr et Nd, mais aussi Sr et U (Paces et Wurster, 2014, Pierret et al., 2014, Prunier et al., 2015, Schaffhauser et al., 2014). Quelques-uns utilisaient simultanément les systèmes isotopiques Sr, Nd et Pb pour tracer l'évolution crustale à travers les sédiments fluviaux et les charges en suspension (Allègre et al., 1996 ; Garçon et al., 2014), les poussières atmosphériques (Biscaye et al., 1997 ; Grousset et Biscaye, 2005, Guéguen et al., 2012) et les profils d'altération (Hissler et al., 2015). Des études utilisant ces trois outils ont également démontré leur grande valeur ajoutée pour caractériser la composition de base naturelle des poussières, des sols et des eaux et la différencier des différentes interférences anthropiques (Hissler et al., 2016, 2008, M. Lahd Geagea et al., 2008 ; Majdi Lahd Geagea et al., 2008, Steinmann et Stille, 1997). A notre connaissance, les systèmes isotopiques Sr, Nd, Pb et U n'ont jamais été appliqués ensemble dans le même ensemble d'échantillons pour étudier les interactions eau-roche-atmosphère.

Hypothèse, objectifs et plan de thèse

Des recherches antérieures menées dans un bassin versant emboîté dans le bassin de l'Attert (Luxembourg) ont montré, par la combinaison d'études physiographiques et hydrologiques, un fort contrôle géologique des fonctions de captage, de mélange et de rejet de l'eau dans les versants continuum des cours d'eau (Pfister et al., 2017, Wrede et al., 2015). Actuellement, nous ne comprenons pas quels processus déclenchent différentes réponses de ruissellement (pics simples ou doubles) aux événements de précipitations dans la partie dévonienne du bassin de l'Attert. Nous émettons l'hypothèse que le comportement hydrologique très contrasté entre les saisons d'été et d'hiver est largement déclenché par les fluctuations de l'eau souterraine et du sol dans le régolithe d'ardoise.

L'objectif général de ce projet de thèse est donc d'étudier le mélange de l'eau dans la subsurface à travers un portefeuille unique de groupes complémentaires de traceurs (éléments majeurs et isotopes stables et éléments traces et isotopes radiogéniques Sr-Nd-Pb-U) permettant d'étudier processus d'altération (/précipitation) des processus et du transport des solutés dans la ZC.

Dans ce cadre, les objectifs spécifiques étaient :

- 1 - Caractériser les « points chauds » potentiels d'interaction avec l'eau dans le régolithe.
- 2 - Caractériser le comportement hydrologique et géochimique des eaux de Weierbach.
- 3 - Caractériser la dynamique de la circulation de l'eau et la connectivité des réservoirs à l'échelle du bassin versant.

Site d'étude

Tous les travaux de cette thèse sont basés sur le bassin versant expérimental du Weierbach, situé au nord-ouest du Grand-Duché de Luxembourg. Le bassin versant du Weierbach est densément surveillé depuis 2009 par l'Institut luxembourgeois de science et de technologie (LINS, par l'abréviation en anglais), anciennement connu sous le nom de Centre Recherche Public Gabriel Lippmann. Le site d'étude est un bassin amont de 45 ha du bassin de l'Attert (288 ha, latitude 49 ° 50 '05,5 "N, longitude : 05 ° 47' 47,6" E) avec des altitudes comprises entre 422 et 512 m asl., il est formé par une vallée escarpée qui traverse un plateau, étant les pentes remarquablement raides dans le côté est (pente moyenne = 5,25 °). Le bassin du Weierbach a principalement des couvertures de hêtre (*Fagus sylvatica* L.) et de chêne (*Quercus petraea* (Matt.) Liebl.) (70%) et, dans une moindre mesure, d'épicéas (*Picea abies*, 15%) et de douglas (15%). Ces arbres sont soumis à une coupe sélective, pour laquelle plusieurs pistes de terre autour du bassin versant sont mises en place. Une zone du plateau utilisée pour des champs agricoles et prairies entoure le bassin versant boisé. Des études antérieures effectuées dans la zone indiquent une déconnexion totale entre les terres agricoles et le réseau hydrographique (Martínez-Carreras et al., 2010).

Paramètres géologiques et géomorphologiques

Sur le plan géologique, le bassin du Weierbach est situé dans le Massif des Ardennes luxembourgeois (Oesling), près de la frontière belge. Le plateau étudié est supposé être représentatif de l'unité de relief régolitique appelée « haute surface de l'Oesling » à Luxembourg, qui s'est développée à 500 m d'altitude. (Désiré-Marchand, 1985). Le profil étudié présente une partie de régolite transportée constituée de dépôts de pente périglaciaire du pléistocène (PPSD, abrégée en anglais) au-dessus du substrat in situ altéré par l'ardoise et est organisée comme suit:

- 1) Une couche arable organique, qui englobe l'horizon O et constitue la partie supérieure du solum.
- 2) Un compartiment organo- minéral développé dans la PPSD qui peut être subdivisé en solum et subsolum supérieur. La partie solum est composée d'horizons Ah et B. Le subsolum supérieur

peut être divisé en horizons 2Cg1 et 2Cg2 et contient un matériau régolitique selon Juilleret et al. (2016).

3) Un sous-sol minéral inférieur, qui contient des matériaux saprolithiques et paralytiques selon Juilleret et al. (2016). Ce troisième compartiment représente le profil régolitique in situ constitué de substrat d'ardoise altérée et appelé couches 3CR et 3R (SP). Ces couches sont séparées du compartiment PPSD ci-dessus par une discontinuité lithique.

Le profil régolitique étudié peut être classé comme HEMIMODER Haplique (Jabiol et al., 2013) se développant sur un Cambisol Dystrique (Ruptic, Endoskeletal, Siltic, Protosodic) (IUSS Working Group, 2015) recouvrant une Saprolite Régolithique (Gleyique, Ruptique, Rootique, Siltic, Skeletic) [Slatic] (Juilleret et al., 2016).

Climat et paramètres hydrologiques

Le bassin versant du Weierbach est dominé par un climat semi-océanique avec des précipitations totales moyennes annuelles uniformément réparties de 953 mm et une évapotranspiration potentielle annuelle moyenne de 593 mm (2006-2014, Pfister et al., 2017). Les moyennes mensuelles de la température de l'air calculées pour 1971-2000 donnent un maximum de ca. 18°C en juillet et un minimum de 0 °C en janvier, avec environ 80 jours par an de valeurs inférieures à 0 °C à 2 m du sol (Martínez-Carreras et al., 2010, Pfister et al., 2005). Bien que les valeurs de débit moyen annuel du Weierbach sont autour 478 mm (2006-2014, Pfister et al., 2017), le flux subit une forte saisonnalité, au point de sécher complètement pendant quelques jours ou semaines au cours des étés extrêmement secs.

Matériaux et méthodes

Différents échantillons de poussières atmosphériques (2 échantillons), de litières (1), de régolithe (10 échantillons sélectionnées : 4 PPSD et 5 SP) et d'eau ont été collectés dans le bassin versant de Weierbach pour qualifier les interactions eau-système et la dynamique chimique dans ce contexte. Alors que des échantillons de régolite et de litière en vrac ont été collectés ponctuellement au début du projet à partir des fosses de sol et des carottes, des poussières ont été collectées sous couvert forestier et sur des terres agricoles tout au long d'une année hydrologique. D'autre part, grâce au suivi intense développé dans le bassin du Weierbach au cours des années précédentes, nous avons utilisé des données géochimiques des eaux (concentrations en éléments majeurs et en traces, nutriments et isotopes ainsi que paramètres physico-chimiques) issues d'échantillonnages bihebdomadaires à l'échelle du bassin versant de 2009 à 2015. Dans le cadre de ce projet, nous avons réalisé des échantillonnages supplémentaires à l'échelle de bassin versant

entre 2015 et 2016 : deux échantillonnages ponctuels en été 2015 et en hiver 2015, et un échantillonnage d'échelle événementielle en hiver 2016. Les échantillons d'eaux comprennent des eaux de rivière (SW), ripariennes (RP), souterraines (GW), solutions du sol (SS) et pluviolessivat (TF). Les techniques de traitement et analyse appliquées à chaque type d'échantillon sont illustrées à la figure 1 (2.2 dans la thèse complète).

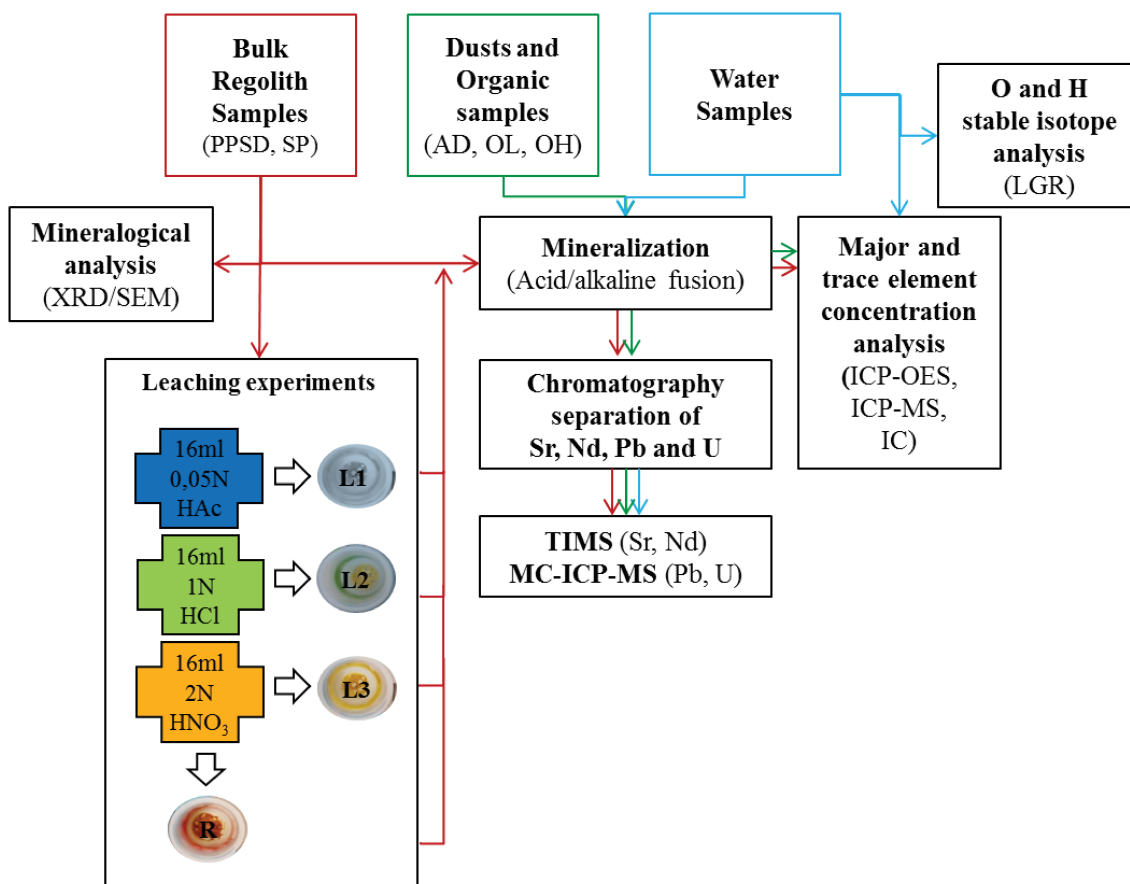


Figure 1. Schéma de toutes les méthodes de traitement et d'analyse utilisées pour l'étude des régolites (PPSD et SP), des poussières atmosphériques (AD), de la litière (OL), de l'humus (OH) et des échantillons d'eau du bassin versant du Weierbach. Dans la section "Expériences de lixiviation", L1 : lixiviat 1, L2 : lixiviat 2, L3 : lixiviat 3 et R : Résidu.

Résumé du travail de recherche, conclusions et perspectives

Dans le présent travail, nous avons combiné plusieurs traceurs géochimiques, à savoir les éléments majeurs et traces et les isotopes O-Sr-Nd-Pb-U, pour éclairer les mécanismes responsables des processus de vieillissement et de lixiviation du régolithe qui contrôlent largement la dynamique chimique de l'eau à l'échelle de captage. Dans ce but, nous avons caractérisé différents compartiments de régolithe comme des « points chauds » potentiels d'interaction avec l'eau circulant dans le système et les eaux elles-mêmes.

Dans une première partie, l'étude minéralogique et géochimique du régolithe a apporté des informations utiles sur l'origine et le comportement des « points chauds » potentiels. Il a ensuite permis une première approximation de l'hydrochimie des bassins versants, en facilitant l'association des régolites et des bassins d'eau. Cependant, c'est avec l'étude combinée finale du régolithe et des eaux, à travers des expériences de lixiviation et l'ensemble de la boîte à outils-traceurs, que nous avons pu identifier précisément deux contributions principales contrôlant les caractéristiques hydrochimiques et isotopiques du bassin, à savoir :

- Une contribution anthropique dérivée de l'atmosphère
- Apports de l'altération des phases minérales du régolithe, principalement des phases de plagioclase et de phosphate riche en Ca

Connaissant les compositions géochimiques et isotopiques de ces sources, nous avons ensuite pu évaluer la dynamique de la circulation de l'eau à l'échelle du bassin versant.

Contributions atmosphériques

Les contributions dérivées de l'atmosphère ont été identifiées dans les poussières atmosphériques, les horizons organiques du sol (0-45 cm de profondeur) et les sédiments par les enrichissements en Pb, As, Hg et Sb et $^{87}\text{Sr}/^{86}\text{Sr}$ entre 0.714-0.722, $^{143}\text{Nd}/^{144}\text{Nd}$ entre 0.51204 et des compositions isotopiques de 0,51208 et $^{206}\text{Pb}/^{207}\text{Pb}$ comprises entre 1,153 et 1,185, fréquemment associées à une teneur élevée en matière organique. Le fond « naturel » des ardoises de Weierbach était caractérisé par des concentrations relativement plus faibles dans les rapports Pb, As, Hg et Sb, $^{87}\text{Sr}/^{86}\text{Sr}$ et $^{206}\text{Pb}/^{207}\text{Pb}$ ($\sim 0,739$ et $\sim 1,2$ respectivement) et généralement $^{143}\text{Nd}/^{144}\text{Nd}$ ($\sim 0,5119$). Les isotopes de Pb et la combinaison des isotopes Sr-Nd ont permis de faire la distinction entre les contributions atmosphériques et les signatures minérales dans les eaux de captage.

Un faible $^{206}\text{Pb}/^{207}\text{Pb}$ trouvé dans les poussières atmosphériques et dans les compartiments de surface et de subsurface supérieure du bassin versant (horizon PPSD supérieur) indique un apport anthropique réel à ces compartiments qui sont également enrichis en Pb, Sb, As et Hg. D'autre part, des Pb anthropogènes plus anciens ont été détectés dans les eaux souterraines (GW1, GW5, GW6) par des rapports $^{206}\text{Pb}/^{207}\text{Pb}$ (1,14-1,146) et $^{206}/^{204}\text{Pb}$ (17,581-17,814 pour les GW comparée aux rapports > 18.72 pour l'ardoise) proches de ceux de Pb provenant de gisements australiens traditionnellement utilisés comme additif dans l'essence avant son interdiction au début des années 2000. Ces signatures trouvées dans les eaux souterraines n'étaient pas détectables dans les échantillons de poussière et de régolithe échantillonnés (en vrac, de lixiviat ou de résidus). Cependant, ils sont venus avec des enrichissements en Pb, Rb, SO_4^{2-} ou DOC dans la charge dissoute, initialement associés à des pluies acides et / ou des apports pluviométriques atteignant l'aquifère par des voies d'écoulement préférentielles. Compte tenu des teneurs élevées en COD

rapportées pour les eaux souterraines, nous suggérons que ce Pb soit lié aux complexes de matière organique en solution et / ou sur les parois rocheuses des aquifères et mobilisé selon la dynamique de saturation. La composition des éléments majeurs et des éléments traces dissous des solutions de sol et des cours d'eau a également montré un impact important de la chute. Dans ce cas, leurs rapports isotopiques étaient intermédiaires entre ceux des intrants anthropiques (actuels et anciens) et le fond naturel, indiquant un mélange des deux composants.

Contributions des altérations minérales

La partie inférieure de la PPSD et la SP contenaient des traces négligeables de dépôts atmosphériques, selon leurs compositions chimiques et isotopiques « naturelles ». Au lieu de cela, ils ont été définis par des produits géogènes.

La partie inférieure du PPSD (45-110 cm de profondeur) a été caractérisée par l'impact d'anciens événements volcaniques, comme en témoigne une minéralogie réfractaire (Ti-magnétite, chamosite, orthose) et des enrichissements en Nb et Ti. Cette minéralogie ne devrait pas contribuer grandement à la chimie des eaux, et montre donc peu de potentiel en tant que « point chaud » de l'interaction de l'eau. Cette suggestion a été appuyée par les faibles rendements obtenus pour la plupart des éléments chimiques dans les lixiviats de laboratoire de ces horizons. Cependant, les minéraux contenant des REE présents dans les horizons les plus bas de la PPSD, tels que la monazite et la florencite, ont été reconnus comme une réserve labile de REE. En effet, les eaux souterraines peu profondes autour de ces profondeurs (SS60, GW1), ne sont pas seulement affectées par la chute et la végétation, comme en témoignent leur richesse en chlorure et en sulfate, mais aussi par les plus hautes concentrations de REE. Les expériences de lixiviation effectuées sur tous les échantillons de PPSD ont suggéré que les patrons REE des solutions de sol sont en effet hérités de la PPSD. Les lixiviats et les solutions de sol (SS20 et SS60) ont été caractérisés par de légers enrichissements en MREE et des anomalies positives en Ce, indiquant que les horizons PPSD contiennent des MREE labiles et Ce, qui peuvent être mobilisés dans des conditions réductrices ou anoxiques probablement déclenchées par l'activité biologique. Il est intéressant de noter que les eaux GW1 collectées seulement pendant les conditions d'humidité à la profondeur de l'horizon PPSD4 (~ 108 cm) sont les plus enrichies en REE et montrent une anomalie en Ce négative. Nous suggérons que cela pourrait être simplement dû aux concentrations plus élevées et à la labilité de tous les autres REE par rapport à Ce dans PPSD4 ; et / ou un changement vers un environnement plus oxydant (comme en témoignent les propriétés gleyiques) à cette profondeur, permettant la précipitation de Ce.

La PPSD4 et l'ensemble du profil d'altération de l'ardoise (SP) ont été fortement affectés par la dynamique saisonnière de saturation de l'eau. Les patrons REE normalisés des matériaux

saprolitiques et des eaux qu'ils hébergent ont montré des enrichissements en MREE et des anomalies de Ce associés aux oxydes de Fe, Mn, indiquant l'impact des processus redox forts dus aux fluctuations de la nappe phréatique. De même, des rapports d'activité U très élevés (jusqu'à 2,2) dans les eaux stockées et circulant à travers la saprolite ont indiqué l'existence de fortes réactions chimiques d'altération, en particulier dans les puits GW1 et GW5 (près de 2,3). Ces rapports élevés d'activité en U s'expliquent par de longues interactions (comme c'est le cas pour les échantillons de flux de base) avec des réservoirs labiles, dont l'occurrence a été corroborée par les rapports d'activité élevés des échantillons L1 et L2 SP. Il est bien connu que la lixiviation préférentielle de ^{234}U par rapport à ^{238}U en raison de l'alpha-recul produit des eaux avec des rapports d'activité U élevés et des saprolites résiduelles avec des taux inférieurs. Nous suggérons en outre que l'effet de recul pourrait être renforcé dans l'ardoise de Weierbach en raison de la petite taille des minéraux en jeu, où une plus grande surface est disponible pour réagir et, par conséquent, produire des rapports d'activité U très élevés.

En effet, l'analyse isotopique Sr et Nd appliquée sur des échantillons d'eau et de régolithe en vrac et de lixiviat a permis d'élucider les deux phases minérales précitées contrôlant les compositions des eaux :

- (i) Plagioclase, avec une composition isotopique similaire à celle des échantillons de régolithe en vrac ($^{87}\text{Sr}/^{86}\text{Sr}$: 0,739, $^{143}\text{Nd}/^{144}\text{Nd}$: 0,5119)
- (ii) Phosphates contenant du Ca, avec un faible $^{87}\text{Sr}/^{86}\text{Sr}$ (0,715) et un maximum de $^{143}\text{Nd}/^{144}\text{Nd}$ (0,51225)

Ce n'est que grâce à l'utilisation combinée des isotopes Sr et Nd, et à l'aide des expériences de lixiviation, que l'élément terminal phosphaté contenant du Ca pourrait être identifié et distingué du phosphore atmosphérique, car ils ont des rapports $^{87}\text{Sr}/^{86}\text{Sr}$ très similaires. Cette information n'a pas pu être déduite de nos études individuelles de régolithe et d'eau, car il s'agit de phases métastables, difficiles à reconnaître par de simples analyses minéralogiques ou chimiques. Par conséquent, les expériences de lixiviation et en particulier les lixiviats L1 et L2 SP (et dans une moindre mesure PPSD4) ont été extrêmement utiles pour représenter l'altération naturelle des phases minérales de plagioclase et de Ca-P par les eaux, ce qui est suggéré d'être plus haut à les couches plus profondes. De plus, la suggestion selon laquelle les minéraux phosphatés contenant du Ca contribueraient grandement à la chimie des eaux était corroborée par la corrélation entre des rapports d'activité U plus élevés avec des compositions isotopiques Sr et Nd analogues à l'apatite. D'autres minéraux comme le mica ($^{87}\text{Sr}/^{86}\text{Sr} > 0,77$, $^{143}\text{Nd}/^{144}\text{Nd} \sim 0,51205$) ont été suggérés comme importants dans la composition isotopique du régolithe, en particulier dans les horizons SP supérieurs, mais pas dans la composition isotopique des eaux dissoutes.

Fonctionnement hydrologique selon les contributions définies contrôlant la chimie des eaux

Une fois définies les caractéristiques géochimiques et isotopiques des extrémités minérales et atmosphériques, nous avons pu suivre l'évolution des rapports isotopiques O, Sr, Pb et U dans les eaux collectées dans différentes conditions hydrologiques et évaluer la dynamique principale de circulation et de mélange de l'eau au profil et échelle de captage.

Nous avons observé que, pendant les conditions de débit de base (sec), le réservoir de PPSD est « sec » et que l'eau du cours d'eau est principalement alimentée par les eaux souterraines profondes « permanentes ». Plus précisément, les eaux de puits GW5 du plateau se sont avérées être la principale source contribuant au flux, qui présentait des compositions isotopiques $^{87}\text{Sr}/^{86}\text{Sr}$ (0.716) et $^{206}\text{Pb}/^{204}\text{Pb}$ (18.165) tout aussi faibles que les autres eaux GW et rapports d'activité $^{234}\text{U}/^{238}\text{U}$ (1.6) maximaux. Cette suggestion a été appuyée par des compositions de carbonate et de Mg-bicarbonate dans les courses d'eau (SW et les eaux souterraines du fond (GW2, GW3) similaires à celles de GW5. En conditions sèches, de longs temps de séjour et l'absence de dilution par de nouvelles eaux entraîneront de fortes réactions aux intempéries dans les aquifères saturés en permanence (comme en témoignent les taux d'activité élevés) impliquant des minéraux riches en calcium tels que le plagioclase ou les apatites et du CO_2 libérée par l'activité bactérienne. En effet, bien qu'il n'y ait pas de minéraux carbonatés primaires dans notre système, la première expérience de lixiviation a clairement indiqué la présence de phases très labiles contenant du Ca, comme les carbonates secondaires.

Au contraire, nous avons montré que lorsque la saturation augmente dans le bassin versant et que nous passons des conditions de base à haut débit, les compositions isotopiques des eaux souterraines et des cours d'eau se rapprochent de celles des SS, indiquant une connectivité élevée du système. Ceci était également observable dans la tendance de toutes les eaux souterraines et de ruisseau provenant des compositions de bicarbonate à sulfate-chlorure comme celles des compartiments souterrains supérieurs (SS et GW1 ou GW6). Néanmoins, nous avons pu noter que les différents réservoirs (PPSD et GW plus profonds) restent isotopiquement différents même lorsqu'ils sont connectés. Cela nous a permis de distinguer que, dans des conditions de débit élevé (et maximal), le réservoir SS contribue à la composition isotopique du cours d'eau, qui adopte alors des rapports $^{87}\text{Sr}/^{86}\text{Sr}$ et $^{206}\text{Pb}/^{204}\text{Pb}$ plus élevés (0,717 et 18,22 respectivement) et des rapports d'activité $^{234}\text{U}/^{238}\text{U}$ comparativement bas (1,4).

Les variations observées dans $\delta^{18}\text{O}$ indiquent que le bassin de Weierbach se comporte comme un système plutôt ouvert et bien connecté. Cependant, dans notre étude, ce traceur n'a pas permis de différencier davantage les réservoirs contribuant au cours d'eau dans différentes conditions hydrologiques. Ici, la caractérisation d'un membre final anthropogénique dérivé de l'atmosphère, en particulier à travers les isotopes de Pb, a été particulièrement utile pour déterminer les sources

contributives. Cependant, il faut noter que ni les poussières forestières ($^{87}\text{Sr}/^{86}\text{Sr} = 0,713726$, $^{234}\text{U}/^{238}\text{U} = 1,0057$) ni les chutes ($^{87}\text{Sr}/^{86}\text{Sr} = 0,71166$, $^{234}\text{U}/^{238}\text{U} = 1,1192$) n'ont un impact direct sur la dynamique isotopique des échantillons d'eau, mais indirecte à travers les réservoirs PPSD ou SP « contaminés ». Par conséquent, ces résultats isotopiques ne permettent pas de confirmer les hypothèses précédentes sur la contribution directe des précipitations sur le cours d'eau du Weierbach lors des orages (Martínez-Carreras et al., 2016 ; Wrede et al., 2015).

D'autre part, le fait que les signatures SS se trouvent dans le cours d'eau indique qu'une partie de ces eaux a traversé un écoulement latéral sous la surface ou à travers le substrat rocheux fracturé, en contournant les autres réservoirs. Ces résultats corroborent les conclusions antérieures de Martínez-Carreras et al. (2016) et Scaini et al. (2017), qui suggère la contribution des réservoirs de PPSD à travers l'interface PPSD-SP ou les fractures du substratum rocheux dans des conditions de forte saturation dans le bassin versant de Weierbach. La mesure dans laquelle ces contributions proviennent spécifiquement du plateau ou des zones de collines, comme suggéré par Martínez-Carreras et al (2015), ne peut être évaluée ici en raison du manque de données isotopiques SS autour du bassin versant. Un échantillonnage amélioré pour le bassin versant du Weierbach, y compris les transects de pente, serait idéal pour une telle évaluation des isotopes radiogéniques complémentaires. Néanmoins, il faut considérer que, dans le cas du bassin versant du Weierbach et des conditions hydrologiques considérées ici, les isotopes radiogéniques ne semblent pas permettre des études hydrologiques à l'échelle temporelle d'un orage, mais uniquement « saisonnières ».

Perspectives

En résumé, l'étude simultanée du régolithe (y compris les apports atmosphériques) et des eaux par l'utilisation combinée de données isotopiques et chimiques a permis de mieux comprendre le puzzle de la zone critique en renseignant sur les mécanismes responsables du relargage et du transport du soluté. À notre connaissance, ce travail vise le tout premier traçage d'un système hydrologique complet avec des concentrations d'éléments traces et les isotopes radiogéniques Sr-Nd-Pb-U, qui sont présentés comme un outil complémentaire fiable des principaux éléments et isotopes O-H pour l'étude des processus hydrologiques souterrains.

En perspective, ce type d'étude pourrait être étendu en développant la caractérisation de aspects microscopiques telles que les phases minérales métastables et les complexes colloïdaux (organiques / inorganiques), susceptibles de contrôler le comportement des éléments traces au cours des processus de météorisation et de transport. En ce sens, la surveillance du potentiel redox

dans les différents réservoirs serait également intéressante pour mieux comprendre la chimie de l'eau des éléments traces et des terres rares.

D'autre part, l'extension des échantillonnages sur le terrain vers des échelles spatiales plus représentatives, telles que les transects de pente, y compris les points d'échantillonnage des eaux souterraines, terrestres et riveraines, permettrait une évaluation plus précise de la connectivité à l'échelle des bassins versants. Ceci, conjointement avec le calcul des flux élémentaires et / ou des taux d'altération, peut permettre l'utilisation d'éléments traces et de rapports isotopiques pour le développement d'analyses de mélange d'éléments finaux plus réalistes (EMMA) et de modèles hydrologiques. La combinaison d'éléments traces et d'isotopes radiogéniques comme traceurs hydrologiques spatiaux avec des isotopes stables O et H mis en œuvre dans les calculs de temps de transit (/résidence) montre un grand potentiel pour améliorer notre compréhension du fonctionnement des bassins versants.

Naturellement, la question se pose de savoir si les concentrations et la variabilité temporelle des isotopes radiogéniques, ainsi que les coûts analytiques seraient une limitation pour les études hydrologiques dans différents bassins versants. Des bassins de différentes tailles et propriétés de subsurface offriront différentes possibilités pour ce type d'études. Enfin, il faut noter que même pour un même bassin versant, différentes typologies d'inondation (en fonction de l'intensité des précipitations et des conditions d'humidité antécédentes) devraient être considérées afin d'évaluer l'utilité des isotopes radiogéniques comme traceurs hydrologiques.

Cristina MORAGUES-QUIROGA

**Water mixing processes in the
Critical Zone: evidence from trace
elements and Sr-Nd-Pb-U isotopes**

Résumé

Les fonctions hydrologiques de captage, stockage et rejet d'eau ont des signatures géochimiques dans les cours d'eau reflétant énormément celles trouvées dans les compartiments de la zone critique. Ces signatures sont fortement contrôlées par des processus bio-géophysico-chimiques produits dans l'interface régolite-plante. Jusqu'à présent, les recherches sur régolithes et processus hydrologiques sont restées largement découplées - conduisant à une utilisation généralisée de traceurs non conservateurs d'origines multiples, bloquant ainsi notre capacité à identifier les sources et les voies d'écoulement d'eau. Nous étudions ici le mélange d'eau dans la subsurface à travers un portefeuille unique de traceurs (éléments traces et isotopes O-H-Sr-Nd-Pb-U) permettant d'étudier les processus d'évolution du régolithe et le transport des solutés dans la zone critique. Nous signalons l'intérêt de cette approche pour renforcer la caractérisation des sources et voies d'écoulement d'eau.

Zone critique ; Régolithe ; Éléments traces ; Isotopes O-H-Sr-Nd-Pb-U ; Stockage d'eau ; Écoulement d'eau ; Source d'eau ; Interactions eau-roche.

Résumé en anglais

Catchment hydrological functions of water collection, storage and release have geochemical signatures in stream water largely mirroring those found in critical zone compartments. These signatures are strongly controlled by the different bio-geo-physico-chemical processes that occur within the regolith-plant interface. Until now, investigations into the critical zone's regolith and hydrological processes research have largely remained uncoupled –leading to a widespread use of non-conservative tracers with multiple origins and thereby stymieing our capability for identifying water pools and flow paths. Here we study the mixing of water in the subsurface through a unique portfolio of complementary groups of tracers (trace elements O-Hand Sr-Nd-Pb-U isotopes) which enables investigating regolith evolution processes and solutes transport within the critical zone. We report the interest of this approach to strengthen water flowpaths and end-members characterization.

Critical zone; regolith; trace elements; O-H-Sr-Nd-Pb-U isotopes; water storage; water flowpaths; water sources; water-rock interactions.